Geometry and dynamics of coherent structures in the stably stratified atmospheric boundary layer

Dissertation
zur Erlangung des Grades eines
Doktors der Naturwissenschaften
(Dr. rer. nat.)

am Fachbereich Mathematik und Informatik
der Freien Universität Berlin

vorgelegt von
Abhishek Paraswarar Harikrishnan

Berlin 2023

Erstgutachterin & Betreuerin	**Prof. Dr. Nikki Vercauteren**
	Universität zu Köln
	Mathematisch-Naturwissenschaftliche Fakultät
	Department Geowissenschaften
	Pohligstraße 3
	50969 Köln, Deutschland
Zweitbetreuer	**Prof. Dr.-Ing. Rupert Klein**
	Freie Universität Berlin
	Fachbereich Mathematik und Informatik
	Institut für Mathematik
	Arnimallee 6
	14195 Berlin, Deutschland
Zweitgutachter	**Prof. Dr. Elie Bou-Zeid**
	Princeton University
	Department of Civil and Environmental Engineering
	E209A Engineering Quadrangle
	Princeton, New Jersey 08544 USA
Tag der Disputation:	**08.09.2023**

Declaration of authorship

Name: Paraswarar Harikrishnan

First name: Abhishek

I declare to the Freie Universität Berlin that I have completed the submitted dissertation independently and without the use of sources and aids other than those indicated. The present thesis is free of plagiarism. I have marked as such all statements that are taken literally or in content from other writings. This dissertation has not been submitted in the same or similar form in any previous doctoral procedure.

I agree to have my thesis examined by a plagiarism examination software.

Date: Signature:

Abstract

Turbulence in stable boundary layers (SBL) is often accompanied by the presence of large patches of non-turbulent flow regions, even close to the wall, a phenomenon referred in literature as global intermittency. Understanding the physical processes and dynamics of this mode of rotating, stratified and intermittent turbulence is important for the improvement of existing and/or development of new parametrizations of the SBL, which in turn, may be useful for many applications, including but not limited to numerical weather prediction, modeling gas dispersion events and understanding the Arctic climate system. In this thesis, the SBL is investigated by establishing a detailed comparison with the well-studied neutrally stratified atmospheric boundary layer. The datasets examined here were inherited through the work of Ansorge (Dissertation, Springer 2016). They used a simplified physical configuration, namely, an Ekman flow over a smooth wall where global intermittency is known to occur beyond a certain stability despite the absence of surface heterogeneities and other external perturbations.

Comparisons between both regimes is accomplished with the help of coherent structures, particularly with their geometry. This is motivated from previous observations where a change in the geometry of these structures from hairpin vortices under neutral conditions to thermal plumes under unstable conditions (where there is a positive buoyancy flux) has been detected. However, very little is known about the geometry of these structures, especially their three-dimensional character, when buoyancy has a stabilizing effect. Since a well-accepted definition of a coherent structure has not yet surfaced, the classification of boundary layer structures introduced by Robinson (Dissertation, Stanford 1991), henceforth referred to as Robinson structures, is used to study the various structures identified in literature in an organized manner. Suitable scalar indicators are identified for all eight categories of Robinson structures and they are grouped as quantitative and qualitative, the former of which can be extracted and geometrically characterized.

First, a framework to characterize the geometry of quantitative Robinson structures is developed. There are two main steps: extraction and geometrical characterization. In the extraction step, individual structures are obtained by thresholding scalar indicators. An improvement to the neighbor scanning procedure of Moisy and Jiménez (J. Fluid Mech. 2004) with the marching cubes algorithm is developed to extract visualization accurate structures. Optimum thresholds are identified with the percolation analysis approach of Del Álamo et al. (J. Fluid Mech. 2006). However, it is seen that this fails when the flow is strongly intermittent. Therefore, an extension of this method where percolation analysis is applied in an iterative manner is introduced. In the second step, noise-like structures are filtered out by discarding structures having a fractal dimension less than 1. The remaining structures are subjected to the non-local methodology of Bermejo-Moreno and Pullin (J. Fluid Mech. 2008) to classify a structure as blob-like, tube-like or sheet-like based on its location within a three-dimensional visualization space composed of two differential geometry parameters - shape index and curvedness, and a stretching parameter.

Next, the framework is applied to structures obtained from instantaneous neutral and stably stratified Ekman flow fields with increasing stability. Results are discussed by dividing the flow field into four layers in the wall-normal direction: viscous sublayer, buffer, inner and outer layers. Geometrical characterization reveals that the structures are moderately stretched

tube-like or moderate to strongly stretched sheet-like regardless of the strength of stratification. Furthermore, in the strongly stratified case, it is shown that global intermittency has a direct impact in the viscous sublayer where a large portion of the domain is occupied by a single low-speed streak which is reminiscent of the non-turbulent region aloft. Conclusions derived from the geometrical characterization are also compared with those obtained from conditional one-point statistics. To this end, a new definition of intermittency factor based on coherent structures is proposed to segregate the flow into turbulent and non-turbulent parts.

Since global intermittency is known to exhibit spatio-temporal variability, it may have an impact on the dynamics of coherent structures which can induce changes in their geometry. The geometrical characterization framework is modified with the addition of a region-based tracking procedure where correspondence is determined by measuring the degree of spatial overlap. Starting with structures having a similar geometry, i.e., with similar shape index, curvedness and stretching parameters from the instantaneous Ekman fields analyzed previously, the Robinson structures are tracked in time and temporal changes in their geometry are recorded. Similar to previous observations, these results also suggest mostly tube-like and sheet-like geometry for all Ekman flow cases. While all these results indicate that the geometry is mostly unaffected for increasing stability, the presence of non-turbulent flow patches that extend throughout the vertical length of the flow alters the spatial organization of coherent structures. This is particularly visible for hairpin-like vortex structures, whose abundance increases with stability and at the strongest stratification the head regions of these structures appears to be oriented in similar directions in the turbulent patches.

Finally, the orientation and abundance of hairpin-like structures are investigated. The region-based tracking scheme is improved to overcome the limitation of using a constant threshold in time by dynamically adjusting the thresholds such that the feature can freely grow or shrink in time. This is used to track hairpin-like structures from both neutral and stably stratified cases. Results show that the hairpin-like structures experience longer lifetime and higher number of interactions with increasing stability and a link between the number of split events and the autogeneration mechanism is proposed to be the underlying cause of the abundance of hairpins with increasing stability. To gain a better understanding of the dynamics, hairpin-like structures are also studied with a slender vortex filament approach, i.e., a vortex filament whose diameter d is much smaller than its characteristic radius of curvature R. The corrected thin-tube model of Klein and Knio (J. Fluid Mech. 1995) is used to calculate the motion of these filaments with the mean velocity profiles of the Ekman flow as the background flow. These results suggest that orientation of the filament in the spanwise direction is linked to its initial starting height under stable stratification whereas no such dependency can be observed with the neutrally stratified background flow.

Zusammenfassung

Die Turbulenz in stabilen Grenzschichten (SG) geht häufig mit dem Vorhandensein großer Bereiche nichtturbulenter Strömungsregionen selbst in Wandnähe einher, ein Phänomen, das in der Literatur als globale Intermittenz bezeichnet wird. In dieser Arbeit wird die SG untersucht, indem ein detaillierter Vergleich mit der gut untersuchten neutral geschichteten atmosphärischen Grenzschicht angestellt wird. Die hier untersuchten Datensätze stammen aus der Arbeit von Ansorge (Dissertation, Springer 2016). Sie verwendeten eine vereinfachte physikalische Konfiguration, nämlich eine Ekman-Strömung über einer glatten Wand, bei der bekanntlich jenseits einer bestimmten Stabilität eine globale Intermittenz auftritt.

Vergleiche zwischen beiden Regimen werden mit Hilfe kohärenter Strukturen, insbesondere ihrer Geometrie, durchgeführt. Wurde die von Robinson (Dissertation, Stanford 1991) eingeführte Klassifizierung von Grenzschichtstrukturen erwendet, die im Folgenden als Robinson-Strukturen bezeichnet werden, um die verschiedenen in der Literatur identifizierten Strukturen in geordneter Weise zu untersuchen. Es wird ein Rahmen für die Charakterisierung der Geometrie von Robinson-Strukturen entwickelt. Einzelne Strukturen werden aus Skalarfeldern extrahiert, und die nichtlokale Methodik von Bermejo-Moreno und Pullin (J. Fluid Mech. 2008) wird verwendet, um eine Struktur als tropfen-, röhren oder blattartig zu klassifizieren.

Anschließend wird der Rahmen auf Strukturen angewandt, die sich aus momentanen neutralen und stabil geschichteten Ekman-Strömungsfeldern mit zunehmender Stabilität ergeben. Die geometrische Charakterisierung zeigt, dass die Strukturen unabhängig von der Stärke der Schichtung mäßig gestreckt röhrenförmig oder mäßig bis stark gestreckt blattförmig sind. Die aus der geometrischen Charakterisierung abgeleiteten Schlussfolgerungen werden auch mit denen verglichen, die sich aus der bedingten Ein-Punkt-Statistik ergeben. Zu diesem Zweck wird eine neue Definition des Intermittenzfaktors auf der Grundlage kohärenter Strukturen vorgeschlagen.

Da die globale Intermittenz bekanntermaßen eine räumlich-zeitliche Variabilität aufweist, kann sie sich auf die Dynamik kohärenter Strukturen auswirken, was zu Veränderungen ihrer Geometrie führen kann. Der Rahmen wird durch die Hinzufügung eines regionenbasierten Verfolgungsverfahrens modifiziert, und die Robinson-Strukturen werden zeitlich verfolgt, wobei zeitliche Veränderungen ihrer Geometrie aufgezeichnet werden. Diese Ergebnisse deuten ebenfalls darauf hin, dass die Geometrie in allen Fällen der Ekman-Strömung überwiegend röhren- und flächenförmig ist. Das Vorhandensein von nicht-turbulenten Strömungsfeldern, die sich über die gesamte vertikale Länge der Strömung erstrecken, verändert die räumliche Organisation der kohärenten Strukturen und ist besonders bei haarnadelartigen Wirbelstrukturen sichtbar, deren Häufigkeit mit der Stabilität zunimmt, und bei der stärksten Schichtung scheint der Kopfbereich dieser Strukturen in den turbulenten Teile in ähnliche Richtungen ausgerichtet zu sein. Schließlich werden die Ausrichtung und Häufigkeit haarnadelartiger Strukturen untersucht. Ersteres wird mit einem neuartigen Verfolgungsschema untersucht, das die Beschränkung der Verwendung eines zeitlich konstanten Schwellenwerts überwindet, indem die Schwellenwerte dynamisch angepasst werden, so dass das Merkmal im Laufe der Zeit frei wachsen oder schrumpfen kann, und letzteres mit einem schlanken Wirbelfadenansatz.

Dedicated to,
my parents Vijaya and Harikrishnan,
my wife Srishti.

Table of Contents

Title Page i

Abstract iv

Zusammenfassung vi

List of Figures xiii

List of Tables xxiii

Abbreviations xxv

Symbols xxvii

1 Background and introduction 1

1.1 The atmospheric boundary layer . . . 1
1.2 Turbulence and global intermittency in the SBL . . . 3
1.3 A structure-based approach to study the ABL . . . 6
1.4 Simulation database . . . 8
1.5 Research objectives . . . 11
1.6 Outline . . . 15
1.7 Related works . . . 15

2 A framework for the geometrical characterization of coherent structures 17

2.1 Robinson's taxonomy of boundary layer structures . . . 18
2.1.1 Streaks . . . 18
2.1.2 Sweeps and ejections . . . 20
2.1.3 Vortices . . . 21
2.1.4 Shear layers and backs . . . 24
2.1.5 Pockets . . . 24
2.1.6 Bulges . . . 24
2.2 Extraction of structures from scalar fields . . . 25
2.2.1 Neighbor scanning algorithm . . . 25
2.2.2 Marching cubes correction . . . 26
2.2.3 Validation of the NS+MC algorithm . . . 29
2.3 On the choice of a threshold . . . 30
2.3.1 Multilevel percolation analysis . . . 32

2.4 Geometrical characterization . . . 35
2.4.1 Fractal dimension . . . 35
2.4.2 Shape index, curvedness, stretching . . . 37
2.4.3 Visualization space . . . 38
2.5 Summary and conclusions . . . 40

3 Geometry of Robinson structures in stratified Ekman flows 43
3.1 Geometry of structures in the ABL . . . 45
3.1.1 Viscous sublayer . . . 45
3.1.2 Buffer layer . . . 49
3.1.3 Inner and outer layer . . . 53
3.1.4 $\delta-$scale structures . . . 54
3.1.5 Hairpin-like structures . . . 58
3.2 A general definition of intermittency factor for wall-bounded flows . . . 61
3.3 Conditional one-point statistics . . . 63
3.4 Physical interpretation and discussion . . . 64
3.5 Summary and conclusions . . . 68

4 Temporal evolution of the geometry of Robinson structures 71
4.1 Methodology for tracking coherent structures in time . . . 74
4.1.1 Tracking procedure for individual structures . . . 74
4.1.2 Tracking procedure for interactions . . . 75
4.1.3 Validation of the tracking procedure with interactions . . . 77
4.2 Temporal evolution of geometry of Robinson structures in the ABL . . . 77
4.2.1 Results and discussion . . . 80
4.3 Temporal evolution of hairpin-like structures . . . 83
4.3.1 Multilevel percolation thresholding in time (MLPT) . . . 84
4.3.2 Comparison of tracking results with constant and MLPT thresholds . . . 86
4.3.3 MLPT tracking applied to the Ekman flow cases . . . 87
4.4 Summary and conclusions . . . 90

5 A thin filament approach for the dynamics of hairpin structures 93
5.1 Slender vortex filaments . . . 95
5.1.1 Thin filament approximations . . . 96
5.2 Numerical schemes . . . 98
5.2.1 Local Induction Approximation . . . 98
5.2.2 Corrected thin-tube model . . . 99
5.3 Validation of the slender vortex filament code . . . 103
5.3.1 Sinusoidal plane curve test . . . 103
5.3.2 Hairpin evolution in stagnant background flow . . . 105
5.3.3 Hairpin evolution in shear flow . . . 110
5.4 Hairpin evolution in ABL background flow . . . 110
5.4.1 Background flow profiles and initial conditions for the simulation . . . 112
5.4.2 Temporal evolution of hairpin filaments in the outer layer . . . 114

5.4.3 Evolution of hairpin filaments at other heights . . . 118
5.5 Comparison with MLPT tracking . . . 119
5.6 Summary and conclusions . . . 122

6 Summary and conclusions **125**
6.1 Geometry of coherent structures with increasing stability . . . 125
6.2 Abundance and similar orientation of hairpin-like structures . . . 128
6.3 Computing facilities . . . 129
6.4 Future perspectives . . . 130

References **137**

Appendix A Grouping indices for marching cubes correction **149**

Appendix B Surface curvature **151**
B.1 Regular surfaces and fundamental forms . . . 151
B.2 Principal, Gaussian and mean curvatures . . . 152
B.3 Shape index and curvedness . . . 154

Appendix C Geometry of structures for case S_2 and S_3 **157**
C.1 Viscous sublayer . . . 157
C.2 Buffer layer . . . 159
C.3 Inner and outer layer . . . 161
C.4 $\delta-$scale structures . . . 163
C.5 Hairpin-like structures . . . 164

Appendix D Supporting results for chapter 4 **165**

Appendix E Data and code availability **167**

List of Figures

1.1 The Atmospheric Boundary Layer highlighted by naturally generated fog showing intermittent patches. The picture is an own work of the author captured in Gif-sur-Yvette, France. 2

1.2 Horizontal vorticity magnitude slices normalized with its RMS over that slice are shown here at $y^+ \approx 100$ ($(\cdot)^+$ indicates wall units) for 1/6 of the full simulation domain. (a, b, c, d) correspond to the neutrally stratified case N and the stably stratified cases S_1, S_2, S_3 respectively. All simulation cases are described in table 1.3. 4

1.3 The schematic shows the three types of grids - A, B and C used in the paper. x, y, z correspond to the streamwise, wall-normal and spanwise directions respectively. $(\cdot)^+$ indicates viscous units as described in (1.6). 12

2.1 Isosurfaces of $u' < \tau_p$ representing the low-speed streaks are shown here. (a, b, c, d) correspond to the neutrally stratified case N and stably stratified cases S_1, S_2, S_3 respectively. Computation of τ_p for low-speed streaks is described in section 2.3. The streaks are visualized for 1/3 of the computational domain until $y^+ \approx 1550$. 19

2.2 Definition of quadrants of the instantaneous $u'v'$ plane. Figure adapted from Robinson (1991). 20

2.3 A vertical slice for the entire wall-normal height of the simulation is shown for (a) finite-time Lyapunov exponent and (b) vorticity magnitude corresponding to case S_1. T and NT denote turbulent and nonturbulent regions respectively. 21

2.4 A comparison among (a) Q, (b) λ_2 and (c) Δ vortex criteria are shown here for a small subset of channel flow data obtained from the Johns Hopkins Turbulence Database (Graham et al., 2016). All three criteria are visualized at the equivalent thresholds proposed by Chakraborty et al. (2005) (see equation 5.2). The thresholds are $\tau = 49, -49, 4357.37$ for Q, λ_2 and Δ criterion respectively. 22

2.5 Two random hairpin-like structures are extracted from different regions of the flow for the case S_1. (a) shows $Q-$criterion structures oriented in similar directions and (b) shows structures identified with FTLE also oriented in similar directions. In both cases, the horizontal slice is at $y^+ \approx 10$. 23

2.6 A drawback of the NS algorithm is shown here where two individual structures (colored blue and red) is misidentified as a single structure. Examining a plane reveals the reason for the misidentification and is shown in the right. When a point belonging to the blue structure (at the tail end of all arrows) is considered to be the center of the 3×3 cube, one of its neighbors is a point belonging to the red structure. 25
2.7 Difference between continuous and discontinuous mesh. 26
2.8 Examples of surface mesh generation for (a) continuous surface mesh corresponding to case 49 and (b, c, d) discontinuous mesh surfaces corresponding to cases $53, 37$ and 90 respectively. 26
2.9 Algorithm for the extraction of individual structures from scalar fields with neighbor scanning algorithm and marching cubes correction 28
2.10 Sample Q-critrion data chosen for validation of the NS+MC algorithm. Here structures are visualized at thresholds $\tau = 100$ (Left), 549 (Right). Clearly, the complexity of structure extraction increases for lower thresholds. 29
2.11 A comparison among the surface extraction algorithm (square marker), NS+MC algorithm (diamond marker) and NS algorithm (circle marker) for (a) extraction of structures at various thresholds and (b) the time taken for extraction are shown here. 29
2.12 Percolation analysis on seven indicators from table 2.1 are shown here. (a - g) are the high-speed streaks, low-speed streaks, sweeps, ejections, vortices, shear layers and backs. Solid line is the neutrally stratified case (N) and the dashed and dotted lines are the various stably stratified cases (S_1, S_2, S_3). Line specification is shown in (a). Red portion of the lines indicate the region of percolation transition. 31
2.13 The $Q-$criterion structures are highlighted for case N. Isosurfaces at (a) $\tau = 0.0017$ and (b) $\tau = 10$ are visualized. In the latter case, the effect of nondimensionalization with the RMS over every wall normal planes is visible and structures are highlighted throughout the flow. Here, the $y^+ \approx 1550$ which includes a significant portion of the outer layer. 32
2.14 When $Q-$criterion applied to case S_1 and thresholded at the global percolation threshold τ_p, an entire cluster colored in gold is identified as a single structure as shown in (a). A small region chosen for MLP analysis is shown in (b) and the result is shown in (c). 33
2.15 A schematic for MLP is shown. Here, τ_p is the global percolation threshold and $\langle D_\alpha \rangle$ is the mean fractal dimension (see subsection 2.4.1 for an explanation) of the structure. When $V_{\max}/V > 0.5$ for the entire threshold range, then the structure is classified as simple and the minimum threshold is chosen for the structure. If the structure is deemed complex, the procedure is repeated. 33
2.16 The effect of choosing a minimum value of the ratio $V_{\max}/V$ as (a) 1 and (b) 0.5 respectively is shown. A proof-of-concept for MLP is shown in (c). The highlighted thresholds correspond to $\tau = 0.0625, 0.334, 3.01$. 35

2.17 The $Q-$criterion scalar fields for case N are reconstructed for (a) $\langle D_Q \rangle < 1$, (b) $1 \leq \langle D_Q \rangle \leq 2$ and (c) $\langle D_Q \rangle > 2$. 36
2.18 Probability density function of the mean fractal dimension $\langle D_Q \rangle$ for the neutrally stratified case is shown here. Box-counting is performed for grid B until $y^+ \approx 1550$. 36
2.19 For the torus shown in (a), the jpdf of S and C, along with their marginal p.d.f. (top and right side of the plot respectively) are shown in (b). The stretching parameter λ is shown below the plot. The gray marker indicates the mean and the red marker indicates the feature center. The errorbars show the upper and lower distances which can be computed from (2.12). Figure is based on the work of Bermejo-Moreno and Pullin (2008). 38
2.20 Workflow for the geometrical characterization of an individual structure 39
2.21 The three-dimensional visualization space along with a set of two-dimensional orthogonal projections composed of $\lambda\hat{C}$ and $\hat{S}\hat{C}$ is shown in panel (a). The scatter markers are colored by the cluster labels identified with the K-means algorithm. This figure is adapted from the work of Bermejo-Moreno and Pullin (2008). The non-local shape index ($\hat{S}$) is shown in panel (b) for some common structures like a sphere (A), ellipsoid (B), torus (C), cylinder (D), and the Robinson structures ($E-K$) for case N. Coloring of the structures is according to table 2.1. 40

3.1 Isosurfaces of $u' < 0$ (low-speed streak) and $u' > 0$ (high-speed streak) are shown for case (a) N and (b) S_1 in the viscous sublayer with grid C. The color specification for the structures is according to table 2.1 for the low-and high-speed streak. The longest structure for the former is highlighted with light green and the longest structure for the latter is highlighted in pale yellow. . . . 45
3.2 Joint p.d.f. of the streamwise (Δx^+) and the spanwise (Δz^+) coherence for (a) high-speed streaks, (b) low-speed streaks, (c) sweeps and (d) ejections. The neutrally stratified case N is represented by solid line (—) and the stably stratified cases S_1, S_2, S_3 are represented by dotted (...), dashed (- - -) and dash patterned (– — –) lines respectively. 46
3.3 Contour plots for case N are shown with (a) ejections and low-speed streaks, (b) sweeps and low-speed streaks at $y^+ \approx 3.58$ with grid C. The color specification is according to table 2.1. 46
3.4 Contour plots for case S_1 are shown with (a) ejections and low-speed streaks, (b) sweeps and low-speed streaks at $y^+ \approx 3.58$ with grid C. The color specification is according to table 2.1. 47
3.5 Three pocket regions are highlighted with diverging streamlines for (a) case N and (b) case S_1 at $y^+ \approx 3.58$. Overlayed are sweeps and ejections. Color specification for sweeps and ejections are according to table 2.1. 48

3.6 Visualization space for all quantitative Robinson structures except backs are shown with joint pdfs for the buffer layer. From (a - f) are the high-speed streaks, low-speed streaks, sweeps, ejections, vortices and shear layers. The geometry of structures is compared with case N (unfilled contours with dashed lines) and case S_1 (filled cotours). The number of structures for each contour level is indicated in black for case N and dark blue for case S_1. Numbers within paranthesis (a - d) are those which start from the viscous sublayer and end in the buffer layer. Numbers outside paranthesis are those which start and end within the buffer layer itself. $\hat{S}, \hat{C}, \lambda$ are the shape index, curvedness and stretching parameters respectively. 51
3.7 Sheet-like shear layers are visualized with blue isosurfaces of vorticity magnitude. Q-criterion contours are shown in red at the global percolation threshold. . . . 52
3.8 Isosurfaces of vorticity magnitude extracted from case S_1 are shown on the left column to illustrate (a) tube-like structure and (b) sheet-like structure. On the right column, a velocity vector plot is shown which shows that the tube-like structures are vortex regions whereas sheet-like structures are shearing regions. 52
3.9 Visualization space to geometrically characterize vorticity magnitude structures. Here, A and B are examples of tube-like and sheet-like structures, both of which are visualized in figure 3.8 (a, b) respectively. $\hat{S}, \hat{C}, \lambda$ are the shape index, curvedness and stretching parameters respectively. 53
3.10 Similar to the previous subsection, the visualization space for all quantitative Robinson structures except backs are shown with joint pdfs for the inner and outer layer. From (a - f) are the high-speed streaks, low-speed streaks, sweeps, ejections, vortices and shear layers. The geometry of structures is compared with case N (unfilled contours with dashed lines) and case S_1 (filled cotours). The number of structures for each contour level is indicated in black for case N and dark blue for case S_1. Numbers which are within paranthesis (a - d) are those which start from the viscous sublayer and end in the outer layer. Numbers outside paranthesis are those which start beyond the buffer layer and end within the outer layer. $\hat{S}, \hat{C}, \lambda$ are the shape index, curvedness and stretching parameters respectively. 56
3.11 A hairpin packet is visualized with Q-criterion for case N at the percolation threshold. An example sheet-like shear layer structure is shown in blue. A vertical contour slice of vorticity magnitude colored red highlights shear layer structures. 56
3.12 Visualization space for backs is shown for case N with unfilled contours and S_1 with filled contours. The number of structures between contours are indicated in dark blue for case S_1 and black for case N. $\hat{S}, \hat{C}, \lambda$ are the shape index, curvedness and stretching parameters respectively. 56
3.13 Vorticity magnitude contours along the (x, y) plane are shown here for (a) case N and (b) case S_1 for grid A until $y^+ \approx 1550$. In each case, a $\delta-$scale bulge is highlighted. The wall-normal direction is exaggerated three times to show the structures clearly. 57

3.14 The top panel shows isosurfaces of Q-criterion at $\tau = 0.6$ for case S_1 until $y^+ = 200$. The blue arrow points towards the streamwise direction whereas the white arrow is an approximate orientation of the majority of hairpin-like structures. Similarly, Q-criterion isosurfaces are visualized for cases (a) S_2 and (b) N in the bottom panel until $y^+ = 200$. 57
3.15 Visualization of a hairpin packet with the Q-criterion at τ_p is shown for case N. The blue structure between the legs of the primary hairpin is the low-speed streak. Q_2 and Q_4 indicate ejection and sweep events respectively (bottom right visualization). A pocket structure is highlighted on the bottom left. Velocity vector plots for both legs of the primary hairpin are visualized on the top left and top right. 58
3.16 Side view of the hairpin packet visualized in figure 3.15 is shown here. The angle between the line connecting the head of the hairpin-like structures and the wall is the growth angle θ. 59
3.17 The geometry of 100 hairpin-like structures are compared in the visualization space for case N and S_1. Isosurfaces of two tube-like examples from each case are shown on the right. Filled contours represent case S_1 whereas unfilled contours represent case N. $\hat{S}, \hat{C}, \lambda$ are the shape index, curvedness and stretching parameters respectively. 60
3.18 Intermittency profiles are shown with various values of ω_{τ_p}. In (a), ω is used as an indicator for case N without nondimensionalization with its RMS over every wall-normal plane. (b) shows the same indicator again for case N with nondimensionalization. (c, d, e, f) show the Q-criterion as an indicator with nondimensionalization for case N, S_1, S_2, S_3 respectively. Dashed lines from left to right indicate increasing values of the threshold starting from 0. Solid lines show the global percolation threshold. 62
3.19 Vertical profiles of conditional one-point statistics applied to (a) high-speed streaks, (b) low-speed streaks, (c) sweeps and (d) ejections are shown here. Black profiles indicate turbulent regions and teal profiles correspond to the non-turbulent regions. 63
3.20 Vertical profiles indicating the fraction of the volume occupied by high- and low-speed streaks are shown on the left for case (a) N, (b) S_1, (c) S_2 and (d) S_3. Except for case N, the height at which the profiles intersect is visualized on the right. For case S_1, S_2 and S_3, the profiles intersect at $y^+ \approx 31.26$, $y^+ \approx 6.18$ and $y^+ \approx 7.55$ respectively. For case N, a height of $y^+ \approx 13.45$ is visualized. 66
3.21 A sketch of the conceptual model discussed in the text is shown here. The color specification of the structures is according to table 2.1. 67
3.22 Visualization space showing the geometry of all structures analysed for all simulation cases. The neutrally stratified case N is represented by solid line (—) and the stably stratified cases S_1, S_2, S_3 are represented by dotted (...), dashed (- - -) and dash patterned (– — –) lines respectively. 67

4.1 A schematic representation of the steps involved in tracking the Robinson structures in time. An additional step (step III) is introduced to the geometrical characterization framework from chapter 2. 72
4.2 Spatial or volume overlap of a feature at different times t_n (solid line) and t_{n+1} (dashed line). The overlap region is highlighted with a darker shade of blue. . . 75
4.3 A sketch of the temporal graph indicating a merge event (colored blue) and a split event (colored red). The coloring scheme is used throughout the chapter unless otherwise indicated. Figure adapted from Lozano-Durán and Jiménez (2014). 75
4.4 Two synthetic test cases for validation of the tracking methodology are shown. (a) shows a simple branching event with one incoming and one outgoing branch whereas (b) exhibits a complex branching event where branches themselves have interactions. The arrows ($\rightarrow$) indicate the direction of time and black circle markers ($\bullet$) indicate that the structure doesn't exist after that time step. The coloring of branches for the temporal graphs are according to figure 4.3 and the scatter points indicate time steps. 78
4.5 Visualization space for the high-speed streaks for stably stratified (S_1, S_2) and neutrally stratified (N) cases are shown. $\hat{S}, \hat{C}, \lambda$ are the shape index, curvedness and stretching parameters respectively. A sphere of radius $r = 0.05$, with origin at the centroid of the cluster, identifies geometrically similar structures for tracking. These structures, shaded gray, are projected on the planes $\hat{S}\hat{C}$ and $\lambda\hat{C}$. 79
4.6 In the top panel, isosurfaces of a tracked high-speed streak are visualized at different viscous times. The bottom panel shows the temporal evolution of the geometry of the same high-speed streak until $t^+ = 9.24$. The black circle surrounding the marker indicates the viscous time $t^+ = 8.54$ when the structure being tracked merges with a larger one. 80
4.7 Contour lines of the joint p.d.f. of $\lambda, \hat{C}$ (left) and $\hat{S}, \hat{C}$ (right) are shown for all tracked (a) high-speed streaks, (b) low-speed streaks, (c) sweeps, (d) ejections, (e) vortices and (f) shear layers. Contours are drawn for 2% of the maximum value. Case N, S_1 and S_2 are represented with solid, dotted and dashed lines respectively. The blue circle indicates the region where structures having similar geometry were identified from the instantaneous Ekman flow fields analyzed in chapter 3 to initiate the tracking. 82
4.8 Top panel shows the isosurfaces of a tracked high-speed streak at different viscous times for the neutrally stratified case. The temporal evolution of the geometry of this streak is shown in the bottom panel. P, Q, R correspond to viscous times $t^+ = 0, 1.68, 3.92$ respectively. 82

4.9 The technique of MLPT to choose an optimum threshold for a subsequent time step is illustrated here. In the scenario shown in (a) the structure is initially simple and therefore the thresholds are decreased until a complex structure is found. The opposite scenario is shown in (b) where the structrue is initially complex and therefore, the thresholds are increased until it can be deemed simple. Both (a, b) illustrate that the structure is allowed to grow or shrink freely in time. 85
4.10 Track of a hairpin-like structure from case S_1 with (a) constant thresholding and (b) MLPT thresholding. Isosurfaces of Q-criterion are plotted at multiple time instances. 86
4.11 Time history of the (a) wall-normal extent (Δy^+) and (b) inclination angle of the hairpin-like structure tracked in figure 4.10 plotted every 8 time steps. Solid and dashed lines correspond to tracking with constant and MLPT thresholds respectively. 87
4.12 Visualization space for the structure tracked in figure 4.10 with (a) constant thresholding and (b) MLPT thresholding. Markers correspond to the geometrical state of the hairpin structure at a time instant. 88
4.13 A track of the hairpin packet from figure 3.15 for the neutrally stratified case is shown here. The hairpin packet autogenerates a tertiary hairpin (seen in the bottom panel) at $t^+ = 20$. The autogeneration process is shown on the left panel. 89
4.14 (a) Average lifetime of the primary branch tracked by the feature tracking procedure for all Ekman flow cases. (b) Average number of interactions experienced by the hairpin-like structures for all Ekman flow cases until $t^+ = 10$. Ri_B is the bulk Richardson number which quantifies the strength of stratification. 90

5.1 A portion of a slender vortex filament is shown. Vorticity ($\boldsymbol{\omega}$) is concentrated in a thin tube having a diameter d and a characteristic radius of curvature R. $\mathcal{L}(t)$ is a smooth time-dependent curve. Sketch adapted from Klein and Knio (1995). 95
5.2 Illustration of vortex lines and vortex tube. Figure adapted from Zhou (1996). 97
5.3 A hairpin filament when viewed from (a) front and (b) side. Here, $\mathbf{Q}_2$ is a background shear flow acting on the filament, y_{initial} is the initial distance from the wall, θ_i is the angle the filament makes with the wall and Γ is the circulation. 99
5.4 Illustration of the boundary conditions. A long filament is envisioned, periodic in the axial direction. The domain of integration, of length L, contains one complete period. 101
5.5 The solid line shows the maximum binormal velocity along the filament with the M1 KK method for the sinusoidal plane curve test with increasing node counts. The region shaded red region shows $N \geq 316$ which satisfy the overlap condition given in (5.16). The shaded blue region shows the difference between the maximum binormal velocity obtained at $N = 316$ and the maximum binormal velocity at other N. 104
5.6 Velocity prediction in the binormal direction for LIA (dashed line) and the M1 KK method (solid line). 104

5.7 For the static test described in subsection 5.3.1, the number of images P are varied and the maximum binormal velocity is plotted. 105
5.8 Similar to figure 5.7, the static test is repeated by varying the values of K (Left) and ϕ (Right) and the maximum binormal velocity is plotted. The solid, dashed and dotted lines show the differences with the number of nodes N. 106
5.9 Temporal evolution of a hairpin vortex in a stagnant background flow. (a, b, c) are the top, side and front view of the hairpin respectively. The simulation performed with LIA and M1 KK schemes are shown in the top and bottom panels respectively. 106
5.10 The test shown in figure 5.9 is repeated with $\beta = 15, 50$ for both schemes. (a, b) show the temporal evolution of the hairpin with LIA whereas (c, d) shows the temporal evolution with the M1 KK scheme. The insets in (a, b, c, d) show magnified portion of the filaments. Further magnified portion of the LIA (solid line) and the M1 KK (dashed line) cases with $\beta = 50$ at $t = 0.1$ is plotted in (e) with the scatter point indicating the origin of the filament. 108
5.11 Temporal evolution of a hairpin vortex in a shear background flow. The top panel shows the side view until $t = 0.44$ and the solid line indicates that the wall boundary condition was enforced. The bottom panel shows the front view from $t = 0.2$ to $t = 0.4$. The red dashed line indicates y_s which is the top of the shear flow. 109
5.12 Mean velocity profiles for each wall-normal height are plotted until $y^+ = 1500$ for all velocity components. $(\cdot)^+$ indicates viscous or wall units. (a, b, c) corresponds to the streamwise, wall-normal and spanwise velocities, respectively. In (a), the red dash dot line shows both the viscous law of the wall $u^+ = y^+$ and the logarithmic law $u^+ = \kappa_v^{-1} \log(y^+) + A$ with the von Kármán constant $\kappa_v = 0.41$ and $A = 5$ for the neutrally stratified case. 111
5.13 The uncertainty of core size estimation is shown in (a) where the isosurface of the same structure at at two thresholds are visualized. The core size is illustrated at two points in (b). Here, τ is the threshold and δ is the dimensionless core size parameter. 113
5.14 Side view of an active/turbulent patch of $Q-$criterion criterion structures for the case S_1 until $y^+ = 100$. 114
5.15 (a) Temporal evolution for all four cases listed in table 5.6 are plotted every 20 time steps for case S_1. The dotted region is zoomed in for initial condition R_3 in (b). 115
5.16 Time history of the inclination angle θ_i computed for (a) all four initial conditions from table 5.6 until $t^+ = 28$ and (b) only initial condition R_2 until $t^+ = 110$. The solid, dashed and dotted lines correspond to the different cases N, S_1, S_2 respectively. The red markers indicate the time at which the hairpin filament reaches the maximum inclination angle. 116
5.17 A comparison of self-induced velocity summed over the all nodes of the filament is shown for the initial conditions R_2 and R_3 with the mean background flow of S_1. 116

5.18 Temporal evolution of a hairpin filament for case S_1 with (a) initial condition R_2 and (b) initial condition R_3. Front view of the filaments are plotted at $t^+ = 0, 27.8, 55.7, 83.5, 111.4$ in (a) and $t^+ = 0, 2.2, 4.4, 11.1, 22.3$ in (b). 117
5.19 Temporal evolution for R_2 is shown for cases N, S_1, S_2. The top panel shows a side view of the filaments and the bottom panel shows the front view. In the bottom panel, (a, b, c) correspond to case N, S_1 and S_2 respectively. The filaments are plotted at $t^+ = 0, 14, 28, 42, 56$ in the bottom panel. 118
5.20 A comparison of the spanwise advection among the three cases N, S_1 and S_2 is shown until $t^+ = 56$ where the hairpin is initialized at $y^+ = 50$. 118
5.21 Time history of the inclination angle θ_i computed for initial condition R_2. The solid, dashed and dotted lines correspond to the different cases N, S_1, S_2 respectively. 119
5.22 Temporal evolution for R_2 is shown for cases N, S_1, S_2. The top and bottom panels show the side view of the filaments at $y^+_{\text{initial}} = 30$ and $y^+_{\text{initial}} = 15$ respectively. 120
5.23 Comparison of spanwise advection for case (a) N (b) S_1 and (c) S_2 at three initial heights $y^+ = 15, 30, 50$. The solid black line shows the spanwise advection with initial condition R_3 wheras all others are shown with initial condition R_2. 120
5.24 Track of a hairpin-like structure from the strongly stratified case S_1 with MLPT thresholding. The complex geometry of the extracted structures may result in a network of centerlines. Since we are only interested in the main centerline defining the hairpin structure, the remaining are discarded. 120
5.25 Temporal evolution of the tracked hairpin-like structure with MLPT thresholding. Left and right figures show the side view and the front view of the feature tracking results respectively. 121
5.26 Temporal evolution for a larger hairpin filament at $y^+_{\text{initial}} = 125$. Left and right figures show the side and front view of the temporal development respectively. 122
5.27 Isosurfaces of the Q-criterion for case S_1 are shown here for the initial time step. The structure tracked with MLPT is highlighted in blue. 122

A.1 Grouped indices for every case in the marching cubes algorithm. 149

C.1 Isosurfaces of $u' < 0$ (low-speed streak) and $u' > 0$ (high-speed streak) are shown for case (a) S_2 and (b) S_3 in the viscous sublayer with grid C. The color specification for the structures is according to table 2.1 for the low-and high-speed streak. The longest structure for the former is highlighted with light green and the longest structure for the latter is highlighted in pale yellow. . . . 157
C.2 Contour plots for case S_2 are shown with (a) ejections and low-speed streaks, (b) sweeps and low-speed streaks at $y^+ \approx 3.58$ with grid C. The color specification is according to table 2.1. 157
C.3 Contour plots for case S_3 are shown with (a) ejections and low-speed streaks, (b) sweeps and low-speed streaks at $y^+ \approx 3.58$ with grid C. The color specification is according to table 2.1. 158

C.4 Three pocket regions are highlighted with diverging streamlines for (a) case S_2 and (b) case S_3 at $y^+ \approx 3.58$. Overlayed are sweeps and ejections. Color specification for sweeps and ejections is according to table 2.1. 158

C.5 Similar to figure 3.6, visualization space for all quantitative Robinson structures except backs are shown with joint pdfs. From (a - f) are the high-speed streaks, low-speed streaks, sweeps, ejections, vortices and shear layers. The geometry of structures is compared between case S_3 (unfilled contours with dashed lines) and case S_2 (filled cotours). The number of structures for each contour level is indicated in black for case S_3 and dark blue for case S_2. Numbers within paranthesis (a - d) are those which start from the viscous sublayer and end in the buffer layer. Numbers outside paranthesis are those which start and end within the buffer layer itself. $\hat{S}, \hat{C}, \lambda$ are the shape index, curvedness and stretching parameters respectively. 160

C.6 Similar to figure 3.10, visualization space for all quantitative Robinson structures except backs are shown with joint pdfs. From (a - f) are the high-speed streaks, low-speed streaks, sweeps, ejections, vortices and shear layers. The geometry of structures is compared between case S_3 (unfilled contours with dashed lines) and case S_2 (filled cotours). The number of structures for each contour level is indicated in black for case S_3 and dark blue for case S_2. Numbers within paranthesis (a - d) are those which start from the viscous sublayer and end in the outer layer. Numbers outside paranthesis are those which start beyond the buffer layer and end within the outer layer. $\hat{S}, \hat{C}, \lambda$ are the shape index, curvedness and stretching parameters respectively. 162

C.7 Visualization space for backs is shown for case S_3 with unfilled contours and S_2 with filled contours. The number of structures between contours are indicated in dark blue for case S_2 and black for case S_3. $\hat{S}, \hat{C}, \lambda$ are the shape index, curvedness and stretching parameters respectively. 163

C.8 Vorticity magnitude contours along the (x, y) plane are shown here for case (a) S_2 and (b) S_3 for grid A until $y^+ \approx 1550$. For each case, a $\delta-$scale bulge is highlighted. The wall-normal direction is exaggerated three times to show the structures clearly. 163

C.9 Geometry of 100 hairpin-like structures are compared in the visualization space for case S_2 (filled contours) and S_3 (unfilled contours). $\hat{S}, \hat{C}, \lambda$ are the shape index, curvedness and stretching parameters respectively. 164

D.1 Top panel shows the isosurfaces of a tracked high-speed streak at different viscous times for the case S_2. The temporal evolution of the geometry of this streak is shown in the bottom panel. P, Q, R correspond to viscous times $t^+ = 0, 1.78, 6.98$ respectively. 165

D.2 The final time instant for all tracked vortex structures are shown for stably stratified (S_1, S_2) and neutrally stratified (N) cases. The size of the markers represents (in logarithmic scale) the volume of the structure. 165

List of Tables

1.1 A comparison of the classification of boundary layer structures presented by Fiedler (1988) and Robinson (1991). 9

1.2 Friction velocity calculated for an instantaneous time step for all cases. 10

1.3 The various cases analysed in this thesis are listed here. Cases with the prefix S refer to stratified flows and N corresponds to the neutrally stratified case. Reynolds number can be defined with δ_h and the laminar boundary layer depth. The value of the former case is shown here. If we define Re with the latter, then the value is 1000. Further simulation details can be found in Ansorge and Mellado (2016). 11

2.1 A summary of coherent structures and their indicators are shown here. The region column specifies where the dataset is cut in the wall-normal direction. . 18

4.1 The table from chapter 1 is repeated here with the omission of case S_3. Δt^+ is the time separation between consecutive time steps. It should be noted that the friction velocity u_τ which is used for normalization of quantities including time is not known *a priori* for Ekman flows and generally varies with time. Therefore, an averaged value of u_τ is used to compute these quantities (see table 1.2). . . 74

5.1 Parameters used for the static test comparisons. 103

5.2 Parameters used for the stagnant flow test. 106

5.3 Parameters used for the shear flow test. 110

5.4 The minimum, maximum and mean values of the dimensionless core size parameter estimated along the centerline of three hairpin-like structures are shown for case N, S_1 and S_2. 112

5.5 The minimum, maximum and mean values of Circulation estimated along the centerline of three hairpin-like structures are shown for case N, S_1 and S_2. . 113

5.6 The four initial configurations of the hairpin chosen for the simulations with ABL background flow. 114

5.7 Initial condition for comparison with feature tracking results. 121

6.1 List of storage facilities used for this work. 130

B.1 Surface shapes with the signs of principal curvatures k_1 and k_2. Table is extracted from figure 3.4(a) of Besl (2012). 153

B.2 Surface shapes with the signs of Gaussian K and mean curvature H. Table is extracted from figure 3.4(b) of Besl (2012). 154

Abbreviations

ABL Atmospheric Boundary Layer

CBL Convective Boundary Layer

CPU Central Processing Unit

DNS Direct Numerical Simulation

DSC Dice Similarity Coefficient

FD Fractal Dimension

FPBL Flat Plate Boundary Layer

FTLE Finite-Time Lyapunov Exponent

GPU Graphics Processing Unit

jpdf joint probability density function

LCS Lagrangian Coherent Structures

LES Large Eddy Simulation

LIA Local Induction Approximation

LIC Line Integral Convolution

LSM Large Scale Motions

M1 KK Method 1 optimized Klein-Knio scheme

MC Marching Cubes

MLP Multilevel Percolation Analysis

MLPT Multilevel Percolation Thresholding in Time

MOST Monin-Obukhov Similarity Theory

NS Neighbor Scanning

RAM Random-Access Memory

RBC Rayleigh-Bérnard Convection

Abbreviations

RMS Root Mean Square

SBL Stable Boundary Layer

SGS Subgrid Scale models

TFA Thin-Filament Approximation

TKE Turbulent Kinetic Energy

TNTI Turbulent/Non-Turbulent Interface

VLSM Very Large Scale Motions

VSBL Very Stable Boundary Layer

WSBL Weakly Stable Boundary Layer

Symbols

α_{τ_p}	Global percolation threshold of the indicator α
A	Amplitude of the disturbance
α	One of several indicators listed in table 2.1
$\overline{\alpha'^2(y)}^{1/2}$	RMS of the indicator α over wall-normal planes
B_0	Buoyancy difference between wall and free-stream
b	Buoyancy
β	Large value which controls the initial width of the disturbance
C, C^{ttm}	Physical and numerical core structure coefficient
C	Curvedness parameter
C_v, C_w	Local swirling and axial velocity distribution contribution
d	Averaged diameter of the vortex core
δ_{95}	Height at which the total stress is approximately 5% of the wall shear stress
Δ	Δ vortex indicator. $\Delta > 0$ indicates vortex regions
δ_{h}	Boundary layer height under neutral conditions
δ^{ttm}	Numerical core radius
Δy	Distance in the wall-normal direction
δ	$\delta = d/R$ is the dimensionless core size parameter
D_α	Fractal dimension of the indicator α
δ_{ij}	Kronecker delta symbol
D	Laminar Ekman layer depth $D = \sqrt{\frac{2\nu}{f}}$
d_l, d_u	Lower and upper distances of a p.d.f.
δ_v	$\delta_v = \nu/u_\tau$ is the viscous length scale
$\mathcal{E}$	Enstrophy
η	Kolmogorov length scale
ϵ_{ijk}	Lévy-Civita symbol

Symbols

f_δ	Spherical core smoothing function
f	Coriolis parameter
Fr	Froude number
Γ	Circulation
γ_E	Euler's constant
G	Geostrophic wind velocity magnitude
g	Gravitational acceleration
γ	Intermittency factor to segregate the turbulent and non-turbulent parts of the flow
H	Heaviside function
I	Three-dimensional scalar field
κ	Curvature
κ_H	Thermal diffusivity
K, ϕ	Constants of the M1 optimization scheme
κ_δ	Velocity smoothing function
$\mathcal{L}(t)$	$\mathcal{L}(t) : s \rightarrow \mathbf{X}(s,t)$ is the filament centerline
L	Domain of integration
λ_2	λ_2 vortex indicator. $\lambda_2 < 0$ indicates vortex regions
L_x, L_y, L_z	Domain size in streamwise, wall-normal and spanwise directions
λ	Stretching parameter
m	Axial flux within the filament core
μ	$\mu = 3V_s/A_s$ is the parameter used to non-dimensionalize the curvedness parameter
N	Neutrally stratified Ekman flow case
N_α	Number of boxes satisfying the threshold for a box size r
$N_{\text{interactions}}$	Number of interactions experienced during the lifetime of a structure
ω	Vorticity magnitude
$\mathbf{\Omega}$	Vorticity/spin tensor $\mathbf{\Omega} = \frac{1}{2}(\nabla \boldsymbol{v} - (\nabla \boldsymbol{v})^T)$
$\mathcal{P}$	Area-based joint p.d.f.
P	Number of images
$\boldsymbol{P}$	Point outside the filament core
π	Normalized pressure $\pi = \frac{p}{\rho_0}$

κ_1, κ_2	Principal curvatures
$\boldsymbol{Q}_2$	Background flow
Q, R	Q, R are the second and third invariants of the velocity gradient tensor $\nabla \boldsymbol{v}$ respectively
$\boldsymbol{Q}_1$	Velocity induced by a filament at point $\boldsymbol{P}$ and time t
$\boldsymbol{Q}_f$	Non-singular remainder of the line-Biot-Savart integral
Q	Q-criterion vortex indicator. $Q > 0$ indicates vortex regions.
Q_1, Q_2, Q_3, Q_4	Quadrant events - Q_1, Q_3 are outward and inward interactions respectively, Q_2 and Q_4 are ejection and sweep motions respectively
Ri_B	Bulk Richardson number
ρ	Density
R	Characteristic radius of curvature
Re_τ	Friction Reynolds number
S_1, S_2, S_3	Stably stratified Ekman flow cases
S_0	Initial length of the filament
S	Shape index parameter
$\boldsymbol{S}$	Strain-rate tensor $\boldsymbol{S} = \frac{1}{2}(\nabla \boldsymbol{v} + (\nabla \boldsymbol{v})^T)$
θ	Growth angle, i.e., the angle between the line connecting the heads of the hairpin packet and the wall
θ_i	$\theta_i = \arctan(\Delta y^+ / \Delta x^+)$ is the inclination angle of a structure
$\tau_{overlap}$	User defined overlap threshold
τ_p	Percolation threshold
θ	Potential temperature
τ	Threshold chosen for a scalar field
$\boldsymbol{t}, \boldsymbol{n}$	Mutually orthogonal unit vectors
t^+	Time in viscous units
u'	Fluctuating streamwise velocity
u_τ	Friction velocity
$u_i, \boldsymbol{v}$	Velocity vector
V	Volume of all structures in the domain
$\boldsymbol{v}_{\text{center}}, \boldsymbol{v}_{\text{image}}$	Velocity contribution from the central part of the domain and the image system

Symbols

$\nabla \boldsymbol{v}$	Velocity gradient tensor
v'	Fluctuating wall-normal velocity
$V_{\max}$	Volume of the largest structure in the domain
V_p	$V_p = \{v_0, ..., v_7\}$ is a set of vertices for each subcube of the large 3×3 cube.
$\boldsymbol{v_1}, \boldsymbol{v_2}$	Velocity due to two large core sizes σ_1 and σ_2
$\boldsymbol{v}_{\text{corr}}^{\text{ttm}}$	Corrected thin tube velocity
$\boldsymbol{v}^{\text{ttm}}$	Thin-tube velocity
ν	Kinematic viscosity of air
V_s	Volume of a structure
$\omega_{\text{threshold}}, \omega_\tau$	Threshold chosen for vorticity magnitude
$\boldsymbol{\omega}$	Vorticity vector
$\boldsymbol{x}$	Space coordinate vector
x, y, z	Streamwise, wall-normal and spanwise directions
$\hat{x}$	Feature center for the area-based joint p.d.f.
$\boldsymbol{\chi}_i^c$	Lagrangian variable denoting the centers that approximate the centerline
$\delta\boldsymbol{\chi}_i$	Lagrangian variable denoting the secant vectors that approximate the centerline
$\boldsymbol{X}$	Position vector
$x_{\text{initial}}, y_{\text{initial}}$	Initial streamwise and wall-normal distance of the filament
y_s	Shear flow height
$y_{\max}$	Maximum wall-normal distance
$(\cdot)^+$	Variable in viscous or wall-units (normalized with u_τ and ν)

1

Background and introduction

> The idea is that they [coherent structures] are regions of space and time (significantly larger than the smallest flow or turbulence scales) within which the flow field has a characteristic coherent pattern.
>
> *Stephen B. Pope, Turbulent flows, 2001*

It is well known that the study of turbulence is important in science and engineering. Turbulent flows can be encountered over a vast range of scales, from astrophysical and geophysical phenomena to the flow past an aircraft wing, reactive flow through combustion engines etc. The atmospheric boundary layer (ABL), which is the lowest part of the atmosphere that humans primarily interact with, is also turbulent. It governs the vertical exchange of meteorologically relevant variables such as momentum, heat and moisture between the Earth's surface and the free atmosphere (Nieuwstadt and Duynkerke, 1996). Realistic models of ABL representing all major physical processes in the atmosphere are necessary for numerical weather prediction and climate simulations (Garratt, 1994). However, to build accurate models, the intricacies associated with ABL turbulence need to be thoroughly understood.

The overarching goal of this thesis is to improve our knowledge of ABL turbulence, particularly in the very stable regime where turbulence is weak. This is accomplished with the help of coherent structures whose geometry and dynamics are compared for increasing stability. This chapter is organized as follows: a brief introduction to the ABL is first presented in section 1.1. This is followed by a discussion on the complexity of turbulence in the stable boundary layer (SBL) in section 1.2. Section 1.3 presents the approach employed to studying the ABL. Details of the simulation datasets analysed in this thesis are discussed in section 1.4. The research objectives, outline of the thesis and related posters/paper/preprints generated during the course of this work are presented in the rest of the chapter (sections 1.5 - 1.7).

1.1 The atmospheric boundary layer

The ABL is a part of the atmosphere which is in direct contact with the Earth's surface, resembling a wall-bounded flow. It is formed due to the combined action of turbulent friction from the wall (surface) and the Coriolis force as a result of the rotation of the Earth (Monin, 1970). Although it shares many similarities with canonical examples in fluid mechanics such as flat plate boundary layers (FPBL) and channel flows, there are two key differences:

Figure 1.1: The Atmospheric Boundary Layer highlighted by naturally generated fog showing intermittent patches. The picture is an own work of the author captured in Gif-sur-Yvette, France.

- The ABL is influenced by the Coriolis force where the mean wind direction turns towards the right (northern hemisphere) or left (southern hemisphere) with increasing height (Cermak, 1971).
- Strong heating or cooling, corresponding to daytime or nocturnal conditions respectively, at the surface causes density variations penetrating throughout the ABL and turbulence is affected through buoyant forces.

Thus, the ABL can be thought of as a rotating, stratified turbulent boundary layer. Its height is determined by the capping inversion atop within which the flow is statistically stable and turbulent motions from below do not penetrate. This height varies between 0.2 km under nocturnal conditions up to 2 km during daytime conditions (Garratt, 1994). This large length scale implies that ABLs typically have large Reynolds numbers on the order of $10^6 - 10^8$ which is significantly higher than that which is achievable today in laboratory experiments or numerical simulations of the boundary layer (Hommema and Adrian, 2003).

A source of complexity in studying the ABL stems from the diurnal cycle of surface heating and cooling. For instance, when the surface gets heated during daytime, it causes the air to rise up due to buoyancy resulting in strong mixing away from the surface. This is commonly referred to as the unstably stratified ABL or convective boundary layer (CBL). Absence of buoyancy effects results in a neutrally stratified ABL within which turbulence is essentially shear-driven and shares many similarities with the canonical FPBL (Fang and Porté-Agel, 2015). On the other hand, when the surface is sufficiently cooled relative to the free atmosphere, the density stratification is stable and turbulence is weak or intermittent (Van de Wiel et al., 2012). This is referred to in the literature as the stable atmospheric boundary layer (SBL). Often, a distinction is made between the weakly stable boundary layer (WSBL) and the very stable boundary layer (VSBL) (Malhi, 1995; Ohya et al., 1997; Mahrt, 1998b). The former is regarded as the "textbook" SBL which is known to occur during windy and/or cloudy conditions and for which surface cooling is relatively slow. Turbulence in this regime is more or less continuous and it has a well-defined height (Mahrt, 1998a). Along with the CBL and near-neutral ABL, the WSBL has been extensively investigated through field measurements

(e.g., Willis and Deardorff (1974), Willis and Deardorff (1979), Schmidt and Schumann (1989), and Lenschow et al. (1988)) and numerical simulations (e.g., Mason (1989), Lin et al. (1996), and Deusebio et al. (2014)).

The latter regime, VSBL, is characterized by weak winds and relatively stronger radiative cooling at the surface. The turbulence can be weak or virtually absent and is generally accompanied by the occurrence of non-turbulent patches even close to the surface (Mahrt, 1998a; Van de Wiel et al., 2012; Ansorge, 2016). In such cases, it may be difficult to define the boundary layer depth as turbulence may be generated by vertical shear above the surface inversion layer and then brought down to the surface. Therefore, numerical models requiring the depth may not be very successful (Smedman et al., 1993; Mahrt, 1998a; Mahrt and Vickers, 2003). Furthermore, the well-established Monin–Obukhov similarity theory (MOST) for the surface layer, which relates the flux-gradient relationship to the stability parameter in stationary flow over horizontally homogeneous surfaces, is applicable from unstable to weakly stable conditions but breaks down under strong stability (Ha et al., 2007; Optis et al., 2014). Optis et al. (2016) associated this breakdown to the increasing impact of the Coriolis force under weak turbulence and frequent low-level jets. Since the SBL is important for numerous applications such as numerical weather prediction which relies on MOST (Atlaskin and Vihma, 2012), modeling gas dispersion events (Sharan and Gopalakrishnan, 1997), understanding the Arctic climate system (Kral et al., 2021), and studying global warming trends which are seemingly pronounced during night time (McNider et al., 2010), an improved understanding of the underlying physical processes and dynamics can pave the way for newer parameterizations. The SBL, which is the object of research in this thesis, is investigated by establishing a detailed comparison with the well-studied neutrally stratified ABL.

1.2 Turbulence and global intermittency in the SBL

Apart from the presence of non-turbulent patches, turbulence in the SBL is accompanied by complex events such as microfronts (Mahrt, 2010), internal gravity waves (Sun et al., 2004), density currents (Sun et al., 2002), solitary waves (Terradellas et al., 2005), wave-turbulence interactions (Sun et al., 2015) and other complex modes which are grouped under the umbrella term “submeso motions”. Mahrt (2014) suggests that submeso motions refer to any non-turbulent motions which are less than 2 km in size. Under atmospheric conditions, the presence of these motions along with orographic obstacles lends to further complexity in studying the SBL. Therefore, one can choose a simplified physical configuration such as the Ekman flow over a smooth wall, where effects of both stratification and rotation are present without complex orography, as indicated in the work of Ansorge and Mellado (2014) and Shah and Bou-Zeid (2014b).

As mentioned previously, the SBL is characterized by intermittent turbulence featuring brief episodes of turbulence interspersed with relatively weak or unmeasurable fluctuations (Van de Wiel et al., 2002). This intermittency tends to occur on scales larger than the coherent eddies and is classified by Mahrt (1989) as *global intermittency*. An example can be seen from figure 1.2(b) which shows a horizontal vorticity magnitude (ω) slice of the strongly stratified Ekman flow simulation. The dark regions signify little to no turbulent activity. This

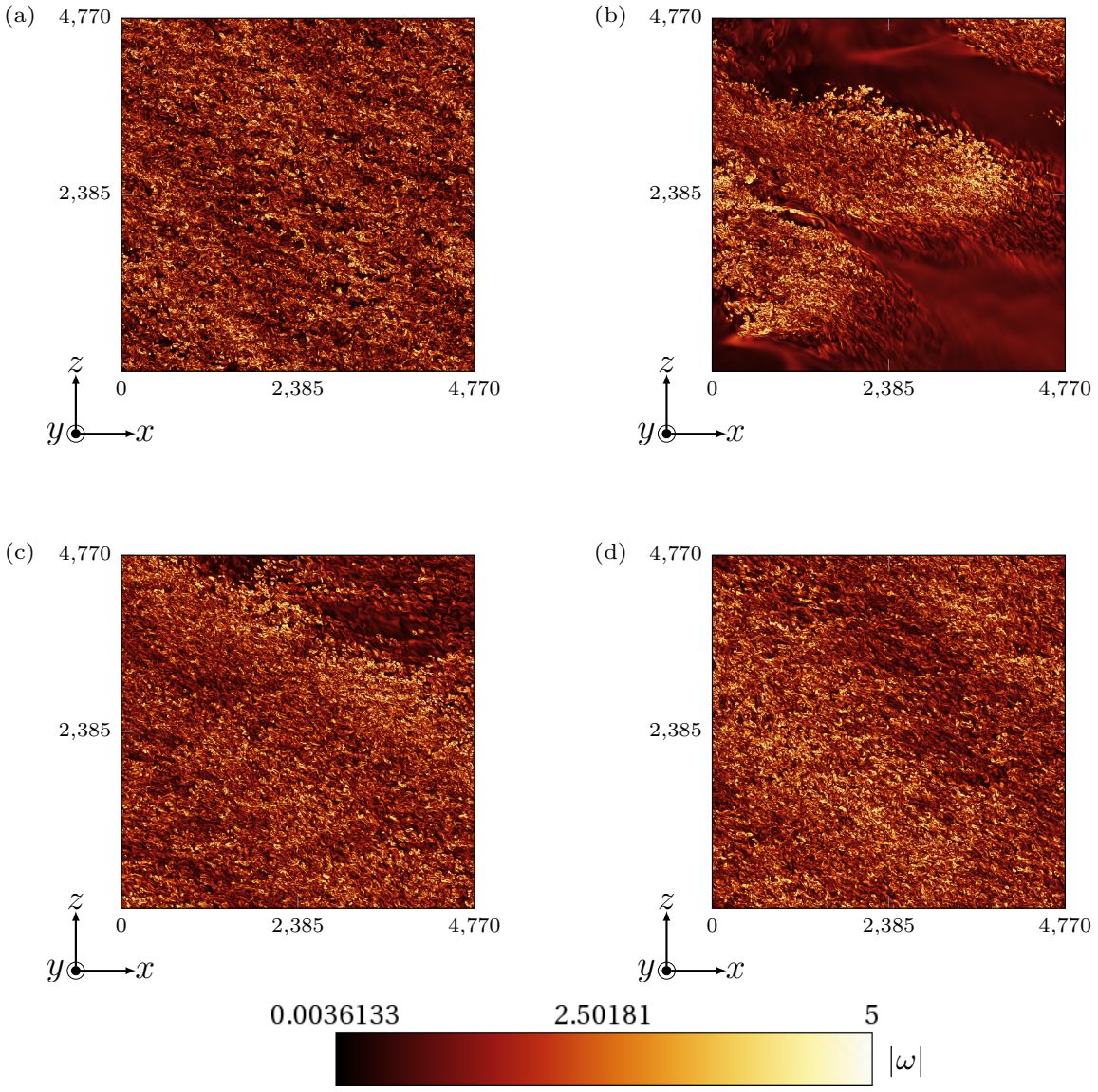

Figure 1.2: Horizontal vorticity magnitude slices normalized with its RMS over that slice are shown here at $y^+ \approx 100$ ($(\cdot)^+$ indicates wall units) for 1/6 of the full simulation domain. (a, b, c, d) correspond to the neutrally stratified case N and the stably stratified cases S_1, S_2, S_3 respectively. All simulation cases are described in table 1.3.

intermittency is different from the *small or fine scale intermittency* which occurs within larger eddies themselves. Through observations, it was previously suggested that globally intermittent turbulence is due to external triggering mechanisms including orographic obstacles, wind gusts, density currents and other submeso motions (Acevedo and Fitzjarrald, 2003; Sun et al., 2012). However, with the direct numerical simulations (DNS) of Ekman flows, Ansorge and Mellado (2014) found that global intermittency can manifest without any external perturbations and suggested that it is an intrinsic property of the SBL which will occur beyond a certain stability. This indicates the suitability of this flow configuration for our study and the DNS database of Ansorge (2016) is described in section 1.4.

The demarcation of the flow into turbulent and non-turbulent regions was already investigated by Townsend (1948) in the wake of a circular cylinder. This was facilitated with an *intermittency factor*, denoted by γ. Pope (2001), Bisset et al. (2002), Da Silva et al. (2014), and Ansorge and Mellado (2016) suggest a vorticity-based γ to separate the turbulent (rotational) and non-turbulent (irrotational) regions. While applying this to an instantaneous Ekman flow field, Ansorge and Mellado (2016) note that the use of vorticity magnitude ω works well for the outer layer of neutrally stratified flows but has issues close to the wall for globally intermittent flows. A well-known drawback of ω is producing false-positives in shear dominated regions (Lugt, 1979). This means that γ will be close to 1, near the wall, indicating that the flow is more or less turbulent. Ansorge and Mellado (2016) proposed the use of high-pass filters to overcome this issue and found that $\gamma > 0.8$ even for the strongly stratified case at their chosen threshold. A recent review by Günther and Theisel (2018) suggests numerous 'indicators' to identify vortex (rotational) regions within the flow, some of which avoid the drawback of ω (a comprehensive list can be seen in table 1 of Günther and Theisel (2018)). The applicability of these indicators and their subsequent impact on γ are examined in this thesis. Furthermore, a framework is developed in chapter 2 to select a non-subjective threshold value. This allows us to quantify the near-wall effects of global intermittency under stably stratified contexts of the flow. Later in the thesis, evidence is provided that global intermittency has a direct impact even in the viscous sublayer where the flow is locally laminar. This is of immediate relevance to improve wall models of large eddy simulation (LES) in which, typically, the first grid point is well above the viscous sublayer (Chauhan et al., 2013).

Separation of the flow into turbulent and non-turbulent sub-volumes also allows for a direct comparison of turbulence within a turbulent patch under stable stratification and the continuous turbulence from neutral stratification. With conditional one-point statistics, Ansorge and Mellado (2016) concluded that the morphology of turbulence within the turbulent patches remains unchanged regardless of the strength of stratification but the proportion of turbulent fraction changes resulting in order one changes in the conventional statistics. This leads them to suggest the use of a factorized parametrization where γ, expressed as a function of the Obukhov length[1], can be used with the standard approach for modelling the WSBL to determine bulk properties of the flow. However, it should be noted that the conditional analyses of Ansorge and Mellado (2016) pertain to instantaneous snapshots of the

[1]The Obukhov length scale is written as $L = \bar{\theta} u_\tau / \kappa g (\overline{v\theta})_0$ where $\bar{\theta}$ is the mean temperature, u_τ is the friction velocity, $\kappa = 0.41$ is the von Kármán constant, g is acceleration due to gravity and $(\overline{v\theta})_0$ is the kinematic surface heat flux.

flow. Analyses of turbulent heat flux from field data in the past have already established the temporal variability of global intermittency (Poulos et al., 2002; Van de Wiel et al., 2002). To the author's knowledge, it is currently unknown if the morphology of turbulence within the turbulent patches remains unchanged in time. This is investigated in chapter 4 of this work.

1.3 A structure-based approach to study the ABL

One approach to comparing the neutral and stably stratified contexts of the ABL can be accomplished by comparing the geometry of *coherent structures* or patterns observed within the flow. For instance, Belušić and Mahrt (2012) compared the frequency of occurrence of four predefined patterns (sine, step, ramp-cliff and cliff-ramp) in time series of wind speed and temperature between stable and unstable conditions of the atmospheric boundary layer. They found that large-scale coherent structures were more common under stable conditions than under unstable conditions and speculated that these differences could be attributed to the preference of horizontal and vertical growth of perturbations respectively. Although coherent structures such as the hairpin vortex have been proposed much earlier (Theodorsen, 1952), the structural view of turbulence started to gain momentum since the pioneering work of Kline et al. (1967) who experimentally revealed the existence of wall streaks in turbulent boundary layers. Studies focusing on the neutrally stratified ABL found structures similar to those observed in flat plate boundary layers (FPBL) such as low-speed streaks, sweeps, ejections, hairpin vortices and large-scale motions (Hommema and Adrian, 2003; Carper and Porté-Agel, 2004; Huang et al., 2009a; Inagaki and Kanda, 2010; Li and Bou-Zeid, 2011; Fang and Porté-Agel, 2015). However, it can be expected that the structures under stable and unstable conditions may be different as they can be modulated by the surface buoyancy flux. In fact, through smoke visualization experiments, Hommema and Adrian (2003) found ramp-like structures (which are interpreted as hairpin packets) under neutral conditions and thermal plumes under unstable conditions. Li and Bou-Zeid (2011) linked this change in topology of the coherent structures to the reduction in momentum transport efficiency with increasing instability.

In the other limit, i.e., under stable conditions, reviews by Hopfinger (1987) and Mahrt (2014) suggest the coexistence of internal waves and quasi two-dimensional modes with little vertical coherence, thereby hinting at pancake-like structures. However, recent results obtained from the DNS of stably stratified shear layers indicate the presence of hairpin vortices (Watanabe et al., 2019; Jiang et al., 2022). A systematic and detailed comparison on the geometry of coherent structures can not only help clarify the type of geometries observed but also how they change under increasing stability.

Before a method to determine the geometry of coherent structures is chosen, an important question needs to be addressed: "what are coherent structures?". To date, there is no generally-accepted definition of a coherent structure. Previous attempts include,

- Fiedler (1988): *".. a flow structure with discernible correlation, i.e., an element of turbulent motion which is set off against the stochastic background and which by its repetitive specific properties characterizes a specific flow."*

- Robinson (1991): *"a three-dimensional region of the flow over which at least one fundamental flow variable such as velocity component, density, temperature, etc. exhibits significant correlation with itself or with another variable over a range of space and/or time that is significantly larger than the smallest local scales of the flow".*

- Pope (2001): *".. they are regions of space and time within which the flow field has a characteristic coherent pattern".*

A common element among all three definitions is that they are too general and do not point to any particular structure identified through flow visualization experiments. The vast literature on boundary layers presents a zoo of coherent structures educed through various means, for instance, wall streaks (Kline et al., 1967), sweeps and ejections (Wallace et al., 1972) and hairpin vortices (Head and Bandyopadhyay, 1981). Therefore, it is useful to categorize these structures in various classes and use that as a starting point to studying the ABL. Two existing classifications of boundary layer structures are the Fiedler (1988) classification and the Robinson (1991) classification. As seen from table 1.1, most coherent structures are common between the two classification systems with the addition of shear layers and backs in the Robinson classification. In this thesis, the latter classification is used to study the ABL in an organized manner.

Several methods exist in the literature to determine the geometry of three-dimensional coherent structures. For instance, with a classical box-counting technique, Moisy and Jiménez (2004) studied intense structures[2], i.e., structures that exist at large thresholds extracted from scalar fields of vorticity magnitude and strain-rate magnitude in isotropic turbulence. They found that these structures had a mean fractal dimension of 1.1 ± 0.1 (filament-like geometry) and 1.7 ± 0.1 (sheet- or ribbon-like geometry) corresponding to vorticity structures and strain-rate structures respectively. Since the mean fractal dimension presents only a rough indication of the type of geometry, they further defined three characteristic lengths (r_1, r_2, r_3) for each structure and calculated two dimensionless aspect ratios $(r_1/r_2, r_2/r_3)$. These aspect ratios allowed them to relate the structures to four ideal objects namely, sphere $(1, 1)$, tube $(1, 0)$, ribbon $(0, 0)$ and sheet $(0, 1)$. The results of this geometrical analysis were found to be consistent with the mean fractal dimension indicating tube-like geometry for intense vorticity structures and ribbon-like or sheet-like geometry for strain-rate structures. The same box-counting technique was also used by Schumacher et al. (2005) who found that intense regions of the scalar dissipation in isotropic turbulence had a fractal dimension close to 2, indicating sheet-like geometry. However, this is a global measure which was applied over the entire scalar field.

Bermejo-Moreno and Pullin (2008), on the other hand, applied a non-local, multi-scale methodology to characterize the geometry of structures from a passive scalar field of isotropic turbulence. Iso-surfaces of individual structures were extracted with the help of a curvelet transform from the largest to the smallest scales and three parameters were used to characterize their geometry namely, shape index ($\hat{S}$), curvedness ($\hat{C}$) and stretching (λ). Since shape index and curvedness are local properties, i.e., they are obtained at all points of the surface, a

[2]Moisy and Jiménez (2004) defined a structure as a set of connected points satisfying a threshold. They extracted individual structures with a neighbor scanning procedure which visits all points in the scalar field that satisfies the threshold and groups together points having neighbors.

feature center (weighted mean) for the area-based joint probability density functions of those local properties were calculated which enables the local to non-local transition. Depending on their position within a three-dimensional feature space composed of these parameters, the structures can be related to blob-like $(1, 1, 1)$, sheet-like $(\hat{S}, \hat{C} \approx 0, \lambda)$ or tube-like $(0.5, 1, \lambda)$ geometries. They found a transition in geometry of structures from blob-like at the largest scale to tube-like at moderate scales to sheet-like at the smallest scales. This method is more precise as the geometry is determined from the surfaces of the extracted individual structures rather than from the aspect ratios of the embedding as was done in Moisy and Jiménez (2004). In this thesis, this non-local methodology, without the multi-scale decomposition, is used to study the geometry of Robinson structures in the ABL.

1.4 Simulation database

The datasets analysed in this thesis were inherited through the work of Ansorge (2016). In their set-up, the atmospheric boundary layer (ABL) is represented with a simplified physical configuration, i.e., a turbulent Ekman flow over a smooth, flat wall. This describes the flow over a smooth, flat, rotating plate with a temperature difference between the wall and the free stream.

The governing equations are the Navier-Stokes equations for an incompressible, rotating, stratified viscous fluid which are solved in the Boussinesq limit, so that density variations are neglected except when acted upon by gravity. This leads to the following simplified set of equations (Ansorge and Mellado, 2014),

$$\frac{\partial u_i, \boldsymbol{v}}{\partial t} = -u_j \frac{\partial u_i}{\partial x_j} + \nu \frac{\partial^2 u_i}{\partial x_j^2} - \frac{\partial \pi}{\partial x_i} + f \epsilon_{i3k}(u_k - G\delta_{k1}) + b\delta_{i3} \tag{1.1a}$$

$$\frac{\partial b}{\partial t} = -u_j \frac{\partial b}{\partial x_j} + \kappa_H \frac{\partial^2 b}{\partial x_j^2} \tag{1.1b}$$

$$\frac{\partial u_i}{\partial x_i} = 0 \tag{1.1c}$$

where $u_{i,i\in\{1,2,3\}}$ are the velocity components, $b = g\theta/\theta_0$ is the buoyancy. θ is the potential temperature, θ_0 is a reference temperature which is constant and g is gravity. The buoyancy $b = 0$ under neutral stratification. $\pi = p/\rho_0$ is the pressure where ρ_0 is the reference density, ν is the kinematic viscosity, κ_H is the diffusivity, G is the geostrophic wind velocity magnitude and f is the Coriolis parameter. Here, the f-plane approximation is applied with $f = 2\Omega \sin\Phi \boldsymbol{e}_y$ where Ω is the Earth rotation rate, Φ is the latitude and $\boldsymbol{e}_y$ is the vertical unit vector. This corresponds to a system which is subjected only to a vertical rotation rate with an intensity $\Omega \sin\Phi$. For the lower and upper boundary, no-slip and free-slip conditions are implemented which represent a wall and the free stream, respectively. The domain is doubly periodic in the horizontal directions to capture the largest, relevant turbulent structures.

In the neutrally stratified case, once turbulence has fully developed, the flow is governed by the quantities G, f, ν, κ_H. The Coriolis parameter f is replaced by the laminar Ekman layer depth $D = \sqrt{2\nu/f}$ in the dimensional analysis. The corresponding Reynolds number is defined as $Re = GD/\nu$ and the Prandtl number $Pr = \nu/\kappa_H$ is set to 1. The Ekman flow

<table>
<tr><th>Fiedler (1988) classification</th><th>Robinson (1991) classification</th></tr>
<tr><td colspan="2">Wall region only:

Wall streaks: These are regions of alternating low- and high-speed fluid seen close to the wall (up to $y^+ = 40$) of a turbulent boundary layer. They are known to have a streamwise extent of more than 1000 viscous units.

Pockets: These are predominantly circular regions observed in the wall region of the boundary layer. They are thought to be the imprint of an outer layer structure which induces wallward flow.</td></tr>
<tr><td colspan="2">Wall and outer region:

Ejections (bursts): The wall streaks which often lift-up away from the wall are termed ejection motions. These structures show less coherence than wall streaks and several ejections may emanate from a single low-speed streak.

Sweeps: The fluid pumped outwards during ejection activity is balanced by wallward motions named sweeps. These structures along with ejections are known to have a significant contribution to the Reynolds shear stress.

Vortical structures (eddies): The term “eddy” implies an inherently (whirling) vortical motion. Although there is a lack of a rigorous, accepted mathematical definition of a vortex, structures having a hairpin, arch or cane-like geometry are often identified in wall-bounded flows. These structures are thought to play a central role in the production of turbulence.

Large-scale motions (bulges): Existing at the interface of the boundary layer and the free stream, these structures are characterized by relatively weak vorticity in the mean flow direction. Often, these structures are known to span $2-3$ times the boundary layer height in the streamwise direction.</td></tr>
<tr><td>—</td><td>Near-wall shear layers: Long, sloping, shear structures have been identified in regions close to the wall ($y^+ < 80$). They are known to retain coherence of 1000 viscous units and can be seen on the upstream side of a low-speed streak.</td></tr>
<tr><td>—</td><td>Backs: Near-wall shear layers which extend further outward in the outer layer are categorized as backs. Although these δ- scale structures (here, δ is the mean boundary layer thickness) have been reported in previous studies, it is unclear if the distinction between these two structures is useful.</td></tr>
</table>

Table 1.1: A comparison of the classification of boundary layer structures presented by Fiedler (1988) and Robinson (1991).

Case	u_τ
N	0.052826
S_1	0.047248
S_2	0.0482142
S_3	0.0471626

Table 1.2: Friction velocity calculated for an instantaneous time step for all cases.

reaches steady state due to the balance of turbulence production due to shear and turbulence suppression as a result of rotation and this steady state solution in terms of a statistical description of turbulence is a function of Re only (Ansorge and Mellado, 2016). After the flow becomes turbulent, the laminar Ekman depth D cannot be used to describe the flow and the boundary layer height under neutral conditions $\delta_h = u_\tau/f$ (determined through averages over the last inertial period) is used instead. The Reynolds number becomes,

$$Re = \frac{G\delta_h}{\nu} \tag{1.2}$$

and

$$u_\tau^2 = \nu \frac{\partial \sqrt{\langle u \rangle^2 + \langle v \rangle^2}}{\partial z}\Big|_{y=0} \tag{1.3}$$

is the corresponding friction velocity. Ansorge (2016) notes that u_τ is not a fixed parameter in the simulation and exhibits a weak dependence on Re. Therefore, u_τ is calculated a posteriori for an instantaneous time step with (1.3) and listed in table 1.2 for all cases analysed in this thesis. For the neutrally stratified case, Re= 26 450. It should be noted that the fully turbulent, statistically-steady and neturally-stratified Ekman flow is used as an initial condition to simulate the stably stratified cases. A fixed surface buoyancy is used which is imposed via a Dirichlet boundary condition,

$$b(x, y = 0, z, t > 0) = 0, \quad b(x, y = y_{\max}, z, t > 0) = B_0 \tag{1.4}$$

where B_0 is the buoyancy difference between the wall and free stream. Since the Froude number is described as $Fr = G^2/(B_0 D)$, where D is the laminar Ekman depth, it looses relevance once the flow becomes turbulent. Hence, the global bulk Richardson number defined as,

$$Ri_B = \frac{B_0 \delta_h}{G^2} \tag{1.5}$$

is used instead. The initial buoyancy profile is given by an error function in the wall-normal direction (see equation (2.14) of Ansorge (2016)). For stronger stratification, cases with intermediate stratification are used as an initial condition and the buoyancy field is multiplied by some value to match the required bulk stratification. In all simulations, the horizontal domain size, expressed in terms of the neutral reference, is $20.4 \times 20.4\delta_h$. A high-order finite-difference scheme was used to integrate the governing equations on a structured, collocated grid composed of $3072 \times 512 \times 6144$ points along the streamwise, wall-normal and spanwise directions

Case	Line specification	Ri_B	Fr	Re	L_x	L_y	L_x^+	L_y^+
N	————	0	∞	26 450	20.4δ	20.4δ	28 620	28 620
S_1	.....	2.64	0.02					
S_2	- - - - - - -	0.76	0.07					
S_3	– — – —	0.58	0.09					

Table 1.3: The various cases analysed in this thesis are listed here. Cases with the prefix S refer to stratified flows and N corresponds to the neutrally stratified case. Reynolds number can be defined with δ_h and the laminar boundary layer depth. The value of the former case is shown here. If we define Re with the latter, then the value is 1000. Further simulation details can be found in Ansorge and Mellado (2016).

respectively. The grid is unequally spaced in the wall-normal direction with $\Delta y^+|_{y=0} = 1.15$ and $\Delta y^+|_{y\approx 3\delta_h} = 45.31$. $(\cdot)^+$ indicates viscous or wall units,

$$y^+ \equiv \frac{y u_\tau}{\nu} \tag{1.6}$$

The time integration was carried out with a fourth-order Runge-Kutta algorithm. All simulations and their parameters are summarized in table 1.3. The database is composed of a neutrally stratified case, henceforth denoted N and three stably stratified cases which are denoted S_1, S_2, S_3. Although the stably stratified cases have different global bulk Richardson numbers, analysis of the time evolution of vertically integrated turbulent kinetic energy (TKE) suggests that all three cases fall under the very stable regime (Ansorge, 2016). In this regime, turbulence nearly dies out which is evident from figure 1.2(b, c, d) and subsequently recovers. The intensity of turbulence also reduces with increasing height and beyond a certain point is unaffected by stratification and decays slowly. This type of decaying turbulence is most commonly observed in nocturnal atmospheric boundary layers (Stull, 1988) which suggests the suitability of these simulations to study stable boundary layers.

For convenience, results are communicated with three horizontal grid sizes as indicated in figure 1.3. Grid A represents the entire computational domain whereas grids B and C show 1/3 and 1/6 of the domain respectively.

1.5 Research objectives

In his review paper, Mahrt (2014) points out that the very stable regime of the ABL is poorly understood due to reasons including but not limited to, "..complex interactions between turbulence and wave-like and other submeso motions". As a result, under strong stratification where the flow is globally intermittent, assumptions made for common turbulence closures break down. Therefore, to pave the way for newer parametrizations, a detailed comparison is established with the Ekman flow datasets under stable and neutral stratification. This forms the starting point for our research. To enable this comparison, the flow is decomposed in terms of its coherent structures which can be extracted for further analysis. An immediate question that follows is "what are coherent structures?". As elucidated in section 1.3, coherent structures are generally understood as characteristic patterns that persist in space and time.

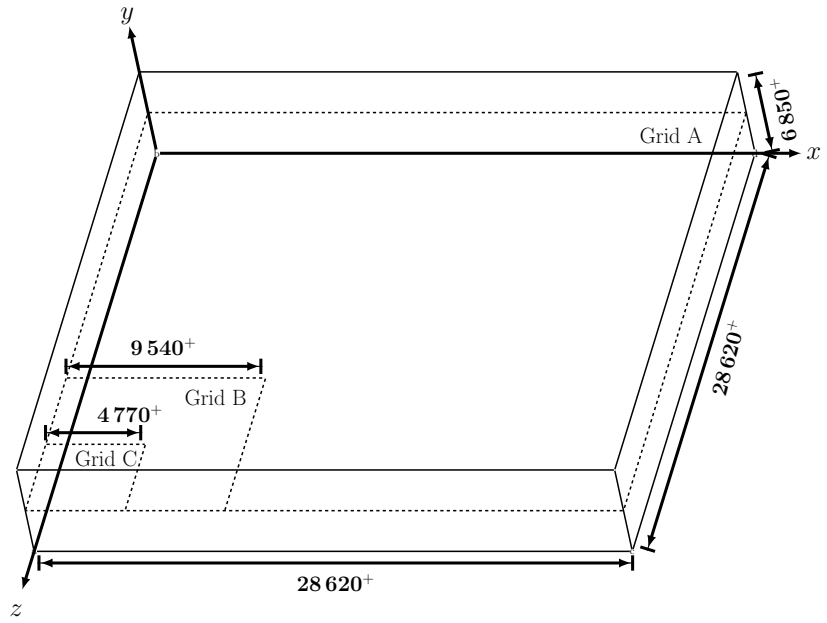

Figure 1.3: The schematic shows the three types of grids - A, B and C used in the paper. x, y, z correspond to the streamwise, wall-normal and spanwise directions respectively. $(\cdot)^+$ indicates viscous units as described in (1.6).

Although coherent structures lack a precise mathematical definition, the literature on boundary layers identifies numerous types of structures educed through various scalar criteria. The classification of boundary layer structures developed by Robinson (1991), henceforth called Robinson structures, is used to study them in an organized manner. Our first objective is as follows,

(1) Identify suitable scalar indicators for the eight categories of Robinson structures listed in table 1.1.

The identified scalar indicators are listed in table 2.1 and they are grouped as quantitative and qualitative. With quantitative structures, the three-dimensional scalar field is thresholded and individual structures can be extracted while qualitative structures are only observable through visualization. For the former group of structures, a threshold needs to be chosen first. As noted by Green et al. (2007), an important issue when dealing with any Eulerian (where structures are identified through quantities derived from instantaneous velocity fields) criteria is its reliance on a subjective, user-defined threshold value. Apart from this, once the structures have been extracted at some threshold for increasing stratification, a methodology needs to be developed to establish a comparison. Therefore, our second objective is,

(2) Develop a non-subjective method for choosing a threshold value pertaining to wall-bounded flows and subsequently, a methodology to compare the extracted structures for increasing stratification.

The methodology used for selecting non-subjective threshold values is discussed in section 2.3. This is based on the work of Del Álamo et al. (2006) who proposed a systematic way to partition the flow by identifying the region of 'percolation' transition between two threshold

limits. This defines a threshold which retains most of the enstrophy[3] and still identifies individual structures (Jiménez, 2018). However, it is shown in subsection 2.3.1 that this method does not work well under strong stratification as choosing a single global threshold value tends to identify a large cluster of structures as an individual structure (see figure 2.14). This leads to a subsidiary objective,

(2a) Modify the percolation analysis methodology such that individual structures can be educed for strongly stratified flows.

Once the thresholds are identified, individual structures are extracted with the neighbor scanning algorithm of Moisy and Jiménez (2004) which is extended with the marching cubes algorithm (Lorensen and Cline, 1987) to ensure accurate extraction even at smaller thresholds (see the issue pointed out in figure 2.6). Accurate structure extraction is necessary due to the method employed to compare the extracted structures. The method is as follows: first, the noise-like structures having a fractal dimension less than 1 are filtered out. The remaining structures are geometrically characterized with two local (i.e., at all points on the surface of the structure, thereby necessitating the accurate structure extraction) differential-geometry parameters and a global parameter as shown in Bermejo-Moreno and Pullin (2008). By calculating area-based probability density functions, the local properties are made non-local. These three parameters broadly classify whether a structure is tube-like, sheet-like or blob-like depending on its location within a three-dimensional visualization space composed of these parameters (see figure 2.21). As elucidated before, the choice of geometry-based classification is motivated from the literature wherein changes in the geometry of coherent structures have been reported from eddies under neutral conditions to thermal plumes under unstable conditions (Hommema and Adrian, 2003). Under strong stratification, reviews by Hopfinger (1987) and Mahrt (2014) note the coexistence of internal waves and horizontal two-dimensional modes suggesting (pancake-) sheet-like geometry having little vertical coherence. This leads to the third objective,

(3) Determine if geometry of the quantitative Robinson structures become sheet-like with increasing stability.

Apart from changes in geometry, studies by Hommema and Adrian (2003) and Carper and Porté-Agel (2004) suggest an increase in the inclination angles of hairpin vortex structures with increasing instability. A related objective is therefore,

(3a) Identify the changes in the inclination angle of hairpin structures with increasing stability.

The geometry of Robinson structures are compared under increasing stability in section 3.1 by dividing the flow field into four layers: viscous sublayer, buffer, inner and outer layers. Results show that similar geometrical features for all quantitative Robinson structures could be seen for both neutrally stratified and stably stratified cases. This is plainly emphasized in figure 3.22 and suggests no inclination towards sheet-like geometry with increasing stability. However, the presence of non-turbulent patches (due to global intermittency) which extends

[3]Enstrophy determines the rate of dissipation of kinetic energy and for a viscous, incompressible flow is defined as $\mathcal{E}(\boldsymbol{u}) = \int_\Omega |\boldsymbol{\omega}(\boldsymbol{x})|^2 d\boldsymbol{x}$ where Ω is the domain and $\boldsymbol{\omega}$ is the vorticity vector (Foias et al., 2001).

throughout the flow and even affects the viscous sublayer (see figures 3.1(b) and C.1(a, b)) in which the flow is locally laminar, has an impact on the spatial organization of coherent structures. Previous time series analysis, for instance by Van de Wiel et al. (2002), show that global intermittency alternates between strongly turbulent and non-turbulent periods, thereby exhibiting temporal variability. This spatio-temporal variability of the global intermittency may have an impact on the dynamics and therefore, the geometry of coherent structures. This leads to the fourth objective,

(4) Starting from the instantaneous Ekman flow fields analyzed for objective (3), identify if there are changes in the temporal evolution of the geometry of coherent structures for increasing stability by tracking them in time.

While investigating the inclination angles of hairpin-like structures, some interesting characteristics pertaining to these structures can be observed. Even though these structures are present for all cases, an abundance of them confined to the turbulent patches of the flow, most of which are oriented in a similar direction, can be seen for the strongly stratified case. While hairpin-like structures have been reported in previous works under stable stratification (Oncley et al., 2016; Watanabe et al., 2019), the source of their abundance and similar orientation, to the author's knowledge, have not been examined. Furthermore, dynamical aspects of hairpin-like structures are relatively unexplored for stratified flows but have been extensively studied for unstratified fluid flows (see Moin et al., 1986; Acarlar and Smith, 1987; Hon and Walker, 1991; Zhou et al., 1996; Zhou et al., 1999; Adrian et al., 2000). These studies show that once the hairpin structures lift-up due to self-induction from their initial state, they are stretched by the mean background flow as they are advected downstream. This suggests that the hairpin structure grows in size over time. Since the region-based feature tracking scheme used for objective (4) cannot capture changes in size of the structure as the same initial threshold is used for all subsequent time steps, the fifth objective is therefore,

(5) Modify the region-based feature tracking scheme to account for changes in the size of the structure by altering the thresholds in time. By tracking hairpin-like structures and their interactions, can the abundance of these structures in the strongly stratified case be explained?

Although the modified feature-tracking scheme is capable of adapting to the dynamical changes in the size of the hairpin-like structure, a complete understanding of its dynamics cannot be achieved. This can be attributed to interactions, specifically split events which can cause an ambiguity in following the "correct" structure and the use of thresholds which may not represent the "full" structure (see the discussion in subsection 5.4.1). Moreover, hairpin-like structures are generally identified and tracked only from a later stage in their lifetime and therefore, the evolution from their origin is not clear. To alleviate these issues, a more fundamental approach is sought where the hairpin-like structures are treated as slender vortex filaments. The sixth and final objective is,

(6) With the filament approach, identify the impact of stratification on the dynamical characteristics (for instance inclination angles, orientation, streamwise and spanwise

stretching) of a hairpin filament. By studying these characteristics, can the orientation of these structures in the strongly stratified case be explained?

At this stage, the intricacies of SBL turbulence are examined with coherent structures to gain an insight into their geometry and dynamics. The next stage of research would involve using these results to improve existing/build new parametrizations of the SBL. Possible directions are discussed in chapter 6.

1.6 Outline

The rest of the thesis is organized as follows. In the subsequent chapter, a means of identifying the eight classes of Robinson structures with numerous indicators are presented. The Robinson structures are broadly divided into two categories: quantitative and qualitative. Structures belonging to the former category can be extracted and geometrically characterized with a modular framework based on methodology of Bermejo-Moreno and Pullin (2008). The geometry of the latter category of Robinson structures are qualitatively described. Results of the geometrical analysis applied to the Ekman flow datasets are shown in chapter 3. Furthermore, in chapter 3, a novel definition of the intermittency factor based on coherent structures is proposed for wall-bounded flows. With this definition, the flow is split into turbulent and non-turbulent subvolumes and one-point statistics are obtained for some of the quantitative Robinson structures to complement the geometrical analysis. Results from the geometrical analysis suggests that similar geometrical features can be found regardless of increase in the strength of stratification, i.e., the negative buoyancy flux does not have a significant impact on the geometry of coherent structures. This is investigated further in chapter 4, where the coherent structures are tracked in time with a region-based feature tracking scheme. The limitation of using a constant threshold in time is overcome by developing a method capable of altering the thresholds in time. However, since interactions such as split events can complicate the tracking in DNS datasets, the thin filament approach is used to understand the motion of hairpin filaments in time in chapter 5. The final conclusions and outlook are discussed in chapter 6.

1.7 Related works

Some parts and figures of this thesis can be found in the following list of posters, paper and preprints.

→ The contents and figures of chapters 1, 2 and 3 are based/adopted from the following posters and preprint.

Harikrishnan, A., Ansorge, C., Klein, R., & Vercauteren, N. (2020). *The curious nature of hairpin vortices.* Gallery of Fluid Motion.

Harikrishnan, A., Ansorge, C., Klein, R., & Vercauteren, N. (2021). *Geometry and organization of coherent structures in stably stratified atmospheric boundary layers.* arXiv preprint. arXiv:2110.02253.

Harikrishnan, A., Ernst, N., Ansorge, C., Klein, R., & Vercauteren, N. (2021). *Lagrangian hairpins in atmospheric boundary layers.* Gallery of Fluid Motion.

→ The spatial overlap method used to track Robinson structures in time in chapter 4 is based on the following preprint.

von Lindheim, J., Harikrishnan, A., Dörffel, T., Klein, R., Koltai, P., Mikula, N., Müller A., Névir P., Pacey G., Polzin R. & Vercauteren, N. (2021). *Definition, detection, and tracking of persistent structures in atmospheric flows.* arXiv preprint. arXiv:2111.13645.

→ The technique of multilevel percolation thresholding in time (MLPT) which is used to obtain optimum thresholds in time, presented in chapter 4, is adopted from appendix D of the following paper. Chapter 5 is also largely based on the numerical analysis of slender vortex filaments discussed in sections I - V and appendices A - C of the following paper.

Harikrishnan, A., Rodal, M., Klein, R., Margerit, D., & Vercauteren, N. (2023). *On the motion of hairpin filaments in the atmospheric boundary layer.* Physics of Fluids, 35 (7).

2

A framework for the geometrical characterization of coherent structures

As elucidated in the previous chapter, there is still no widely accepted definition of a coherent structure. Some of the previous attempts suggest definitions which are too general and do not identify a particular structure seen in flow visualization studies. Hence, the classification introduced by Robinson (1991) is chosen to study the different categories of coherent structures in an organized manner. The geometry of these structures, henceforth referred as Robinson structures, are used to compare the Ekman flow datasets at different strengths of stratification. This allows us to understand the changes in geometry of these structures in response to changes in the strength of stratification. Towards this end, the goal of this chapter is to develop a methodology to quantify the geometry of individual coherent structures.

An overview and a means of identifying the eight categories of Robinson structures are presented in section 2.1. These structures, summarized in table 2.1, can be broadly divided into two major categories namely, quantitative and qualitative. Quantitative structures are those for which individual structures can be extracted by thresholding scalar fields, whereas qualitative structures are only observable with visualization and are therefore, not extracted.

To extract individual coherent structures from three-dimensional scalar fields, the neighbor scanning algorithm of Moisy and Jiménez (2004) is considered. It is seen in section 2.2 that this algorithm tends to group together two or more individual structures which are closely spaced, especially at small thresholds. Since this may result in a misclassification of the geometry, a correction of this algorithm is sought and is presented in subsection 2.2.2.

A criticism frequently pointed out in previous works (Green et al., 2007) is that *Eulerian* criteria, for which an instantaneous spatial field is used in identifying coherent structures, are dependent on subjective, user-defined thresholds. This subjectivity is overcome with the percolation analysis of Del Álamo et al. (2006) for wall-bounded flows in which a single, global threshold is computed for the entire flow field. However, as revealed in subsection 2.3.1, this tecnhique fails for globally intermittent flows in which turbulent and nonturbulent regions co-exist and therefore a global threshold is insufficient for identifying individual structures. Therefore, an extension of this method is presented in subsection 2.3.1 in which percolation analysis is applied in an iterative manner such that individual structures can be extracted at different thresholds.

Once the individual structures are extracted with non-subjective thresholds, they are geometrically classified as tube-like, blob-like or sheet-like structures with the non-local methodology of Bermejo-Moreno and Pullin (2008). An additional step is added to this method in that structures having a fractal dimension less than 1 are considered noise-like and

Type	Coherent structure	Indicator	Region	Color specification
Quantitative	High-speed streaks	$u' > 0$	$y^+ < 40$	●
	Low-speed streaks	$u' < 0$	$y^+ < 40$	●
	Sweeps	$u' > 0, v' < 0$	$y^+ < 1550$	●
	Ejections	$u' < 0, v' > 0$	$y^+ < 1550$	●
	Vortices	$\frac{1}{2}(\|\|\Omega\|\|^2 - \|\|S\|\|^2) > 0$	$y^+ < 1550$	●
	Shear layers	$\|\omega\|$	$y^+ < 80$	●
	Backs	$\|\omega\|$	$y^+ < 1550$	●
Qualitative	Pockets	streamlines	$y^+ < 5$	-
	Bulges	$\|\omega\|$	$y^+ < 1550$	-

Table 2.1: A summary of coherent structures and their indicators are shown here. The region column specifies where the dataset is cut in the wall-normal direction.

are excluded from the geometrical analysis. This modified methodology is presented in section 2.4. Together, all of the methods discussed above constitute a framework for the geometrical classification of individual coherent structures in wall-bounded fluid flows. Results of the geometrical classification of the Ekman flow datasets described in section 1.4 are discussed in chapter 3. In chapter 4, individual coherent structures are followed in time and the geometrical characterization procedure is used to describe changes in geometry during their temporal evolution.

2.1 Robinson's taxonomy of boundary layer structures

In this section, a brief overview of the eight categories of coherent structures identified by Robinson (1991) are discussed and a means of identifying them in data are presented.

2.1.1 Streaks

Through the experimental work of Kline et al. (1967), *streaks* or *wall-layer streaks* are known to exist close to the wall of a turbulent boundary layer. These structures were highlighted with hydrogen bubbles, which tend to accumulate in regions of slow moving fluid. Such structures are termed in the literature as *low-speed streaks*. Kline et al. (1967) also revealed that the streamwise vorticity resulted in the movement of these structures gradually away from the wall. At some point, this gradual movement is followed by a 'breakup' or 'bursting' phenomenon by which the low-speed fluid is ejected into the outer flow regions. The authors suggest that this violent bursting process plays an important role in the transfer of momentum between the inner and outer regions of the boundary layer.

The viscous sublayer region of the boundary layer is also composed of faster moving fluid regions known as *high-speed streaks*. Both low-and high-speed fluid regions alternate in a repeatable manner and are known to have a well-defined spanwise mean spacing of 100^+ viscous units for flat plate boundary layers (FPBL) (Kline, 1978). Kline (1978) also notes that streaks are clearly visible in FPBLs until $y^+ \approx 40$. To inspect our dataset in this respect, low-speed streaks are visualized by computing the streamwise fluctuating velocity and the resulting scalar

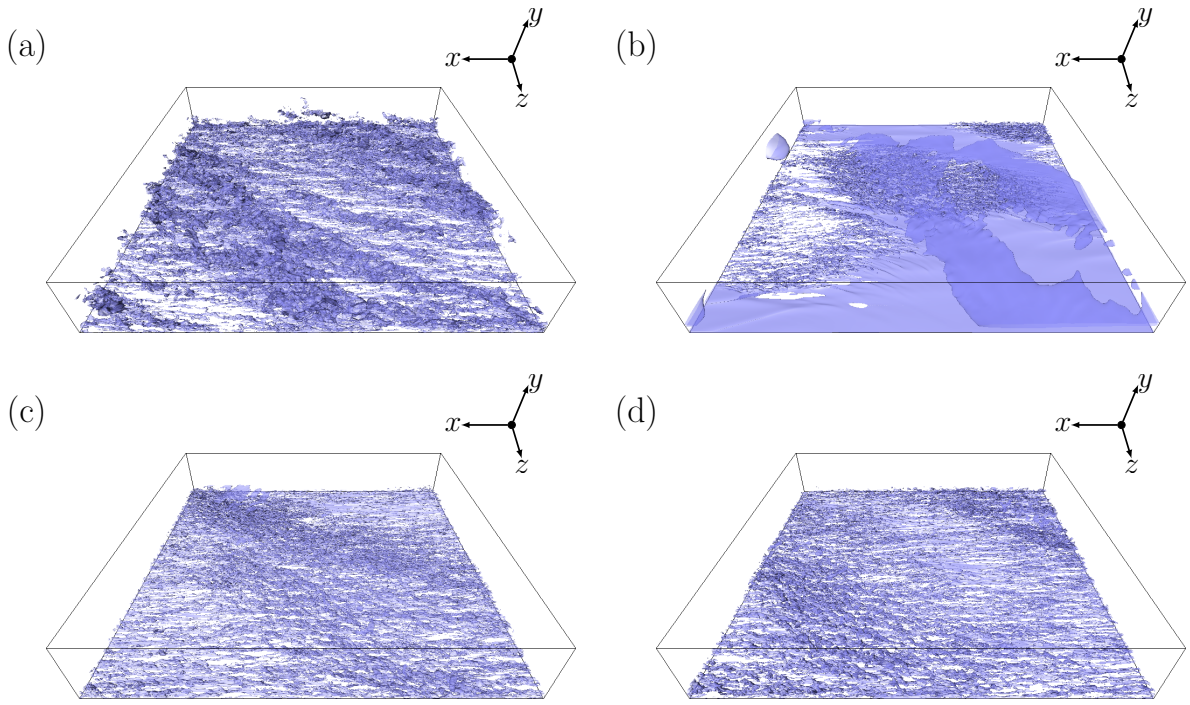

Figure 2.1: Isosurfaces of $u' < \tau_p$ representing the low-speed streaks are shown here. (a, b, c, d) correspond to the neutrally stratified case N and stably stratified cases S_1, S_2, S_3 respectively. Computation of τ_p for low-speed streaks is described in section 2.3. The streaks are visualized for 1/3 of the computational domain until $y^+ \approx 1550$.

field is thresholded at a value less than 0. As seen from figure 2.1, it is immediately apparent that the nature of streaks has a strong dependence on the strength of stratification. This is further discussed in chapter 3. In all four cases, smaller, individual structures are visible close to the wall. Beyond that, particularly for case S_1, they tend to merge into larger sheet-like structures that sometimes span the entire domain (as seen in the strongly stratified case S_1). Since these larger sheet-like structures are not meaningful for the geometrical analysis (as it requires closed surfaces), the domain is restricted to $y^+ < 40$.

To the author's knowledge, the structure of the streaks within the viscous sublayer of ABLs has not been investigated. This is because the ABL is usually studied with LES, for which the first wall-normal grid point in the domain is far away from the wall such that the viscous sublayer is not resolved. Khanna and Brasseur (1998) and Jayaraman and Brasseur (2021) have visualized the three-dimensional structure of the streaks with LES for various stability states. With increase in the global stability parameter $(-z_i/L)$ from neutral state, i.e., $-z_i/L = 0$, they note that the streamwise coherence of streaks in the surface layer tends to increase until it reaches a critical value and then starts decreasing monotonically. However, the visualization from figure 2.1(b), which visualizes 1/3 of the simulation domain, suggests that a major portion of the domain is composed of a single low-speed streak. Although not visualized here, the single low-speed streak can be seen spanning the full simulation domain as well. This presents a need to study the coherence of streaks at different levels of stratification. Drobinski and Foster (2003) have shown that streaks contribute to surface stress and momentum flux and emphasize that these effects must be accounted for in ABL parametrizations.

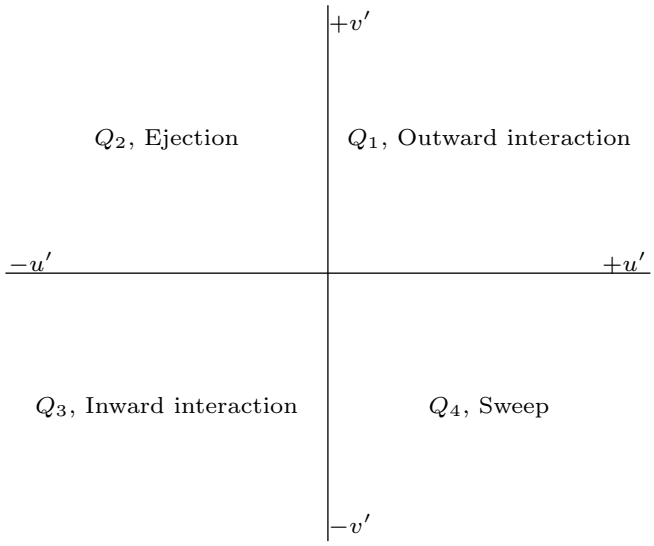

Figure 2.2: Definition of quadrants of the instantaneous $u'v'$ plane. Figure adapted from Robinson (1991).

2.1.2 Sweeps and ejections

With hydrogen bubble experiments, Kim et al. (1971) found that low-speed streaks moving downstream gradually lift up from the wall in FPBLs. This is followed by a bursting process after a critical height which is called *low-speed-streak lifting* or *ejection*. Complementing the outward motion of ejections, Corino and Brodkey (1969) observed that a stream of fluid accelerated downstream to *sweep* away the ejection activity. With the DNS of a channel flow, Kim et al. (1987) noted that sweep events were a dominant contributor to the Reynolds shear stress until $y^+ \approx 12$ beyond which ejection events took over. Willmarth and Lu (1972) reported a similar behavior in their study albeit at a height of $y^+ \approx 15$.

The quadrant-splitting technique of Wallace et al. (1972) in which the product of instantaneous streamwise and wall-normal velocity fluctuations ($u'v'$) is split into four categories: $Q_1(+u', +v'), Q_2(-u', +v'), Q_3(-u', -v'), Q_4(+u', -v')$, corresponding to outward interaction, ejection, inward interaction and sweep respectively as shown in figure 2.2. Q_2 and Q_4 were meant to identify ejection and sweep structures identified by Kline et al. (1967) and Corino and Brodkey (1969) respectively. In the ABL, sweeps (or downdrafts) and ejections (or updrafts) are regarded as the primary constitutive motions to study momentum, heat and mass transport (see Katul et al. (1997a), Katul et al. (1997b)). The contribution of the sweep-ejection cycle to scalar and momentum transport is studied with the quadrant technique and conditional sampling methods in which the four quadrants are considered analogous to four modes of momentum transport: Q_1, Q_2 and Q_3, Q_4 are ejections and sweeps for momentum and scalar fluxes respectively (Katul et al., 1997a; Katul et al., 2006; Shaw et al., 1983; Li and Bou-Zeid, 2011). In particular, Li and Bou-Zeid (2011) were able to observe a change in the topology of coherent structures from eddies to thermal plumes with increasing instability. They link this topological change to an increase in the transport efficiency of both momentum and scalars by the ejections. In chapter 3, the geometry of both sweeps and ejections are investigated under stable and neutral stratification.

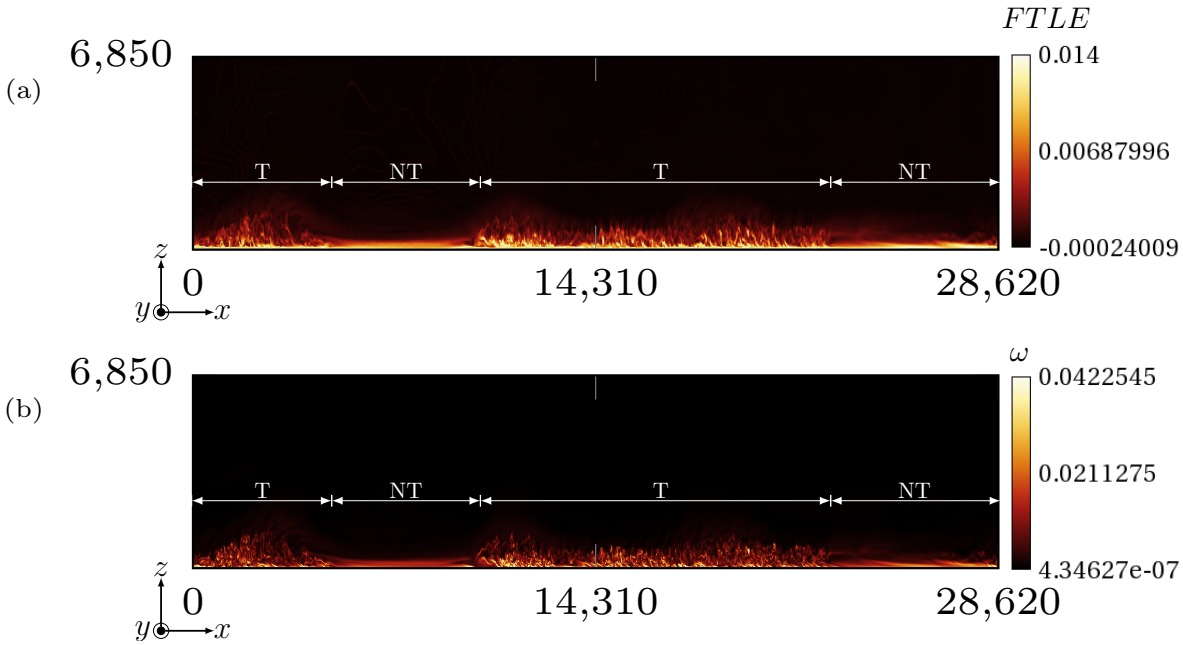

Figure 2.3: A vertical slice for the entire wall-normal height of the simulation is shown for (a) finite-time Lyapunov exponent and (b) vorticity magnitude corresponding to case S_1. T and NT denote turbulent and nonturbulent regions respectively.

2.1.3 Vortices

Described by Küchemann (1965) as the 'sinews and muscles' of fluid flows, *vortices* and their identification is important in turbulence. Currently, there exists no universally accepted definition for a three-dimensional vortex and a vast range of criteria are used to detect these structures. A comprehensive overview of these criteria can be seen in the review papers of Cucitore et al. (1999) and Günther and Theisel (2018). Jeong and Hussain (1995) require that a vortex must possess net vorticity (so as to exclude potential vortex regions having zero cross-section) and that their geometry must be Galilean invariant. Newer criteria have stricter requirements such as objectivity or reference frame invariance (Haller, 2015). All criteria fall under two broad categories - Eulerian criteria involve point-wise characterization of the velocity gradient tensor (∇v) for every instant in time and Lagrangian criteria follow fluid particle trajectories.

In a recent work, Lindheim et al. (2021) showed by tracking coherent structures educed with Q-criterion in ERA 5 reanalysis datasets that Eulerian and Lagrangian techniques provide useful and complementary results. For instance, while the Eulerian tracking method is able to detect structures corresponding to the extratropical cyclones 'Lothar' and 'Martin', the Lagrangian coherent set approach (Banisch and Koltai, 2017) shows the rapid advection of air masses around these storms but does not identify the centers of the storms itself. By analyzing cross-sections of a channel flow, Green et al. (2007) show that the Eulerian $Q-$criterion and the Lagrangian finite-time Lyapunov exponent (FTLE) highlight similar regions as vortices with the latter method having better resolution but at a higher computational cost. In our test, another Eulerian criteria called vorticity magnitude,

$$\boldsymbol{\omega} = \nabla \times \mathbf{v}, \quad |\boldsymbol{\omega}| > \omega_{threshold} \tag{2.1}$$

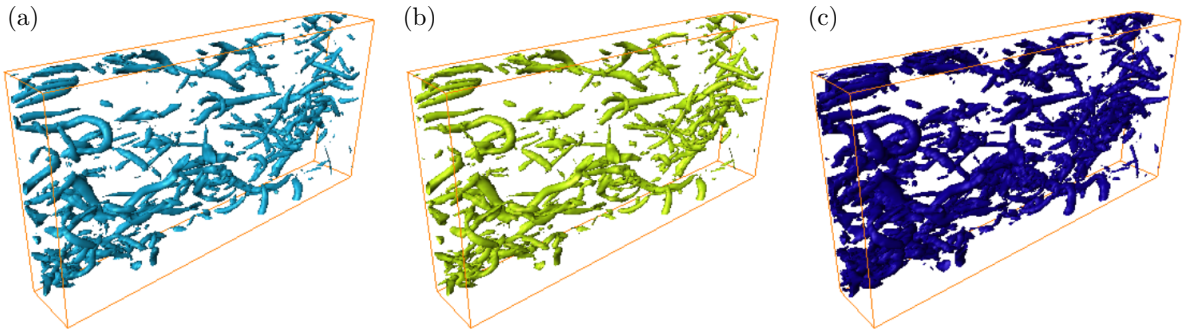

Figure 2.4: A comparison among (a) Q, (b) λ_2 and (c) Δ vortex criteria are shown here for a small subset of channel flow data obtained from the Johns Hopkins Turbulence Database (Graham et al., 2016). All three criteria are visualized at the equivalent thresholds proposed by Chakraborty et al. (2005) (see equation 5.2). The thresholds are $\tau = 49, -49, 4357.37$ for Q, λ_2 and Δ criterion respectively.

where $|\cdot|$ is the magnitude of the vorticity vector $\boldsymbol{\omega}$, $\boldsymbol{v}$ is the velocity vector and $\omega_{threshold}$ is a threshold applied over the entire scalar field, is compared with FTLE. As described in Shadden et al. (2005) and Green et al. (2007), at each point in space, FTLE gives a scalar measure of the maximum rate of separation of a pair of tracer particles initialized near that point. For tracers advected in forward-time, this indicates repelling Lagrangian Coherent Structures (LCS) whereas in backward-time, it indicates attracting LCS. Both $|\boldsymbol{\omega}|$ and FTLE are calculated over the full simulation domain i.e., $3072 \times 512 \times 6144$ points for the case S_1. In the case of FTLE, 5 billion tracers were advected in the flow field in forward time (showing repelling material surfaces) until $t^+ = 1.4$ (about 10 timesteps).

It is easily observable from figure 2.3 that both criteria demarcate the flow into turbulent and non-turbulent regions in a comparable manner. However, it is noted that the Eulerian criterion had a significantly lower computational cost and the computation was possible on a single CPU in few minutes whereas a GPU parallelized code was written for Lagrangian FTLE which was run on the TESLA P100 GPU with 3584 cores for about 7 hours. In this thesis, the Eulerian vortex criteria are preferred over the Lagrangian criteria due to the following reasons: (1) significantly lower computational cost and, (2) the geometrical characterization procedure described later in the chapter requires structures with clearly defined boundaries, i.e., level sets which can be extracted from scalar fields. Although some methods such as the Lagrangian-averaged vorticity deviation (Haller et al., 2016) allow for the extraction of such features, this is not clear for methods such as the FTLE.

To choose an appropriate Eulerian criterion, one can follow the work of Chakraborty et al. (2005) who showed that popular criteria such as Q-criterion (Hunt et al., 1988), λ_2 (Jeong and Hussain, 1995) and Δ (Chong et al., 1990) tend to classify similar points in the spatial domain as belonging to the ranges of vortices. The Q-criterion characterizes regions as vortices when,

$$Q = \frac{1}{2}(||\boldsymbol{\Omega}||^2 - ||\boldsymbol{S}||^2) > 0 \tag{2.2}$$

where $\boldsymbol{\Omega} = \frac{1}{2}[\nabla \mathbf{v} - (\nabla \mathbf{v})^T]$ is the spin tensor and $\boldsymbol{S} = \frac{1}{2}[\nabla \mathbf{v} + (\nabla \mathbf{v})^T]$ is the strain-rate tensor. Therefore, the $Q-$criterion identifies vortices as regions where spin dominates over strain. This criterion overcomes a crucial drawback of vorticity magnitude where shearing motions are misidentified as a vortex (Lugt, 1979). However, $Q > 0$ does not automatically guarantee

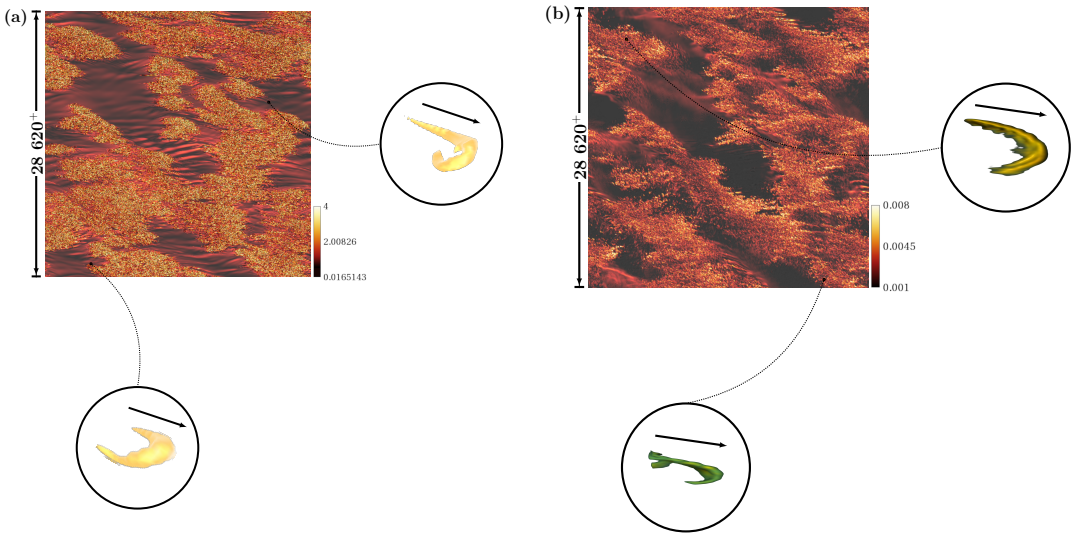

Figure 2.5: Two random hairpin-like structures are extracted from different regions of the flow for the case S_1. (a) shows $Q-$criterion structures oriented in similar directions and (b) shows structures identified with FTLE also oriented in similar directions. In both cases, the horizontal slice is at $y^+ \approx 10$.

a pressure minimum within the vortex region. The λ_2 criterion is based on the observation that a pressure minimum in a plane can be identified if the pressure Hessian has two positive eigenvalues. Starting from the incompressible Navier-Stokes equation and neglecting unsteady and viscous effects, the reduced equation is written as,

$$\mathbf{S}^2 + \mathbf{\Omega}^2 = -\frac{1}{\rho}\nabla(\nabla p) \tag{2.3}$$

where p is the pressure and the right hand side denotes the pressure Hessian. Therefore, the λ_2-criterion identifies vortices as regions where,

$$\lambda_2(\boldsymbol{S}^2 + \mathbf{\Omega}^2) < 0 \tag{2.4}$$

i.e., the intermediate eigenvalue of the symmetric tensor $\boldsymbol{S}^2 + \mathbf{\Omega}^2$, when they are ordered $\lambda_1 \geq \lambda_2 \geq \lambda_3$, is negative. The Δ-criterion, on the other hand, defines vortices as regions where the velocity gradient tensor $(\nabla \mathbf{v})$ admits complex eigenvalues,

$$\Delta = \left(\frac{R}{2}\right)^2 + \left(\frac{Q}{3}\right)^3 \tag{2.5}$$

where Q and R are the second and third invariants of $\nabla \mathbf{v}$ respectively. When $\Delta > 0$, then $\nabla \mathbf{v}$ has complex eigenvalues. Chakraborty et al. (2005) show that it is possible to define an equivalent threshold among these criteria to identify similar structures at a non-zero threshold. An example is illustrated in figure 2.4 which shows that similar regions are identified as vortices with the three criteria. This implies that a choice among these criteria will not affect our qualitative results, therefore the Q-criterion is chosen to identify vortices.

In addition to their importance in turbulence production (Robinson, 1991), vortices, particularly the hairpin-like ones exhibit unique characteristics in strongly stratified flows. As shown in the poster of Harikrishnan et al. (2020), randomly extracted hairpin-like Q-criterion structures from two different regions of the flow field seem to be oriented in a similar direction.

Later, the same was observed with the Lagrangian FTLE haripin-like structures (see poster of Harikrishnan et al., 2021). These results as shown in figure 2.5 seem to suggest an organization of structures at a global level which will be investigated in later chapters.

2.1.4 Shear layers and backs

Zhou et al. (1999) noted that when quasi-streamwise vortices eject fluid up and back, this induced back flow tends to interact with the mean flow which results in the formation of *shear layers* close to the wall. Shear layers are ubiquitous close to the wall of boundary layers. They exist in the buffer layer ($5 < y^+ < 30$) and sometimes extend beyond $y^+ > 80$. These structures, which are characterized by high values of the instantaneous velocity gradient ($\partial u'/\partial y$), are capable of retaining coherence up to 1000^+ viscous units in the streamwise direction (Johansson et al., 1987). In conjunction with vortices, shear layers may be responsible for near-wall turbulence production (Robinson, 1991; Alfredsson et al., 1988).

Since vorticity magnitude is a known indicator for shear regions, it can be used to highlight near-wall shear layers and shear layers on the order of δ-scale (here, δ refers to the mean boundary layer thickness which is the height at which the velocity is 99% of the free stream velocity) termed *backs*.

2.1.5 Pockets

Pockets are 'footprints' of outer layer structures which have not received much attention and they were identified through the work of Falco (1977), Falco (1980), and Kim et al. (1987). Their contribution to turbulence production is not fully understood yet, however Chu and Falco (1988) noted that they may be responsible for the generation of hairpin vortices.

To the author's knowledge, pockets have never been investigated in the context of ABL flows and a goal of this work is to understand if these structures are useful and warrant further investigation in future works. These structures are known to exist within the viscous sublayer and are observable with diverging streamlines (Robinson, 1991).

2.1.6 Bulges

A coherent structure frequently referred to in ABL literature (Shah and Bou-Zeid, 2014a; Katul, 2019) are the *bulges* which are very large scale motions (VLSMs) or superstructures existing between the free stream and the outer edge of the boundary layer. They show numerous narrow incursions, sometimes extending into the buffer layer (Corrsin and Kistler, 1955; Kovasznay et al., 1970). These structures have a tendency to meander in the spanwise direction (Hutchins and Marusic, 2007) and are also known to attenuate small-scale fluctuations close to the wall (Marusic et al., 2010). Recently, Salesky and Anderson (2018) observed that VLSMs show a change in topology with increasing instability in the convective boundary layer. They report a change from being convective rolls under weakly convective conditions to open cells under highly convective conditions.

With vorticity magnitude as an indicator, the geometry, streamwise and spanwise extent of these structures under increasing stratification are investigated in chapter 3.

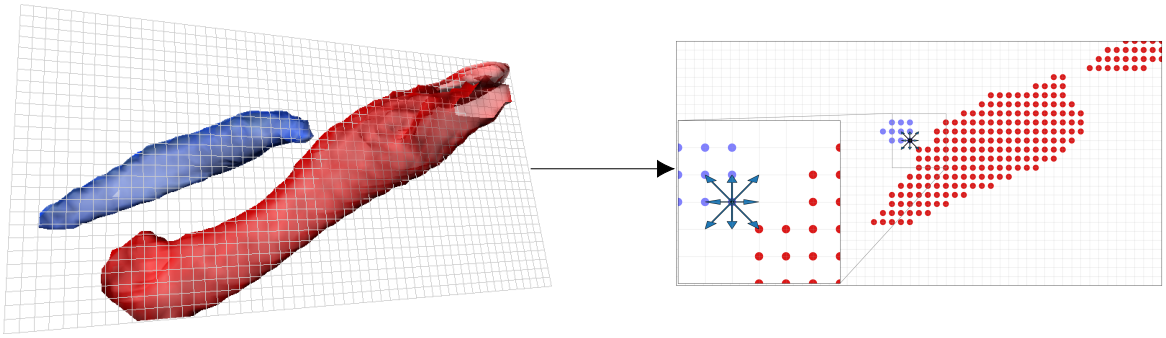

Figure 2.6: A drawback of the NS algorithm is shown here where two individual structures (colored blue and red) is misidentified as a single structure. Examining a plane reveals the reason for the misidentification and is shown in the right. When a point belonging to the blue structure (at the tail end of all arrows) is considered to be the center of the 3×3 cube, one of its neighbors is a point belonging to the red structure.

2.2 Extraction of structures from scalar fields

For any three-dimensional scalar field, the numerical procedure used to extract individual coherent structures is described in this section. Following the work of Moisy and Jiménez (2004), a structure embedded within this scalar field is defined as a set of connected points satisfying a threshold. A point x belongs to a structure if,

$$\alpha(x) > \tau_p \tag{2.6}$$

where α is one of the several indicators from table 2.1 and τ_p is an appropriate threshold. There are numerous ways of choosing a threshold and a systematic, non-subjective approach is developed and discussed in section 2.3. This method of decomposition of the flow field based on a global threshold value is a classic image segmentation technique and an overview of numerous segmentation techniques can be found in the review work of Pal and Pal (1993). To extract individual structures, a new algorithm combining the neighbor scanning procedure of Moisy and Jiménez (2004) and marching cubes algorithm of Lorensen and Cline (1987) is developed and described in the following subsections.

2.2.1 Neighbor scanning algorithm

The neighbor scanning (NS) method of Moisy and Jiménez (2004) is a simple and fast algorithm to extract individual structures. The algorithm initially identifies a 'seed' point by successively scanning points in the domain which satisfies (2.6). When a seed is identified, this is taken as a starting point for the structure. The neighbors of this seed are identified by considering this point to be the center of a 3×3 cube and any of the 26 neighbors (faces, edges and vertices of the cube) are added to the structure if they also satisfy (2.6). New neighbors are added to the structure until no new ones can be found. All points in this structure are given the same label. Then the algorithm proceeds to find a new seed point. Once all structures are identified, they are sorted by size.

While this method yields good results at large threshold values for which the structures are spaced apart, some structures tend to be grouped together at smaller threshold values. This drawback is illustrated in figure 2.6 in which both red and blue regions are extracted as a

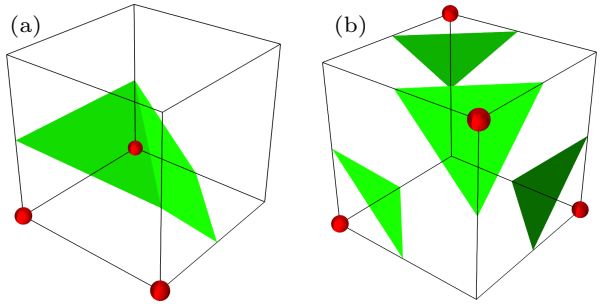

Figure 2.7: Difference between continuous and discontinuous mesh.

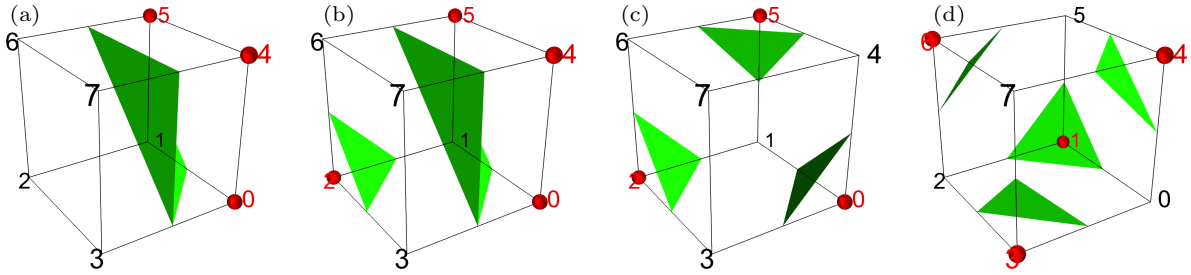

Figure 2.8: Examples of surface mesh generation for (a) continuous surface mesh corresponding to case 49 and (b, c, d) discontinuous mesh surfaces corresponding to cases 53, 37 and 90 respectively.

single structure. An inspection of the plane reveals that a point belonging to the red region is a neighbor to the blue one and hence, both points are added as a part of the same structure. The difference is apparent only upon visualization. In a later part of the chapter that discusses the geometrical characterization procedure (section 2.4), it can be seen that the method relies on local (point-wise) computation of shape and curvature to classify a structure as either blob-like, sheet-like or tube-like. Shortcomings of the NS algorithm will result in an inaccurate classification of the geometry. Therefore, in the following subsection, an improvement of this algorithm is presented.

2.2.2 Marching cubes correction

The reason why the NS algorithm failed to separate the structures in the example shown in figure 2.6 is because the information regarding the surface mesh generation by the visualization algorithm is not incorporated into it. Therefore, to ensure *visualization accurate*[1] structure extraction, the identified neighbors are corrected with the popular marching cubes (MC) algorithm (Lorensen and Cline, 1987). Although numerous visualization algorithms exist Lewiner et al. (2003), Schreiner et al. (2006), Ju et al. (2002), and Dey and Levine (2008), the MC algorithm is chosen as it is employed by our visualization software Amira (Stalling et al., 2005).

For each grid cell (eight vertices of a cube), the MC algorithm determines the vertices which satisfy (2.6) and generates triangles (or surface mesh elements) to represent surfaces at those vertices. For the eight vertices of the cube, the surface mesh can be represented 2^8 ways.

[1]The accuracy of extraction of structures is strongly dependent on the visualization algorithm employed. In this thesis, only the marching cubes algorithm is used for visualization and hence, is combined with the neighbor scanning procedure for accurate extraction of structures. If a different visualization algorithm is employed, the NS+MC algorithm may no longer be adequate. Hence, for visualization accurate extraction of structures, the same algorithm used for visualization must be used during the extraction procedure.

The reader is referred to the original work of Lorensen and Cline (1987) for further information on the MC algorithm. First, a distinction is made between continuous and discontinuous surface mesh elements. For most cases, the mesh element is continuous as shown in figure 2.7(a). This means that all points satisfying the threshold are a part of the same structure. For 92 cases, the mesh element is discontinuous (see figure 2.7(b)) when $2-4$ nonadjacent points satisfy the threshold. In these cases, the discontinuous mesh elements may belong to the same structure or to completely different structures as illustrated in figure 2.6. To rectify this issue, the following correction is applied to the NS algorithm,

(1) *Construction of a lookup table:* The purpose of the lookup table is to enhance the speed of the algorithm. The vertices of the cube are assigned an index from $\{0, ..., 7\}$. Next, all of the 256 cases are visualized to identify the vertices that have to be grouped. When a continuous surface mesh is seen, the lookup table has an empty array meaning no correction is necessary. The same is true for case 0 and case 255 where all or no points satisfy the threshold and hence, no surface mesh is generated. For discontinuous mesh elements, the vertex indices need to be grouped. For instance, in figure 2.8(b) two groups are identified; one with vertex indices $\{0, 4, 5\}$ and the other with vertex index $\{2\}$. The final lookup table with vertex groupings for all cases is shown in appendix A.

(2) *Identifying the case in the lookup table:* Once the 26 neighbors of the large 3×3 cube are identified by the NS algorithm, each of the 8 subcubes are matched with a case from the lookup table. If $V_p = \{v_0, ..., v_7\}$ is the set of vertices for each subcube, the vertex is assigned a value of 1 when the neighbor is added and 0 otherwise. The following equation can be used to identify the case from the lookup table,

$$\text{case} = \sum_{i=0}^{7} 2^i [V_p(i) = 1] \tag{2.7}$$

where $[\cdot]$ denotes an Iverson bracket. For the example shown in figure 2.8(a), the case $= 2^0 + 2^4 + 2^5 = 49$.

(3) *Neighbor correction:* Once all subcubes are associated with a case from the lookup table, the vertex grouping indices are retrieved. No corrections to the neighbors are applied if there are no vertex groupings, i.e., if the array is empty. On the other hand, for a non-empty array, the 'right group' of vertex indices has to be chosen. This is chosen as the one which contains the center point of the 3×3 cube. The reasoning is as follows: since the center point of the 3×3 cube (being the current point of interest) is already a part of a structure, the vertex group which has this center point should be a part of the structure as well. This is repeated for all subcubes, thus correcting the neighbors identified with the NS algorithm.

The complete algorithm for neighbor scanning with the marching cubes correction is shown in figure 2.9.

Input: Scalar indicator α, threshold τ
Output: Scalar field with labels corresponding to individual structures, Structure information data containing the embedding location of each structure, Volume of the biggest structure in the given domain $V_{\max}$, Volume of all structures in the domain V, Auxiliary scalar field with structure labels

```
/* Thresholding the scalar field converts the data from
   floating-point numbers to boolean data type where 1 satisfies the
   threshold indicating the presence of a structure.                  */
```

begin *thresholding the scalar indicator:*
  if $\tau > 0$ **then**
    data $= \alpha > \tau$
  else
    data $= \alpha < \tau$
  end
end
Create an auxiliary scalar field of size α to store the label of structures;

```
/* Main loop                                                          */
```

for *i = 1 to x length* **do**
  for *j = 1 to y length* **do**
    for *k = 1 to z length* **do**
      if *data(i, j, k) == 1* **then**

```
        /* data(i, j, k) == 1 marks the starting point of a
           structure                                                  */
```

        while *neighbors exist* **do**
          Assign a label to data(i, j, k) and store in auxiliary scalar field;
          Consider data(i, j, k) to be the center of a 3×3 cube;
          Identify which of the 26 neighbors satisfy τ;
          begin *marching cubes correction:*
            Split the 3×3 cube into 8 subcubes;
            for *p = 1 to 8* **do**
              Identify the marching cubes case with equation (2.7);
              With the case, the grouping of vertices is inferred from the lookup table in appendix A;
              The group of vertices which contain data(i, j, k) is kept and the remaining neighbors are discarded;
            end
          end
        end
      end
    end
  end
end

Figure 2.9: Algorithm for the extraction of individual structures from scalar fields with neighbor scanning algorithm and marching cubes correction

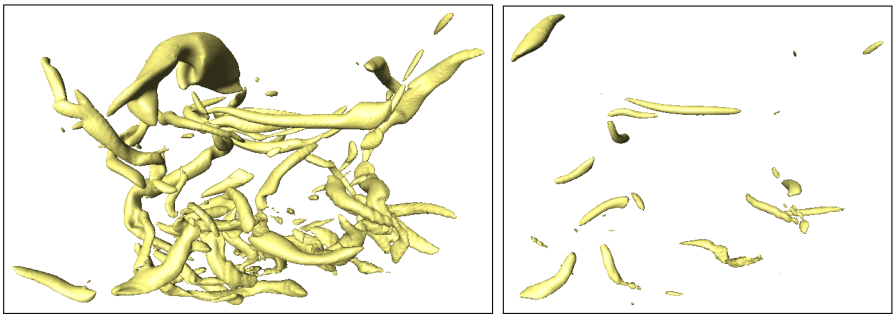

Figure 2.10: Sample Q-critrion data chosen for validation of the NS+MC algorithm. Here structures are visualized at thresholds $\tau = 100$ (Left), 549 (Right). Clearly, the complexity of structure extraction increases for lower thresholds.

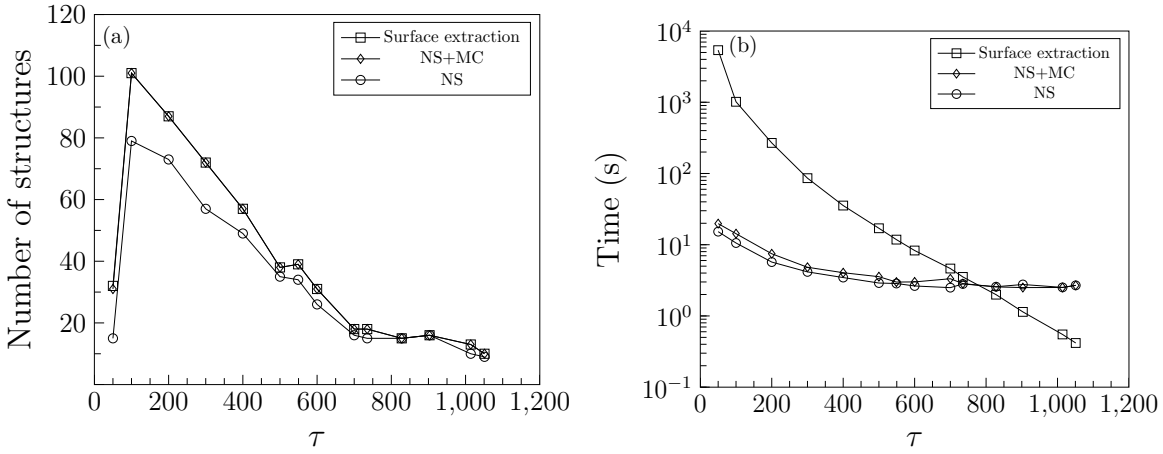

Figure 2.11: A comparison among the surface extraction algorithm (square marker), NS+MC algorithm (diamond marker) and NS algorithm (circle marker) for (a) extraction of structures at various thresholds and (b) the time taken for extraction are shown here.

2.2.3 Validation of the NS+MC algorithm

The goal of this section is to validate the NS+MC algorithm for visualization accurate extraction of structures from three-dimensional scalar fields. To aid with the validation, an alternate method by which structures can be extracted directly from the visualized surfaces is used.

As described in Lorensen and Cline (1987) for the marching cubes algorithm, within a cube, triangles are created at points where the user-defined threshold is satisfied. Depending on which of the points in a cube satisfy the threshold, these triangles are constructed in a specific manner through a lookup table composed of all 256 combinations. Some examples are shown in figure 2.8. To represent the surface composed of these triangles, a list of 3D coordinates and a connectivity list of triangles are necessary (Stalling et al., 2005). Each triangle in the connectivity list has three indices which point to the list of coordinates. By exploiting the fact that connected triangles in a surface share a common edge, the connectivity list can be used to identify and extract connected surfaces or structures. This is henceforth referred to as the surface extraction algorithm.

A sample dataset of a Q-criterion scalar field with size $200 \times 328 \times 234$, as shown in figure 2.10, is chosen for validation. For various thresholds, the extracted structure counts and the corresponding time taken with the surface extraction algorithm (described above), NS+MC algorithm and NS algorithm are plotted in figure 2.11. If the surface extraction algorithm

(square marker) is taken to be the ground truth, one can see that its results compare well to the NS+MC algorithm at all tested thresholds. The disparity between neighbor scanning algorithm (circle marker) and when it is corrected with the marching cubes algorithm (diamond marker) is instantly observable in figure 2.11(a). As expected, the NS algorithm tends to group together structures at smaller thresholds (where they are closely spaced) and therefore, the number of structures is always lower than that obtained with the other two algorithms. Figure 2.11(b) shows the time taken for the extraction of structures with all three algorithms. At the smallest tested threshold, the NS algorithm is the fastest taking only 15 seconds, NS+MC with 19 seconds and surface extraction taking about 5387 seconds or approximately 1.5 hours.

2.3 On the choice of a threshold

Green et al. (2007) noted that the crux when dealing with any Eulerian criterion is its reliance on a user-defined threshold to identify individual structures. Over the years, numerous justifications have been provided for the choice of the threshold. In general, it can be seen that a low value of threshold often yields a complex, interconnected, sponge-like structure whereas a high value will result in few intense regions. Moisy and Jiménez (2004) proposed to consider this problem to be analogous to that of a *percolation transition* in which the complex cluster appears above a critical threshold. This threshold, henceforth referred to as a *percolation threshold,* τ_p, presents a natural, non-subjective way of choosing a threshold value. In the context of channel-flow turbulence, Del Álamo et al. (2006) pointed out that τ_p is similar for increasing Reynolds numbers.

Percolation analysis on the seven quantitative indicators of table 2.1 is shown in figure 2.12 (a - g). The ratio $V_{\max}/V$, where $V_{\max}$ is the volume of the largest structure in the domain and V is the sum of the volume of all structures at a threshold τ, is computed for increasing values of τ. $V_{\max}/V = 1$ implies that a large interconnected structure spans the entire domain. As the threshold is increased, the magnitude of the slope of $V_{\max}/V$ increases and reaches a maximum at τ_p. It should be noted that the percolation analysis is computed on grid A ($3072 \times \text{ylen} \times 6144$). The number of grid points in the wall-normal direction (ylen) is based on the indicator (see table 2.1). Ideally, the computation should also be performed for the entire threshold range of the indicator. However, due to the high computational cost especially at lower values of τ, the threshold range is discretized so that the transition is seen with fewer values of τ. The threshold range is initially split with a chosen number (usually 1000) of evenly spaced values. Generally, a smooth plot can be generated with the first 50 values of τ. If the transition is not seen in this region, the order of magnitude of the chosen number is changed.

It was noted by Del Álamo et al. (2006) that the inhomogeneity of the flow in the wall-normal direction for wall-bounded flows needs to be taken into account when choosing a global threshold value. If a threshold is chosen to visualize wall features, few structures will be highlighted away from the wall and vice versa (see figure 2.13(a)). Nagaosa and Handler (2003) circumvented this issue by nondimensionalizing the Q-criterion with its root mean square (RMS) at every wall-parallel plane. This resulted in a more uniform spread of structures throughout the channel flow. Equation (2.6), can therefore, be rewritten as,

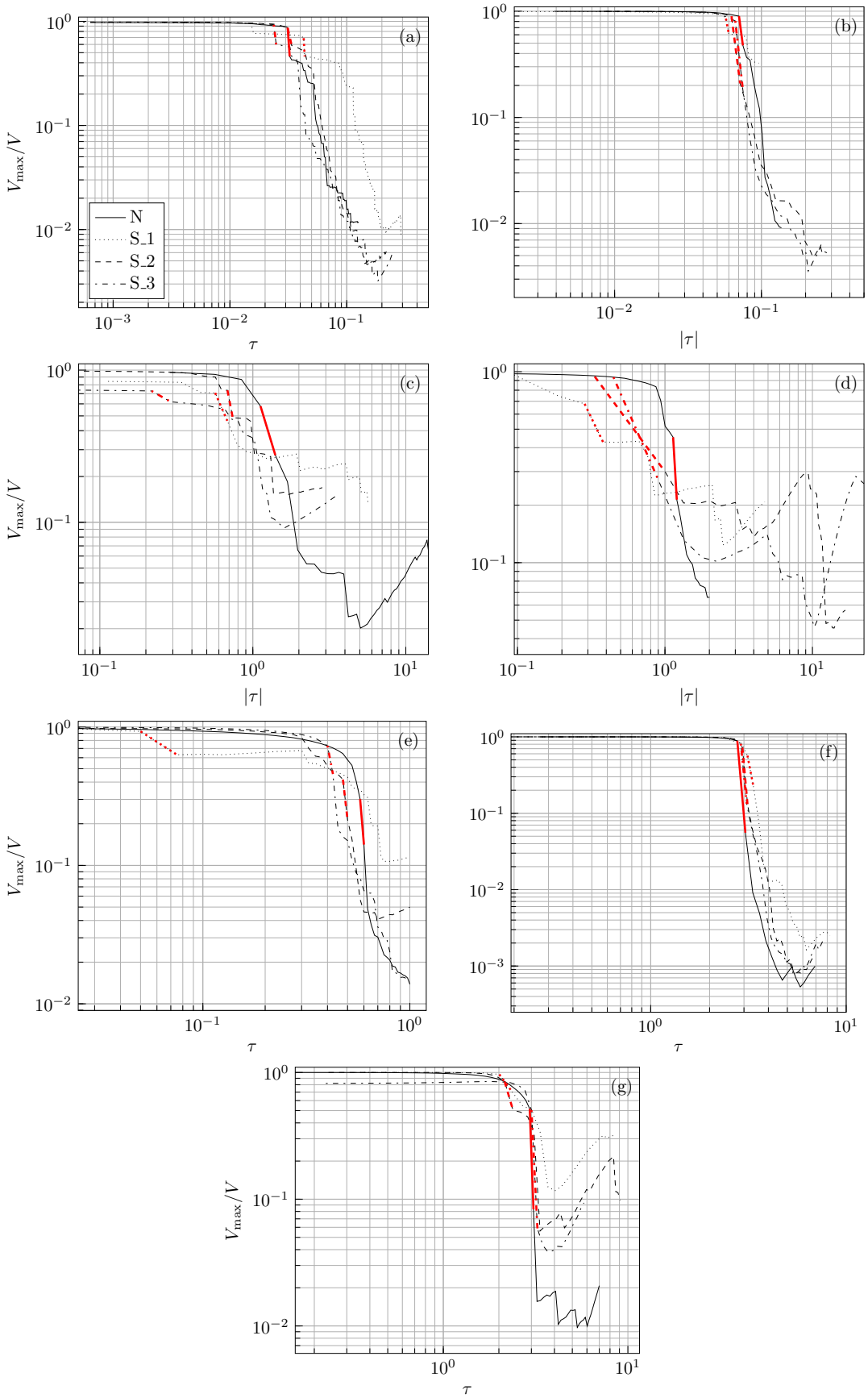

Figure 2.12: Percolation analysis on seven indicators from table 2.1 are shown here. (a - g) are the high-speed streaks, low-speed streaks, sweeps, ejections, vortices, shear layers and backs. Solid line is the neutrally stratified case (N) and the dashed and dotted lines are the various stably stratified cases (S_1, S_2, S_3). Line specification is shown in (a). Red portion of the lines indicate the region of percolation transition.

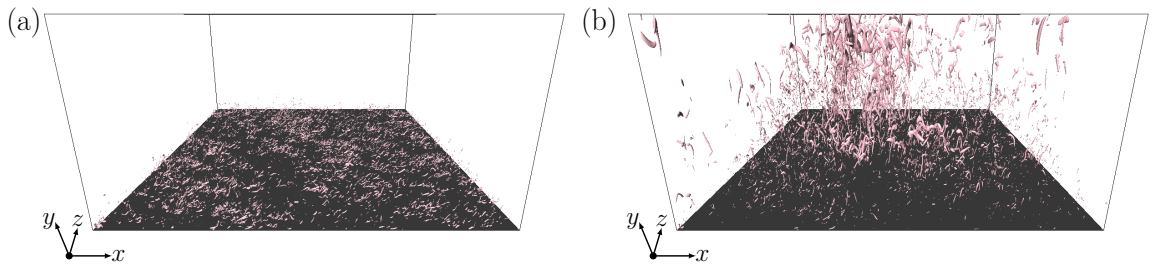

Figure 2.13: The $Q-$criterion structures are highlighted for case N. Isosurfaces at (a) $\tau = 0.0017$ and (b) $\tau = 10$ are visualized. In the latter case, the effect of nondimensionalization with the RMS over every wall normal planes is visible and structures are highlighted throughout the flow. Here, the $y^+ \approx 1550$ which includes a significant portion of the outer layer.

$$\alpha(x) > \tau_p \, \overline{\alpha'^2(y)}^{1/2} \tag{2.8}$$

where $\overline{\alpha'^2(y)}^{1/2}$ is the RMS of the indicator α over wall-normal planes. The effect of this parametrization is visible in figure 2.13(b) where a threshold chosen to highlight wall features also shows structures in the outer layer. This parametrization is only necessary when dealing with large domains where a significant portion of the outer layer is included. In the case of streaks with the domain restricted to $y^+ < 40$, a global threshold value will highlight the structures uniformly without the parametrization.

2.3.1 Multilevel percolation analysis

Although the techniques introduced in the previous subsections to choose a global threshold value with percolation analysis work well for neutral and intermediate levels of stratification (i.e., for cases N, S_2 and S_3), individual structures cannot be educed for high levels of stratification i.e., case S_1. The presence of global intermittency with coexisting turbulent and nonturbulent regions, forces structures to aggregate into clusters at non-zero thresholds. This can be clearly seen from figure 2.14(a) in which the $Q-$criterion thresholded at τ_p identifies an entire region colored gold as a single structure. To avoid this issue, a new technique based on iterative application of percolation analysis is described in this subsection.

The goal of the new technique is to identify suitable thresholds larger than the global percolation threshold τ_p for individual structures i.e., the large structure is broken down into individual structures and each exists at a unique threshold value. The steps of this technique, henceforth called multilevel percolation analysis (MLP), is presented below:

(1) For a given indicator applied to a flow field, the global percolation threshold τ_p is initially computed over the entire domain with the procedures described in the previous subsections.

(2) The structures at τ_p are extracted with the NS+MC algorithm. If an entire cluster is extracted as a structure as in figure 2.14(a), then the entire structure can be subjected to MLP. In this scenario, a small portion of the domain of size $300 \times 90 \times 600$ is chosen to keep the computational costs low.

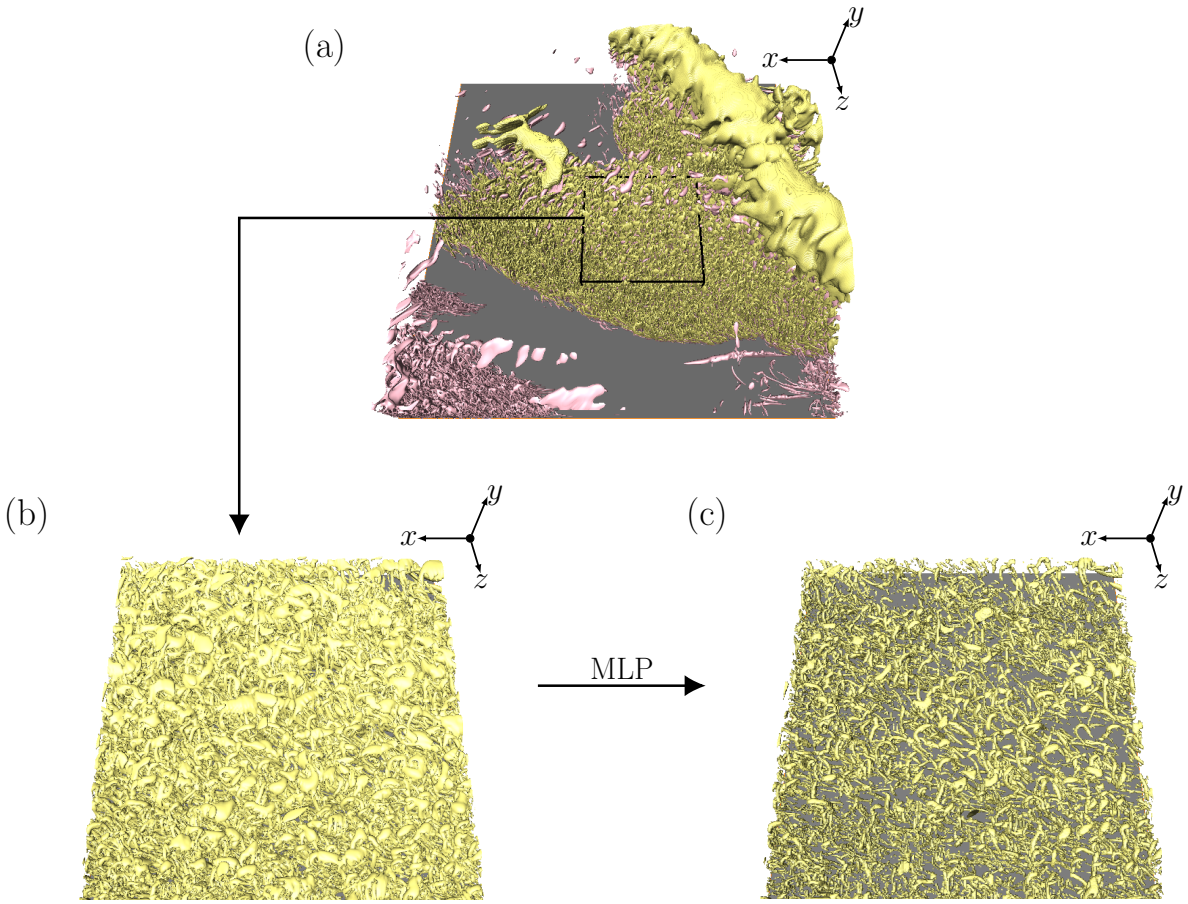

Figure 2.14: When $Q-$criterion applied to case S_1 and thresholded at the global percolation threshold τ_p, an entire cluster colored in gold is identified as a single structure as shown in (a). A small region chosen for MLP analysis is shown in (b) and the result is shown in (c).

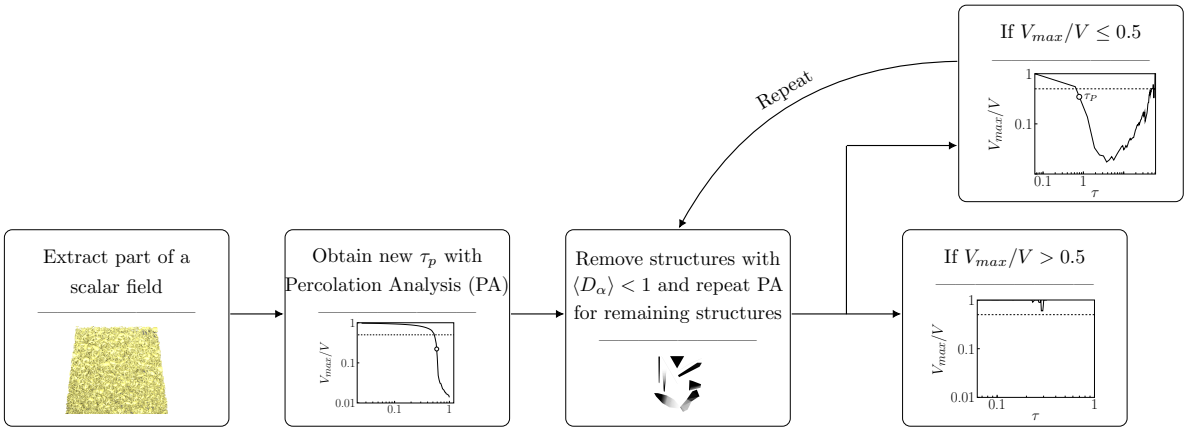

Figure 2.15: A schematic for MLP is shown. Here, τ_p is the global percolation threshold and $\langle D_\alpha \rangle$ is the mean fractal dimension (see subsection 2.4.1 for an explanation) of the structure. When $V_{\max}/V > 0.5$ for the entire threshold range, then the structure is classified as simple and the minimum threshold is chosen for the structure. If the structure is deemed complex, the procedure is repeated.

(3) For the small domain, the percolation analysis is repeated to obtain a new threshold value. It should be noted that the global percolation threshold τ_p obtained in step (1) is the minimum threshold which is checked.

(4) At the new threshold value, the structures are extracted and the fractal dimension for each structure is computed with the method described in subsection 2.4.1.

(5) The structures with a mean fractal dimension $\langle D_\alpha \rangle < 1$ ($\langle \cdot \rangle$ is the mean calculated over the local dimensions corresponding to various box sizes and α is an indicator) are filtered out. This step ensures a noise-free result.

(6) The structures which are filtered out are checked against a stopping criterion to determine if the structure is an individual one or if it still exists as a cluster. The stopping criterion applies the percolation analysis again and computes the minimum value of the ratio $V_{\max}/V$ reached over the threshold range. In this case, the new τ_p obtained from step (3) is the minimum threshold which is checked. If the ratio $V_{\max}/V$ is above 0.5 over the entire threshold range, the structure is deemed as a *simple structure* and the minimum threshold which is checked is taken as the unique threshold for the structure. If, on the other hand, the ratio $V_{\max}/V \leq 0.5$, then the structure is deemed as a *complex structure*. A new percolation threshold is computed for the complex structure and the process from step (3) is repeated.

(7) Steps (3-7) are repeated on all structures extracted in step (2). The entire procedure is shown as a schematic in figure 2.15.

The MLP analysis on a small computational domain as seen in figure 2.14(b) gives the result shown in figure 2.14(c). It is instantly observable that the result is noise-free and the structures are more or less individual. In the current implementation of the algorithm, this computation took 5 days on serial mode.

2.3.1.1 Rationale for the stopping criterion

For simplicity, the stopping criterion chosen is to adopt a minimum value of the ratio $V_{\max}/V$ over the entire threshold range being tested. From a geometric standpoint, it can be understood that when $V_{\max}/V = 1$ or $V_{\max} = V$ at a threshold τ, then a single structure spans the entire domain. If the condition holds over the entire threshold range, this implies that the structure has one local maximum value, i.e., for increasing thresholds the structure will collapse towards one point in space as depicted in figure 2.16(a). In practice, however, this condition is computationally expensive and can be relaxed to $V_{\max}/V > 0.5$. With this condition, at most two structures can exist, i.e., there are two local maximum values and the volume of one structure is always larger than the other (see figure 2.16(b)). It should be noted that choosing $V_{\max}/V$ other than 1 is subjective and should be considered only for very large datasets to lower the computational burden.

Figure 2.16(c) shows a proof-of-concept for a simple and complex structure in which the threshold $V_{\max}/V > 0.5$ is chosen as the condition to identify a simple structure.

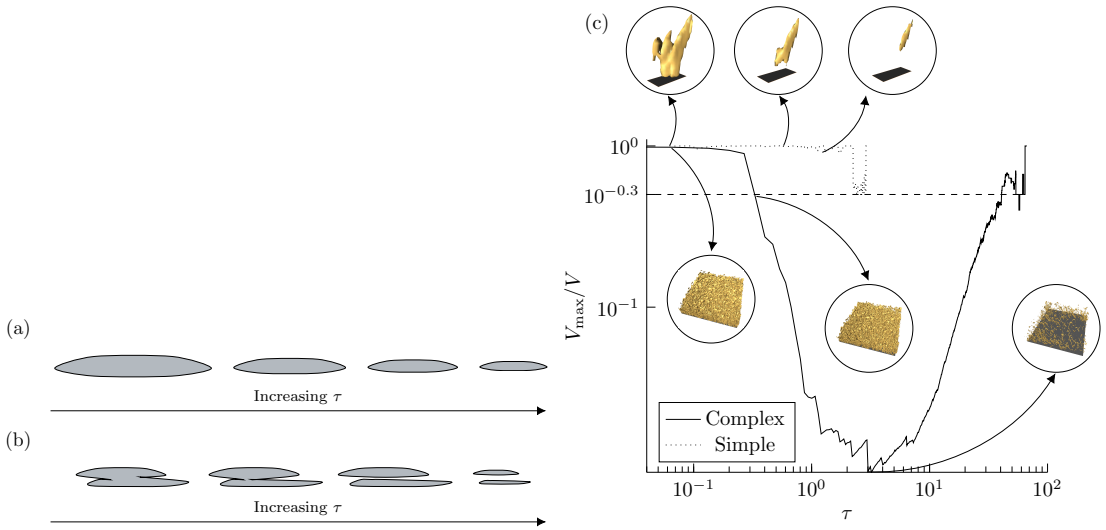

Figure 2.16: The effect of choosing a minimum value of the ratio $V_{\max}/V$ as (a) 1 and (b) 0.5 respectively is shown. A proof-of-concept for MLP is shown in (c). The highlighted thresholds correspond to $\tau = 0.0625, 0.334, 3.01$.

2.4 Geometrical characterization

The necessity of extracting visualization accurate structures with the NS+MC algorithm is exemplified in this section. Once all structures are extracted with the global percolation threshold τ_p, they are geometrically characterized with an approach similar to Bermejo-Moreno and Pullin (2008). The main steps along with the modifications are presented in the following subsections.

2.4.1 Fractal dimension

In the first step, all structures which are sparser than a line i.e., those that have a mean fractal dimension (FD), $\langle D_\alpha \rangle < 1$, are filtered out. There are two important reasons for this filtering step: first, structures consisting of few connected points which are noise-like cannot be meaningfully interpreted. Second, computation of curvedness and stretching parameters described in subsection 2.4.2 are dependent on the volume of a structure and hence require that the structure should have a closed surface. The second reason raises the obvious question of why the structures having a fractal dimension between $1 \leq \langle D_\alpha \rangle \leq 2$ are not discarded. This is answered below.

Following the work of Moisy and Jiménez (2004), the fractal dimension of a structure is estimated with the classical box-counting method. The extracted structure is first placed inside a domain that embeds it. With a fixed grid scan, a box of size r is moved over the entire domain without overlap and the number of boxes i.e., $N_\alpha(r; \tau_p)$ that contain some point belonging to a structure is counted. This grid scan is repeated for decreasing box sizes chosen as $2^{-n}L$, where n is varied between 0 and 9 and L is the largest length of the embedding domain. The fractal dimension defined as,

$$D_\alpha(r) = -\frac{\mathrm{d} \ln N_\alpha(r)}{\mathrm{d} \ln r} \tag{2.9}$$

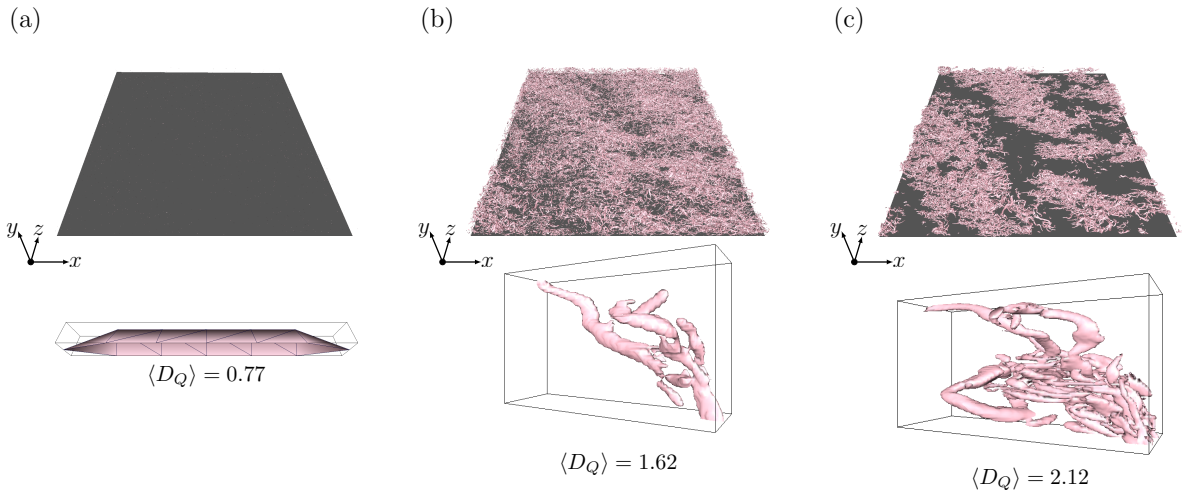

Figure 2.17: The $Q-$criterion scalar fields for case N are reconstructed for (a) $\langle D_Q \rangle < 1$, (b) $1 \leq \langle D_Q \rangle \leq 2$ and (c) $\langle D_Q \rangle > 2$.

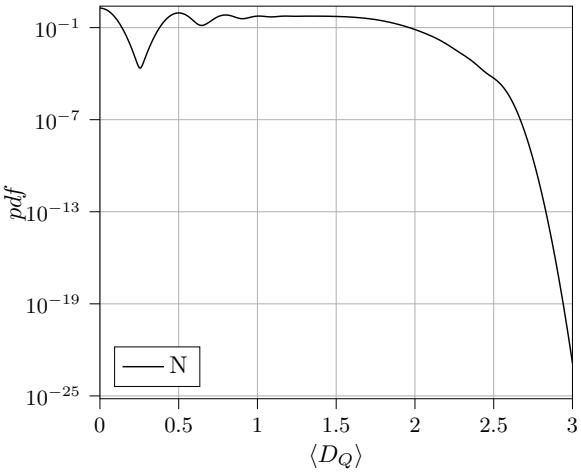

Figure 2.18: Probability density function of the mean fractal dimension $\langle D_Q \rangle$ for the neutrally stratified case is shown here. Box-counting is performed for grid B until $y^+ \approx 1550$.

is the range of box sizes over which this logarithmic slope is approximately constant. Even though, FD estimates are used only for filtering purposes in this procedure, they can already give a first understanding of the geometry of the structures. For instance, FD estimates computed on $Q-$criterion structures for case N are visualized in figure 2.17 and its probability density function (p.d.f.) is shown in figure 2.18. The p.d.f. suggests that a large number of structures have $\langle D_\alpha \rangle < 1$ but they are hardly visible in the visualization (cf. figure 2.17(a)). An example visualization of a structure with its embedding domain shows that it is small-scale, composed of a few connected points and not closed. The p.d.f. also suggests a large number of structures in the range $1 \leq \langle D_Q \rangle \leq 2$. This can be directly observed in the visualization and the example below shows a typical tube-like, closed structure within this category. Since the box-counting dimension is perceived as a space-filling metric, the embedding domain plays an important role in categorizing the extracted structures. This is primarily the reason for not filtering out structures with FD between 1 and 2. Further discussion on fractal dimension of structures is presented in chapter 3.

2.4.2 Shape index, curvedness, stretching

To geometrically characterize the filtered structures, two local (at every point on the surface) differential-geometry parameters and a global parameter are used. The first two are the shape index (S) and curvedness (C) which represent the local shape and intensity of curvature, respectively (Koenderink and Van Doorn, 1992). They can be expressed in terms of the principal curvatures κ_1 and κ_2 (see Appendix B for a detailed description and the advantage for choosing shape index and curvedness over other measures) of a surface as,

$$S = \left| -\frac{2}{\pi} \arctan\left(\frac{\kappa_1 + \kappa_2}{\kappa_1 - \kappa_2}\right)\right|, \quad C = \mu\sqrt{\frac{\kappa_1^2 + \kappa_2^2}{2}} \tag{2.10}$$

The shape index (S) is a scale-independent parameter which ranges between -1 and 1 before taking the absolute value. The positive and negative signs of S distinguish the local shape, for example, between elliptical concave and convex surfaces (cf. figure 5 of Koenderink and Van Doorn (1992)) depending on the direction of the normal. Since this direction of the normal is not of interest, the absolute value of the parameter, denoted by $|\cdot|$, is taken instead. Curvedness (C), on the other hand, is scale dependent with physical dimension of reciprocal length. This parameter is non-dimensionalized with $\mu = 3V_s/A_s$, where V_s and A_s are the volume and surface area of the structure respectively. The area of the structure is computed by summing up the area of all triangles representing the surface mesh. To obtain accurate volume estimation, the vertices of each triangle are connected to the center of the structure forming tetrahedrons and the volume of the structure is then the sum of the volume of all tetrahedral elements (Zhang and Chen, 2001).

Bermejo-Moreno and Pullin (2008) introduced a feature center (corrected mean) for the area-based joint probability density function (jpdf) of S and C to represent these properties in a non-local sense. This correction accounts for the skewness of jpdfs and ensures that the mean will lie closer to the region of higher density. For a real-valued random variable X with a p.d.f $f(x), x \in \mathbb{R}$, the feature center $\hat{x}$ is defined as,

$$\hat{x} \equiv \begin{cases} \overline{x} - d_l\sqrt{1-(d_l/d_u)^2} & \text{if } d_l < d_u \\ \overline{x} + d_u\sqrt{1-(d_u/d_l)^2} & \text{if } d_l > d_u \end{cases} \tag{2.11}$$

where $\overline{x}$ is the mean of X and d_u and d_l which are the upper and lower distances (considered as the RMS of the p.d.f) which are defined as

$$d_l \equiv \sqrt{\frac{\int_{x\le\overline{x}}(\overline{x}-x)^2 f\,dx}{\int_{x\le\overline{x}} f\,dx}}, \quad d_u \equiv \sqrt{\frac{\int_{x\ge\overline{x}}(\overline{x}-x)^2 f\,dx}{\int_{x\ge\overline{x}} f\,dx}} \tag{2.12}$$

The feature centers of both parameters are henceforth denoted as $\hat{S}$ and $\hat{C}$. To validate our scripts, the torus example from Bermejo-Moreno and Pullin (2008) is repeated. The mean and feature center of S and C shown in figure 2.19(b) agree with their results. The third parameter, denoted by λ, is a global parameter which characterizes the amount of stretching experienced by the educed structure and is given by,

$$\lambda = \sqrt[3]{36\pi}\frac{V_s^{2/3}}{A_s} \tag{2.13}$$

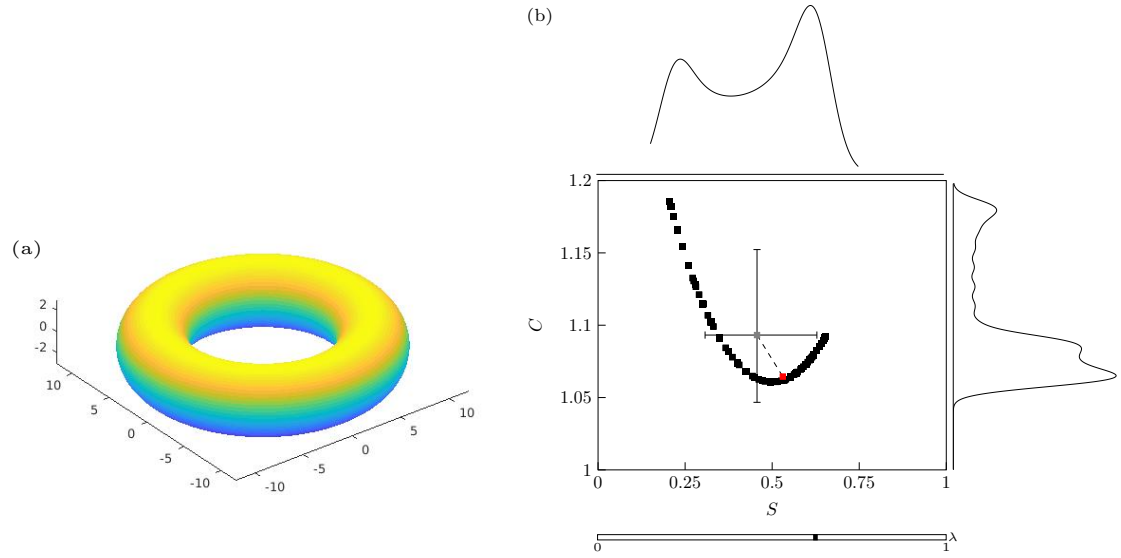

Figure 2.19: For the torus shown in (a), the jpdf of S and C, along with their marginal p.d.f. (top and right side of the plot respectively) are shown in (b). The stretching parameter λ is shown below the plot. The gray marker indicates the mean and the red marker indicates the feature center. The errorbars show the upper and lower distances which can be computed from (2.12). Figure is based on the work of Bermejo-Moreno and Pullin (2008).

The area-based jpdf, hereafter $\mathcal{P}(S, C)$, and λ together characterize the geometry of the structure. These parameters are rotation and translation invariant and are therefore suitable for comparing the geometry of structures. This is further discussed in the following subsection. The complete algorithm for extracting and geometrically characterizing structures from scalar indicators is presented in figure 2.20.

2.4.3 Visualization space

By constructing a 3-dimensional *visualization space* or *feature space* composed of the parameters $\hat{S}, \hat{C}$ and λ, each structure can be represented by a point in this visualization space. When two points lie close to each other, they indicate similar geometry. The distance between the points indicates the degree of similarity. With this idea, the visualization space can be used to broadly classify structures into three categories as blob-like, tube-like or sheet-like. For instance, a sphere having $(\hat{S}, \hat{C}, \lambda) = (1, 1, 1)$ is a blob-like structure and points which lie closer to this region can be thought of as approaching the geometry of a sphere. Similarly, tube-like structures can be localized close to a cylinder with $(\hat{S}, \hat{C}, \lambda) = (0.5, 1, \lambda)$ and λ characterizes the amount of stretching experienced by the cylinder-like object. Small values of λ indicate strong stretching and vice versa. Sheet-like structures are solely characterized by the parameter $\hat{C}$. The limiting case for planar objects is $\hat{C} = 0$. Some examples of commonly encountered structures along with a typical example of each quantitative Robinson structure is shown in figure 2.21.

With visual inspection of the common structures from panel (b) of the figure, one can intuitively categorize A, B as blob-like and C, D as tube-like structures. This is confirmed with the K-means clustering algorithm initialized with 3 clusters. The results are shown in panel (a) where blob-like structures (A, B) are highlighted with yellow markers, tube-like structures (C, D, E, G, H) are marked blue and red markers show sheet-like structures (F, J, K).

Input: Scalar indicator α
Output: Feature centers of shape index and curvedness $(\hat{S}, \hat{C})$ and stretching parameter λ
begin *nondimensionalization of the scalar indicator:*
  The scalar indicator is nondimensionalized with its RMS over wall-normal planes;
end
begin *computation of percolation threshold:*
  Split the entire range of the nondimenstionalized indicator into 1000 linearly spaced values;
  With the first 50 values as thresholds, apply algorithm 1 and obtain the volume of the biggest structure $V_{\max}$ and the volume of all structures V;
  The percolation threshold τ_p is identified when the slope of the ratio $V_{\max}/V$ is maximum;
end
begin *extraction of individual structures and geometrical characterization:*
  Threshold the nondimensionalized scalar indicator, $\alpha/\overline{\alpha'^2(y)}^{1/2} > \tau_p$ and extract structures with algorithm 1;
  for $i = 1$ *to* $n_{structures}$ **do**
    Embed structure i in a box with its maximum extent along every direction;
    Compute mean fractal dimension $\langle D_\alpha \rangle$ of the structure with equation (2.9);
    if $\langle D_\alpha \rangle > 1$ **then**
      Compute shape index (S) and curvedness (C) for each point of the structure;
      Compute their respective feature centers $(\hat{S}, \hat{C})$ with equations (2.11)-(2.12);
      Compute the stretching parameter λ with equation (2.13);
    end
  end
end

Figure 2.20: Workflow for the geometrical characterization of an individual structure

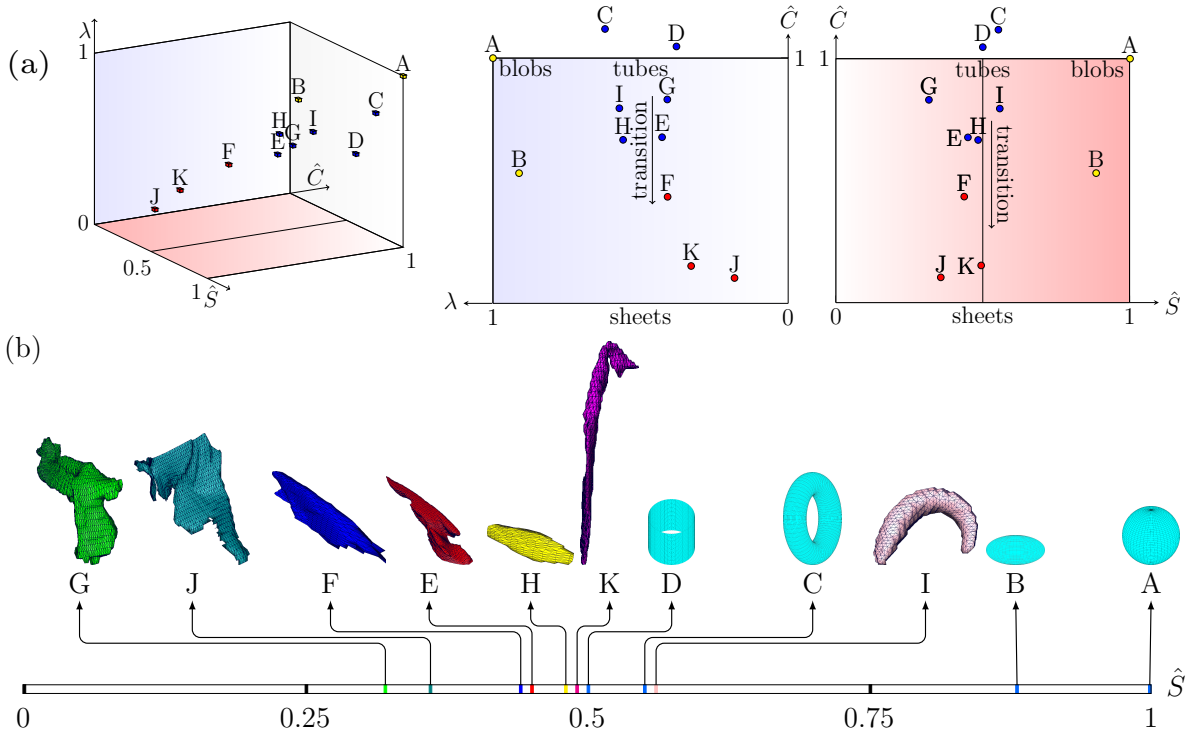

Figure 2.21: The three-dimensional visualization space along with a set of two-dimensional orthogonal projections composed of $\lambda\hat{C}$ and $\hat{S}\hat{C}$ is shown in panel (a). The scatter markers are colored by the cluster labels identified with the K-means algorithm. This figure is adapted from the work of Bermejo-Moreno and Pullin (2008). The non-local shape index ($\hat{S}$) is shown in panel (b) for some common structures like a sphere (A), ellipsoid (B), torus (C), cylinder (D), and the Robinson structures ($E-K$) for case N. Coloring of the structures is according to table 2.1.

2.5 Summary and conclusions

Initially, this chapter presents an overview of the various categories of coherent structures identified by Robinson (1991) which are relevant to turbulent boundary layers. For each category of Robinson structures, an indicator and the region in which these structures can be studied are identified from the literature. Next, a numerical procedure is developed to extract these structures from three-dimensional scalar fields and geometrically characterize individual structures as blob-like, tube-like or sheet-like. In the subsequent chapter, these Robinson structures are studied for the Ekman flow datasets so that changes in their geometry can be examined for increasing levels of stratification. As explained in chapter 1, knowledge of changes in geometry/properties of coherent structures can lead to better parametrizations of the ABL. For instance, since VLSMs are known to attenuate the small-scales near the wall, a mathematical model was proposed by Marusic et al. (2010) to predict the velocity statistics in the near-wall region given the large-scale signal in the log region. Another example can be seen in Chauhan et al. (2013), where inclination angles of vortical features, which are assumed to be pivotal for energy transfer, are used to improve computations of wall shear stress which is used in wall models of LES.

To extract individual coherent structures from three-dimensional scalar fields, an improvement on the neighbor scanning algorithm of Moisy and Jiménez (2004) is proposed. As shown in subsection 2.2.3, this algorithm is fast and capable of visualization accurate

structure extraction. This algorithm has been successfully tested on real world datasets to extract extratropical cyclones and weather fronts (Lindheim et al., 2021).

An important challenge when extracting structures with Eulerian criteria is to choose an 'appropriate' threshold. However, as pointed out in previous studies, these choices are somewhat subjective (Green et al., 2007; Elsas and Moriconi, 2017). Moreover, the inhomogeneity of wall-bounded flows in the wall-normal direction enhances the difficulty in choosing a single global threshold value (Del Álamo et al., 2006). To overcome these difficulties, two strategies are implemented. First, the indicators are nondimensionalized with their root mean square for every wall-normal plane. As shown by Nagaosa and Handler (2003) for Q-criterion, the probability density function of $Q/(\overline{Q'^2})^{1/2}$ becomes homogeneous everywhere except the viscous sublayer. Similar results were reported for the Δ-criterion in Del Álamo et al. (2006) and quadrant events in Lozano-Durán et al. (2012) and Lozano-Durán and Jiménez (2014). In this thesis, this technique is applied for all indicators except the high-and low-speed streaks which is only studied close to the wall until $y^+ = 40$.

Next, a non-subjective threshold is chosen by identifying the region of percolation transition between two limits (Moisy and Jiménez, 2004; Del Álamo et al., 2006). Although this allows for a non-subjective choice of the global threshold value, Jiménez (2018) noted that this analysis will point to a range of thresholds rather than a single value. This can indeed be seen in figure 2.12 for all indicators. Naturally, the mean value was chosen as the threshold but values above and below the mean within this range are also valid choices. Jiménez (2018) further states that due to the inherent ambiguity of the analysis, conclusions deduced with structures at percolation thresholds need to be complemented with other statistical analyses. Therefore, the geometrical results presented in chapter 3 are complemented with conditional analysis of one-point statistics of various coherent structures.

Applying the percolation analysis to the Ekman flow datasets reveals that a global threshold value identified with percolation analysis is insufficient to educe individual structures under strong stratification with coexisting turbulent and nonturbulent regions (see subsection 2.3.1). In this scenario, an entire cluster may be identified as an individual structure. To overcome this, a novel method is proposed in which percolation analysis is applied in an iterative manner to break down the cluster to individual structures, all of which exist at different thresholds. This method relies on a stopping criterion to determine if the structure being examined is simple (hence, individual) or complex. In this thesis, the minimum value of the ratio $V_{\max}/V > 0.5$ ($V_{\max}$ is the volume of the biggest structure in the domain and V is the volume of all structures) over the entire threshold range is chosen as the stopping criterion. Although $V_{\max}/V = 1$ or $V_{\max} = V$ for which only a single structure exists in the domain is the best possible condition to identify individual structures, this can become computationally expensive for large datasets. As percolation analysis relies on the extraction algorithm, future research works can be directed towards making this algorithm more efficient. Another direction is towards identifying alternate stopping criteria. For instance, an example from algebraic topology are the Betti numbers (Gardner, 1971) which describe the connectivity of simplicial complexes (which contain a set of points, lines, triangles or their n-dimensional generalizations). One can compute the second Betti number b_2 which can indicate the number of voids or cavities within the closed surface and a simple structure can be defined as having exactly one void.

Once the individual structures are obtained, they are geometrically characterized with the non-local methodology of Bermejo-Moreno and Pullin (2008). Together with the extraction algorithm and the percolation analysis (sections 2.2 - 2.4), they can be seen as a modular framework for the extraction and geometrical characterization of coherent structures and should facilitate improvements at each step in future works. A natural extension of this methodology is to study the temporal changes in geometry of coherent structures which is presented in chapter 4.

3

Geometry of Robinson structures in stratified Ekman flows

> One-point statistics measure the intensity of the fluctuations, and two-point statistics, such as spectra and correlations, give an idea of their spatial scales ... But they are not enough to describe a functioning turbulent flow.
>
> *Javier Jiménez, Coherent structures in wall-bounded turbulence, 2018*

In the previous chapter, a modular framework is developed to extract individual structures at optimum, i.e., percolation thresholds and geometrically characterize them with a modified non-local procedure of Bermejo-Moreno and Pullin (2008). This enables individual structures to be broadly classified as either blob-like, tube-like or sheet-like, thereby enabling comparison among the different Ekman flow cases. This framework is then applied to the quantitative Robinson structures (see table 2.1) on an instantaneous time step of three stably stratified cases S_1, S_2, S_3 at different levels of stratification and a neutrally stratified case N.

The idea of comparing the geometry of coherent structures among the various Ekman flow cases is motivated from previous observations in neutral and buoyant atmospheric boundary layers wherein changes in geometry and their subsequent impact on transport of momentum and scalars have been reported. Under neutral conditions, in which buoyant forces are absent, coherent structures such as low-speed streaks, sweeps, ejections, counter-rotating vortex pairs (or hairpins), large-scale motions (hairpin packets) and very large scale motions are known to exist (for example, see Hommema and Adrian, 2003; Carper and Porté-Agel, 2004; Huang et al., 2009a; Inagaki and Kanda, 2010; Li and Bou-Zeid, 2011; Fang and Porté-Agel, 2015). This suggests that the neutral ABL has structures similar to those observed in non-rotating, flat plate boundary layers (Robinson, 1991). On the other hand, when buoyancy has a destabilizing effect, the hot (and therefore lighter) air rising from the surface tends to lift the coherent structures away from the wall resulting in sheet-like thermal plumes (see figure 14 of Hommema and Adrian (2003)). Furthermore, the inclination angles of hairpin packets are higher than those observed under neutral conditions (Hommema and Adrian, 2003; Carper and Porté-Agel, 2004). Studies conducted in the limit of the unstable ABL, which closely resemble Rayleigh-Bérnard convection (RBC), show curved, sheet-like plumes near the surface which turn into axisymmetric plumes with mushroom (or blob)-like geometry away from

the wall (Schmidt and Schumann, 1989; Puthenveettil and Arakeri, 2005). These plume structures, analogous to bursts in the boundary layer, are known to be responsible for the bulk of heat transport (Siggia, 1994). Increase in buoyancy is also known to have an impact on the transport of momentum and scalars (such as water vapor and heat) (Katul et al., 1997b; Choi et al., 2004). By analyzing transport efficiencies, Li and Bou-Zeid (2011) show that scalars are efficiently transported whereas momentum transport is less efficient with increasing instability and suggest that the change in topology of coherent structures from eddies (under neutral conditions) which have significant horizontal vorticity to thermal plumes (under unstable conditions) to be the underlying cause.

As pointed out in the introduction, in the other limit, in which buoyancy has a stabilizing effect, reviews by Hopfinger (1987) and Mahrt (2014) suggest the coexistence of internal waves with quasi two-dimensional modes (suggesting pancake or sheet-like geometry with little vertical coherence). However, DNS simulations of the stably stratified shear layers indicate the presence of hairpin vortices suggesting tube-like geometry as well. This naturally raises the following questions,

- Is there a change in geometry/topology of coherent structures with increasing stability? Can an affinity towards pancake (or sheet-like) geometry be established?
- What is the impact of increasing stability on the inclination angle of hairpin structures?

In this chapter, a detailed analysis is carried out comparing the geometry of Robinson structures between the stably stratified and the neutrally stratified cases. Results, presented in section 3.1, are discussed by splitting a flow field into the following classical boundary layer regions, or layers: viscous sublayer, buffer, inner and outer layers based on the wall-normal height y^+. The defining property of each of these layers is explained in table 7.1 of Pope (2001). Comparisons between case N and S_1, for which major differences are expected, are shown in the running text of the thesis whereas comparisons between the other two stably stratified cases S_2 and S_3 are shown in Appendix C. The geometry and inclination angles of hairpin-like vortex structures are investigated in subsection 3.1.5.

Although the geometry of individual structures are calculated at optimum or percolation thresholds, the region of percolation transition typically identifies a range of thresholds which approximately span a decade (see figure 2.12). Naturally, the mean value is chosen as the percolation threshold in the thesis, however any threshold within this range can be considered "optimum". This uncertainty, leads Jiménez (2018) to propose that conclusions derived from thresholding of structures need to be validated against other techniques. Therefore, conditional one-point statistics of four quantitative indicators: low-and high-speed streaks, sweeps and ejections are compared with results obtained from the geometrical analysis.

The conditioning of the flow into turbulent and non-turbulent subvolumes is facilitated with an intermittency factor, denoted by γ. A novel definition of γ is proposed in section 3.2 which aims to overcome the drawback of using vorticity magnitude and an arbitrarily defined threshold to segregate the flow into turbulent and non-turbulent parts (Bisset et al., 2002; Da Silva et al., 2014; Ansorge and Mellado, 2016). Since vorticity magnitude is known to misidentify shear-dominated regions as vortices (see subsection 2.1.3 for an explanation), Q-criterion is suggested along with the percolation threshold. With this new definition,

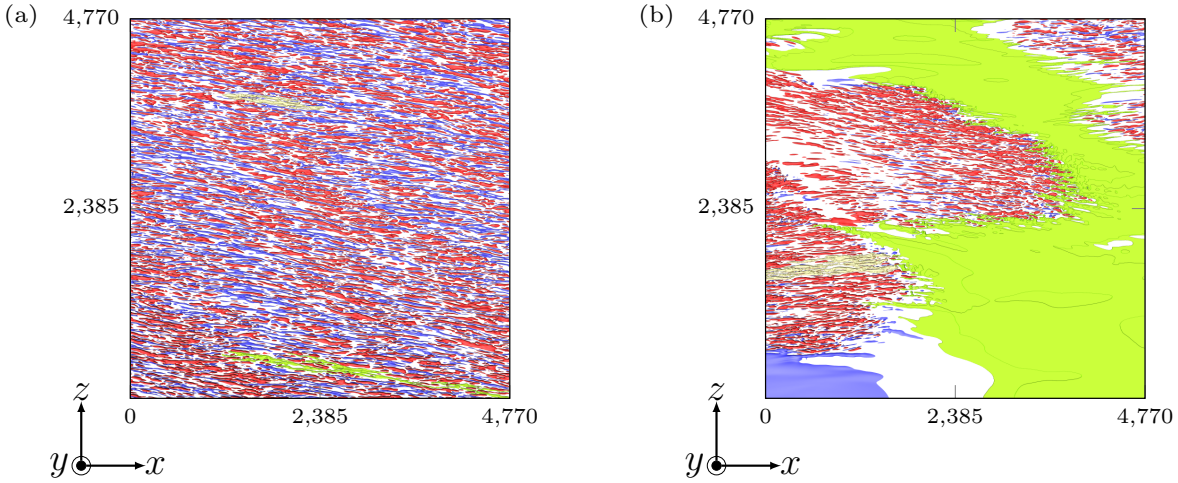

Figure 3.1: Isosurfaces of $u' < 0$ (low-speed streak) and $u' > 0$ (high-speed streak) are shown for case (a) N and (b) S_1 in the viscous sublayer with grid C. The color specification for the structures is according to table 2.1 for the low-and high-speed streak. The longest structure for the former is highlighted with light green and the longest structure for the latter is highlighted in pale yellow.

conditional one-point analysis on all Ekman flow cases are carried out and the corresponding results are discussed in section 3.3.

3.1 Geometry of structures in the ABL

In this section, results of the analysis carried out with the geometrical characterization framework on the Ekman flow datasets are discussed.

3.1.1 Viscous sublayer

In this subsection, the impact of five Robinson structures namely, low-and high-speed streaks, sweeps, ejections and pockets are discussed for the lowest portion of the ABL, i.e., when $y^+ < 5$. Other Robinson structures are not observable in this region as the flow is locally laminar. This portion of the flow field is generally not resolved in LES models as the first grid point is far away from the wall (Khanna and Brasseur, 1998; Chauhan et al., 2013). Therefore, it is crucial to study the impact of this region with coherent structures so that they may be accounted for in ABL parametrizations. It should be noted that this region is excluded from geometrical analysis as structures which have a mean fractal dimension $\langle D_\alpha > 1 \rangle$, i.e., which are not noise-like are not fully formed here and generally extend into the buffer layer and sometimes beyond.

Streamwise low-and high-speed streaks are identified with velocity fluctuations, i.e., $u' = u - \langle u \rangle$, where $\langle u \rangle$ is the space-time averaged velocity computed over wall-normal planes for 5 uncorrelated time steps. When $u' > 0$, high-speed streaks are observed and $u' < 0$ shows low-speed streaks. The isosurfaces of these structures at the global percolation threshold τ_p are visualized for all cases in figures 3.1 and C.1.

It can be instantly observed that the distribution of structures is different for all cases, especially between the neutrally stratified case N and the strongly stratified case S_1. The character of streaks in case N is thin, elongated and are more evenly spread across the domain

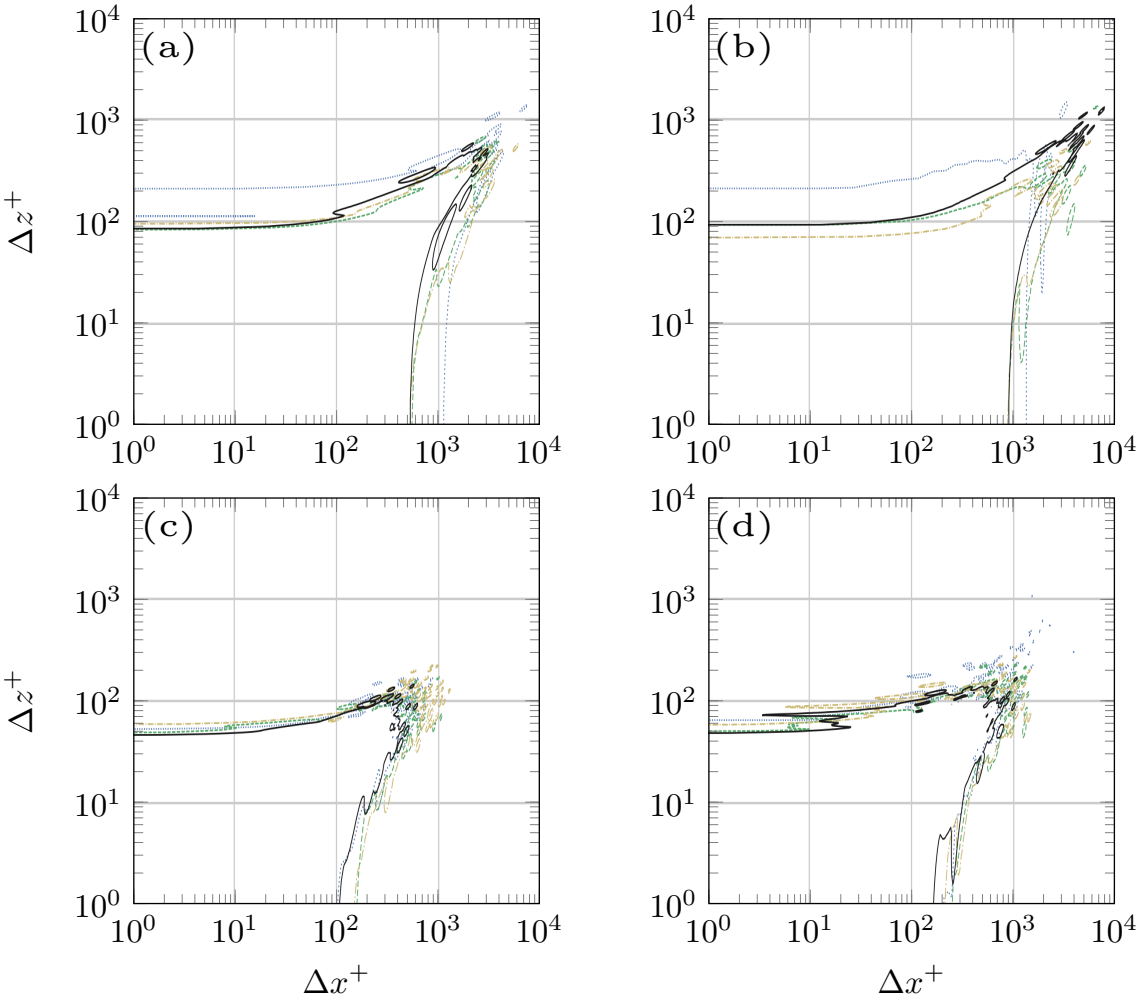

Figure 3.2: Joint p.d.f. of the streamwise (Δx^+) and the spanwise (Δz^+) coherence for (a) high-speed streaks, (b) low-speed streaks, (c) sweeps and (d) ejections. The neutrally stratified case N is represented by solid line (—) and the stably stratified cases S_1, S_2, S_3 are represented by dotted (...), dashed (- - -) and dash patterned (– — –) lines respectively.

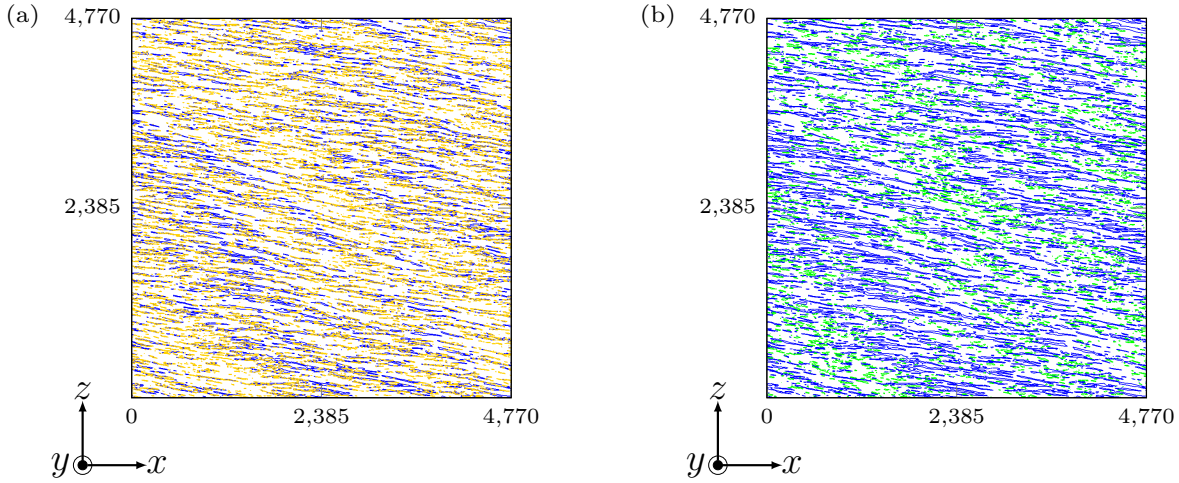

Figure 3.3: Contour plots for case N are shown with (a) ejections and low-speed streaks, (b) sweeps and low-speed streaks at $y^+ \approx 3.58$ with grid C. The color specification is according to table 2.1.

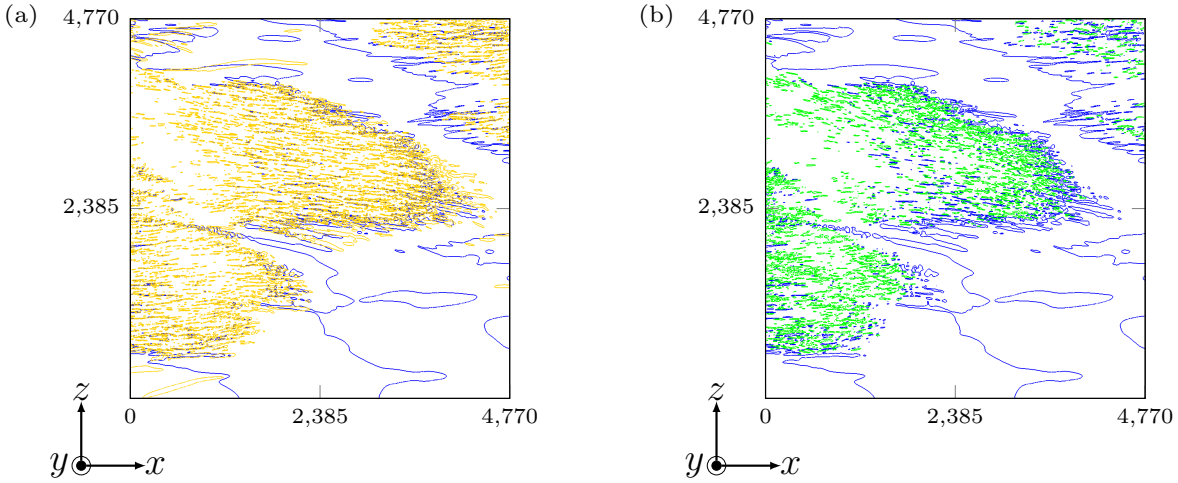

Figure 3.4: Contour plots for case S_1 are shown with (a) ejections and low-speed streaks, (b) sweeps and low-speed streaks at $y^+ \approx 3.58$ with grid C. The color specification is according to table 2.1.

making it comparable to the ones in Flat Plate Boundary Layers (FPBL) (Kline et al., 1967; Kline, 1978; Robinson, 1991). From figure 3.2, it is clear that the strength of stratification has an impact on the streamwise and spanwise coherence of low-speed streaks. With an increase in stratification, i.e., from S_3 to S_1, their coherence increases with the longest low-speed streak (light green region in figure 3.1(b)) spanning the entire domain for S_1. If the low-speed streaks were excluded from figure 3.1(b), the resulting high-speed streaks and the large empty patches are reminiscent of the non-turbulent regions seen from figure 1.2(b) at $y^+ \approx 100$. The presence of the large low-speed streak suggests that global intermittency causes a deceleration of the flow within the patchy regions.

With figures 3.3, 3.4, C.2 and C.3, the interaction of sweeps, ejections and streaks are discussed. Ejections and Sweeps are Q_2 and Q_4 events respectively which are computed with the quadrant technique. The wall-normal velocity fluctuations v' are computed the same way as those of u'. Akin to streaks, sweeps and ejections in case N show similar characteristics to FPBL. They show less streamwise coherence than streaks (cf. figure 3.2) which is in-line with previous studies (Corino and Brodkey, 1969; Bogard and Tiederman, 1986). It is also evident from the contour plots (figures 3.3, 3.4, C.2 and C.3) that several ejections arise out of a single low-speed streak as they are both regions of negative u'. By extracting the structures at this plane, it can be seen that, on average, $2-3$ ejections arise out of a low-speed streak for case N which is higher than the $1-2$ ejections for the stratified cases. This implies a dependence on stratification in which outward motion of the fluid is restricted when the flow is stratified. For the long low-speed streak in case S_1 (see light green region in 3.1(b)), it can be seen that few ejections arise out of it, most of which are confined to the outer edges of the structure. The inner region of this low-speed streak is devoid of ejections, further confirming the idea that these non-turbulent patches are simply decelerated regions of the flow.

For all cases, the sweep events appear to be aligned with the low-speed streaks and ejections. It is known from previous studies (Robinson, 1991) that sweep/ejection pairs support the existence of quasi-streamwise vortices near the wall of the boundary layer. With the extraction algorithm, the structures are extracted at $y^+ \approx 3.58$ and the ratio of sweep/ejection structures

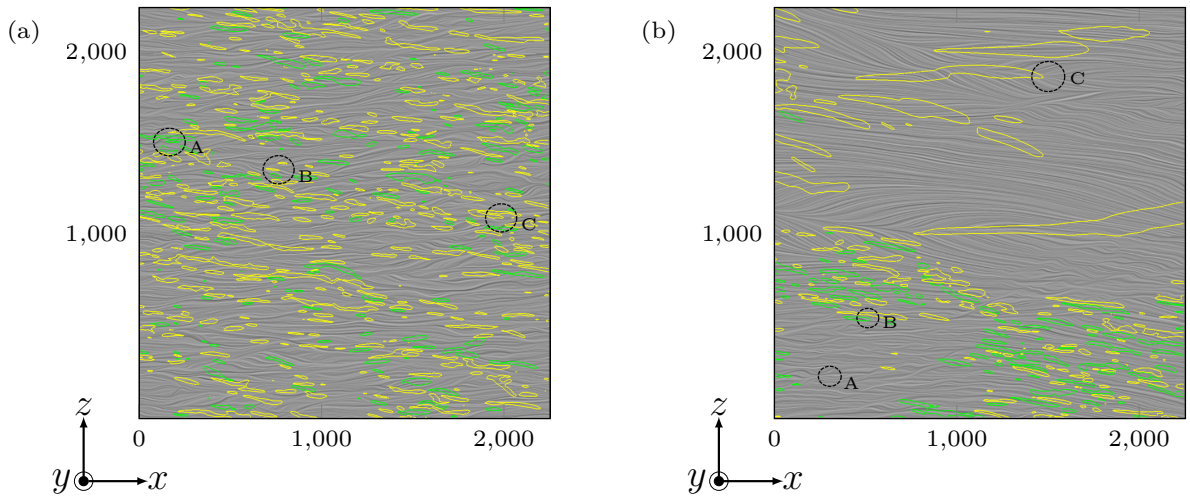

Figure 3.5: Three pocket regions are highlighted with diverging streamlines for (a) case N and (b) case S_1 at $y^+ \approx 3.58$. Overlayed are sweeps and ejections. Color specification for sweeps and ejections are according to table 2.1.

are the following: case N with 3033/6676 (0.45), case S_3 with 3104/4842 (0.64), case S_2 with 2798/4980 (0.56) and case S_1 with 2194/3054 (0.72). These ratios illustrate the following:

(1) While most ejections and sweeps exist as a pair, the number of ejections outweigh the number of sweeps within the domain. This suggests strong outward flow within the ejection regions in the viscous sublayer.

(2) With the difference between cases S_2 and S_3 being minimal, it can be seen that an increase in stratification reduces the number of ejections suggesting stunted outward flow from the wall.

With these observations along with figures 3.3 and 3.4, it can be suggested that the organization of sweep/ejection pairs in clusters as seen in case S_1 will force vortices to be formed directly above it leaving large regions of no vortex activity. This suggestion is revisited in later subsections.

Another Robinson structure which is known to be observed in this region are pockets. Kim et al. (1987) observed these structures by tracking particles/markers which are initially distributed on a plane parallel to the wall. These particles then rearrange themselves over time, essentially carving out pockets of low marker concentration (Chu and Falco, 1988). Since these regions are thought to be influenced by outer region motions that induce wallward motion, pockets are often associated with vortices. Robinson (1991) pointed out that pockets can be identified in instantaneous flow fields with streamlines since wallward fluid motion causes streamlines to diverge. Therefore, the line integral convolution (LIC) technique of Cabral and Leedom (1993) is used to visualize diverging streamlines. Three pockets for each case are identified in figures 3.5 and C.4 and most of them can be associated with a sweep/ejection pair thereby strongly hinting that these regions are associated with vortices. The association of pockets with vortices are reviewed again in subsection 3.1.5.

3.1.2 Buffer layer

As noted in the previous subsection, most of the structures which start within the viscous sublayer are not fully formed and often extend into the buffer layer, i.e., between $5 < y^+ < 30$ and beyond. The goal here is to geometrically characterize all quantitative Robinson structures except backs and compare them for increasing stratification. The comparison is performed for structures which are fully formed within this region, i.e., structures that start and end within the buffer layer itself and also for structures which start from the viscous sublayer and end in the buffer layer.

The procedure for the geometrical analysis for the current and subsequent subsection is briefly reviewed before the results are discussed. For all indicators in table 2.1, the global percolation threshold τ_p is computed with the procedure described in section 2.3 for grid A until $y^+ \approx 1550$. Individual structures are then extracted with the NS+MC algorithm (see subsection 2.2.2) at τ_p. It should be noted that the individual structures are only extracted for grid B, i.e., one-third of the computational domain to keep the computational costs reasonable. Next, the fractal dimension is computed on all structures and those which have a mean fractal dimension $\langle D_\alpha \rangle < 1$ are filtered away. A second filter is applied to exclude structures which intersect with the side walls as they are open surfaces. Finally, the feature centers of shape index and curvedness and the stretching parameter are computed on the surfaces of individual structures with the procedure described in subsection 2.4.2.

The results of the geometrical analysis for the buffer layer are shown in figures 3.6 and C.5 for all cases. Instantly, the lack of blob-like geometry and the prevalence of tube- and sheet-like geometries among all Robinson structures is noted. Additionally, two general observations are made - among all cases, similar geometrical features can be observed within each category of Robinson structures without any obvious distinction. Most structures in the buffer layer are tube-like with few sheet-like structures.

The geometry of high- and low-speed streaks (see figures 3.6(a, b) and C.5(a, b)), which are mostly tube-like, do not appear to change with increasing stratification. This indicates that streaks are generated primarily by shear and their geometry is unaffected by buoyant motions in the buffer layer (Lee et al., 1990; Young et al., 2002). Consistent with visualizations (cf. figure 3.1) and previous studies (Kline et al., 1967; Robinson, 1991), both low- and high-speed streaks are highly stretched structures (indicated by low values of λ). Although it cannot be inferred from the geometrical analysis, visualization of these structures shows that the stretching is in the streamwise direction. It is also worth noting that a large sheet-like, low-speed streak spans the domain for the case S_1, similar to the observation in the viscous sublayer suggesting that the non-turbulent regions are decelerated in the buffer layer as well.

Sweeps are mostly tube-like structures for all cases whereas ejections, particularly for cases S_2 and S_3, show more sheet-like structures. With the K-means clustering algorithm, the structures are separated into tube-like and sheet-like clusters by initializing the number of clusters as 2. When these clustered structures are visualized, no discernable patterns could be identified, i.e., the structures appear to be distributed quite randomly throughout the domain. It is not clear from this analysis if a classification into tube-like and sheet-like structures is useful in understanding the contribution of sweeps and ejections to the Reynolds shear stress term $\rho u'v'$. In general, Willmarth and Lu (1972) note that sweeps have a higher contribution

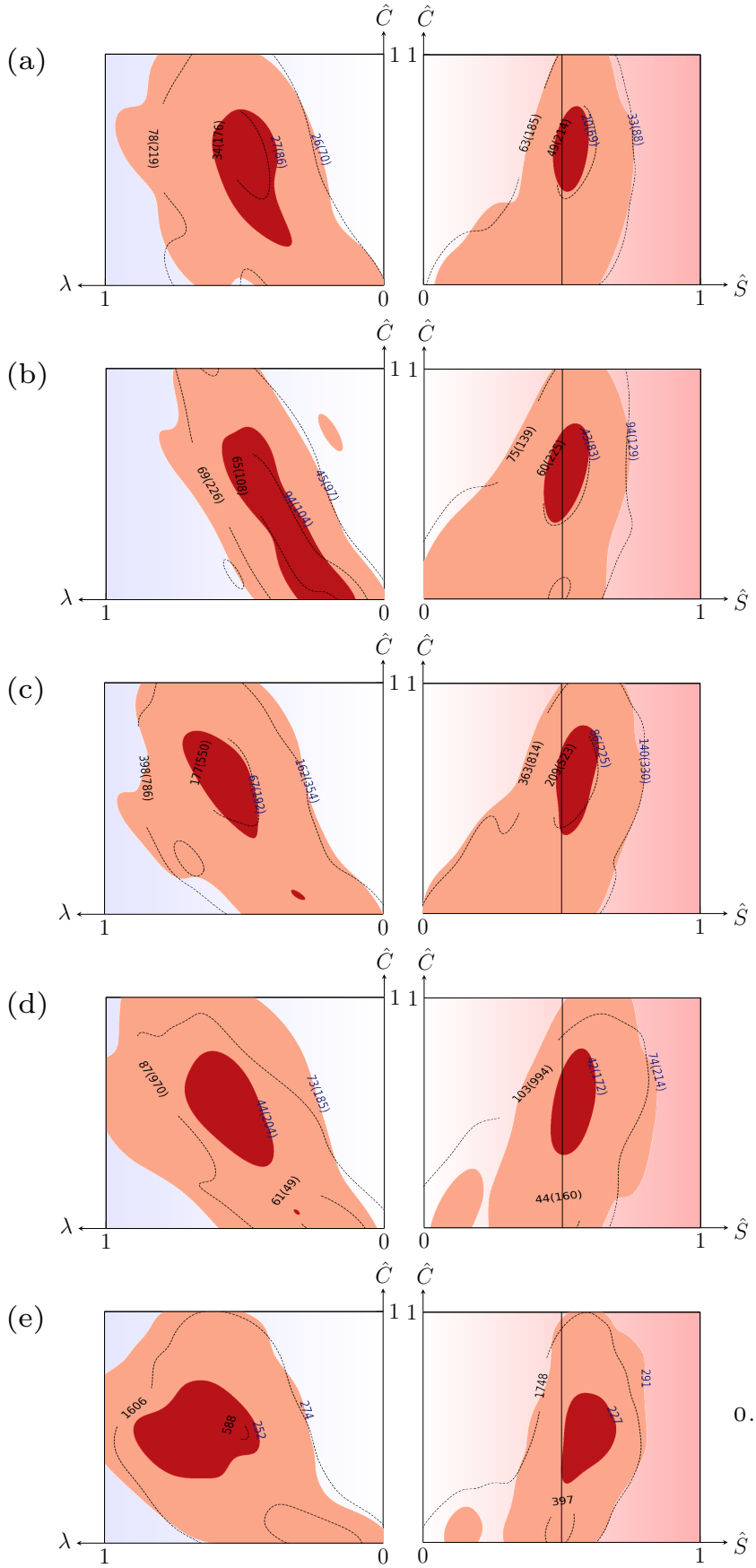

High-speed streaks
$u' > 0$

Low-speed streaks
$u' < 0$

Sweeps
u' > 0, v' < 0

Ejections
u' < 0, v' > 0

Vortices
$0.5(||\Omega||^2 - ||S||^2) > 0$

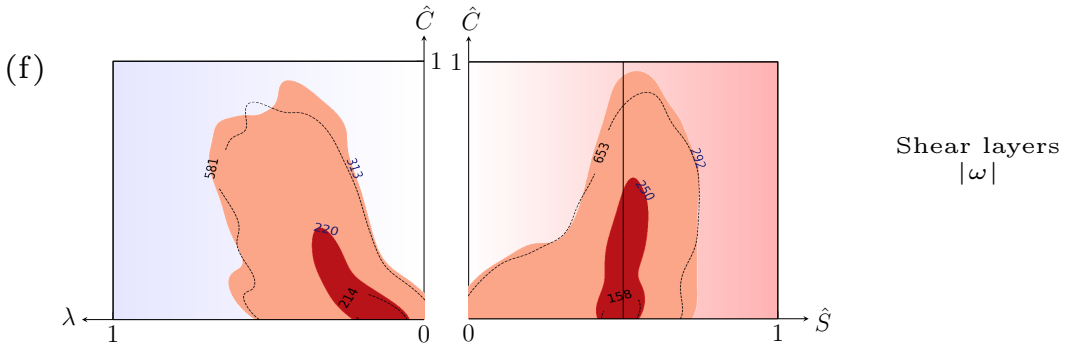

Figure 3.6: Visualization space for all quantitative Robinson structures except backs are shown with joint pdfs for the buffer layer. From (a - f) are the high-speed streaks, low-speed streaks, sweeps, ejections, vortices and shear layers. The geometry of structures is compared with case N (unfilled contours with dashed lines) and case S_1 (filled cotours). The number of structures for each contour level is indicated in black for case N and dark blue for case S_1. Numbers within paranthesis (a - d) are those which start from the viscous sublayer and end in the buffer layer. Numbers outside paranthesis are those which start and end within the buffer layer itself. $\hat{S}, \hat{C}, \lambda$ are the shape index, curvedness and stretching parameters respectively.

to the Reynolds shear stress when $y^+ < 15$ and ejections have a higher contribution when $y^+ > 15$. Kim et al. (1987) confirmed this view by examing the DNS of channel flow at multiple Reynolds numbers. It can be noted from figures 3.6(c, d) and C.5(c, d)) that the number of sweeps within the buffer layer itself is much higher (denoted by number of structures outside paranthesis) than ejections for all cases. This suggests strong wallward flow in the sweep regions of the buffer layer.

It can be observed from figure 3.6(e) that the neutrally stratified case shows higher vortex activity (indicated by the amount of structures plotted within one-third of the entire domain) than the stably stratified cases. However, the lower vortex count for case S_1 can be attributed to the clustering of structures at the percolation threshold due to global intermittency (which was already discussed in subsection 2.3.1) in which the entire cluster is identified as an individual structure. This cluster of structures was excluded from the geometrical analysis as it will be wrongly classified as sheet-like due to its large area, i.e., the ratio $\mu = 3V_s/A_s$ becomes small which implies $\hat{C} \to 0$. For the remaining structures in case S_1, it can be seen that the majority of them are less stretched ($\lambda \to 1$) than in the other cases. This can still be attributed to the exclusion of the large cluster where most hairpin-like structures are seen. For a small region within this cluster, the MLP technique (discussed in 2.3.1) is applied and hairpin-like structures are geometrically characterized. These results are discussed in subsection 3.1.5.

It is interesting to note that both vortices and shear layers which are identified with vortex indicators (Q-criterion and vorticity magnitude respectively) show drastically different geometry of structures. Most Q-criterion structures tend to be less-stretched, tube-like whereas vorticity magnitude shows strongly-stretched, tube- and sheet-like features. If the tube-like and sheet-like structures of vorticity magnitude are separated into clusters with the K-means algorithm (initialized with 2 cluster centers) and visualized for the strongly stratified case S_1 (see figure 3.7), it can be seen that there are numerous stretched sheet-like structures at the turbulent/non-turbulent interface (TNTI) suggesting strong shearing motions at this region. This does not imply that sheet-like structures exist only at TNTI. Zhou et al. (1999) showed

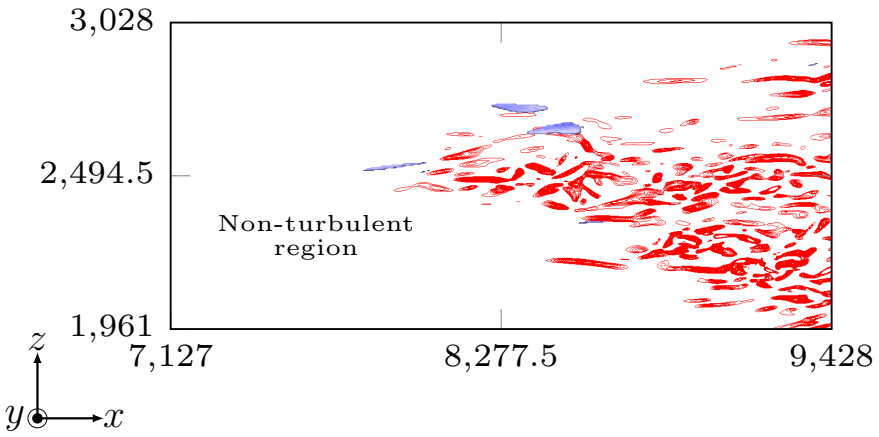

Figure 3.7: Sheet-like shear layers are visualized with blue isosurfaces of vorticity magnitude. Q-criterion contours are shown in red at the global percolation threshold.

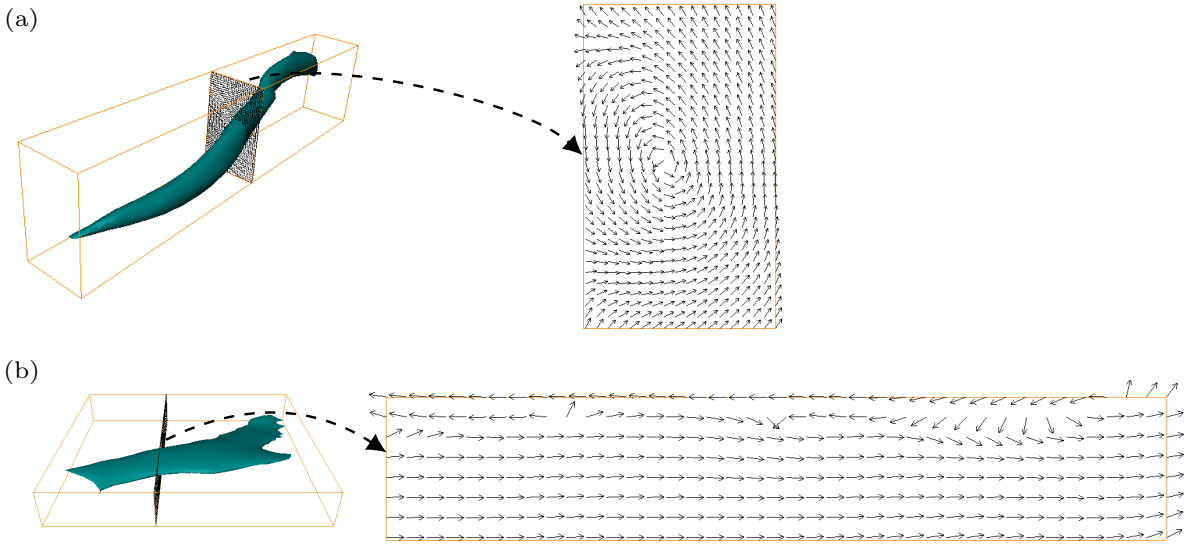

Figure 3.8: Isosurfaces of vorticity magnitude extracted from case S_1 are shown on the left column to illustrate (a) tube-like structure and (b) sheet-like structure. On the right column, a velocity vector plot is shown which shows that the tube-like structures are vortex regions whereas sheet-like structures are shearing regions.

that the quasi-streamwise vortices which push the fluid up and back tend to enounter the mean flow resulting in the formation of a shear layer (cf. figure 5 of Zhou et al. (1999)). If an example of a tube-like and sheet-like structure are examined with cross-sectional velocity vectors, it can be seen from figure 3.8 that the tube-like structure identifies spinning regions whereas the sheet-like structure shows shearing regions. With this interpretation, one can construct a visualization space with a complete geometrical characterization of structures identified with vorticity magnitude as an indicator for wall-bounded flows. This is shown in figure 3.9. The transition from vortex tubes to shear layers can be thought of as the *degree of shearing* where strong shearing occurs when $\hat{C} \to 0$.

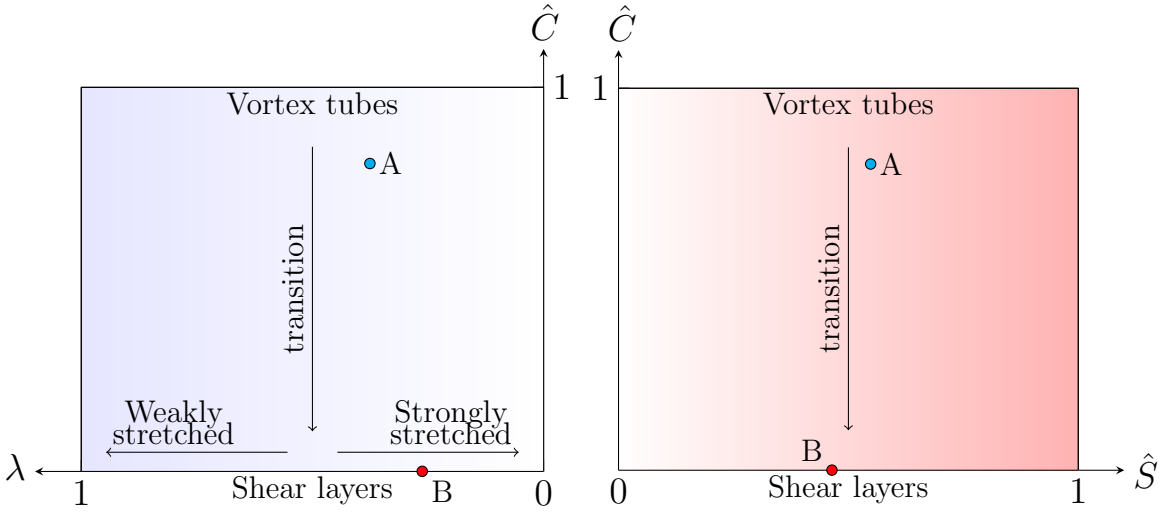

Figure 3.9: Visualization space to geometrically characterize vorticity magnitude structures. Here, A and B are examples of tube-like and sheet-like structures, both of which are visualized in figure 3.8 (a, b) respectively. $\hat{S}, \hat{C}, \lambda$ are the shape index, curvedness and stretching parameters respectively.

3.1.3 Inner and outer layer

This subsection continues the geometrical analysis with the same Robinson structures for the inner and outer regions[1] of the boundary layer. Figures 3.10(a, b) and C.6(a, b) reveal that few streaks are formed after $y^+ > 30$. Streaks are studied only until $y^+ \approx 40$ (as shown in table 2.1) and therefore, one can surmise that there is little activity in the region $30 < y^+ < 40$. Compared to the buffer layer, high- and low-speed streaks for case N and S_1 show a downward shift in both $\hat{S}\hat{C}$ and $\lambda\hat{C}$ planes indicating stretched, sheet-like structures. The geometry of streaks for case S_2 and S_3, however, remain the same as that of the buffer layer.

In this region, both sweeps and ejections for all cases (figures 3.10(c, d) and C.6(c, d)) are tube-like unlike the buffer layer where some ejections were sheet-like. Although the difference is small, it can be noted that the number of sweep structures are higher than ejections within the domain. By extracting the structures in this region, the ratio of sweep/ejection structures are 892/820(1.09) for case N, 296/201(1.47) for case S_1, 614/520(1.18) for case S_2 and 440/635(0.69) for case S_3. Ignoring case S_3, a trend opposite to the one from the viscous sublayer is observed where the sweep events outweigh the ejections. This suggests strong wallward flow within the sweep regions. With all this information, the overall behavior of sweeps and ejections can be commented upon. Within the viscous sublayer, ejections are dominant contributing to strong outwards flow whereas in the other regions (buffer and inner layer) sweeps are dominant contributing to stronger wallward flow. By initializing 2 cluster centers for the K-means algorithm, the tube-like and sheet-like structures are segregated. Similar to the buffer layer, the tube-like and sheet-like sweeps and ejections are distributed quite randomly throughout the domain.

[1]It should be noted that the inner layer is usually defined as $y/\delta < 0.1$ which corresponds to $y^+ < 140$ and the outer layer defined as $y^+ > 50$ (see Pope (2001) and Marusic et al. (2010)). The Ekman flow analysed here has a Reynolds number of 26 500 which is sufficiently high to have an overlap between the inner layer and outer layer which is approximately 90 viscous wall units. In this subsection, the structures are geometrically characterized until $y^+ \approx 1000$ to include a good portion of the outer layer.

As with the buffer layer, the shear layer structures indicated in figure 3.10(f) and C.6(f) are strongly-stretched ($\lambda \to 0$), tube- and sheet-like structures ($\hat{C} \to 0$) and vortices seen in figure 3.10(e) and C.6(e) are less-stretched, tube-like structures. Also similar to the buffer layer, the sheet-like shear layer structures can be seen at the TNTI. Since hairpin-like vortices are fully formed within this region, shear layers can be generally seen above the vortex structures. Figure 3.11 shows a hairpin packet and an example sheet-like shear layer structure highlighted in blue.

3.1.4 $\delta-$scale structures

Since the geometry of structures until $y^+ \approx 1000$ are already studied in the previous subsection, only two $\delta-$scale Robinson structures are discussed here. They include long, sloping shear layer structures also known as backs which originate within the buffer layer and extend beyond $y^+ > 80$ and large scale motions (LSM) called bulges.

Backs are known to span the entire boundary layer and are generally inclined at an angle of $12° - 30°$ from the wall (Robinson, 1991). Since they are essentially shear layers formed on the upstream side of a LSM, vorticity magnitude can be used to locate these structures. In particular, structures which start within the buffer layer and extend beyond $y^+ > 80$ are sought out. The distinction between backs and shear layers is not necessary for inclined structures that extend until $y^+ = 80$. The number of backs detected for the neutrally stratified case is the highest where 165 such structures were classified as backs out of a total of 10^5 structures. Similarly, 11 structures for case S_1, 35 structures for case S_2 and only 8 structures for case S_3 were detected. Their wall-normal extent ranges between $0.2\delta(55^+)$ to $0.32\delta(104^+)$ suggesting that these are not $\mathcal{O}(\delta)$ structures as indicated in previous studies (Chen and Blackwelder, 1978; Robinson, 1991). The mean inclination angle, computed with $\theta_i = \arctan(\Delta y^+/\Delta x^+)$, with respect to the streamwise direction is $67°, 49°, 59°$ and $58°$ for cases N, S_1, S_2 and S_3 respectively suggesting a decrease in the inclination angle with increase in stratification. These inclination angles are much higher than those reported for FPBL. The geometry of these structures as shown in figures 3.12 and C.7 indicate that they are strongly-stretched tube-like or sheet-like features with an affinity towards the latter.

Bulges are most apparent in figure 3.13(a) where the $\delta-$scale structures are clearly visible interspersed with irrotational regions which is a consequence of global intermittency. However, these structures exist in all cases regardless of the strength of stratification. The identified bulges range between $2 - 4\delta$ in the streamwise direction which is similar to the $0.8 - 3\delta$ reported for the FPBL (Robinson, 1991; Kovasznay et al., 1970). It can be seen that the point of interaction of the outer flow and the boundary layer for all cases has a spike in vorticity magnitude which suggests the presence of large scale rolls. For case S_1, this type of rolls was already visualized in figure 2.14(a) in which a large $Q-$criterion structure (above the hairpins) could be seen spanning most of the domain indicating that bulges are three-dimensional events.

Before the importance and physical relevance of all Robinson structures to the ABL are discussed, a specific category of vortices shaped like hairpins are studied in the next subsection.

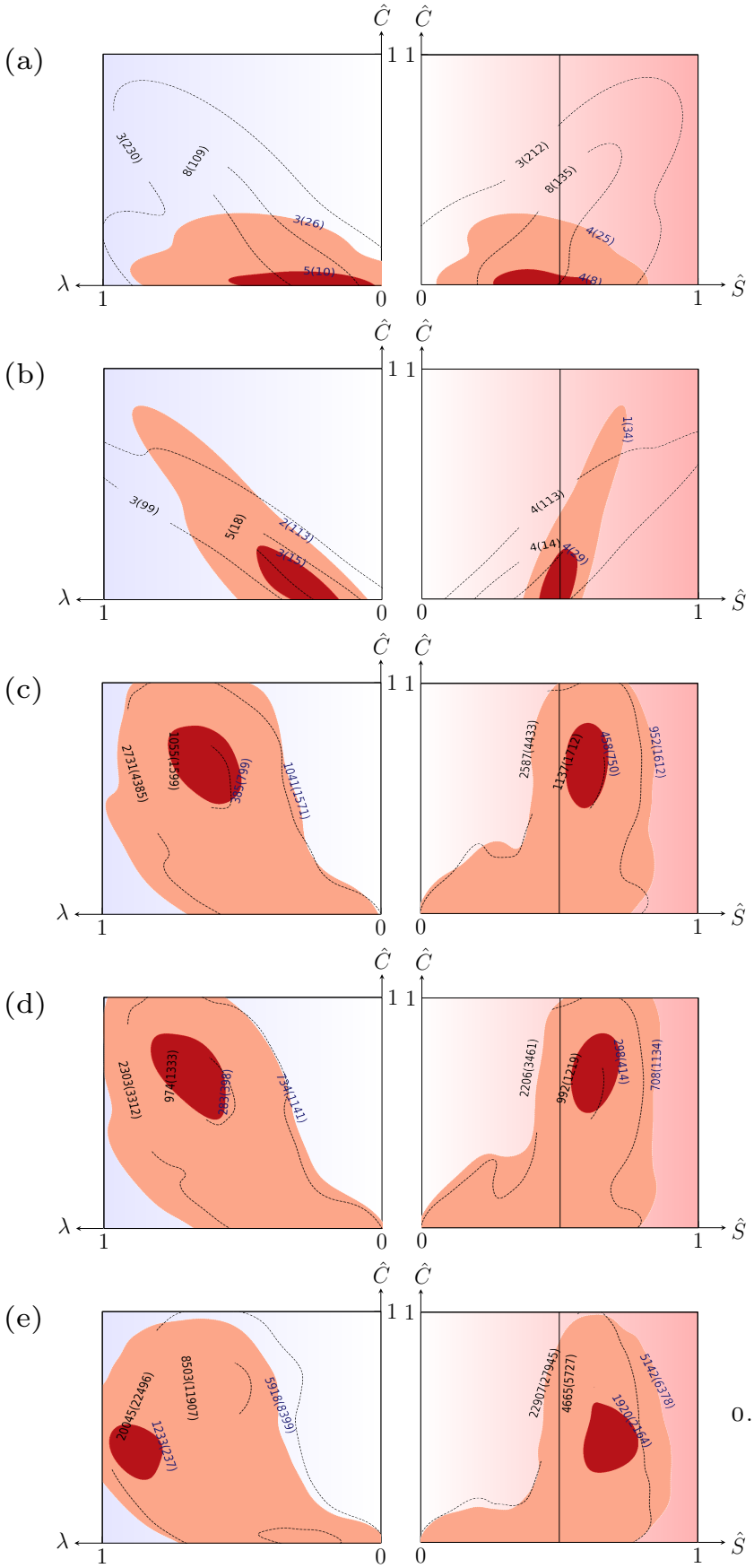
(a)
3(230)
8(109)
3(26)
5(10)
3(212)
8(135)
4(25)
4(8)
High-speed streaks
$u' > 0$
(b)
3(99)
5(18)
2(113)
2(15)
1(34)
4(113)
4(14)
4(29)
Low-speed streaks
$u' < 0$
(c)
2731(4385)
1055(1559)
(676)
1041(1571)
2587(4433)
1137(1712)
458(750)
952(1612)
Sweeps
u' > 0, v' < 0
(d)
2303(3312)
974(1333)
(868)
734(1141)
2206(3461)
992(1219)
298(414)
708(1134)
Ejections
u' < 0, v' > 0
(e)
20045(22496)
8503(11907)
1233(237)
5918(8399)
22907(27945)
4665(5727)
1920(2164)
5142(6378)
Vortices
$0.5(||\Omega||^2 - ||S||^2) > 0$
$\hat{C}$
$\hat{S}$
λ
1
0

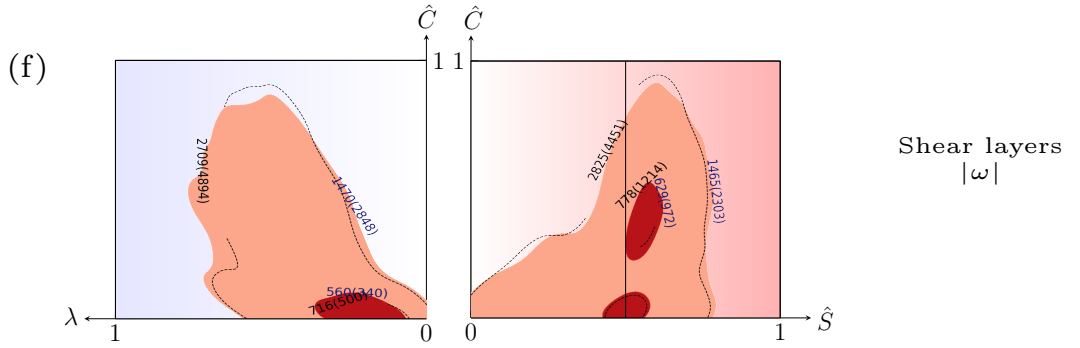

Figure 3.10: Similar to the previous subsection, the visualization space for all quantitative Robinson structures except backs are shown with joint pdfs for the inner and outer layer. From (a - f) are the high-speed streaks, low-speed streaks, sweeps, ejections, vortices and shear layers. The geometry of structures is compared with case N (unfilled contours with dashed lines) and case S_1 (filled cotours). The number of structures for each contour level is indicated in black for case N and dark blue for case S_1. Numbers which are within paranthesis (a - d) are those which start from the viscous sublayer and end in the outer layer. Numbers outside paranthesis are those which start beyond the buffer layer and end within the outer layer. $\hat{S}, \hat{C}, \lambda$ are the shape index, curvedness and stretching parameters respectively.

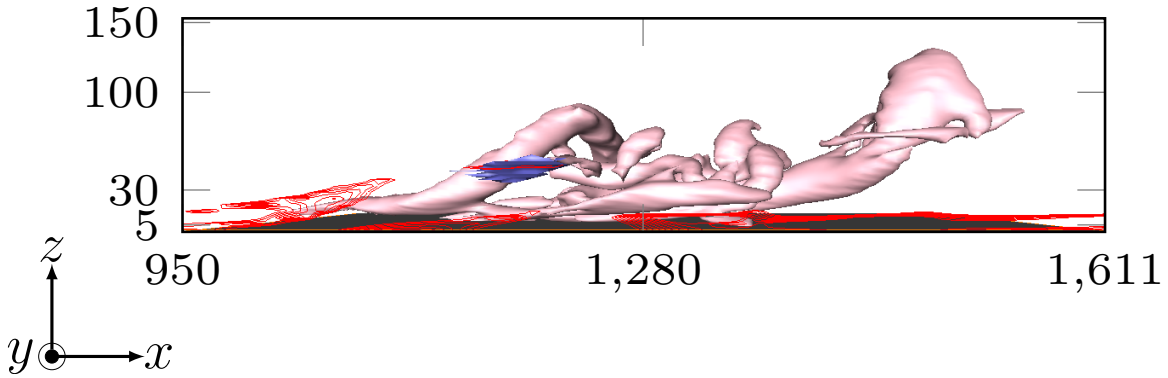

Figure 3.11: A hairpin packet is visualized with Q-criterion for case N at the percolation threshold. An example sheet-like shear layer structure is shown in blue. A vertical contour slice of vorticity magnitude colored red highlights shear layer structures.

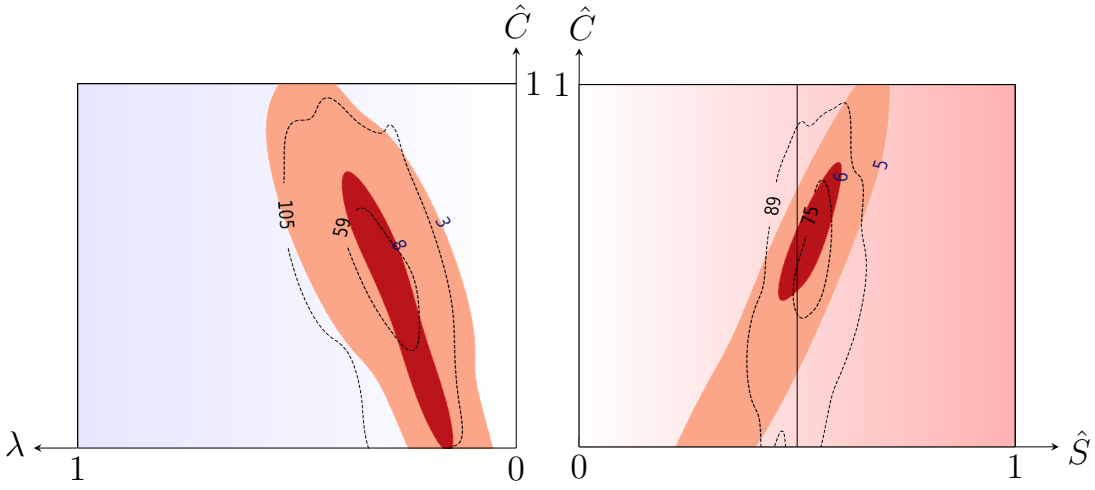

Figure 3.12: Visualization space for backs is shown for case N with unfilled contours and S_1 with filled contours. The number of structures between contours are indicated in dark blue for case S_1 and black for case N. $\hat{S}, \hat{C}, \lambda$ are the shape index, curvedness and stretching parameters respectively.

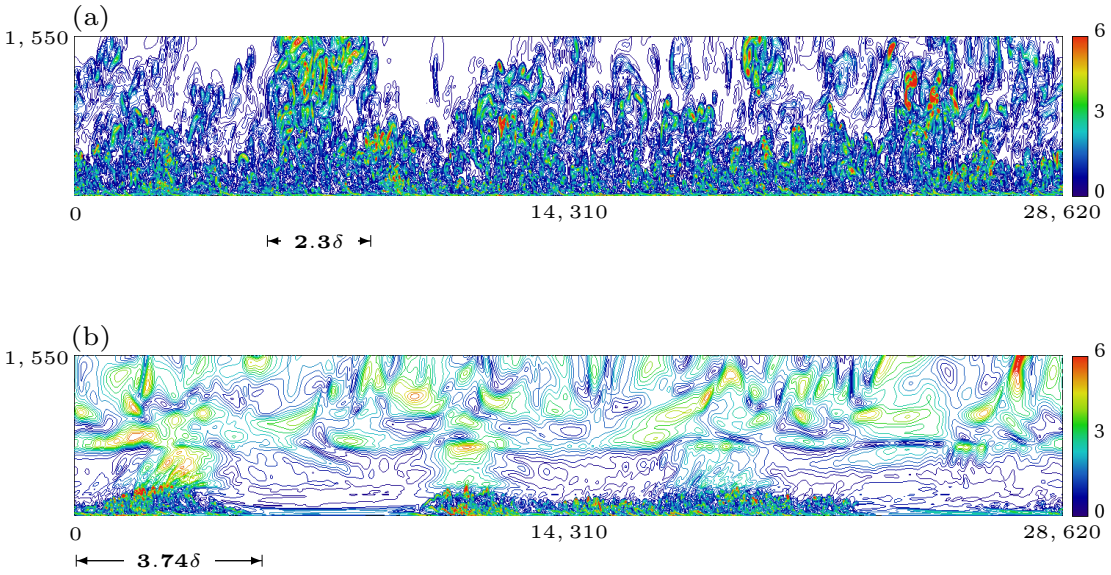

Figure 3.13: Vorticity magnitude contours along the (x, y) plane are shown here for (a) case N and (b) case S_1 for grid A until $y^+ \approx 1550$. In each case, a $\delta-$scale bulge is highlighted. The wall-normal direction is exaggerated three times to show the structures clearly.

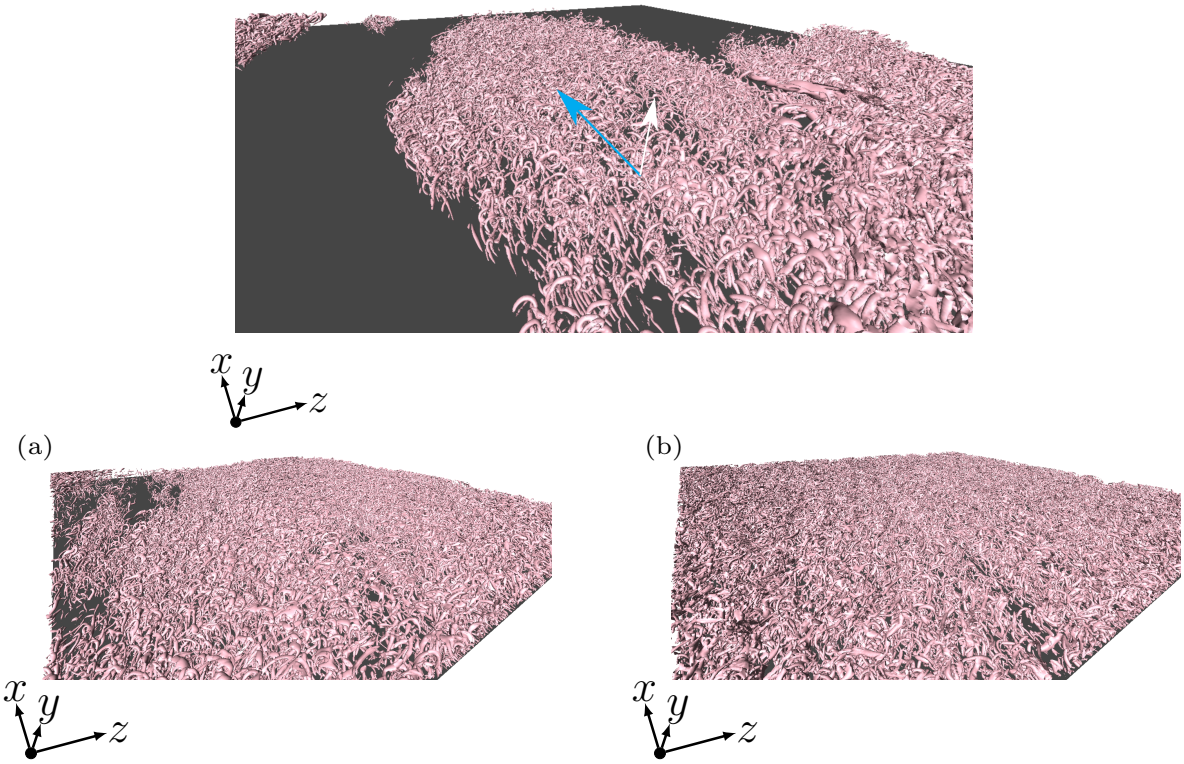

Figure 3.14: The top panel shows isosurfaces of Q-criterion at $\tau = 0.6$ for case S_1 until $y^+ = 200$. The blue arrow points towards the streamwise direction whereas the white arrow is an approximate orientation of the majority of hairpin-like structures. Similarly, Q-criterion isosurfaces are visualized for cases (a) S_2 and (b) N in the bottom panel until $y^+ = 200$.

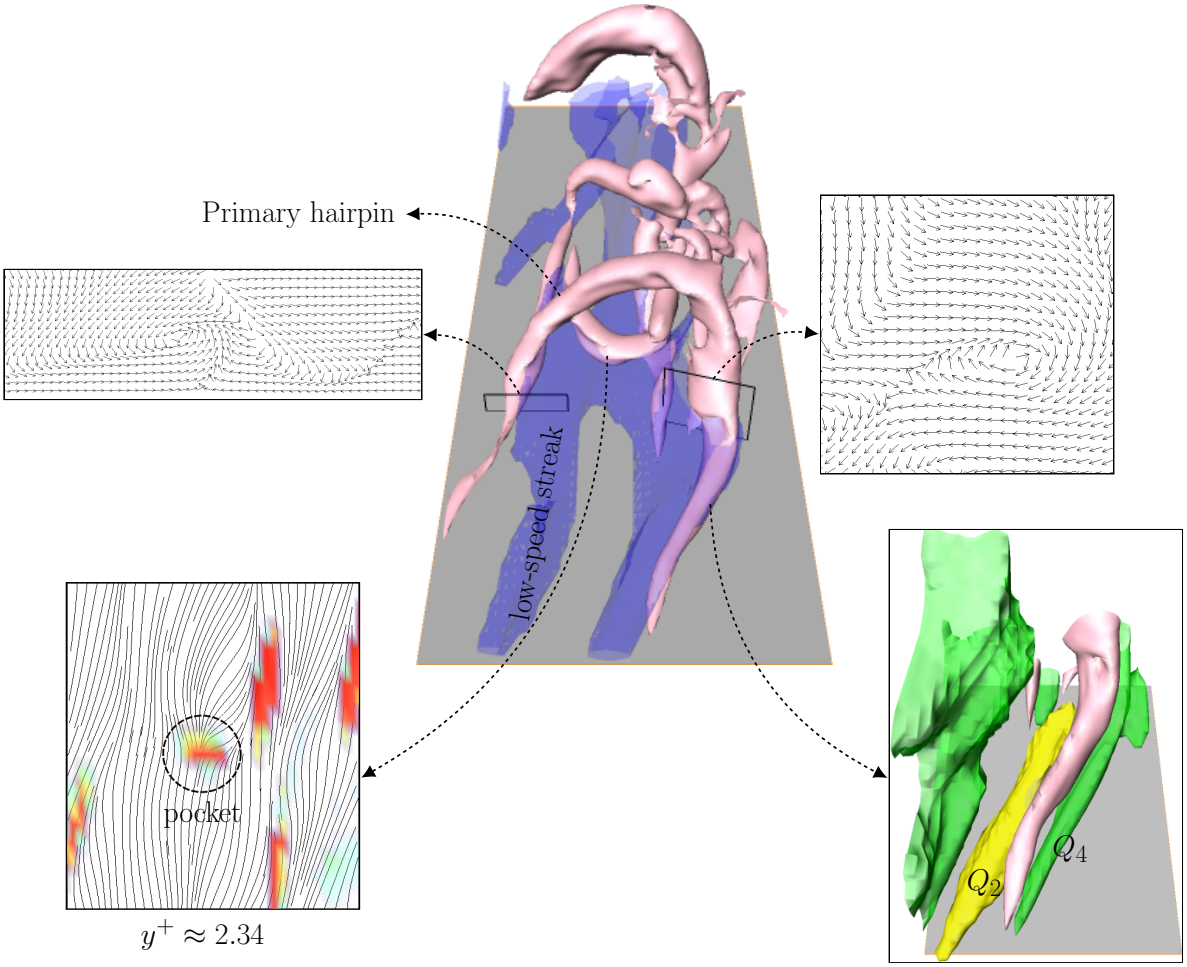

Figure 3.15: Visualization of a hairpin packet with the Q-criterion at τ_p is shown for case N. The blue structure between the legs of the primary hairpin is the low-speed streak. Q_2 and Q_4 indicate ejection and sweep events respectively (bottom right visualization). A pocket structure is highlighted on the bottom left. Velocity vector plots for both legs of the primary hairpin are visualized on the top left and top right.

3.1.5 Hairpin-like structures

The goal of this subsection is to investigate hairpin-like vortex structures. First, the classical hairpin vortex attributes are reviewed and an attempt is made to explain the following observations,

(1) It is immediately apparent that visualization with $Q-$criterion for case S_1 reveals a remarkable number of *hairpin-like* structures (see the top panel of figure 3.14) in the region $y^+ < 200$.

(2) These structures seem to be oriented in a similar direction, even when individual structures are compared far away in the domain (cf. 2.5(a, b)).

(3) As seen from figure 2.14(b), an entire cluster of structures tends to be misidentified as an individual structure when using the global percolation threshold for the case S_1.

Upon visualization of Q-criterion at τ_p for all cases, it is noticeable that stratification has a strong impact on the volume of hairpin-like structures which appears to increase with increasing

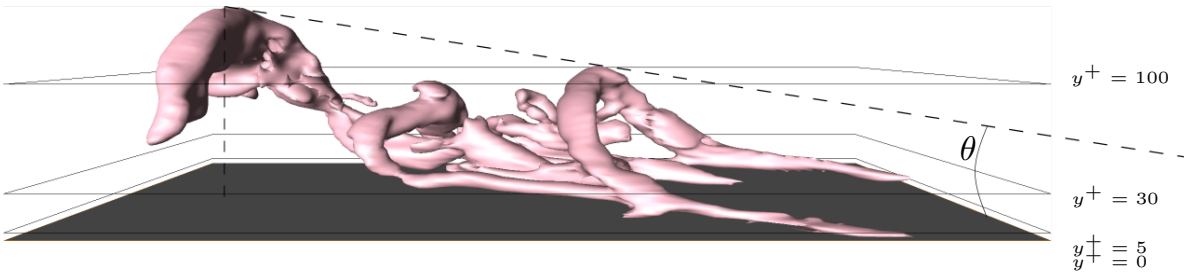

Figure 3.16: Side view of the hairpin packet visualized in figure 3.15 is shown here. The angle between the line connecting the head of the hairpin-like structures and the wall is the growth angle θ.

stratification. While the neutrally stratified case shows the least amount, a prominent example of a hairpin packet resembling the vortex packets of Adrian et al. (2000) is highlighted and discussed from this case (visualization of this packet can be seen in figures 3.15 and 3.16).

Examination of this packet along with the Robinson structures (particularly low-speed streaks, sweeps, ejections and pockets) in figure 3.15 reveals classical hairpin attributes. The (x, y) cross-sectional velocity plots visualized on both legs of the hairpin, henceforth primary hairpin, show that they are indeed counter-rotating. Probing other indicators close to the hairpin allows us to extract nearby Robinson structures. Between the hairpin legs, there appears to be a region of low momentum fluid (blue region of the low-speed streak) passing through all the hairpins which is consistent with previous observations (Zhou et al., 1999; Adrian et al., 2000). Closer inspection on the right hairpin leg also reveals the existence of Q_2 (yellow-colored ejection) and Q_4 (green-colored sweep) events on either side of the leg. Along with the velocity plot, it is easy to understand that the Q_2 event pushes up the fluid whereas the Q_4 event pushes it down. When the fluid is pushed up, it is also pushed downstream where it interacts with the mean flow resulting in the formation of near-wall shear layers (Zhou et al., 1999). The autogeneration mechanism is also evident here. The upstream hairpin induces a strong Q_2 event which interacts with the high-speed fluid behind it which results in the formation of further hairpins downstream (Adrian et al., 2000). Another classic attribute is the growth angle θ which is the angle between the line connecting the heads of the hairpin packet and the wall. In this case, $\theta = 54°$, which is significantly higher than the $12°, 20°$ obtained by Adrian et al. (2000) and Head and Bandyopadhyay (1981) respectively. The inclination angles of individual hairpin-like structures are discussed below.

A pocket region (visualized with diverging streamlines) can also be observed interacting with the $Q-$criterion structure which is a part of the primary hairpin. Although these are intended to be 'footprints' of outer structures, typically eddies (Chu and Falco, 1988), no diverging streamlines are observed for other regions which are also clearly interacting with the wall.

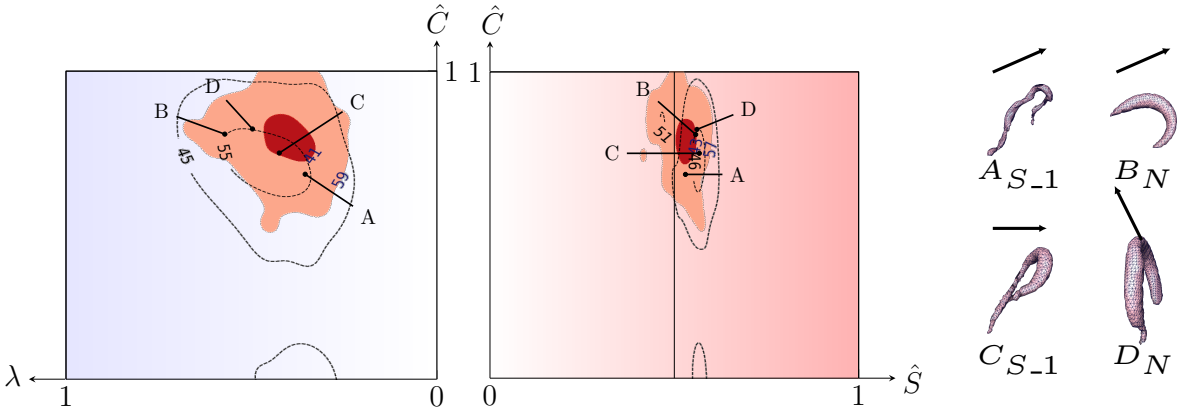

Figure 3.17: The geometry of 100 hairpin-like structures are compared in the visualization space for case N and S_1. Isosurfaces of two tube-like examples from each case are shown on the right. Filled contours represent case S_1 whereas unfilled contours represent case N. $\hat{S}, \hat{C}, \lambda$ are the shape index, curvedness and stretching parameters respectively.

Before the geometrical characterization is applied to the hairpin-like structures, a distinction is made between a hairpin and a hairpin-like structure. While manually probing the datasets, it is possible to encounter a structure which looks like a hairpin but may not contain any of the aforementioned classical hairpin attributes. Therefore, all manually probed and extracted structures are designated 'hairpin-like' throughout the thesis. For the geometrical analysis, 100 hairpin-like structures are manually probed and extracted for case N, S_2 and S_3 at the global percolation threshold. For S_1, in which an entire cluster of structures tend to be misidentified as a single structure, the MLP procedure described in subsection 2.3.1 is applied. A smaller domain of size $300 \times 90 \times 600$ is chosen with a stopping criterion $V_{\max}/V = 0.5$ to keep the computational costs bearable. The chosen subdomain is shown in figure 2.14(a). From the MLP results, 100 hairpin-like structures are identified.

The results of the geometrical characterization are shown in figures 3.17 and C.9. Interestingly, only the case S_1 has no sheet-like structures and $\hat{C}$ is above 0.5. This can be attributed to the MLP procedure which identifies only simple structures thereby limiting the possibility of choosing a complex structure which may resemble a hairpin. Apart from a few anomalous sheet-like structures, most of the structures are tube-like as expected with negligible difference in geometry for changes in strength of stratification.

Finally, the inclination angles of hairpin-like structures are examined. For the 100 structures chosen from each case, the inclination angle ($\theta_i = \arctan(\Delta y^+/\Delta x^+)$) is computed. The average inclination angles are $\theta_i = 35.4°, 27°, 26.6°, 25.4°$ for case N, S_1, S_2 and S_3 respectively. This suggests that the hairpin-like structures from the neutrally stratified case N have a higher inclination angle than the stably stratified cases (all of which seem to have similar inclination angles). Also, while θ_i for case N is much higher than those reported in previous studies (for example - 18°, Brown and Thomas (1977); 18.7°, Hommema and Adrian (2003); 16°, Carper and Porté-Agel (2004); 14.4°, Marusic and Heuer (2007); 25°, Hutchins et al. (2012); 13.7°, Chauhan et al. (2013)), it should be noted that these estimations may involve hairpin-like structures which are far away from the wall. Adrian et al. (2000) note that θ_i tends to increase as the hairpin ages and moves away from the wall. Therefore, if the structures only close to the wall are considered, i.e., structures which start within the buffer layer, then

the mean inclination angles are $\theta_i = 19.7°, 21°, 19.2°, 19.2°$ for case N, S_1, S_2 and S_3 respectively. This is in-line with previous observations and also indicates that, close to the wall, the inclination angles do not change much with increase in stratification. While the geometry and inclination angles of hairpin-like structures are addressed, their orientation and abundance require further investigation which is carried out in subsequent chapters.

3.2 A general definition of intermittency factor for wall-bounded flows

From the previous sections, it is evident that global intermittency has a significant impact on every layer of the stably stratified ABLs. Although the geometry of coherent structures are thoroughly quantified for increasing levels of stratification, it is important to note that this is achieved through: (a) thresholding of scalar indicators to identify individual structures, (b) limiting the analysis to one-third of the computational domain. Jiménez (2018) points out that,

> *"It is clear that the percolation threshold is only one among many possible threshold choices, and that conclusions derived from the structures thus obtained have to be tested against other methods of analysis."*

Therefore, to complement the results of the geometrical analysis presented in the previous sections, we turn towards conditional one-point statistics. The conditioning is based on a quantitative description of global intermittency to segregate the turbulent and non-turbulent regions. The goal of this section is twofold: to review the previous definitions of the *intermittency factor*, and to suggest possible improvements for the same.

Corrsin and Kistler (1955) have shown that the non-turbulent regions are comprised of irrotational fluctuations. Since irrotational regions have no vorticity, Bisset et al. (2002) and Da Silva et al. (2014) used the magnitude of vorticity to separate the turbulent and non-turbulent regions. The intermittency factor according to Pope (2001) is given by,

$$\gamma(x,t) = \langle H(|\omega(x,t)| - \omega_\tau)\rangle \tag{3.1}$$

where H is a Heaviside function, $|\omega|$ is the magnitude of vorticity, ω_τ is a small threshold below which the flow is assumed to be approximately irrotational, x is a streamwise location, t is time and $\langle\cdot\rangle$ is the averaging over wall-normal planes. Da Silva et al. (2014) observed that the geometric shape of the turbulent/non-turbulent interface (TNTI) has a weak dependence on the value of ω_τ. There are many ways to choose ω_τ. For instance, in Ekman flows, Ansorge and Mellado (2016) define $\omega_\tau = 7\omega_{rms}(\delta_{95})$, where δ_{95} is the height at which the total stress is approximately 5% of the wall shear stress. However, as pointed out in section 2.3, the inhomogeneity of the flow in the wall-normal direction has to be taken into account while choosing a non-subjective global threshold value. Hence, (3.1) can be written as,

$$\gamma(y) = \langle H(\alpha(x,y,z) - \alpha_{\tau_p})\rangle \tag{3.2}$$

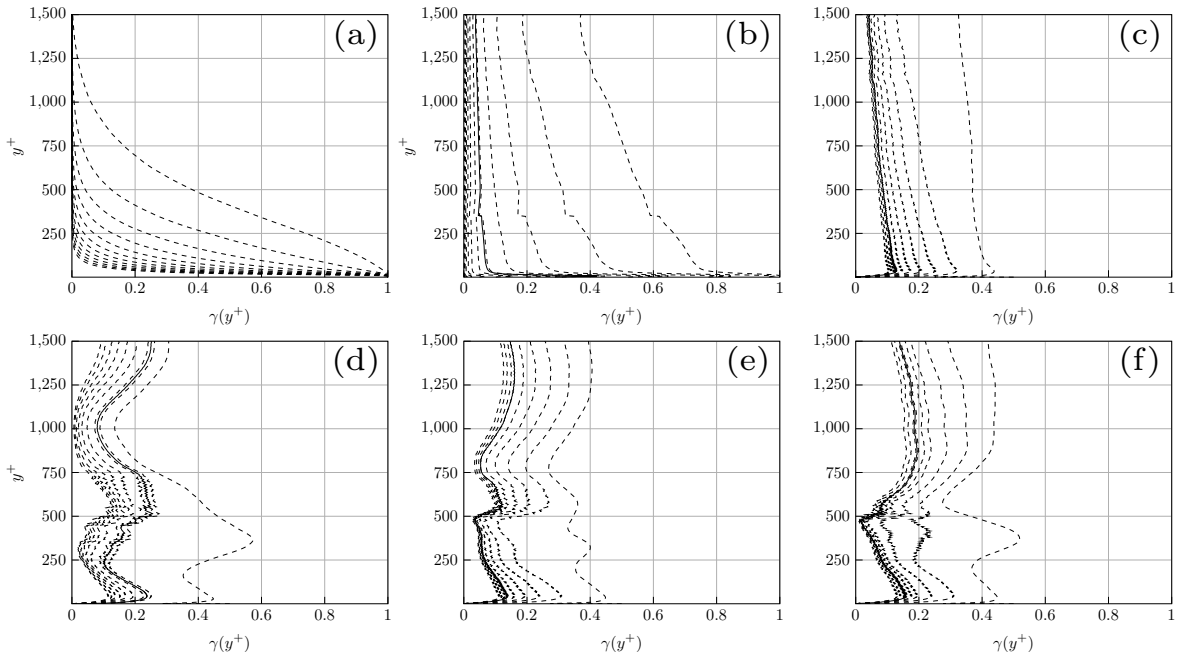

Figure 3.18: Intermittency profiles are shown with various values of ω_{τ_p}. In (a), ω is used as an indicator for case N without nondimensionalization with its RMS over every wall-normal plane. (b) shows the same indicator again for case N with nondimensionalization. (c, d, e, f) show the Q-criterion as an indicator with nondimensionalization for case N, S_1, S_2, S_3 respectively. Dashed lines from left to right indicate increasing values of the threshold starting from 0. Solid lines show the global percolation threshold.

where α is a vortex indicator normalized with its RMS over wall-parallel planes and α_{τ_p} is the global percolation threshold of the indicator. This is a generalization of (3.1) as α can be any vortex indicator. The time t is excluded as a single time step of the flow is analyzed in this chapter.

The advantage of (3.2) is shown in figure 3.18. In figure 3.18(a), ω is chosen as the vortex indicator. The profile is similar to that found for a non-rotating boundary layer as seen in figure 2 of Kovasznay et al. (1970), figure 9(a) of Da Silva et al. (2014) and rotating, stratified Ekman flow seen in figure 3 of Ansorge and Mellado (2016). Close to the wall, γ is more or less equal to 1 suggesting that this region is completely turbulent. As pointed out previously in subsection 2.1.3, ω misidentifies shearing motions as vortices and is hence responsible for a large value of γ. Furthermore, since ω is not nondimensionalized with its RMS, small threshold values will highlight structures only in the wall region of the boundary layer. If ω is nondimensionalized with its RMS over wall-parallel planes, the results from 3.18(b) indicate a more uniform spread of structures throughout. However, γ is still 1 close to the wall. An alternate indicator such as the Q-criterion can be used to rectify this issue. This is shown in figure 3.18(c) for case N. The profile correctly shows that regions close to the wall are relatively *less filled* with structures compared to the previous two cases. It is interesting to note that at the global percolation threshold τ_p (shown with solid line), the profiles for 3.18(b, c) are similar after $y^+ > 30$.

While the non-dimensionalized Q-criterion shows a minor variability of γ in the wall-normal direction for case N, the impact of global intermittency can be clearly seen in figure 3.18(d,

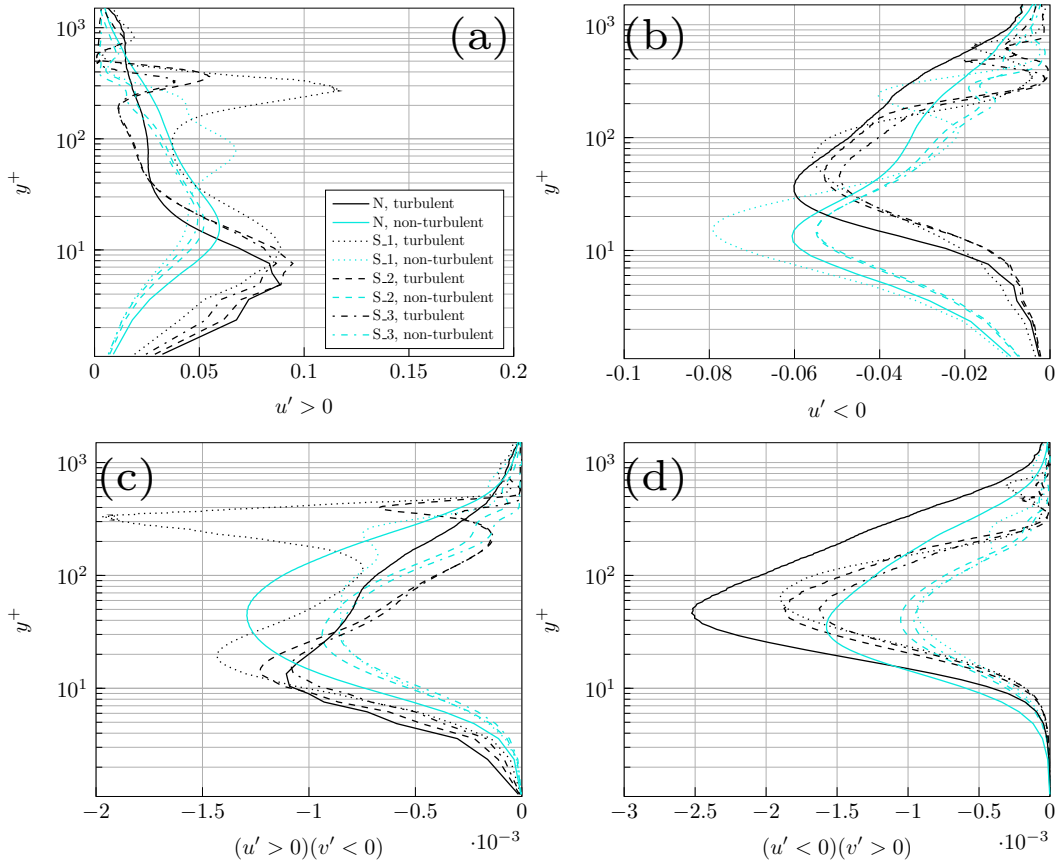

Figure 3.19: Vertical profiles of conditional one-point statistics applied to (a) high-speed streaks, (b) low-speed streaks, (c) sweeps and (d) ejections are shown here. Black profiles indicate turbulent regions and teal profiles correspond to the non-turbulent regions.

e, f) for which γ shows significant variations. The effect of these variations on conditional one-point statistics of streaks, sweeps and ejections are presented in the next section.

3.3 Conditional one-point statistics

The intermittency factor definition introduced in (3.2) is used to split the flow into turbulent and non-turbulent regions with α as Q-criterion. This conditioning is applied to four quantitative indicators namely, high-speed streaks, low-speed streaks, sweeps and ejections to complement the results obtained in section 3.1. Unlike the geometrical analysis which is restricted to grid B (1/3) of the computational domain, conditional statistics are applied to grid A (full domain). Once the flow is partitioned, vertical profiles are obtained by averaging the wall-parallel planes and the results are shown in figure 3.19.

Conditioning of the high-speed and low-speed streaks reveals a striking difference between the lower region of the boundary layer ($y^+ < 30$) and the region aloft. The lower region of the boundary layer is discussed first. In accordance with the results presented in subsection 3.1.1, it can be seen from figure 3.19(b) that the low-speed streaks in the non-turbulent region (blue dotted line) for case S_1 are dominant over those of the other cases. This is to be expected since it was shown that global intermittency affects the lower regions of the boundary layer including the viscous sublayer (as seen from figure 3.1(b)) in which the non-turbulent regions were occupied by low-speed streaks. For all four cases, figure 3.19 shows that the high-speed

streaks, which are regions of fast moving fluid, belong to the turbulent part of the flow. This is in accordance with the origin of turbulence within the buffer layer, in which strong shear is dominant leading to turbulence production.

Above the buffer layer, the streaks were examined only until $y^+ \approx 40$ in the geometrical analysis. Beyond that, it is observable from figure 3.19(a, b) that the non-turbulent regions of the flow are composed of high-speed streaks, i.e., faster moving fluid, whereas the turbulent region is occupied by the low-speed streaks. While these structures are still denoted as streaks, one must be aware that these are no longer the 'wall streaks' understood from the classical sense of the term. The behavior of these streaky regions can be explained with the non-locality of turbulence. Since turbulence mostly originates near the wall and is slower, it is manifested as low-speed streaks in the turbulent regions whereas the non-turbulent fluid originates from above and is therefore faster, which is seen with the high-speed streaks in the non-turbulent regions (Ansorge and Mellado, 2016).

In subsection 3.1.1 (on the viscous sublayer), a single low-speed streak was seen spanning the domain leading to the conclusion that non-turbulent regions are decelerated regions of the flow. This view is now examined here. For the non-turbulent regions of the flow, the ratio of the number of high- or low-speed streaks over the total number of non-turbulent points is computed over every wall-parallel plane and is shown in figures 3.20(a - d) for all cases. Apart from the neutrally stratified case in which the non-turbulent regions are composed of predominantly high-speed streaks until $y^+ \approx 1550$, it can be seen that low-and high-speed streaks tend to alternate for the stratified cases. This is most visible for case S_1 shown in figure 3.20(b) where the low-speed streaks are dominant until $y^+ \approx 31.26$, after which the non-turbulent region is composed of high-speed streaks. This behavior is seen for cases S_2 and S_3 where the switch happens at a lower height of $y^+ \approx 6.18$ and $y^+ \approx 7.55$ respectively.

The conditioning of sweeps (cf. 3.19(c)) and ejections (cf. 3.19(d)) also reveals interesting behavior. It was seen in subsection 3.1.2 that significant sweep activity is observed in the buffer layer, which is also evident in the turbulent regions when comparing figures 3.19(c, d). Sweeps in the non-turbulent regions also show significant wallward activity beyond $y^+ \approx 200$ for the stably stratified cases, which indicates that the non-turbulent fluid originates from above. Figure 3.19(d) also suggests significant ejection activity within the turbulent regions of the flow beyond the buffer layer but within $y^+ \approx 200$. This was not seen in section 3.1 and indicates alternating regions of outward and wallward flow in all cases.

3.4 Physical interpretation and discussion

If the geometry of all Robinson structures analysed in section 3.1 are plotted for each case as shown in figure 3.22, it can be seen that the envelopes of the joint p.d.f. are very similar regardless of the impact of global intermittency. Most structures within the ABL are moderately stretched tube-like or moderate to strongly stretched sheet-like with no blob-like structures. In previous works, sheet-like structures were observed at small scales in homogeneous, isotropic turbulence (Schumacher et al., 2005). Both flat and curved sheet-like features, having a fractal dimension of 2 (obtained through box-counting), were seen at the most intense regions[2] of

[2]Intense regions can be thought of as those parts of the scalar field which satisfy a large threshold relative to the maximum possible threshold.

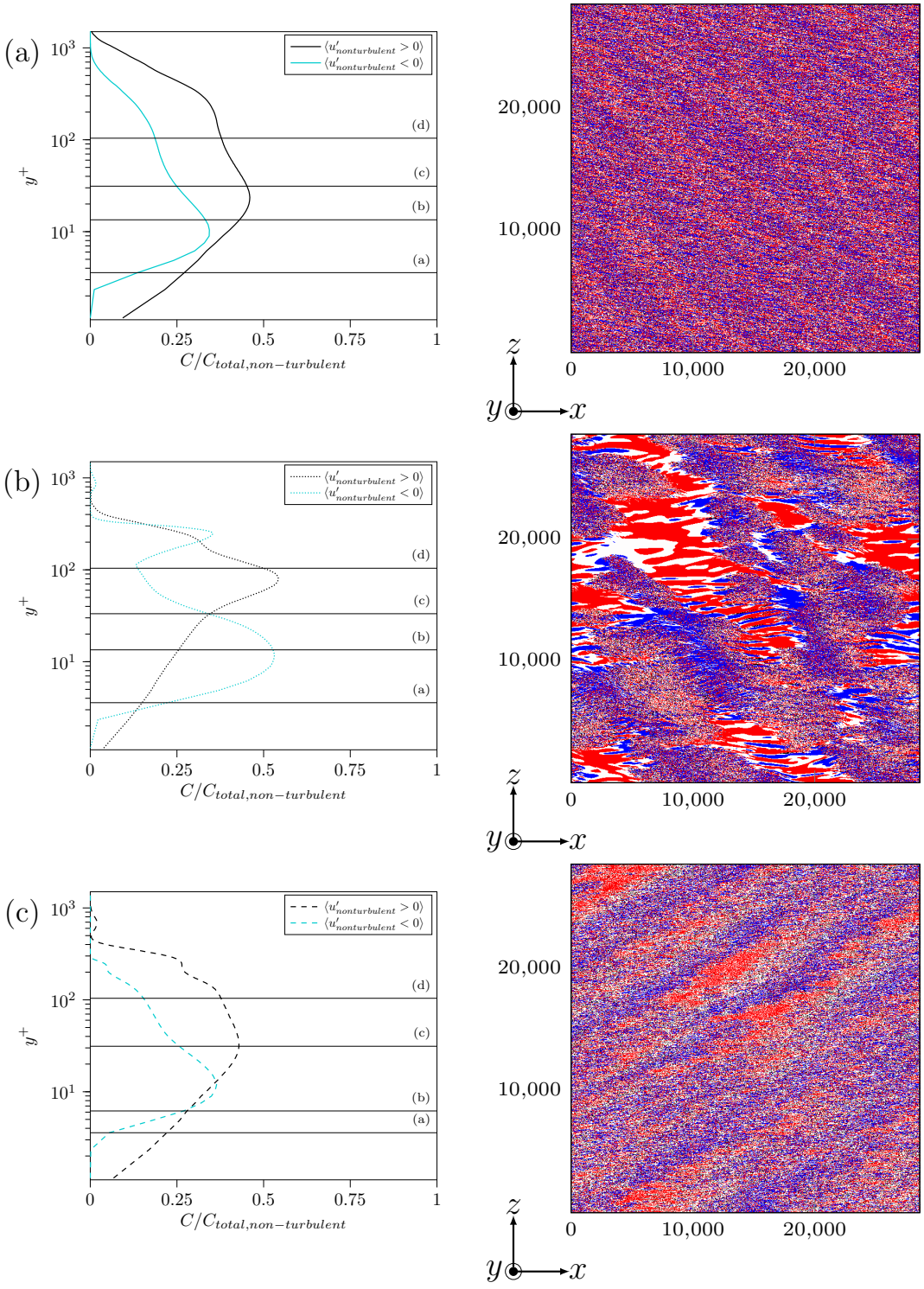
(a)
$\langle u'_{nonturbulent} > 0 \rangle$
$\langle u'_{nonturbulent} < 0 \rangle$
(d)
(c)
(b)
(a)
y^+
10^3
10^2
10^1
0
0.25
0.5
0.75
1
$C/C_{total,non-turbulent}$
20,000
10,000
0
10,000
20,000
z
y
x
(b)
$\langle u'_{nonturbulent} > 0 \rangle$
$\langle u'_{nonturbulent} < 0 \rangle$
(d)
(c)
(b)
(a)
y^+
10^3
10^2
10^1
0
0.25
0.5
0.75
1
$C/C_{total,non-turbulent}$
20,000
10,000
0
10,000
20,000
z
y
x
(c)
$\langle u'_{nonturbulent} > 0 \rangle$
$\langle u'_{nonturbulent} < 0 \rangle$
(d)
(c)
(b)
(a)
y^+
10^3
10^2
10^1
0
0.25
0.5
0.75
1
$C/C_{total,non-turbulent}$
20,000
10,000
0
10,000
20,000
z
y
x

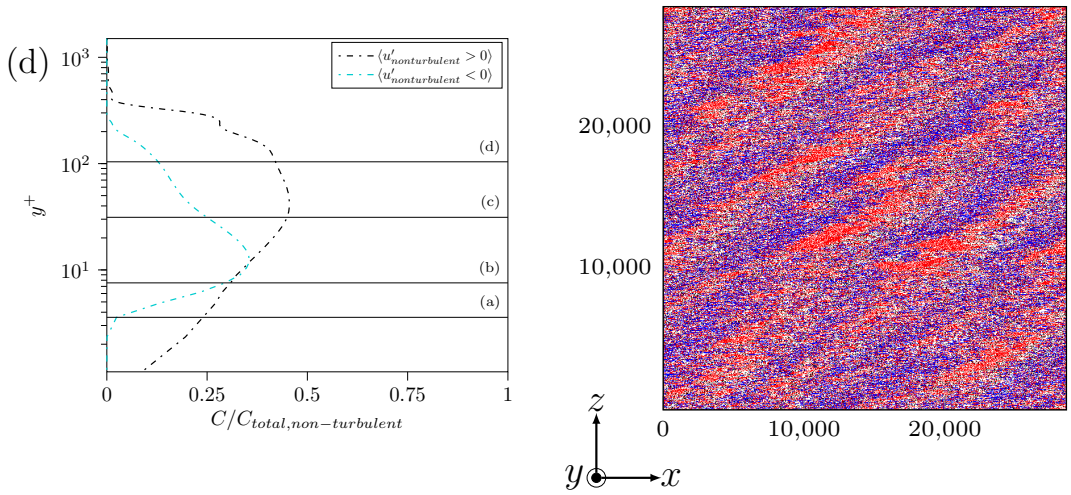

Figure 3.20: Vertical profiles indicating the fraction of the volume occupied by high- and low-speed streaks are shown on the left for case (a) N, (b) S_1, (c) S_2 and (d) S_3. Except for case N, the height at which the profiles intersect is visualized on the right. For case S_1, S_2 and S_3, the profiles intersect at $y^+ \approx 31.26$, $y^+ \approx 6.18$ and $y^+ \approx 7.55$ respectively. For case N, a height of $y^+ \approx 13.45$ is visualized.

the scalar dissipation. Similarly, Bermejo-Moreno and Pullin (2008) applied the curvelet transform on a passive scalar field of forced, isotropic turbulence and reported the presence of sheet-like structures at the smallest scales. They also found a continuous transition from blob-like structures with moderate stretching at the largest scales, tube-like in the middle scales and stretched sheet-like structures in the smallest scales. Moisy and Jiménez (2004), by computing the aspect ratios of three-dimensional structures extracted from scalar fields, found that intense strain-rate regions were predominantly sheet-like with a fractal dimension of 1.7 (obtained with a box-counting analysis). Although a scale-by-scale analysis was not performed in this work, it was shown in figure 3.11 that small ($\approx 100^+$ viscous units in the streamwise direction and 37^+ viscous units in the spanwise direction), intense sheet-like shear layer structures are formed in the vicinity of hairpin packets. Figures 3.18(a, b, c) also suggest the presence of intense shearing regions close to the wall. If the geometry of structures within the wall region of the ABL can be clarified with a multi-scale analysis, it could be used to improve, for instance, structural models of LES in which the subgrid stress is modeled as a superposition of velocity fields from an ensemble of tube-like structures (Misra, 1997; Misra and Pullin, 1997).

The analysis of numerous Robinson structures allows for a comparison with previously known results, for instance, the conceptual hairpin-packet model of Adrian et al. (2000). A sketch of the Robinson structures is shown in figure 3.21(a, b). It should be noted that high-speed streaks, pockets and backs are omitted here. The existence of high-speed streaks is ubiquitous and can be seen alternating with the low-speed streaks (cf. figures 3.1 and C.1). Although the latter two structures were detected in the ABL, numerous Q-criterion events interacting with the wall showed no pocket-like regions in the viscous sublayer (see discussion in subsection 3.1.5) and their contribution to turbulence generation is not immediately apparent. Far fewer backs (extended shear layers) were detected in the flow field for all simulation cases, particularly for case S_1. The detected structures were not on the order of $\delta-$scale as shown

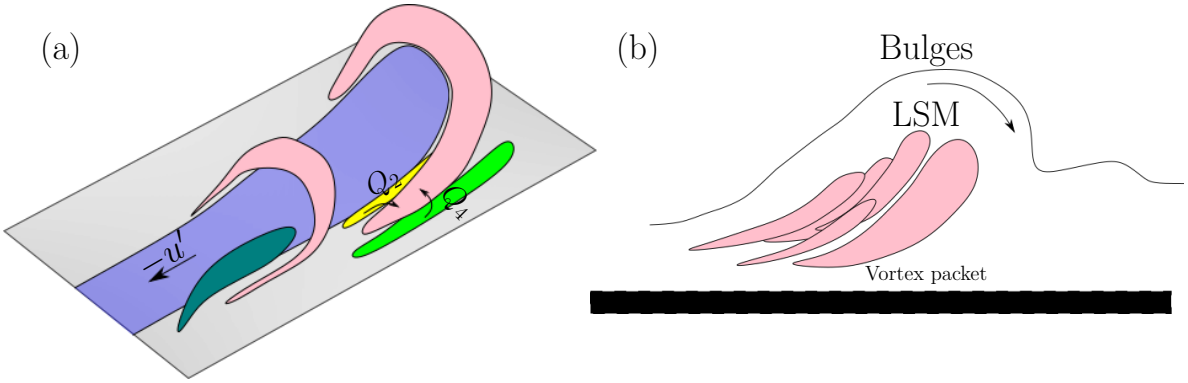

Figure 3.21: A sketch of the conceptual model discussed in the text is shown here. The color specification of the structures is according to table 2.1.

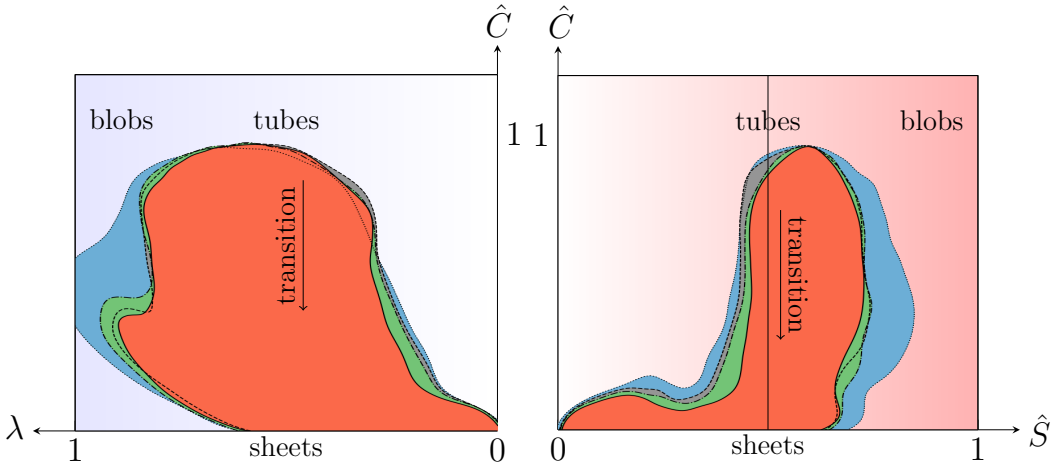

Figure 3.22: Visualization space showing the geometry of all structures analysed for all simulation cases. The neutrally stratified case N is represented by solid line (—) and the stably stratified cases S_1, S_2, S_3 are represented by dotted (...), dashed (- - -) and dash patterned (– – –) lines respectively.

in the literature. Therefore, it remains unclear if backs are a part of the ABL or if more sophisticated methods are necessary for their detection.

The hairpin packet discussed in subsection 3.1.5 is useful to understand the interactions of various Robinson structures which are shown in figure 3.21(a). A low-speed streak (colored blue) is seen in-between the legs of a primary hairpin. Zhou et al. (1999) proposed that low-speed streaks are generated due to the backward pumping of the fluid by the hairpin packet. Close to the leg of a hairpin, a Q_2 ejection event (colored yellow) and a Q_4 sweep event (colored green) can be seen on either side. The Q_2 event which pushes the fluid up can be seen arising out of the low-speed streak as they are both regions of $-u'$. The fluid which is pushed up interacts with the mean flow which results in the formation of shear layers (colored magenta) (Zhou et al., 1999). The primary hairpin autogenerates a new hairpin with a strong Q_2 event which interacts with the high-speed fluid (Adrian et al., 2000). This results in the formation of a hairpin packet. Streamwise coalescence of these hairpin packets results in the formation of large scale motions (Katul, 2019) as sketched in figure 3.21(b).

3.5 Summary and conclusions

To understand the intricacies associated with stable boundary layers, the modular framework developed in the previous chapter has been used to examine the geometry of all Robinson structures among three stably stratified and a neutrally stratified case of the Ekman flow. For an instantaneous time step of each case, the structures were extracted at the percolation threshold and geometrically characterized. About 10^6 structures were analyzed. The results are reported by segregating the ABL into different layers or regions based on the wall-normal height y^+.

Within the viscous sublayer ($y^+ < 5$), particularly with the low-speed streaks, an increase in their streamwise coherence was observed with increase in stratification. For the strongly stratified case S_1, a large portion of the domain is occupied by a single low-speed streak (cf. figure 3.1(b)). Notably, this low-speed streak has few ejections arising out of it (both low-speed streaks and ejections are regions of $-u'$), most of which are confined to the outer edges of the structure. The inner region which is completely devoid of ejections is comparable to the non-turbulent regions seen above the viscous sublayer. This suggests that global intermittency has a direct impact in this layer, although partitioning of the flow into turbulent and non-turbulent regions isn't applicable here since the flow is locally laminar. Therefore, global intermittency should be generalized to indicate active/inactive regions rather than turbulent/non-turbulent regions to account for its impact within the viscous sublayer.

Since the geometrical analysis requires structures to be closed and not noise-like, i.e., having a mean fractal dimension $\langle D_\alpha \rangle > 1$, it is only performed for structures in the buffer layer and beyond. In general, figures 3.6, 3.10, C.5, C.6 suggest that structures with similar geometrical features exist for all stratifications, i.e., an affinity towards sheet-like (or pancake-like) geometry cannot be established for increasing stability at an instantaneous snapshot of the flow. This result is surprising since changes in geometry have been observed with increasing instability (see the discussion in the introduction of this chapter). It should be noted that the discrepancy observed in figure 3.10(a, b) between case N and S_1 for high-and low-speed streaks, where S_1 shows sheet-like structures, can be attributed to the small sample size, given that structures were analyzed only in the region $30 < y^+ < 40$. Although this result was unexpected, it is in-line with recent results reported by Gucci et al. (2023), who found that one-component turbulence[3] (associated with very stable stratification) does not lead to two-dimensional (or pancake-like) turbulence.

Examination of hairpin-like structures in subsection 3.1.5 shows that they possess similar tube-like geometry inclined at approximately $19° - 21°$ (close to the wall) regardless of changes in strength of stratification. While these results suggest that the geometry of coherent structures and inclination angles of hairpin-like structures do not change much with increasing stability, numerous visualizations (for instance, figures 3.1, 3.3, 3.4, 3.13, 3.14) clearly indicate the presence of quasi-laminar patches (due to global intermittency) for the case S_1 extending throughout the vertical length of the flow which has a strong impact on the spatial organization

[3]Here, one-component refers to a limiting state of the anisotropic Reynolds stress tensor, where one eigenvalue is much larger than the other two (See Pope (2001), table 11.1 for a list of all limiting states and their corresponding shape). In stable boundary layers where submeso motions exist, it was shown by Vercauteren et al. (2019) that flow configurations influenced by these submeso motions have a preference towards one-component axisymmetric stress.

of coherent structures. By analyzing the time series of turbulent heat flux from the CASES-99 data (Poulos et al., 2002), Van de Wiel et al. (2002) (see figure 1) show that global intermittency also exhibits temporal variability in which strongly turbulent periods (negative heat flux) are interspersed with quiet periods (no heat flux). This spatio-temporal variability of global intermittency can have a direct influence on the dynamics of coherent structures. Therefore, to fully comprehend the impact of stability on the geometry of coherent structures, one must extend current results by studying the temporal evolution of geometry for which these structures are tracked in time. This is pursued in the subsequent chapter.

Since there is an ambiguity in choosing the "optimum" threshold value from percolation analysis, conclusions derived from the geometrical analysis are complemented with those from conditional one-point statistics. The flow is conditioned into turbulent and non-turbulent subvolumes with an intermittency factor γ. Previous definitions of γ used the magnitude of vorticity (ω) with an appropriate threshold to segregate the turbulent (rotational) and non-turbulent (irrotational) parts. Two improvements to this definition are proposed in section 3.2. Since shearing motions are misidentified as vortices by ω, it is suggested to replace ω with alternate Eulerian vortex indicators, for instance with the Q-criterion. It should be noted that this is important only for wall-bounded flows, in which strong shearing motions exist close to the wall. If the analysis is conduced far away from the wall or for other flow conditions such as homogeneous isotropic turbulence, vorticity magnitude will be sufficient to partition the flow field. As shown in subsection 2.1.3 and Chakraborty et al. (2005), popular vortex criteria such as Q, λ_2 and Δ tend to identify very similar regions as vortices and therefore, a particular choice among these should not affect the conclusions presented in this thesis. The second improvement concerns the threshold. Since the flow is inhomogeneous in the wall-normal direction, using a single, global threshold value may not highlight features evenly for the entire flow field. This effect has already been illustrated in figure 2.13. Therefore, the vortex indicator is nondimensionalized with its RMS over wall-parallel planes before percolation analysis is carried out to choose the threshold.

Results of the conditioning applied to streaks, sweeps and ejections are discussed in section 3.3. It should be noted that the conditional analysis is performed on grid A (full domain), unlike the geometrical analysis which was restricted to grid B (1/3 of the domain) to lower computational costs. Similarities between the results of the geometrical analysis and the conditional statistics can be seen in low-speed streaks, both of which suggest a dominant presence in non-turbulent flow regions close to the wall for the strongly stratified case S_1 (see figures 3.1(b), 3.19(b)) suggesting that non-turbulent patches are decelerated regions of the flow. However, analysing the volume fraction occupied by low- and high-speed streaks in figure 3.20(b) reveals a switching behavior where the outer non-turbulent regions are occupied by high-speed streaks which was not seen in the geometrical analysis since it was restricted to $y^+ < 40$. This switching behavior, also mirrored in sweeps and ejections (see figures 3.19(c, d)), suggests that the outer non-turbulent patches is composed of fast moving fluid. This makes sense as non-turbulent fluid originates from the free stream (Ansorge and Mellado, 2016) and is therefore faster.

4

Temporal evolution of the geometry of Robinson structures

In the last chapter, a detailed geometrical analysis on the Robinson structures was carried out on an instantaneous snapshot of the Ekman flow at different levels of stratification. The modular geometrical characterization framework from chapter 2 was used to characterize the geometry of individual structures as blob-like, tube-like or sheet-like depending on their location within a three-dimensional visualization space composed of three parameters: shape index $\hat{S}$, curvedness $\hat{C}$ and stretching λ. Results indicate that, despite the influence of global intermittency extending until the viscous subalyer, similar geometrical features are observed with increasing stability and an affinity towards a certain geometrical type (for instance, sheet-or pancake-like) could not be established. However, visualizations show that global intermittency in the stably stratified cases has an impact on the spatial organization of coherent structures. Since global intermittency is known to exhibit temporal variability (Van de Wiel et al., 2002), one can expect that the dynamics of coherent structures will be affected, which in turn, can lead to temporal variations in their geometry. Therefore, the purview of the first part of this chapter is to study the temporal evolution of the geometry of quantitative Robinson structures and compare the same for increasing stratification. Specifically, the following question is addressed,

- With the instantaneous Ekman flow fields analyzed in the previous chapter as a starting point, is there a dissimilarity in the temporal evolution of the geometry of the quantitative Robinson structures for increasing stability?

Dynamical aspects of coherent motions have been investigated in numerical simulations of channel flows in prior works (Johansson et al., 1991; Robinson, 1991; Zhou et al., 1999; Lozano-Durán and Jiménez, 2014). Recently, Lozano-Durán and Jiménez (2014) studied the dynamics of sweeps, ejections and vortices on spatially and temporally well-resolved DNS of channel flow data by tracking them in time. Their results show that most structures are small with short lifetimes while the ones which are large were found to be geometrically self-similar with more or less constant aspect ratios. Observations from similar studies have been useful to build/improve models of wall-bounded turbulence based on coherent structures (Panton, 2001). Examples of such models include the hairpin-packet model (due to Adrian et al. (2000)) discussed in the previous chapter and a model for the logarithmic layer in terms of sweeps, ejections and clusters of vortices proposed by Del Álamo et al. (2006), Flores and Riley (2011), and Lozano-Durán et al. (2012), both of which are based on the attached-eddy model of Townsend (1961). In the ABL, coherent structures such as hairpin-like structures, hairpin

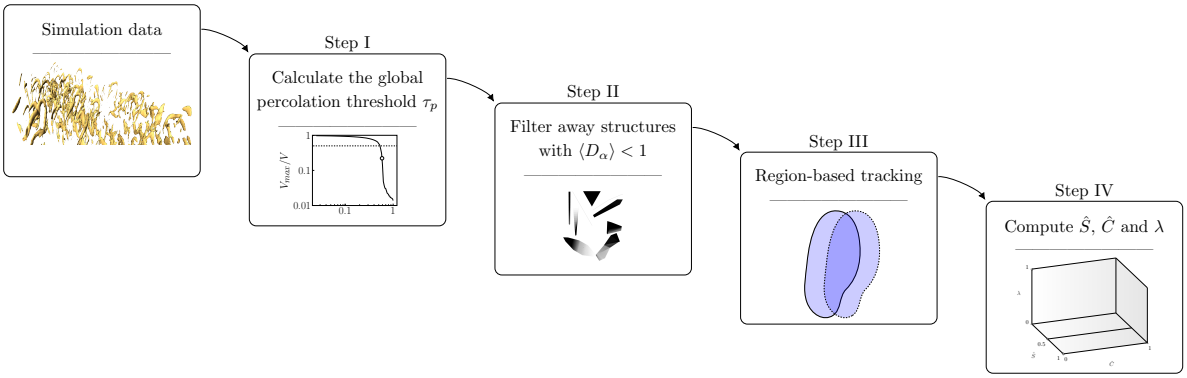

Figure 4.1: A schematic representation of the steps involved in tracking the Robinson structures in time. An additional step (step III) is introduced to the geometrical characterization framework from chapter 2.

packets, sweeps, ejections and large-scale motions have been detected and studied in field experiments (Hommema and Adrian, 2003; Carper and Porté-Agel, 2004; Horiguchi et al., 2010; Li and Bou-Zeid, 2011; Oncley et al., 2016; Heisel et al., 2018) under a variety of stability conditions. However, to the author's knowledge, the dynamics of these structures - particularly their three-dimensional extent, has received less attention. Even less attention has been paid to their geometry. While structures with ramp-like geometry have been identified in time-series data of stable boundary layers (Belušić and Mahrt, 2012; Halios et al., 2014), Mahrt (2014) points out that only limited inferences regarding the physics can be made with time-series data and stresses the need for detailed analysis in the spatial domain. This motivates the necessity to track three-dimensional coherent structures in time and quantify changes in their geometry.

Tracking of structures (or features) in time-dependent data sets has been studied extensively in the computer graphics community. To successfully track a structure, one needs to match the same structure at different instances in time. This is known as the *correspondence problem* (Ballard and Brown, 1982). For an overview on the various approaches to solve the correspondence problem, the reader is referred to the review paper of Post et al. (2003). In this thesis, a *region-based* correspondence technique is used in which correspondence is determined by volume or spatial overlap of structures between successive time steps. Tracking progresses only when the overlap threshold, denoted $\tau_{overlap}$, is satisfied. This method is chosen due to its simplicity in implementation and to keep the computational costs low. It has been previously applied for tracking vorticity magnitude structures in isotropic turbulence (Silver, 1995; Silver and Wang, 1996; Silver and Wang, 1997; Silver and Wang, 1998) and hairpin vortices, sweeps and ejections in channel flows (O'Farrell and Martín, 2009; Lozano-Durán and Jiménez, 2014). A common issue associated with this method is that it requires a rather high temporal sampling rate to track small, fast moving structures. Recently, a workaround was proposed by Badel (2021) and Lindheim et al. (2021) in which volume overlap can be combined with medical image registration to solve correspondence of non-overlapping structures. Other techniques also exist for which global spatial and physical attributes can be used to obtain the best matching result (Ji and Shen, 2006; Bußmann et al., 2022). Since these modifications/methods will increase the computational costs and it is desirable to keep them as low as possible (due to the large size of the dataset), the former method with spatial overlap is preferred and the snapshots of the simulation are output at full temporal resolution, i.e., every iteration. This ensures that most

structures having lifetimes greater than Δt^+ (which is the sampling interval) can be tracked. The sampling intervals are shown in table 4.1 for all cases. To keep the storage requirements reasonable, only the first 1000 snapshots starting with the instantaneous snapshot analyzed in chapter 3 are stored.

To compute the temporal evolution of the geometry of quantitative Robinson structures, an additional step is introduced in the geometrical characterization framework as shown in figure 4.1. The tracking methodology is described in section 4.1. While the method is capable of identifying and tracking interactions (such as split and merge events), only the primary structure is tracked for the Robinson structures. This is because interactions (specifically, merge events) can significantly alter the geometrical state of the structure as shown in figure 4.6. Results of tracking applied to Robinson structures are discussed in section 4.2.

In the previous chapter, visualization with the Q-criterion in figure 3.14 revealed interesting characteristics of hairpin-like structures. While these structures are observable for all cases, an abundance of them, most of which appear to be oriented in a similar spanwise direction, can be seen for the strongly stratified case S_1. It should be noted that hairpin-like structures have already been identified in previous studies for various stability conditions. For instance, in field experiments, signatures of hairpin vortices have been detected in unstable and neutral conditions of the ABL (Hommema and Adrian, 2003; Li and Bou-Zeid, 2011; Heisel et al., 2018). Oncley et al. (2016) also report the presence of counter-rotating vortices which can be interpreted as the legs of a hairpin structure under stable conditions. Furthermore, Watanabe et al. (2019) and Jiang et al. (2022), while studying the DNS of a stably stratified shear layer, not only found a large number of hairpin-like structures but also noted that they were oriented in the streamwise and spanwise directions at the middle and top of the shear layer respectively. Dynamical aspects of these structures have also been well documented for unstratified fluid flows (Acarlar and Smith, 1987; Zhou et al., 1999; Adrian et al., 2000). However, they remain relatively unexplored for stratified flows.

While studying the motion of an isolated hairpin vortex in the DNS of a channel flow, Zhou et al. (1999) observed that, after the initial lift-up due to self-induction, the hairpin structure is stretched in the streamwise direction due to the mean background flow. They further note that the head of the hairpin continues to lift upwards and assumes a near vertical orientation over time. This suggests that the hairpin structure grows in size as it is advected downstream. Since the feature tracking scheme, discussed in section 4.1, uses the same initial threshold to identify the structures in subsequent time steps, changes in size of the feature may not be adequately captured. Therefore, the following question is raised,

- Can the region-based feature tracking scheme be modified to account for changes in the size of the feature by dynamically adjusting the thresholds in time? How much would the temporal evolution of the geometry of the tracked feature differ with those obtained using constant threshold in time?

Steps of the modified feature tracking scheme are presented in subsection 4.3.1 and results of the geometrical comparison with constant and varying thresholds in time are discussed in subsection 4.3.2. With this modified feature tracking scheme, hairpin-like structures along with their interactions are tracked for all cases listed in table 4.1 and an attempt is made

Case	Line specification	Ri_B	Fr	Δt^+	Re
N	————	0	∞	0.14	
S_1	.....	2.64	0.02	0.125	26 450
S_2	- - - - - - -	0.76	0.07	0.254	

Table 4.1: The table from chapter 1 is repeated here with the omission of case S_3. Δt^+ is the time separation between consecutive time steps. It should be noted that the friction velocity u_τ which is used for normalization of quantities including time is not known *a priori* for Ekman flows and generally varies with time. Therefore, an averaged value of u_τ is used to compute these quantities (see table 1.2).

to explain the abundance of hairpin-like structures found in the strongly stratified case S_1. This is presented in subsection 4.3.3.

4.1 Methodology for tracking coherent structures in time

In this section, the region-based tracking procedure is described. The procedure for tracking individual structures is described in the subsequent subsection. Here, only the structure of interest is tracked and any interactions (split or merge events) which may occur during its lifetime are ignored. Lozano-Durán and Jiménez (2014) noted that interactions form a substantial part of the temporal evolution of structures (vortex structures, sweeps and ejections) in turbulent channel flows. They further note that large structures (on the order 100η[1]) are more susceptible to interactions, some of which may be complex, i.e., structures which are split from or merging with the primary structure may have experienced split or merge events of their own. An example of a complex vortex interaction can be seen in figure 5 of Lozano-Durán and Jiménez (2014). Therefore, a tracking procedure accounting for all interactions is described in subsection 4.1.2. Although both tracking procedures employ concepts similar to those described in Silver and Wang (1996) and Lozano-Durán and Jiménez (2014), they are differentiated by the use of the NS+MC algorithm which extracts visualization accurate structures from three-dimensional scalar fields (see subsection 2.2.2).

4.1.1 Tracking procedure for individual structures

In this scenario, the structure of interest (which can be a vortex identified with the Q-criterion, Q_2, Q_4 event etc.) is chosen by the user at time t_n. With the NS+MC algorithm, this structure is extracted at the global percolation threshold τ_p from the three-dimensional scalar field, denoted by I. The next stage of tracking is to determine correspondence between the source structure (or structure of interest) and target structures at later times.

In the consecutive time step t_{n+1}, the scalar field is thresholded at τ_p and all resulting structures are extracted with the NS+MC algorithm. Each structure is assigned a label $\{1\,, ..., N\}$. To identify potential target structures, the space (location of points) occupied by the source structure is searched at t_{n+1}. This space may be occupied by a single structure (one

[1]Here, η is the Kolmogorov length scale which is defined as $\eta = (\nu^3/\epsilon)^{(1/4)}$ where ν is the kinematic viscosity and ϵ is the mean dissipation rate of kinetic energy.

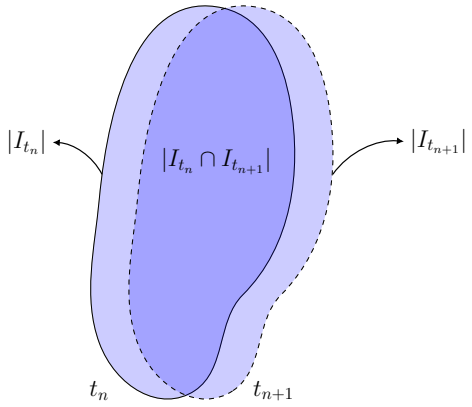

Figure 4.2: Spatial or volume overlap of a feature at different times t_n (solid line) and t_{n+1} (dashed line). The overlap region is highlighted with a darker shade of blue.

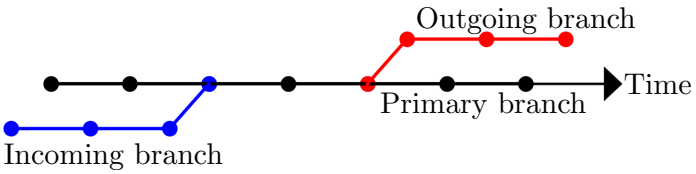

Figure 4.3: A sketch of the temporal graph indicating a merge event (colored blue) and a split event (colored red). The coloring scheme is used throughout the chapter unless otherwise indicated. Figure adapted from Lozano-Durán and Jiménez (2014).

unique label) or multiple structures (multiple labels) in case of a split event. Correspondence is determined by measuring the degree of spatial overlap between the source and each target structure with the dice similarity coefficient (DSC) (Dice, 1945),

$$DSC(I_{t_n}, I_{t_{n+1}}) = \frac{2|I_{t_n} \bigcap I_{t_{n+1}}|}{|I_{t_n}| + |I_{t_{n+1}}|} \tag{4.1}$$

where $|\cdot|$ denotes the volume of the structure. DSC can range between 0...1, where 0 indicates no spatial overlap and unity indicates a perfect overlap. The target structure which satisfies the user-defined overlap threshold, denoted $\tau_{overlap}$, is identified as the correct structure to follow. The overlap condition can be written as,

$$DSC(I_{t_n}, I_{t_{n+1}}) > \tau_{overlap} \tag{4.2}$$

In the case for which there are multiple target structures which satisfy $\tau_{overlap}$, the one with the highest DSC value is followed. Tracking continues until the structure *dissipates*, i.e., the structure becomes noise-like or when $\tau_{overlap}$ is not met.

4.1.2 Tracking procedure for interactions

In the previous procedure, structure interactions such as split or merge events are not followed. Previous works such as Lozano-Durán and Jiménez (2014) and Bußmann et al. (2022) have shown that coherent structures undergo numerous complex interactions during their lifetime. According to Samtaney et al. (1994), these interactions can be one of the following,

- *Bifurcation:* This is where the source structure at t_n can *split* into two or more structures at t_{n+1}.
- *Amalgamation:* The inverse of bifurcation is also possible where two or more structures at t_n *merge* with the source structure at t_{n+1}.
- *Creation:* A new structure may be created at a later point in time that merges with the source structure.

A branching event is said to have occured when there is an interaction with the source structure in the form of a split or merge. The split is termed as an *outgoing branch* and the merge is termed as an *incoming branch* (Lozano-Durán and Jiménez, 2014). A temporal graph is shown in figure 4.3 where an incoming structure attaches itself to the primary structure followed by a split of the primary structure into two. This is an example of a *simple branching event* in which the primary branch has only one interaction at any given time, i.e., a split or a merge. When these interacting structures undergo further split or merge events of their own, then a *complex branching event* ensues.

The procedure to track structures with interactions involves the following steps:

(1) *Correspondence determination:* In the first time step t_n, the scalar field is thresholded at τ_p and all resulting structures are extracted and labeled $\{1, ..., N\}$. This is repeated for t_{n+1}. For every source structure at t_n, the procedure described in the previous subsection is carried out in which the space occupied by the source structure is searched at t_{n+1}. If one unique label exists, then the source structure is said to have evolved without any interaction and can unambiguously be matched to the target structure as long as the overlap condition (4.2) is satisfied.

(2) *Split and merge detection:* If multiple labels exist, then the target structure which satisfies the overlap condition is identified as part of the primary branch as shown in figure 4.3. Other target structures are identified as split events and linked with the primary branch. To detect merge events, the procedure is carried out in reverse, i.e., the space occupied by every source structure at t_{n+1} is searched at t_n. Additional target structures apart from the one which satisfies the overlap condition are said to have merged with the primary branch. An additional lifetime constraint is imposed for merge events where the structure should have existed at t_{n-1} to avoid spurious connections. For instance, structures which are created at a time step t_n (as they satisfy the threshold) may immediately undergo a merge event at t_{n+1}.

(3) *Updating structure interactions:* Interactions between structures in consecutive time steps are stored as key-value pairs. For instance, when a structure splits, the target structures which do not satisfy the overlap condition (and hence, are not a part of the primary branch) are assigned new labels (or values) and linked with the label of the primary branch (or key). The process is reversed for merges. It is important to note that during merges, the merged structure continues with the label of the structure having the largest volume. Apart from the key-value pairs, the time instance of interactions

are also stored. With both sets of information, all connected components are organized into a large supergraph similar to Lozano-Durán and Jiménez (2014) and Bußmann et al. (2022) where each node identifies an instantaneous structure and the edges show their temporal connections. Connections are updated for every time step and structures created at a later point that interact with the primary structure are assigned new labels.

4.1.3 Validation of the tracking procedure with interactions

In this subsection, a validation of the tracking methodology is presented in order to ensure precise tracking of individual structures and branches. Two synthetic test cases, one representing a simple branching event and the other representing a complex branching event, were developed as shown in figure 4.4(a, b) respectively.

In the first test, there is exactly one incoming (merge) and one outgoing branch (split) interacting with the primary branch. This is captured by the tracking algorithm correctly and the results are shown in the forward temporal graph. The test was also repeated in backward time by reversing the order of the dataset and it can be seen that the roles of split and merge are exchanged. This is expected as a split in forward time becomes a merge in backward time.

In the second test, three structures not only interact with the primary branch, but they have interactions on their own. The results shown in the forward temporal graph reveal that all interactions are captured correctly, including a structure which exhibits both a split from a secondary branch and a merge to the primary branch. As expected, the picture is inverted in the backward temporal graph where the roles of splits and merges are reversed. A difference can be observed where the splits (red branches) from the forward temporal graph have different temporal lengths as merges (blue branches) in the backward temporal graph. This difference can be explained by how splits and merges are handled by the tracking algorithm as described in step 3. It should be noted that each structure is assigned a label by the algorithm. When a structure is split, a new label is assigned to the split structure and both structures are tracked with individual labels until they dissipate. However, when two structures merge, the label of the structure with the smaller volume is discarded and the merged structure is tracked with the label of the structure with larger volume. Although the method is clearly capable of tracking complex branching events, only simple branching events are tracked in this thesis.

4.2 Temporal evolution of geometry of Robinson structures in the ABL

In this section, the geometrical analysis from chapter 3 is continued by tracking the geometrical evolution of Robinson structures in time. The goal of this section is to test the hypothesis of whether the spatio-temporal variability of global intermittency has an impact on the geometrical evolution of structures.

Initially, a pre-processing step is carried out on the DNS database before the structures are temporally tracked. For the three cases listed in table 4.1, six scalar indicators corresponding to the low- and high-speed streaks, sweeps, ejections, vortices and shear layers are computed for all available time. Since this is storage intensive, the domain is restricted to grid B, i.e., 1/3 of the computational domain and wall-normal height $y^+ \approx 1300$. Additionally, all

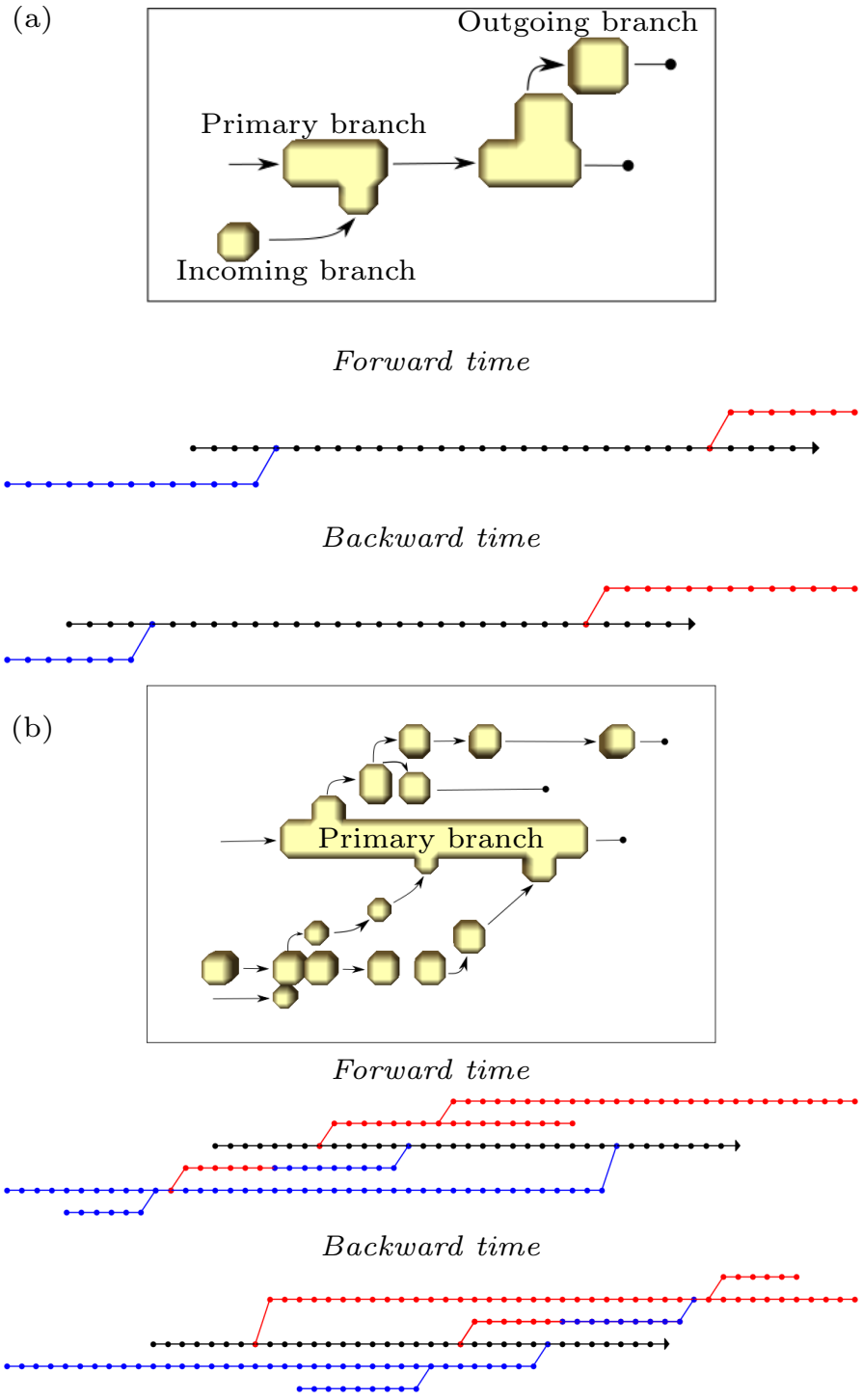

Figure 4.4: Two synthetic test cases for validation of the tracking methodology are shown. (a) shows a simple branching event with one incoming and one outgoing branch whereas (b) exhibits a complex branching event where branches themselves have interactions. The arrows (→) indicate the direction of time and black circle markers (•) indicate that the structure doesn't exist after that time step. The coloring of branches for the temporal graphs are according to figure 4.3 and the scatter points indicate time steps.

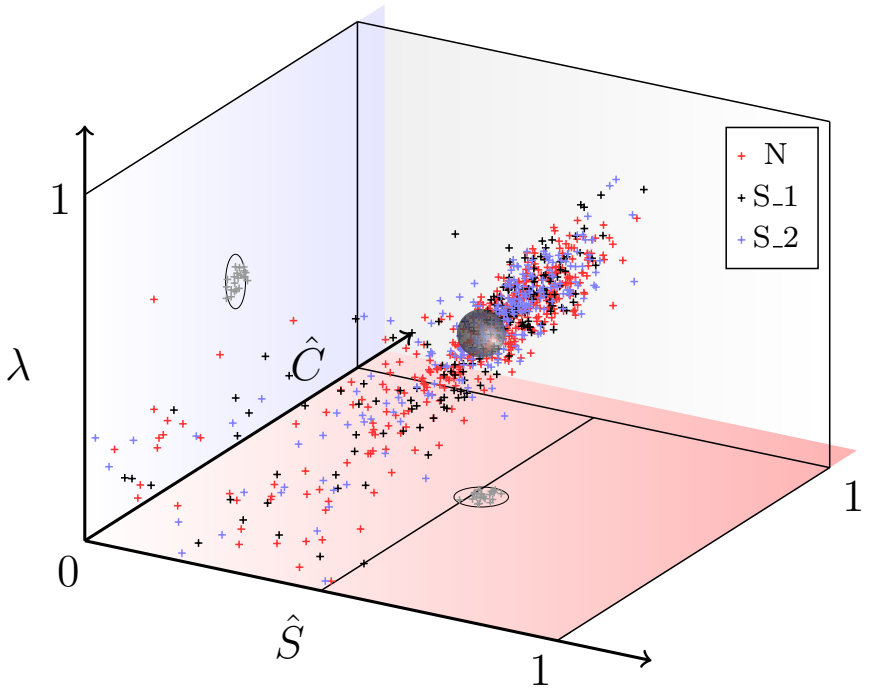

Figure 4.5: Visualization space for the high-speed streaks for stably stratified (S_1, S_2) and neutrally stratified (N) cases are shown. $\hat{S}, \hat{C}, \lambda$ are the shape index, curvedness and stretching parameters respectively. A sphere of radius $r = 0.05$, with origin at the centroid of the cluster, identifies geometrically similar structures for tracking. These structures, shaded gray, are projected on the planes $\hat{S}\hat{C}$ and $\lambda\hat{C}$.

indicators except for the low- and high-speed streaks are normalized with their RMS over every wall-parallel plane such that a single global threshold will highlight the structures evenly throughout the domain (see the description in section 2.3 for choosing a global threshold).

In order to establish a comparison among the stably stratified (S_1, S_2) and neutrally stratified (N) cases, the tracking is initiated by identifying geometrically similar structures, i.e., structures having similar values of $\hat{S}, \hat{C}, \lambda$ from the instantaneous Ekman flow fields analyzed in chapter 3. An example is shown in figure 4.5 for which the geometry parameters of high-speed streaks for all three cases are plotted. At the centroid of the cluster of all points, a small sphere of radius $r = 0.05$ is used to identify structures having similar geometry. This is the minimum radius at which few structures can be consistently identified for each case. Smaller radii may result in too few or no structures being identified for some cases and a larger radius will result in too many structures being identified, thereby increasing computational time. This process is repeated for other Robinson structures.

To investigate the geometrical evolution of structures, only the primary branch is tracked and all emerging structures after branching are ignored. Furthermore, a constraint is imposed on the tracking scheme in which the structure being tracked merges with a much larger structure, the tracking is terminated. This is because merges with larger structures tend to significantly alter the geometry of the structure. An example is shown in figure 4.6 where the high-speed streak after merging exhibits strong decrease in both λ and $\hat{C}$, the former implying strong stretching and the latter indicating that the structure is becoming sheet-like. Finally, it should be noted that when comparisons are made among the different Ekman flow cases, it is always done in terms of viscous time units. This is because the friction velocity u_τ is not a

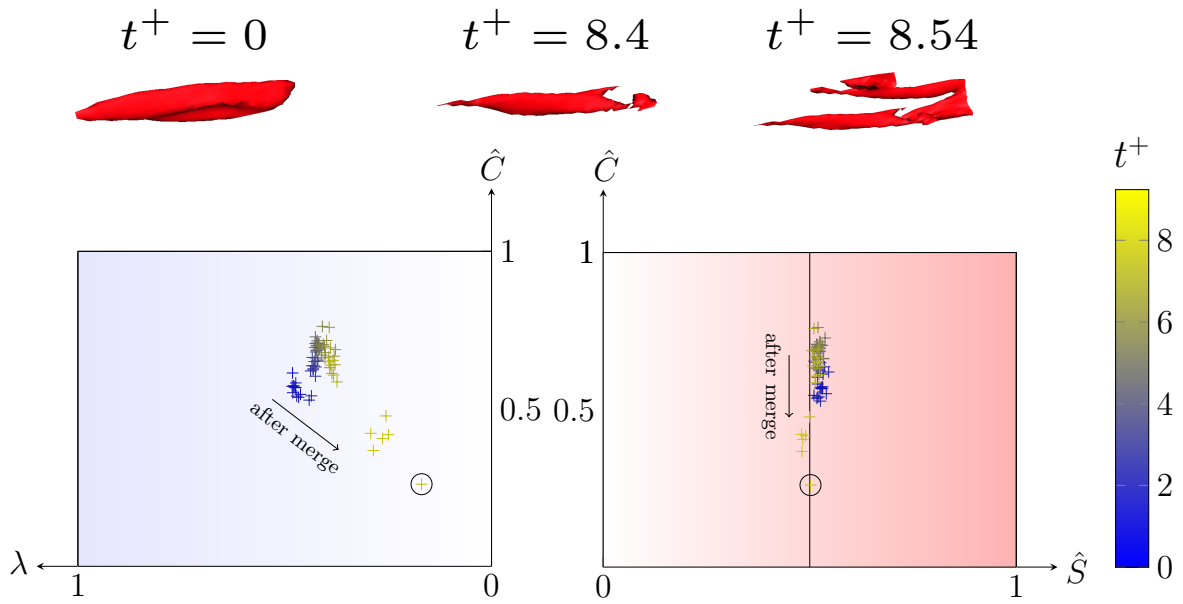

Figure 4.6: In the top panel, isosurfaces of a tracked high-speed streak are visualized at different viscous times. The bottom panel shows the temporal evolution of the geometry of the same high-speed streak until $t^+ = 9.24$. The black circle surrounding the marker indicates the viscous time $t^+ = 8.54$ when the structure being tracked merges with a larger one.

fixed parameter in Ekman flow simulations (Ansorge, 2016). The mean values of u_τ listed in table 1.2 are used to calculate viscous times $t^+ = t\nu/\delta_v^2$ where $\delta_v = \nu/u_\tau$ is the viscous length scale.

In total, about 600 structures have been tracked and geometrically characterized. The results are discussed in the following subsection.

4.2.1 Results and discussion

Results of the geometrical analysis for quantitative Robinson structures are shown with joint pdfs of $\hat{S}, \hat{C}$ and $\lambda, \hat{C}$ in figure 4.7 for cases N, S_1 and S_2. The contour lines are drawn for 2% of the maximum value which encompasses most of the data. Similar to the observation in chapter 3, the lack of blob-like geometry is instantly noticeable. Most structures appear to be moderately stretched tube-like and moderate to strongly stretched sheet-like structures. While this characteristic also appears to be unchanged from the results of the instantaneous flow field analyzed in chapter 3, minor differences in the geometry with increasing stratification can be discerned.

The geometry of high-speed streaks (see figure 4.7(a)) shows a marked difference between the stably stratified (dotted and dashed contours) and neutrally stratified case (solid contour). Although very few structures were tracked for the case S_1 (the tracking for the remaining structures were terminated due to mergers with large structures), both stably stratified cases indicate that the dimensionless curvedness parameter $\hat{C} > 0.3$. For the neutrally stratified case, more stretched (low λ) and sheet-like geometry ($\hat{C} \to 0$) can be observed. The source of this sheet-like tendency can be understood from the example shown in figure 4.8. Starting from point P, the high-speed streak becomes more tube-like over time and eventually reaches Q, after which the structure starts to dissipate becoming more stretched and sheet-like. Similar temporal developments can also be observed for case S_2 and an example is shown in figure D.1

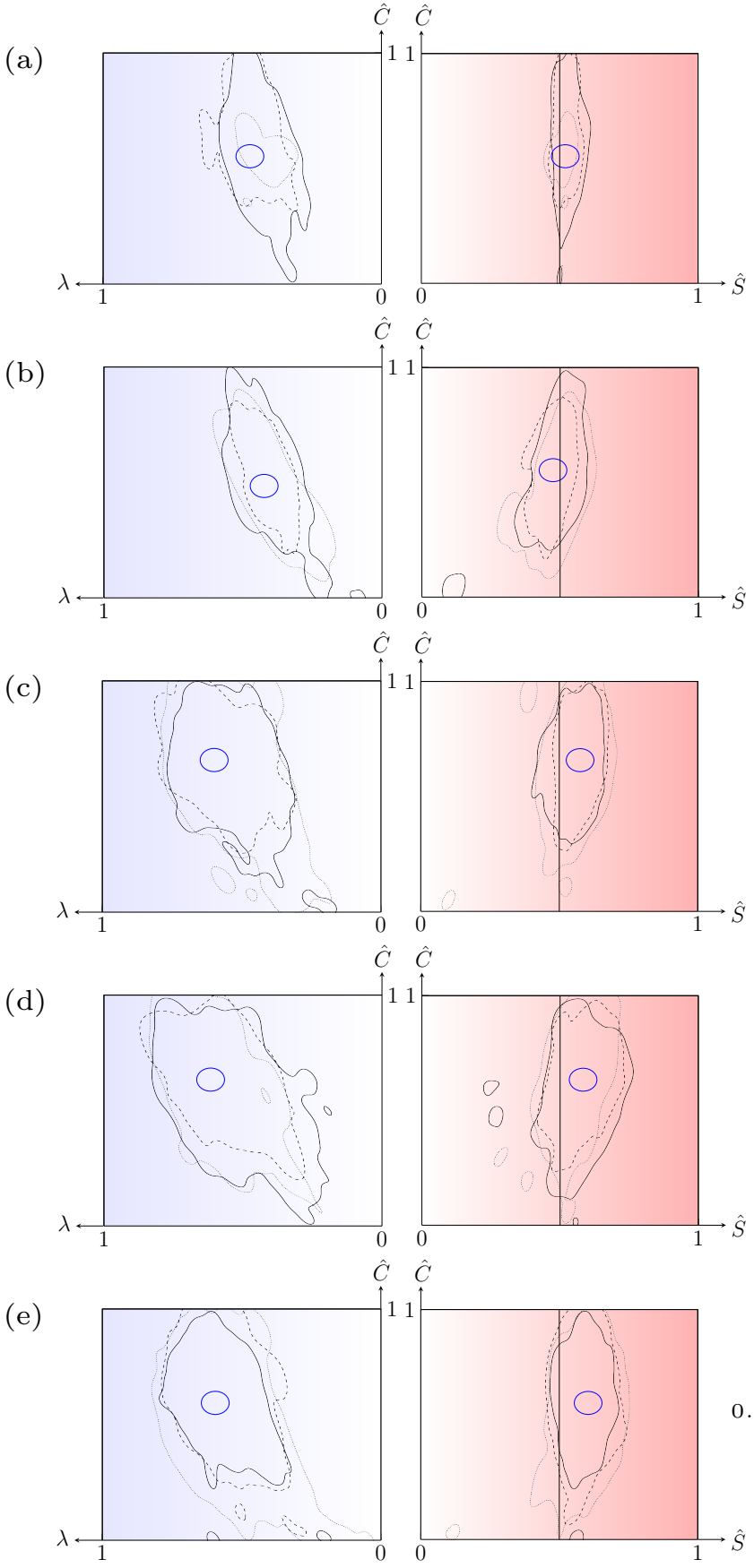
(a)
(b)
(c)
(d)
(e)
$\hat{C}$
$\hat{S}$
λ
1
0
High-speed streaks
$u' > 0$
Low-speed streaks
$u' < 0$
Sweeps
$u' > 0, v' < 0$
Ejections
$u' < 0, v' > 0$
Vortices
$0.5(||\Omega||^2 - ||S||^2) > 0$

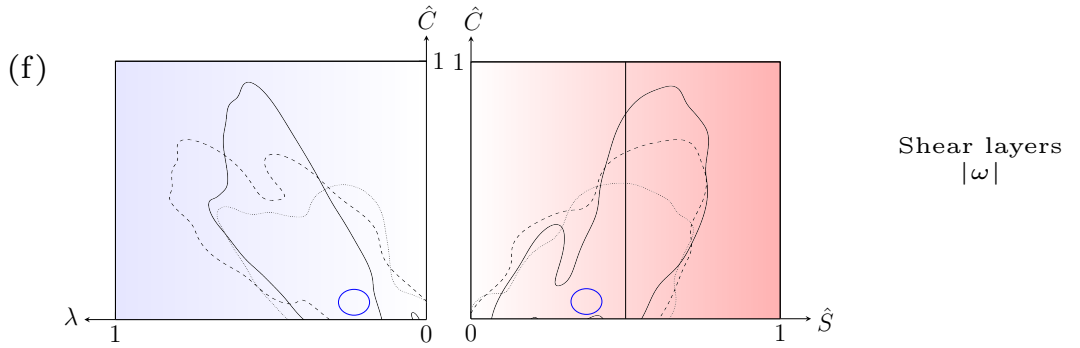

Figure 4.7: Contour lines of the joint p.d.f. of $\lambda, \hat{C}$ (left) and $\hat{S}, \hat{C}$ (right) are shown for all tracked (a) high-speed streaks, (b) low-speed streaks, (c) sweeps, (d) ejections, (e) vortices and (f) shear layers. Contours are drawn for 2% of the maximum value. Case N, S_1 and S_2 are represented with solid, dotted and dashed lines respectively. The blue circle indicates the region where structures having similar geometry were identified from the instantaneous Ekman flow fields analyzed in chapter 3 to initiate the tracking.

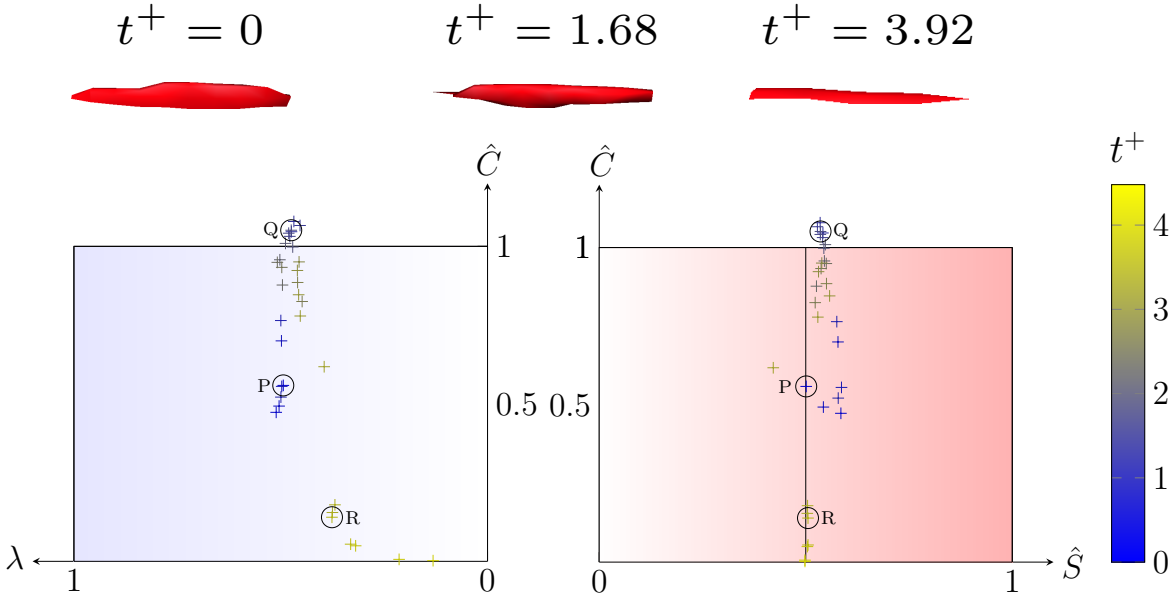

Figure 4.8: Top panel shows the isosurfaces of a tracked high-speed streak at different viscous times for the neutrally stratified case. The temporal evolution of the geometry of this streak is shown in the bottom panel. P, Q, R correspond to viscous times $t^+ = 0, 1.68, 3.92$ respectively.

where the structure initially becomes more tube-like with $\hat{C} \approx 1$ followed by a strong reduction in $\hat{C}$ indicating that the structure becomes sheet-like as it reaches the end of its lifetime. This suggests that the differences observed in figure 4.7(a) between the stably stratified and neutrally stratified cases can be attributed to the constraint placed on the tracking procedure in which structures are often not followed until they dissipate. The geometry of the low-speed streaks as seen in figure 4.7(b) do not appear to change much with increasing stratification. The left panel of figure 4.7(b) suggests that the low-speed streaks are more stretched than the high-speed streaks. This behavior was already seen in chapter 3 and is consistent with previous studies (Kline et al., 1967; Robinson, 1991; Jayaraman and Brasseur, 2021).

For the remaining Robinson structures, two cluster centers were identified with the K-means algorithm which segregates the structures into tube-like and sheet-like clusters. Structures having similar tube-like and sheet-like geometry are then identified with a ball of radius

$r = 0.05$ as described previously. Since the sheet-like sweeps and ejections were often found to be short-lived, lasting only a few time steps before dissipation or merger with large structures, they are excluded from the geometrical analysis. From figures 4.7(c, d), it can be seen that the geometry of sweeps and ejections are quite similar for increasing stratification. This means that the temporal evolution of the geometry of sweeps, ejections (and also, streaks) are not hindered by the presence of non-turbulent patches in the stably stratified cases. This, in turn, suggests that, within the turbulent patches of the flow, the dynamical evolution of these structures may be similar to those seen in the neutrally stratified case.

Finally, figures 4.7(e, f) show the temporal evolution of the geometry of tube-like vortices and sheet-like shear layers. It should be noted that for the strongly stratified case S_1, in which a large cluster of structures was misidentified as a single structure (see the discussion in section 2.3), the small domain of size $300 \times 90 \times 600$ subjected to MLP analysis as shown in figure 2.14(c) is used to identify the initial similar structures for tracking. The tracking is conducted using distinct threshold values for each structure because MLP analysis decomposes the large cluster into individual structures that possess unique threshold values. Apart from a minor inclination towards sheet-like geometry for the case S_1, no significant change in geometry can be seen with increasing stratification in figure 4.7(e). The tendency towards sheet-like geometry can be explained with figure D.2 where only the last time instant of tracking is plotted. It can be observed that relatively fewer structures from cases N and S_2 can be seen close to $\hat{C} = 0$. This combined with the structures having larger volume (indicated by the size of the marker) away from $\hat{C} = 0$ suggests that the tracking for most structures was terminated due to merge events with large structures. In the case of shear layers (see figure 4.7(f)), it can be seen that most structures do not stay sheet-like and appear to become less-stretched (higher λ) and more tube-like ($\hat{S} \approx 0.5$ and high $\hat{C}$) over time. Robinson (1991) notes that shear layers tend to develop a vorticity concentration near their mid-point (see figure 10.8.4 of Robinson (1991)) which may be responsible for the change in geometry. A minor trend can be noticed for which an increase in the strength of stratification leads to lower $\hat{C}$, i.e., more flattened structures.

In summary, tracking the temporal evolution of the geometry of Robinson structures, starting from structures possessing similar geometry, yields only minor geometrical differences for changes in the strength of stratification. This hints that spatio-temporal variability of global intermittency may not have a significant impact on the dynamics of the Robinson structures.

4.3 Temporal evolution of hairpin-like structures

The goal of this section is twofold: first, a comparison of the temporal evolution of the geometry of a hairpin-like structure is made when a constant threshold (to identify the feature) is applied and when the thresholds are dynamically adjusted in time. Second, with the modified tracking procedure, an attempt is made to investigate the source of abundance of the hairpin-like structures seen in the strongly stratified case S_1. To this end, the hairpin-like structures identified in subsection 3.1.5 are followed in time along with their primary interactions and compared among cases N, S_1 and S_2.

4.3.1 Multilevel percolation thresholding in time (MLPT)

Since this method relies on multilevel percolation (MLP) analysis discussed in subsection 2.3.1, it is briefly reiterated here. Once the global percolation threshold τ_p is identified for a given indicator, the resulting structures are extracted at that threshold. These structures are then subjected to percolation analysis in an iterative manner until they can be classified as a *simple structure*. A simple structure is obtained when the ratio $V_{\max}/V$ (where $V_{\max}$ is the volume of the largest structure in the domain and V is the volume of all structures) is above 0.5 (or a higher value chosen by the user). If a *complex structure* is encountered, then the percolation analysis is repeated until only simple structures remain. These definitions of simple and complex structures can be used to obtain optimum thresholds in time. The combination of the region-based spatial overlap technique with identifying optimum thresholds in time, henceforth called as multilevel percolation thresholding in time (MLPT), is presented in the following steps:

(1) Once the structure of interest is chosen by the user for tracking, the initial threshold is set as either the global percolation threshold τ_p or the MLP threshold. The former is used when tracking structures from cases N, S_2 and the latter is used for case S_1. At this threshold, the structure of interest is extracted with the NS+MC algorithm for the first time step.

(2) As shown in figure 4.9(a, b), an overlapped structure at t_{n+1} is initially extracted at the same threshold and is classified as simple or complex. If the structure is deemed simple, then the algorithm checks for structure growth first by decreasing the threshold. It should be noted that decreasing the threshold results in a larger structure which signals that the structure is growing in time and increasing the threshold results in a smaller structure which signals that the structure is shrinking in time. The minimum threshold to check is given by the indicator itself. For instance, when the $Q-$criterion is used, smaller thresholds are checked as long as the condition $Q > 0$ is satisfied.

(3) For each decrease in the threshold, the structure at t_n is overlapped with the one at t_{n+1} and classified as simple or complex. Once a complex structure is identified at t_{n+1}, this indicates to the algorithm that the maximum growth of the structure is reached i.e., it can no longer be considered as an individual structure. Therefore, the previous threshold for which the structure could still be identified as simple is chosen as the optimum threshold for t_{n+1}.

(4) On the other hand, if the first overlap test with the structure at t_{n+1} results in a complex structure as shown in figure 4.9(b), then the thresholds are increased to check if the structure is shrinking in time. The steps are similar to point (3) in which each increase in the threshold, the structure at t_n is overlapped with the one at t_{n+1}. This process is repeated until the structure at t_{n+1} can be deemed simple. The threshold for which the structure is deemed simple is chosen as the optimum one.

(5) The steps described in (2-4) are repeated for every time step.

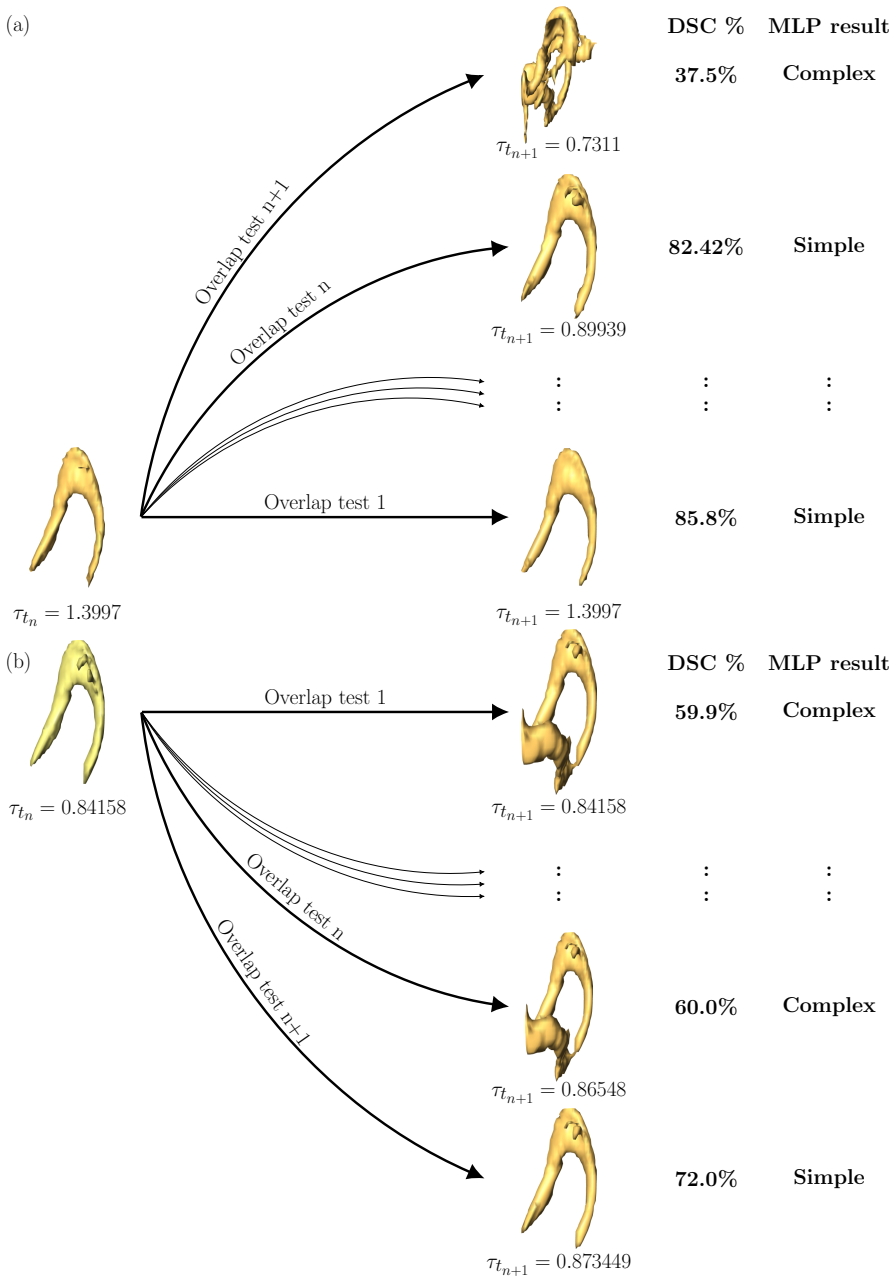

Figure 4.9: The technique of MLPT to choose an optimum threshold for a subsequent time step is illustrated here. In the scenario shown in (a) the structure is initially simple and therefore the thresholds are decreased until a complex structure is found. The opposite scenario is shown in (b) where the structrue is initially complex and therefore, the thresholds are increased until it can be deemed simple. Both (a, b) illustrate that the structure is allowed to grow or shrink freely in time.

Optimization strategies:

The addition of MLPT to the feature tracking scheme can become computationally expensive, especially when tracking structures across a large computational domain. Hence, two key optimization strategies are sought,

(1) Since temporally well-resolved DNS data is used for tracking of coherent structures in this thesis, an assumption can be made that the structure is not advected by the mean flow too far away in the domain between consecutive time steps. This enables one to use a smaller computational box around the structure to reduce the search space for the extraction algorithm. This, in turn, reduces the time necessary for obtaining optimum thresholds in time. The exact performance gain depends on the size of the smaller computational domain used.

(2) In conjunction with the previous optimization step, the memory or RAM overhead can be reduced by reading only specific bytes of the binary file which correspond to the smaller computational box.

4.3.2 Comparison of tracking results with constant and MLPT thresholds

To enable this comparison, a candidate hairpin-like structure is first chosen. During testing of the tracking algorithm, it was seen that the hairpin-like structures from the strongly stratified case S_1 could be tracked for several hundred time steps before dissipation suggesting that they possess much longer lifetimes than the other cases. Since this trait is useful to elicit a detailed comparison, the candidate structure is chosen from S_1.

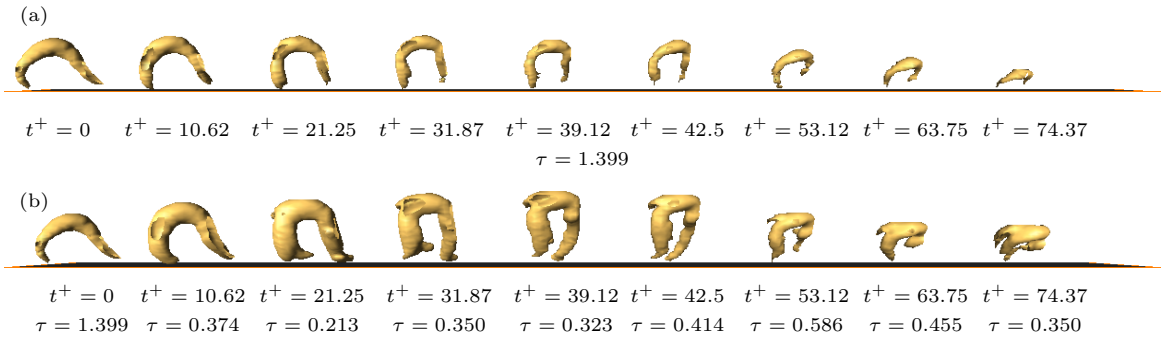

Figure 4.10: Track of a hairpin-like structure from case S_1 with (a) constant thresholding and (b) MLPT thresholding. Isosurfaces of Q-criterion are plotted at multiple time instances.

Initially, the candidate structure is tracked with a constant threshold of $\tau = 1.399$ (identified with MLP analysis, see subsection 3.1.5) and the results of the tracking for various time instances are visualized in figure 4.10(a) until $t^+ = 74.37$. As expected, the structure appears to be constantly shrinking in time until it dissipates at a much later viscous time of $t^+ = 83.3$. For MLPT tracking, the ratio $V_{\max}/V$ which determines whether a structure is simple or complex needs to be set. For all subsequent tracking with MLPT, $V_{\max}/V = 0.8$. This condition is sufficient to educe more or less individual structures. Results of the MLPT tracking for the same hairpin-like structure are visualized in figure 4.10(b) which suggests that the hairpin initially grows until a viscous time of $t^+ = 42.5$ after which it appears to shrink. It should be

noted that the results for MLPT are truncated until $t^+ = 83.3$ to make it comparable to the constant thresholding case. Plotting the wall-normal extent of the hairpin-structure over time as shown in figure 4.11(a) confirms that the structure is indeed growing reaching $\Delta y^+_{\max} = 119.3$ at $t^+ \approx 42$. The spikes and valleys in the plot can be attributed to the interactions (split and merge events) experienced by the structure during its lifetime. Zhou et al. (1999) observed that hairpin structures tend to grow as they are advected downstream due to the competing effects of the self-induced velocity generated by the hairpin structure itself and the shear induced stretching as a result of the mean background flow. This suggests that the MLPT technique is capable of capturing changes in the size (growth or deterioration) of the structure by actively modifying the thresholds in time.

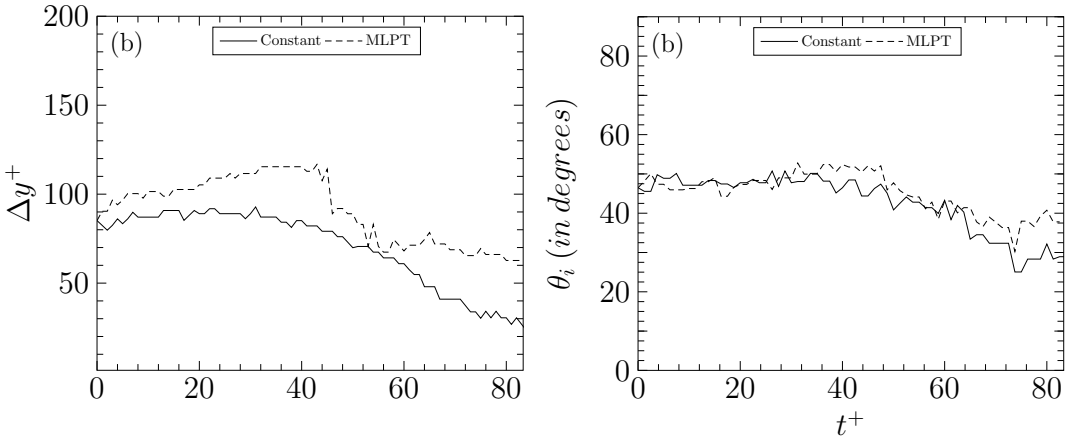

Figure 4.11: Time history of the (a) wall-normal extent (Δy^+) and (b) inclination angle of the hairpin-like structure tracked in figure 4.10 plotted every 8 time steps. Solid and dashed lines correspond to tracking with constant and MLPT thresholds respectively.

Changes in the inclination angle over time are plotted in figure 4.11(b). Both methods initially suggest $\theta_i \approx 46°$ which is consistent with the findings of Head and Bandyopadhyay (1981) who found that hairpin structures in the outer regions of the boundary layer were inclined at a characteristic angle of 45° with respect to the wall. Over the entire tracking period, the hairpin-like structure exists at a wall-normal height $80 < y^+ < 180$, i.e., in the outer layer. Figure 4.11(b) also shows only minor differences in θ_i between both methods. This is likely due to the changes in the threshold value in MLPT which alters both the streamwise and wall-normal extent of the structure. Finally, a comparison of the temporal changes in the geometry between both methods is illustrated in figure 4.12. Figure 4.12(a), showing the temporal evolution of the geometry with constant threshold, suggests that the hairpin-like structure becomes less stretched (high λ) and approaches blob-like geometry (high $\hat{S}$) as it dissipates. On the other hand, a dense clustering of points with relatively modest changes in $\hat{S}, \hat{C}, \lambda$ can be seen for the MLPT case in figure 4.12(b) which indicates that the structure remains tube-like over the same time period. This hints that the structure might persist for a longer duration than what was predicted by tracking with constant threshold.

4.3.3 MLPT tracking applied to the Ekman flow cases

With the MLPT tracking procedure, hairpin-like structures are tracked along with their interactions for both stably stratified (S_1, S_2) and the neutrally stratified case (N). Tracking

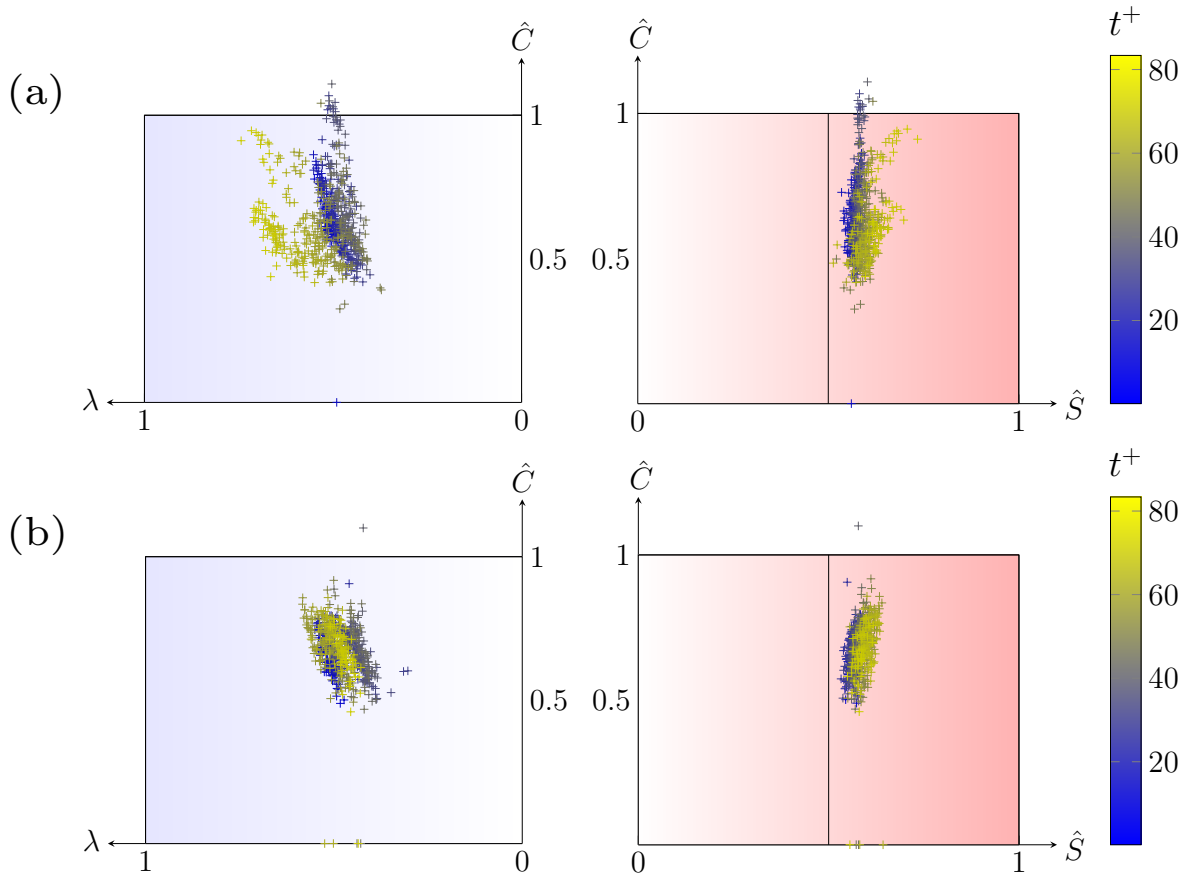

Figure 4.12: Visualization space for the structure tracked in figure 4.10 with (a) constant thresholding and (b) MLPT thresholding. Markers correspond to the geometrical state of the hairpin structure at a time instant.

is initiated with the manually identified structures from subsection 3.1.5 for all cases. Similar to the procedure described for vortices in subsection 4.2.1, hairpin-like structures are identified from the MLP results for the strongly stratified case S_1 and therefore, each structure has a unique starting threshold. First, an estimation of the lifetime of the structures is sought. Although MLPT is capable of capturing the dynamical changes in size of the structure which may result in a better evaluation of its lifetime, it should be noted that these structures are only tracked from a later stage of their evolution and the time elapsed from their source (or birth) to the later stage is not accounted for. Furthermore, while tracking interactions, it is unclear if the lifetime should also include split or merge events. For instance, structures which split from the primary branch can prevail long after the primary branch ceases to exist. To circumvent this, the definition from Lozano-Durán and Jiménez (2014) is adopted in which the time elapsed from a structure's first appearance in the primary branch to its last appearance is taken to be its lifetime.

With this definition, the average lifetime of all tracked hairpin-like structures for the three cases are plotted in figure 4.14(a). It can be seen that the average lifetime from both stably stratified cases is more than twice that of the neutrally stratified case. Unlike the previous subsection where a constraint had to be placed to exclude merges with large structures, MLPT will simply classify such merges as a complex structure and continue to increase the threshold

until a simple structure is found. Therefore, tracking with MLPT only terminates when the structure dissipates, becomes noise-like or when the overlap condition $\tau_{overlap}$ is not met.

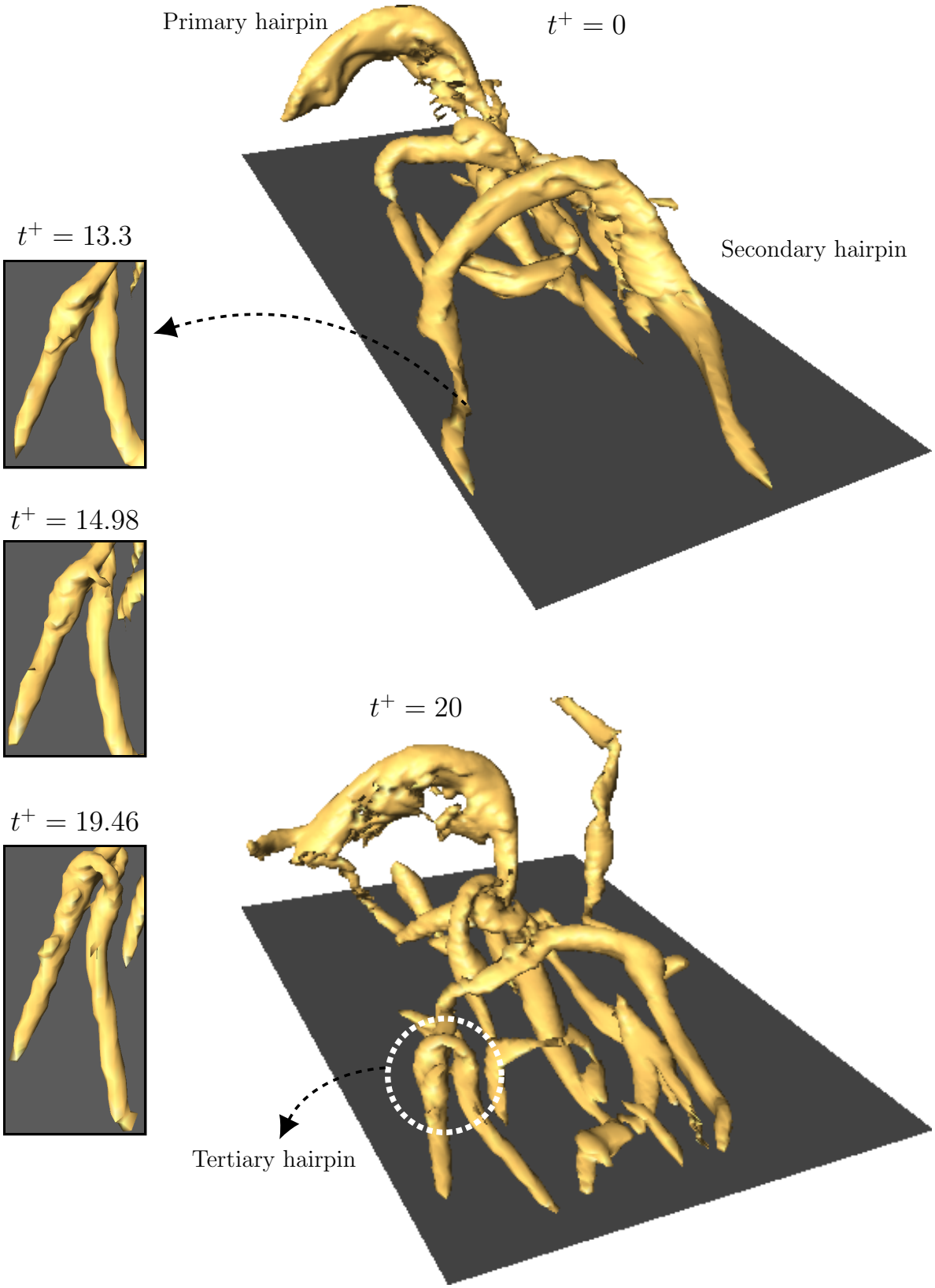

Figure 4.13: A track of the hairpin packet from figure 3.15 for the neutrally stratified case is shown here. The hairpin packet autogenerates a tertiary hairpin (seen in the bottom panel) at $t^+ = 20$. The autogeneration process is shown on the left panel.

The average number of split and merge events encountered by the structure until a viscous time $t^+ = 10$ is plotted for the three Ekman flow cases in figure 4.14(b). It should be noted that only simple branching events are recorded and complex interactions (where interactions have their own interactions) are ignored. It can be observed from figure 4.14(b) that the number of interactions increase with an increase in the strength of stratification. This result is surprising since, in conjunction with the result from figure 4.14(a), it suggests that the hairpins from the strongly stratified case S_1 have a longer lifetime while experiencing a relatively large number of interactions, 67% of which are merges. Interestingly, the number of splits for the case S_1 is also more than 3 times higher than that of the neutrally stratified case. A likely explanation may involve the autogeneration mechanism previously discussed in section 3.4. For instance, if the hairpin packet shown in figure 3.15 is tracked in time, it can be seen from figure 4.13 that a new tertiary hairpin is autogenerated over time. Although not shown, this autogenerated hairpin splits away from the hairpin packet and continues as a separate entity. If new hairpin structures are continuously autogenerated this way, the high number of splits may explain the abundance of hairpin structures seen in the strongly stratified case S_1. However, it is currently not known if after the autogeneration of a secondary hairpin which splits over time, the primary hairpin is capable of autogenerating another secondary hairpin. Zhou et al. (1999) note that autogeneration of new hairpins depends on the strength of the initial event and its location. They argue that hairpins far away from the wall, where the effect of the mean shear reduces, need to have a sufficiently higher strength to autogenerate new hairpins. However, the presence of quasi-streamwise vortices on either side of the older primary hairpin seen in figure 10 of Zhou et al. (1999) suggests that autogeneration of new hairpins at a later stage may not be an entirely implausible scenario.

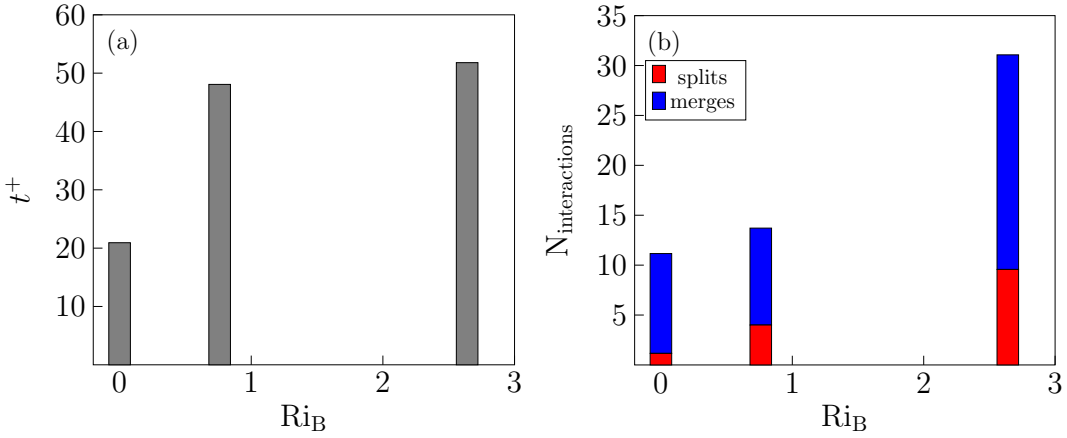

Figure 4.14: (a) Average lifetime of the primary branch tracked by the feature tracking procedure for all Ekman flow cases. (b) Average number of interactions experienced by the hairpin-like structures for all Ekman flow cases until $t^+ = 10$. Ri_B is the bulk Richardson number which quantifies the strength of stratification.

4.4 Summary and conclusions

The first part of the chapter builds upon the geometrical analysis of quantitative Robinson structures performed for an instantaneous snapshot of the Ekman flow in chapter 3 by comparing the temporal changes in their geometry. This is facilitated with the addition of a

region-based feature tracking scheme to the geometrical characterization framework as shown in figure 4.1. Since results from chapter 3 suggested that similar geometrical features could be observed for increasing stability, it was hypothesized that the spatio-temporal variability of global intermittency could have an impact on the temporal evolution of the geometry of Robinson structures.

First, a region-based tracking procedure in which correspondence is calculated by measuring the degree of spatial overlap of structures between consecutive time steps is discussed in section 4.1. A differentiating feature of this tracking procedure compared to other overlap approaches (Silver and Wang, 1996; Lozano-Durán and Jiménez, 2014) is the use of NS+MC algorithm to extract visualization accurate structures from scalar fields as shown in section 2.2. Next, structures having similar geometry, i.e., similar values of $\hat{S}, \hat{C}, \lambda$ are selected from the instantaneous Ekman flow fields analysed in chapter 3 as those that fall within a small ball of radius 0.05 centered at the centroid of the cluster of all points as exemplified in figure 4.5. To get a precise sense of the temporal changes in the geometry, only the primary branch is tracked and split and merge events are ignored. Additionally, it was seen that merges with much larger structures could significantly alter the geometry of the structure (for instance, see figure 4.6) and hence, when such interactions are encountered, the tracking is terminated.

Akin to the observations in chapter 3, results in figure 4.7 show a lack of blob-like geometry and suggest that most structures are moderately stretched tube-like and moderately to strongly stretched sheet-like structures. Apart from the minor trend seen for shear layer structures in figure 4.7(f) where structures become more flattened (or pancake-like) with increasing stability, no further distinction can be made for other Robinson structures. Although this hints that the spatio-temporal variability of global intermittency may not have a significant impact on the geometry of Robinson structures, this result should not be seen as conclusive due to the following reasons: (i) the tracking was performed with a constant threshold in time which does not adapt to the dynamical changes in the structure, (ii) the tracking procedure also involves the use of another subjective threshold $\tau_{overlap}$ to determine correspondence, (iii) in some cases (for instance, high-speed streaks of case S_1) too few structures were identified and tracked with a ball of radius 0.05. While the first and third issue can be fixed by repeating the geometrical analysis with multilevel percolation thresholding in time (MLPT) and increasing the radius of the ball respectively, MLPT still involves using the subjective $\tau_{overlap}$. Therefore, as pointed out by Jiménez (2018), one needs to complement the conclusions derived from threshold-based analysis with other statistical methods as conducted in chapter 3. Future research work can be directed towards improving the analysis presented in this chapter by using MLPT combined with image registration to effectively remove the requirement for structure overlap (see Badel (2021) and Lindheim et al. (2021) where this was achieved with constant thresholding in time). Other tracking approaches where global spatial and physical attributes are used to determine correspondance can also be considered (Ji and Shen, 2006; Bußmann et al., 2022).

The second part of the chapter is concerned with the dynamics of hairpin-like structures. Visualization of Q-criterion structures in figure 3.14 clearly show a marked increase in the number of hairpin-like structures with increasing stability. To investigate this, manually probed hairpin structures from subsection 3.1.5 are tracked in time along with their interactions (which

include only simple branching events) with the novel MLPT technique. This method relies on percolation analysis to find simple structures in time by dynamically altering the thresholds. A comparison of tracking a hairpin-like structure with constant and MLPT thresholding as shown in subsection 4.3.2 reveals that the latter technique is capable of capturing the growth phase of the hairpin structure which known to occur as a result of the shear induced stretching by the mean background flow (Zhou et al., 1999). Results of the average lifetime of the primary branch and the number of interactions as a function of the bulk Richardson number shown in figure 4.14 suggest that hairpin-like structures from both stably stratified cases have a much longer lifetime and experience relatively higher interactions than the neutrally stratified case. Although a link between the number of split events and the autogeneration mechanism is suggested, in that higher number of splits as seen in the strongly stratified case S_1 may lead to a higher autogeneration rate which can explain the abundance of hairpin-like structures, it is still unclear if older hairpins are capable of continuously autogenerating new vortices as they are advected downstream and away from the wall. It should also be noted that the cause of the high number of merges for the case S_1 is not known and needs further investigation.

5

A thin filament approach for the dynamics of hairpin structures

A major goal of this thesis is to understand the changes in geometry and dynamics of coherent structures in response to changes in stratification of the atmospheric boundary layer (ABL). Among all the examined Robinson structures, hairpin-like vortex structures, in particular, appear to exhibit interesting characteristics in the stably stratified contexts of the ABL. In chapter 3, it was seen that at an instantaneous time step, an abundance of these structures (identified with the $Q-$criterion indicator) with tube-like geometry can be observed in the turbulent/active patches of the strongly stratified case S_1. The head region of these structures also appear to have similar spanwise orientation (cf. figure 3.14(a)). In the previous chapter, these structures were temporally tracked with a feature tracking method capable of automatically identifying optimum overlap thresholds in time. The results show that these structures have clearly defined growth and deterioration phases and also undergo numerous interactions (split or merge events) during their lifetime. A link between the number of split events and the hairpin autogeneration mechanism is proposed and the relatively high number of split events seen in the strongly stratified case S_1 leading to a higher autogeneration rate could possibly explain their abundance in this regime. However, the similar orientation of these structures remains unexplained. Furthermore, the feature tracking method prevents us from gaining a complete view of the dynamics due to the following issues,

(1) When structures interact during a split or merge event, there is an inherent ambiguity in following the "correct" structure. This ambiguity is exacerbated when the structure being tracked undergoes further interactions during its lifetime.

(2) Although optimum overlap thresholds are identified with multilevel percolation analysis at every instantaneous time step, thresholding often results in some useful features being lost and the "full" structure is not represented. An example is shown in figure 5.13.

(3) The hairpin-like structures were identified and tracked only from later stages in their lifetime and so, their evolution from the point of origin remains unclear.

Therefore, in this chapter, a somewhat fundamental approach is sought, in which hairpin-like structures are treated as slender vortex filaments (see section 5.1 for a description). This is motivated through previous studies for which the motion of hairpin filaments have been examined under the influence of shear. For instance, Moin et al. (1986) initialized isolated hairpins as parabolic filaments and showed that the tip region of the filament, which has no initial inclination, tends to lift-up due to self-induction. They also note that the nodes in

the tip region are stretched rapidly apart in the wall-normal direction under the influence of uniform shear. Similar results were also reported by Hon and Walker (1991) who subjected a hairpin filament to a strong shear flow. They used a different initial configuration in which the parabolic filament was extended with a straight portion on either side as shown in figure 5.3. In addition to the lift-up due to self-induction, their results also showed the formation of hairpin "legs" moving towards the wall and the development of secondary/tertiary hairpins on both sides of the original disturbance. They note that the development of additional hairpins are regenerative which is similar to the autogeneration mechanism proposed by Zhou et al. (1996) who studied the motion of an isolated hairpin vortex in the DNS of a channel flow in which the initial structure was obtained through a linear stochastic estimation procedure. In later work, Zhou et al. (1999) also reported lift-up of the tip region due to self-induction and the subsequent stretching due to mean shear for the isolated hairpin vortex. This suggests the suitability of the filament approach to study the dynamics of hairpin structures in shear-dominated flows. An attempt is made to explain the similar orientation of hairpin-like structures in the strongly stratified case S_1 by comparing the temporal evolution of hairpin filaments under neutral and stably stratified background flow conditions. Specifically, the following questions are addressed,

(1) How do the changes in stratification of the background flow impact the dynamical characteristics (such as inclination angle, orientation, streamwise and spanwise stretching) of the hairpin structure? By studying changes in these dynamical characteristics, can one explain the similar orientation of the hairpin-like structures in the strongly stratified case S_1?

(2) Does the initial wall-normal location also play a role? How do the dynamical characteristics change with respect to stratification when the hairpin is initialized in the buffer or outer layer of the flow?

(3) Although some issues with the feature tracking method have been pointed out, qualitatively, how much would the results differ from those obtained through simulation with the filament approach?

Details for the extraction of the Ekman background flow profiles are given in subsection 5.4.1. An additional source of motivation for the filament approach is that it may lead to the development of novel subgrid scale models (SGS)[1] for large-eddy simulation of the stably stratified ABL. For instance, Misra (1997) proposed a class of structure-based subgrid models with the assumption that the subgrid structure of turbulence consists of a superposition of stretched vortices whose orientation is governed by the resolved velocity field.

The review paper of Leonard (1985) identifies two methods to calculate the motion of vortex filaments which are the thin-filament (TFA) and the local induction approximation (LIA). TFA is based on the notion that in some applications, for instance, trailing vortices of an aircraft, vorticity is assumed to be concentrated along a "filament centerline" $\mathcal{L}(t) : s \rightarrow \mathbf{X}(s,t)$. The averaged diameter d of the vortex core is assumed to be very small compared to the

[1] In large-eddy simulation, the detailed time and space dependence of fluid motions are resolved for scales larger than a prescribed cutoff. The effects of the eliminated scales, called the subfilter or subgrid scales are modeled.

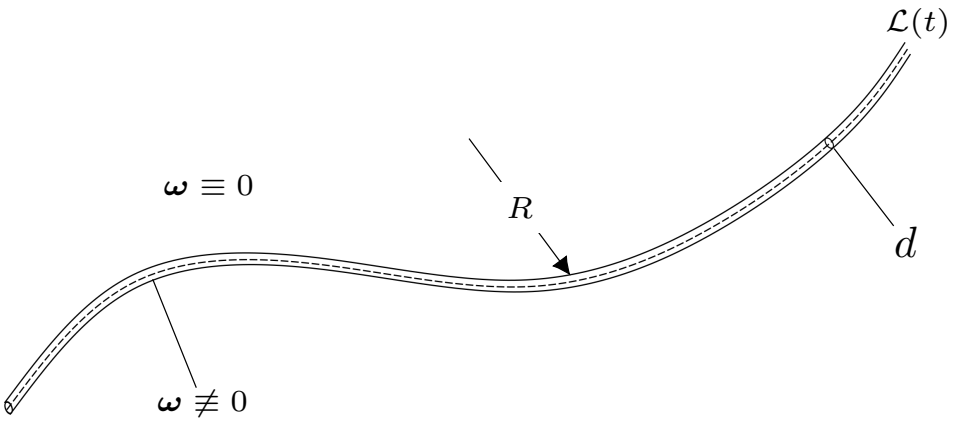

Figure 5.1: A portion of a slender vortex filament is shown. Vorticity ($\boldsymbol{\omega}$) is concentrated in a thin tube having a diameter d and a characteristic radius of curvature R. $\mathcal{L}(t)$ is a smooth time-dependent curve. Sketch adapted from Klein and Knio (1995).

characteristic radius of curvature R of $\mathcal{L}(t)$. An illustration is sketched in figure 5.1. Further details regarding TFA and its numerical implementation with the corrected thin-tube model of Klein and Knio (1995) are discussed in sections 5.1.1 and 5.2.2. LIA, on the other hand, is a simplification of TFA in which all non-local effects of vortex self-induction are neglected and the motion of the filament is due to its curvature alone (Hama, 1962). A brief overview of this method is discussed in subsection 5.2.1 and the impact on the temporal evolution of hairpin filaments due to omission of these non-local effects is exemplified in subsection 5.3.2. In this thesis, LIA is included only for validation purposes while the corrected thin-tube model of Klein and Knio (1995) is used to study the motion of hairpin filaments with the Ekman background flow. Results of this simulation and its subsequent comparison to the feature tracking approach are presented in sections 5.4 and 5.5.

5.1 Slender vortex filaments

The notions of vortex lines, tubes and filaments are introduced in this section. First, let us consider the motion of an incompressible, inviscid flow which is given by the Euler equations,

$$\nabla.\mathbf{u} = 0 \tag{5.1}$$

$$\frac{D\mathbf{u}}{Dt} = \mathbf{g} - \frac{1}{\rho}\nabla p \tag{5.2}$$

where $\mathbf{u} = (u, v, w)$ is the velocity along streamwise (x), wall-normal (y) and spanwise (z) directions respectively, t is time, p is the pressure force, $\mathbf{g}$ is the body force (gravity), ρ is the density, $\nabla = \partial/\partial x, \partial/\partial y, \partial/\partial z$ and $D/Dt = \partial/\partial t + \mathbf{u}.\nabla$ is the material derivative. In the absence of body forces, with unit density and vorticity defined as the curl of the velocity field,

$$\boldsymbol{\omega} = \nabla \times \mathbf{u} \tag{5.3}$$

taking the curl on both sides of (5.2) gives the vorticity transport equation,

$$\frac{D\boldsymbol{\omega}}{Dt} = \boldsymbol{\omega}.\nabla\mathbf{u} \tag{5.4}$$

This equation indicates that vorticity tends to move along particle trajectories while being rotated and stretched by $\nabla\mathbf{u}$. A line which is tangent everywhere to the local vorticity vector is called a *vortex line*. A surface formed by a family of vortex lines passing through a smooth closed curve C is known as a *vortex tube* (Batchelor, 1967). An illustration is shown in figure 5.2. The circulation Γ along the closed curve C is given by,

$$\Gamma = \int_C \mathbf{u}(x,t).d\mathbf{l} \tag{5.5}$$

Around any closed curve, Γ is known to be invariant in time for an inviscid fluid, i.e., $\frac{dC(t)}{dt} = 0$. This is *Kelvin's circulation theorem*. The value of Γ denotes the strength of the vortex tube. If S is the area spanning the closed curve C, applying Stoke's theorem gives,

$$\Gamma = \int_S \boldsymbol{\omega}.ds \tag{5.6}$$

Therefore, circulation around a closed curve is equal to the integral of vorticity over a surface S bounded by the curve. Equivalently, it is also the strength of the vortex tube formed by the family of vortex lines passing through the curve. A vortex tube of small and finite cross section surrounded by irrotational fluid ($\boldsymbol{\omega} = 0$) is called a *vortex filament*. A cross section of this filament constitutes its *core*. Vortex rings, which are often studied, are a special case of vortex filaments having a circular shape of their centerline (Zhou, 1996). Betchov (1965) notes that the same velocity induced at a point on a circular filament can also be obtained for a non-circular filament as long as it is assumed to be *thin* or *slender*, i.e., the typical diameter d of the vortex core is very small compared to its characteristic radius of curvature R such that the dimensionless core size parameter δ satisfies,

$$\delta = \frac{d}{R} \ll 1 \tag{5.7}$$

In an unbounded domain, the velocity induced by this filament at a point $\mathbf{P}$ outside the vortex core and time t is given by the *line-Biot-Savart law* (Callegari and Ting, 1978) as,

$$\mathbf{Q}_1(\mathbf{P},t) = -\frac{\Gamma}{4\pi}\int_{\mathcal{L}} \frac{(\mathbf{P} - \mathbf{X}(s',t)) \times \mathbf{ds}'}{|\mathbf{P} - \mathbf{X}(s',t)|^3}\,, \tag{5.8}$$

where Γ is the circulation or strength, s is the arc length along the line and $\mathcal{L}(t)$ is the "centerline" of the filament along which the vorticity distribution is highly concentrated. Apart from their application to studying the motion of hairpin filaments in shear-dominated flows, slender vortices have many important applications, for instance, predicting the behavior of trailing or tip vortices emanated behind aircraft wings (Crow, 1970; Widnall, 1975) and for theoretical modelling of vortex reconnection (Yao and Hussain, 2022).

5.1.1 Thin filament approximations

Leonard (1985) notes that the structure of the vortex core needs to be taken into account to compute the motion of vortex filaments. This is because as the point $\mathbf{P}$ moves towards the

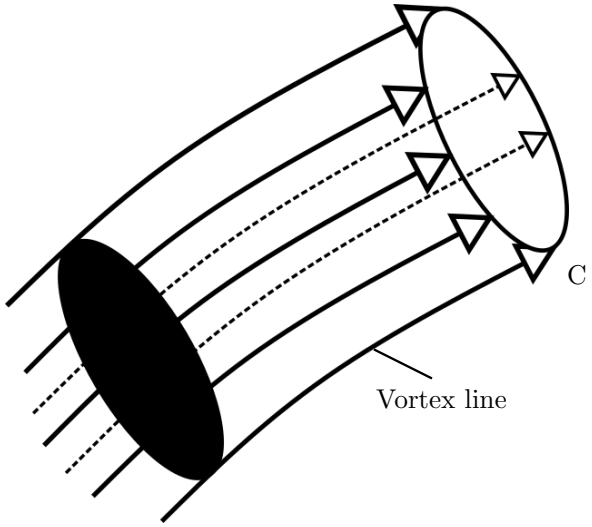

Figure 5.2: Illustration of vortex lines and vortex tube. Figure adapted from Zhou (1996).

centerline, $\mathbf{Q}_1(\mathbf{P}, t)$ becomes singular. This means that the line Biot-Savart law (5.8) alone cannot predict the self-induced motion of the filament. Early *ad hoc* desingularization methods were proposed by Rosenhead (1930) and Moore (1972). In these methods, a small parameter (called the "cut-off" parameter) is introduced in the denominator of the Biot-Savart integral. A particular choice of the cut-off depends on the radius of the filament and the radial distribution of vorticity and axial flow (Moore, 1972). Later, with the method of matched asymptotic expansion, Callegari and Ting (1978) showed how the singularity is naturally regularized within the framework of Navier-Stokes equations and derived an equation of motion for the filament centerline which includes precise mathematical expressions for the non-local induction terms. For a non-closed, infinite filament, the equation of motion is written as,

$$\frac{\partial}{\partial t}\mathbf{X}(s,t) = \frac{\Gamma}{4\pi}\kappa\mathbf{b}(s,t)\left(\ln\left(\frac{2}{\delta}\right) + C(t)\right) + \mathbf{Q}_0(s,t)\,, \tag{5.9}$$

where

$$\mathbf{Q}_0(s,t) = \mathbf{Q}_\mathrm{f}(s,t) + \mathbf{Q}_2(\mathbf{X}(s,t)) \tag{5.10}$$

and $C(t)$ represents the local effects from the core vorticity distribution. $\mathbf{Q}_0(s,t)$ is a superposition of the non-singular remainder of the line-Biot-Savart integral $\mathbf{Q}_\mathrm{f}(s,t)$ and the superimposed background flow $\mathbf{Q}_2(\mathbf{X}(s,t))$ (which, e.g., can be a simple shear or in our case an Ekman background flow). In the Local Induction Approximation (Hama, 1962), both $\mathbf{Q}_0(s,t)$ and $C(t)$ are neglected and the filament motion is due to the curvature $\kappa\mathbf{b}(s,t)$ term alone.

Lagrangian vortex element schemes such as the thin tube model (ttm) of Knio and Ghoniem (1990), in which the filament centerline is discretized with a finite chain of regularized vortex elements with spherical overlapping cores, have also been proposed. This method starts with the discretization of the initial vorticity field into a finite number of N vortex elements with vorticity $\boldsymbol{\omega}_i$. The initial vorticity is segregated into volume elements $dV_i, i = 1, 2, ..N$ and the resulting vorticity is written as (Knio and Ghoniem, 1990),

$$\boldsymbol{\omega}(\mathbf{x},0) = \sum_{i=1}^{N} \boldsymbol{\omega}_i(0) dV_i f_\delta(\mathbf{x} - \boldsymbol{X}_i) \tag{5.11}$$

where $\boldsymbol{X}_i$ is the center of the volume element dV_i which has a vorticity $\boldsymbol{\omega}_i$ and f_δ is a spherical core smoothing function with a core radius δ which smoothes the vorticity in the neighborhood of $\boldsymbol{X}_i$. This core smoothing function f_δ needs to be chosen such that it satisfies the following conditions (for a description on the construction of these functions, see Beale and Majda (1985)),

- $\int f_\delta(\mathbf{x})dx = 1$ and f_δ converges to a Dirac delta function as $\delta \to 0$.
- f_δ is smooth and rapidly decreasing.
- The velocity field of a finite vortex filament is non-singular at its center.

The smoothing function f_δ obeys the following relationship,

$$f_\delta(\mathbf{x}) = \frac{1}{\delta} f\left(\frac{|\mathbf{x}|}{\delta}\right) \tag{5.12}$$

where $f > 0$ for $|\mathbf{x}| < \delta$ and vanishes rapidly for $|\mathbf{x}| > \delta$. In this method, it should be noted that the numerical core size δ is implicitly assumed to be the physical core size. With the Callegari and Ting framework, Klein and Knio (1995) point out that this assumption leads to $\mathcal{O}(1)$ velocity prediction errors due to differences in the numerical and phyiscal core coefficients. This led to a correction of the thin-tube model, hereby referred to as the corrected thin-tube model, and three correction strategies were proposed. The third correction method, which involves an asymptotically motivated rescaling of the numerical core radius, is deemed to be simple to implement (as higher-order arclength derivatives need not be computed) and is used in this thesis. The complete numerical scheme is described in subsection 5.2.2.

5.2 Numerical schemes

Before the numerical methods for solving the local induction approximation and the corrected thin-tube model are presented, the initial hairpin configuration is first discussed. Following the work of Hon and Walker (1991), the hairpin filament is initialized as a small, symmetrical, three-dimensional perturbation of the form,

$$\mathbf{X}(s,t) = A\left[(\cos\theta_i)\hat{\mathbf{i}} + (\sin\theta_i)\hat{\mathbf{j}}\right] e^{-\beta s^2} + \hat{\mathbf{j}} + s\hat{\mathbf{k}} \tag{5.13}$$

where $(\hat{\mathbf{i}}, \hat{\mathbf{j}}, \hat{\mathbf{k}})$ are unit vectors in the streamwise, wall-normal and spanwise directions respectively. Also, A is the amplitude, θ_i is the angle between the plane of the perturbation and the wall and β is a large value which controls the initial width of the perturbation. The hairpin filament is initialized at a distance y_{initial} away from the wall as sketched in figure 5.3.

5.2.1 Local Induction Approximation

Since LIA has been discussed extensively in previous works (Arms and Hama, 1965; Zhou, 1996; Margerit et al., 2004; Batchelor, 1967), only a brief overview of the method is presented

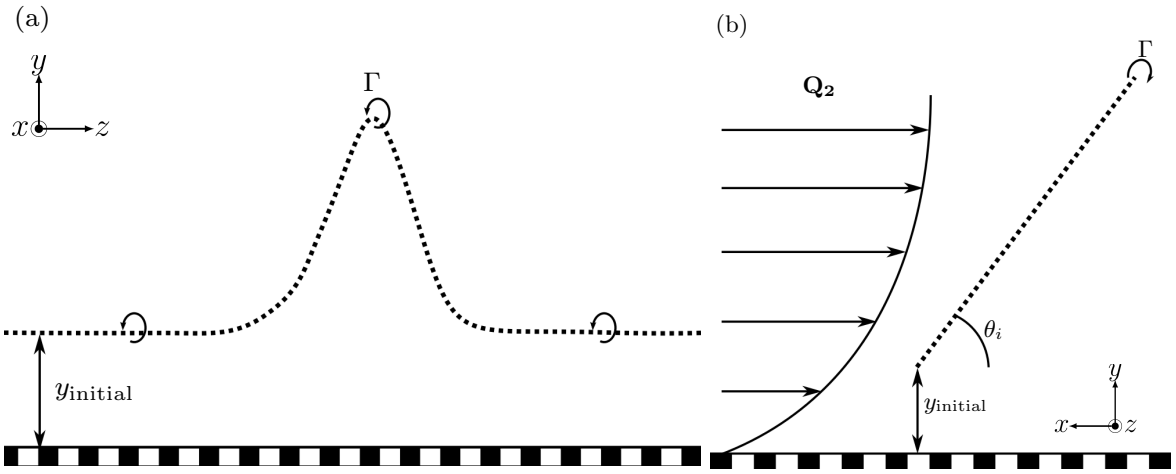

Figure 5.3: A hairpin filament when viewed from (a) front and (b) side. Here, $\mathbf{Q}_2$ is a background shear flow acting on the filament, y_{initial} is the initial distance from the wall, θ_i is the angle the filament makes with the wall and Γ is the circulation.

here. As stated in subsection 5.1.1, LIA neglects the long-distance induction effects, $\mathbf{Q}_0(s,t)$, and the local effects from the core vorticity distribution, $C(t)$. This leads to a simplified equation of motion which is written as,

$$\frac{\partial}{\partial t}\mathbf{X}(s,t) = \frac{\Gamma}{4\pi}\kappa\mathbf{b}(s,t)\ln\left(\frac{2}{\delta}\right) \tag{5.14}$$

where $\kappa\mathbf{b}(s,t)$ is the curvature in the binormal direction. Klein and Majda (1991a) and Klein and Majda (1991b) note that this binormal term alone cannot account for self-stretching of vortex filaments which is due entirely to non-local induction. Therefore, LIA is used only for validation purposes in this thesis. In order to make the results of LIA comparable to the corrected thin-tube model presented in the following subsection, Margerit et al. (2004) suggest using the Callegari and Ting equation (Callegari and Ting, 1978) without the non-local self-induction term $\mathbf{Q}_0(s,t)$. For a non-closed, infinite filament, the equation of motion is as follows,

$$\frac{\partial}{\partial t}\mathbf{X}(s,t) = \frac{\Gamma}{4\pi}\kappa\mathbf{b}(s,t)\left[\ln\left(\frac{2}{\delta}\right) + C(t)\right] \tag{5.15}$$

where $C(t)$ is the core structure coefficient. It is natural to see this local term as an $\mathcal{O}(1)$ correction to the local induction contribution of the self induced velocity and to call it the local induction approximation (or contribution) at $\mathcal{O}(1)$.

5.2.2 Corrected thin-tube model

In this model, a slender vortex is represented as a finite chain of vortex elements which overlap one another by satisfying the following overlap condition,

$$\underset{i=1..N}{max}|\delta\boldsymbol{\chi}_i| < \delta \tag{5.16}$$

where $\{\boldsymbol{\chi}_i\}_{i=1}^{N}$ are N vortex elements or nodes and δ is the core size of the filament. This condition implies that the maximum distance between neighboring nodes in the filament is smaller than its core size. Knio and Ghoniem (1990) reported good accuracy of computational

results when this condition was enforced. Each vortex element has a constant, time-independent circulation Γ and the total vorticity on the filament is given by,

$$\boldsymbol{\omega}(\boldsymbol{x},t) = \sum_{i=1}^{N} \Gamma \delta\boldsymbol{\chi}_i(t) f_\delta(\boldsymbol{x} - \boldsymbol{\chi}_i^c(t)) \tag{5.17}$$

where $\boldsymbol{\chi}_i^c(t)$ and $\delta\boldsymbol{\chi}_i(t)$ are Lagrangian variables denoting the centers and the secant vectors that approximate the filament centerline and are positively aligned with the vorticity. They are computed as follows,

$$\delta\boldsymbol{\chi}_i(t) = \boldsymbol{\chi}_{i+1}(t) - \boldsymbol{\chi}_i(t)\,, \quad \boldsymbol{\chi}_i^c(t) = \frac{\boldsymbol{\chi}_{i+1}(t) + \boldsymbol{\chi}_i(t)}{2}\,. \tag{5.18}$$

In (5.17), the smoothing function f_δ is related to a rapidly decaying numerical core vorticity distribution and is given by,

$$f_\delta = \frac{1}{\delta^3} f\left(\frac{|\boldsymbol{x}|}{\delta}\right) \tag{5.19}$$

The velocity field is constructed by inserting (5.17) in the three-dimensional Biot-Savart integral,

$$\boldsymbol{v}(\boldsymbol{x},t) = -\frac{1}{4\pi} \iiint \frac{\boldsymbol{x} - \boldsymbol{x'}}{|\boldsymbol{x} - \boldsymbol{x'}|^3} \times \omega(\boldsymbol{x'}) d\boldsymbol{x'} \tag{5.20}$$

where $d\boldsymbol{x'} = dx_1' dx_2' dx_3'$ is a volume element. The result reads,

$$\boldsymbol{v}^{\mathrm{ttm}}(\boldsymbol{x},t) = -\frac{\Gamma}{4\pi} \sum_{i=i}^{N} \frac{(\boldsymbol{x} - \boldsymbol{\chi}_i^c(t)) \times \delta\boldsymbol{\chi}_i(t)}{|\boldsymbol{x} - \boldsymbol{\chi}_i^c(t)|^3} \kappa_\delta(\boldsymbol{x} - \boldsymbol{\chi}_i^c(t)) \tag{5.21}$$

where $\kappa_\delta \equiv \kappa(|\boldsymbol{x}|/\delta)$ is the velocity smoothing function which is directly related to the numerical core vorticity distribution f from (5.19). Equation 5.21 is the *standard thin-tube model (ttm)* of Chorin (1980), Knio and Ghoniem (1990), and Knio and Ghoniem (1991). It was noted by Klein and Knio (1995) that the standard ttm does not make a distinction between the numerical core size parameter δ^{ttm} and the physical core size δ and therefore, results in $\mathcal{O}(1)$ errors. With an asymptotic analysis of the numerical vorticity structure, Klein and Knio, 1995 propose three correction strategies to overcome this issue. Due to its simplicity and ease of implementation, the third correction method is employed. The involves a rescaling of the core radius as follows,

$$\delta^{\mathrm{ttm}} = \delta\, \exp\left(C^{\mathrm{ttm}} - C\right). \tag{5.22}$$

Here, C^{ttm} is the numerical core constant. If the velocity core smoothing function is chosen as $\kappa(r) = \tanh(r^3)$, then $C^{\mathrm{ttm}} = -0.4202$ as obtained by Knio and Klein (2000). According to asymptotic theory, the core structure coefficient C includes contributions from the local swirling and axial velocities, denoted by C_v and C_w respectively,

$$C = -1 + C_v + C_w \tag{5.23}$$

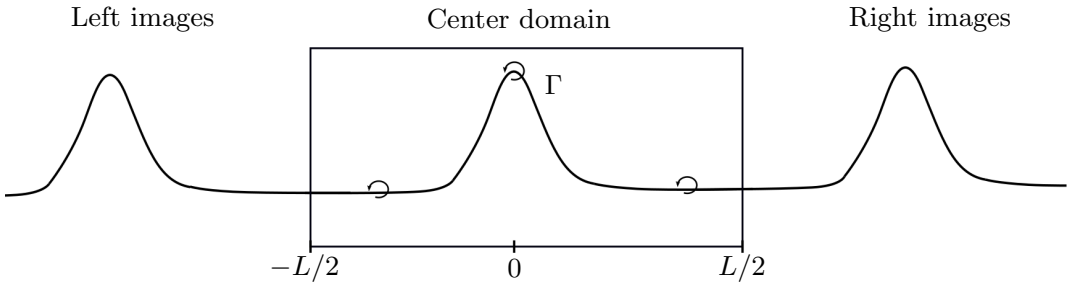

Figure 5.4: Illustration of the boundary conditions. A long filament is envisioned, periodic in the axial direction. The domain of integration, of length L, contains one complete period.

Depending on the presence/absence of viscous effects and the initial leading-order velocity profile in the core, different expressions of the core structure coefficients can be obtained. Following Ting and Klein (1991) for the case of a similar vortex core with the same initial core size and circulation without axial flow, C_v and C_w are given by,

$$C_v = \frac{1 + \gamma_E - \ln(2)}{2} - \ln(\overline{\delta}) \tag{5.24}$$

$$C_w = -2\left[\frac{m(0)}{\Gamma\overline{\delta}}\right]^2\left[\frac{S_0}{S(t)}\right]^4 \tag{5.25}$$

where S_0 is the initial length of the filament, $\overline{\delta}$ is the stretched radius whose exact formula is given in Ting and Klein (1991), $m(0)$ is the initial axial flux of the vortex and $\gamma_E = 0.577$ is Euler's constant. In our case, $m(0) = 0$ implying no contribution from axial velocity.

Remark: Equation (5.23) is usually written as $C = C_v + C_w$ (for instance, see (2) of Knio and Klein (2000)). The inclusion of -1 accounts for the difference in the definition of C_v (compare equations (2.3.73e) of Ting and Klein (1991) and (3) of Knio and Klein (2000)).

5.2.2.1 Periodic boundary conditions

For hairpin filaments which are periodic in the spanwise direction and embedded in an unbounded domain in the other two directions, the total velocity $\boldsymbol{v}^{\text{ttm}}$ requires contributions from an infinite number of images in addition to the elements within the computational domain (Knio and Ghoniem, 1991). Therefore, (5.21) is written as,

$$\boldsymbol{v}^{\text{ttm}}(\boldsymbol{x}, t) = -\frac{\Gamma}{4\pi}\sum_{k=\pm 1}^{\pm\infty}\sum_{i=i}^{N}\frac{(\boldsymbol{x} - \boldsymbol{\chi}_i^c(t)) \times \delta\boldsymbol{\chi}_i(t)}{|\boldsymbol{x} - \boldsymbol{\chi}_i^c(t)|^3}\kappa_\delta(\boldsymbol{x} - \boldsymbol{\chi}_i^c(t)) \tag{5.26}$$

Since it is not practical to evaluate an infinite number of images, the above sum is decomposed into two components,

$$\boldsymbol{v}^{\text{ttm}}(\boldsymbol{x}) = \sum_{i=1}^{N}(\boldsymbol{v}_{\text{center}}(\boldsymbol{x}) + \boldsymbol{v}_{\text{image}}(\boldsymbol{x})) \tag{5.27}$$

where $\boldsymbol{v}_{\text{center}}$ is the contribution from the central part of the domain and $\boldsymbol{v}_{\text{image}}$ is the contribution from the image system. They are computed as,

$$\boldsymbol{v}_{\text{center}}(\boldsymbol{x}) = -\frac{\Gamma}{4\pi}\sum_{i=i}^{N}\frac{(\boldsymbol{x}-\boldsymbol{\chi}_i^c(t))\times\delta\boldsymbol{\chi}_i(t)}{|\boldsymbol{x}-\boldsymbol{\chi}_i^c(t)|^3}\kappa_\delta(\boldsymbol{x}-\boldsymbol{\chi}_i^c(t)) \tag{5.28}$$

$$\boldsymbol{v}_{\text{image}}(\boldsymbol{x}) = -\frac{\Gamma}{4\pi}\sum_{k=\pm1}^{\pm P}\sum_{i=i}^{N}\frac{(\boldsymbol{x}-\boldsymbol{\chi}_i^c(t))\times\delta\boldsymbol{\chi}_i(t)}{|\boldsymbol{x}-\boldsymbol{\chi}_i^c(t)|^3} \tag{5.29}$$

For the image system, it should be noted that the effect of the velocity smoothing function is neglected as it is assumed that $L \gg \delta$. Also, $\pm P$ is the number of images chosen on either side of the domain. In all simulations presented in the thesis, $P = 8$. This choice is explained in subsection 5.3.1.1.

5.2.2.2 Optimization

In order to ensure that the numerical core structure is well defined, the overlap condition must be met. This implies that for thin cores, i.e., when the core size parameter δ is small, a large number of nodes are necessary. Motivated by the observation that the number of nodes necessary for an adequate representation of the centerline is always lower than the number of nodes necessary for overlap, Knio and Klein (2000) proposed three optimization strategies for the corrected thin-tube model. The first method, henceforth denoted $M1$, is chosen as it avoids computation of filament curvature κ and requires little modification of the code. This method uses a Richardson-type extrapolation procedure of the core size parameter as follows,

$$\boldsymbol{v}_{\text{corr}}^{\text{ttm}} = \boldsymbol{v_1} + (\boldsymbol{v_1}-\boldsymbol{v_2})\frac{\ln(\sigma_1/\delta^{\text{ttm}})}{\ln\,\phi} \tag{5.30}$$

where $\boldsymbol{v_1}$ and $\boldsymbol{v_2}$ correspond to velocities due to two large core sizes σ_1 and σ_2. If $\sigma_0(t) = \underset{i=1..N}{max}|\delta\boldsymbol{\chi}_i|$ denotes the inter-element separation distance, then

$$\sigma_1 = K\,\sigma_0, \quad \sigma_2 = \phi\,\sigma_1\,. \tag{5.31}$$

and K and ϕ are constants which are chosen as 3 and 2 respectively. The choice of these parameters are described in subsection 5.3.1.1. It is easy to see that for any value of $K > 1$ and $\phi > 1$, both σ_1 and σ_2 will satisfy the overlap condition. Therefore, the corrected velocity at the centerline is obtained at the cost of two large core evaluations. The vortex elements are transported along Lagrangian trajectories with the following equation of motion,

$$\frac{d\boldsymbol{\chi}_i(t)}{dt} = \boldsymbol{v}_{\text{corr}}^{\text{ttm}}(\boldsymbol{\chi}_i(t),t) \tag{5.32}$$

A summary of the numerical scheme is presented as follows,

(1) First, the initial configuration of the hairpin is setup.

(2) For the chosen velocity core smoothing function $\kappa(r) = \tanh(r^3)$, C^{ttm} is set to -0.4202. The numerical core radius δ^{ttm} is computed from (5.22). With $\sigma_0(t) = \underset{i=1..N}{max}|\delta\boldsymbol{\chi}_i|$, (5.31) can be used to compute the two coarse radii.

(3) For both core radii, (5.21) is evaluated at each node location by applying the periodic boundary condition as illustrated in figure 5.4, i.e., the velocity at a node x inside

Parameter	Value
Core size, δ	0.01
Amplitude, $\widetilde{a}$	0.01
Circulation, Γ	4π
Expansion parameter, ϵ	0.5
Number of nodes, N	1024

Table 5.1: Parameters used for the static test comparisons.

the computational domain is evaluated by applying a translation along the periodicity direction such that x is at the center of the domain.

(4) The corrected velocity is obtained according to (5.30).

(5) Finally, the node positions are updated with the equation of motion (5.32) with a fifth order Adams-Bashforth scheme and Runge-Kutta-Fehlberg initialization (Butcher, 2016; Hairer et al., 1993).

5.3 Validation of the slender vortex filament code

For the two methods described in the previous section, a program is written in python and validation of this code is presented here. Initially, the static test of Klein and Knio (1995) on a sinusoidal plane curve is carried out to compare the binormal velocity prediction of LIA and M1 KK method at an instantaneous time step. This static test is chosen due to the obvious advantage that temporal discretization errors will not be reflected in the velocity predictions. Next, a hairpin filament is initialized and the temporal evolution of this filament in a stagnant background flow is also compared. These tests emphasize the differences between LIA and M1 KK methods where the former method does not include non-local effects of self-induction. Finally, the hairpin filament is advected in a shear background flow with the M1 KK method to (a) test the effect of the background flow on the motion of the filament, (b) test the motion of the filament with/without a wall boundary condition. These results are compared to the one obtained by Hon and Walker (1991) where the cut-off method of Moore (1972) was employed.

5.3.1 Sinusoidal plane curve test

Following Klein and Knio (1995), the sinusoidal plane curve geometry is given by the following equation,

$$\mathbf{X}(s) = s\mathbf{t} + \epsilon^2 \widetilde{a} \sin(2s/\epsilon)\mathbf{n} \tag{5.33}$$

where $\widetilde{a}$ is the amplitude of the curve and $\mathbf{t}, \mathbf{n}$ are mutually orthogonal unit vectors. This equation describes a filament in the $(\mathbf{t}, \mathbf{n})$ plane which will induce a velocity normal to this plane, i.e., in the binormal direction $\mathbf{b}$. The parameters used in this test are given in table 5.1. To satisfy the overlap condition given in 5.16, it can be seen that a minimum of 316 nodes are necessary. However, if the number of nodes are varied from 100 to 1000 and the maximum binormal velocity along the filament is recorded for each case with the M1 KK scheme, the

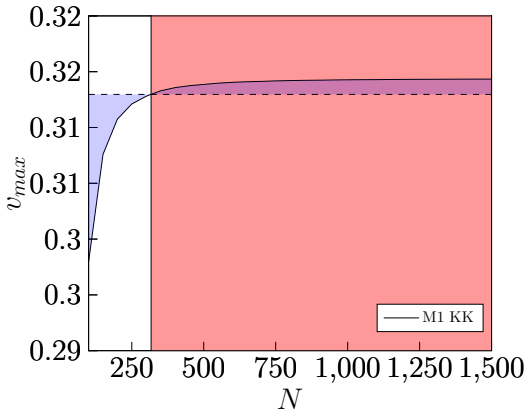

Figure 5.5: The solid line shows the maximum binormal velocity along the filament with the M1 KK method for the sinusoidal plane curve test with increasing node counts. The region shaded red region shows $N \geq 316$ which satisfy the overlap condition given in (5.16). The shaded blue region shows the difference between the maximum binormal velocity obtained at $N = 316$ and the maximum binormal velocity at other N.

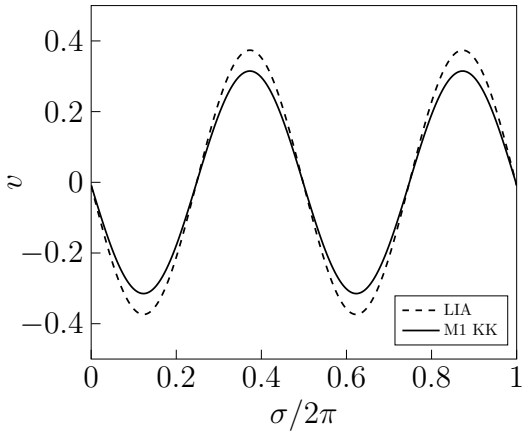

Figure 5.6: Velocity prediction in the binormal direction for LIA (dashed line) and the M1 KK method (solid line).

results as shown in figure 5.5 indicate a minor deviation of 0.42% between the maximum binormal velocity at $N = 316$ and $N = 1000$. Therefore, to eliminate numerical inaccuracies, 1024 nodes are chosen in this test. The filament velocity in the binormal direction is shown for both LIA and the M1 KK scheme in figure 5.6. By comparing LIA and the Klein-Majda asymptotic velocity predictions, Klein and Knio (1995) showed a deviation of $20 - 25\%$. The results shown in figure 5.6 show a deviation of 19% between the LIA and the M1 KK methods. Although this is slightly lower, the differences clearly show the overestimation of velocity by LIA where non-local effects are excluded.

5.3.1.1 Choice of parameters for the M1 KK method

For the M1 KK method, optimal values of two parameters related to the numerical core sizes (K and ϕ) and a third parameter (number of images P) to enforce the periodic boundary conditions need to be chosen. The optimum values are chosen by identifying the minimum value necessary for an accurate prediction of binormal velocity in the sinusoidal plane curve test.

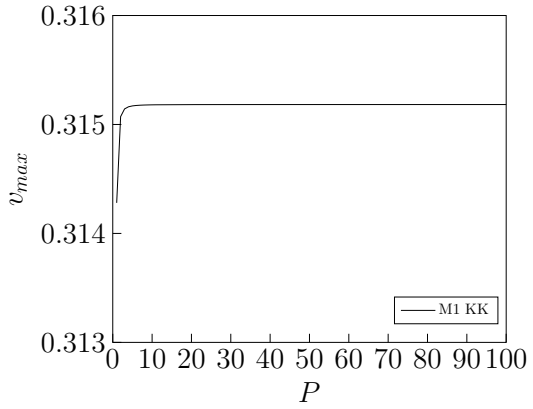

Figure 5.7: For the static test described in subsection 5.3.1, the number of images P are varied and the maximum binormal velocity is plotted.

With the parameters listed in table 5.1, the number of images are varied from $1-100$ and the maximum binormal velocity along the filament is recorded in each case. From figure 5.7, it can be seen that there is no deviation in the maximum binormal velocity after $P \geq 7$. This implies that the first few image pairs (one on each side of the domain) have a greater contribution to the self-induced velocity of the center domain than far away image pairs. Therefore, for all simulations presented in the thesis, 8 image pairs are chosen.

Apart from the number of images, the M1 technique also requires two parameters K and ϕ to be chosen. The former is a ratio of the separation distance between the nodes and the numerical core size and therefore can be seen as an "overlap" parameter (Knio and Klein, 2000). When $K > 1$, then the neighboring cores overlap each other. To examine the effect of K on the self-induced velocity of the filament, the second optimization technique of Knio and Klein (2000), hereafter referred as M2, is used. This method is preferred over M1 as it is independent of the parameter ϕ. The corrected velocity is obtained as follows,

$$\boldsymbol{v}_{\text{corr}}^{\text{ttm}} = \boldsymbol{v}_1 + \frac{\Gamma}{4\pi} \ln\left(\frac{\sigma_1}{\delta^{\text{ttm}}}\right)\kappa\mathbf{b} \tag{5.34}$$

where σ_1 is evaluated dynamically during simulation as shown in (5.31). Again the static test with the parameters in table 5.1 is repeated by varying K from $1-19$. The results from figure 5.8(a) show that for $K > 2$, the velocity predictions show only minor deviations, particularly for the case with 1024 nodes. Therefore, $K = 3$ is used for all further simulations.

Since K has been chosen, the M1 method can now be used to study the effect of ϕ on the self-induced velocity of the filament. With the same test, ϕ is varied from $1-19$ and the results are shown in figure 5.8(b). Similar to the results of K, minor deviations in the maximum binormal velocity can be seen for the case $N = 1024$ when $\phi > 1$. A conservative value of $\phi = 2$ is chosen.

5.3.2 Hairpin evolution in stagnant background flow

In this test, the hairpin filament evolves in the absence of a background flow, i.e., $\mathbf{Q}_2 = 0$ as shown in Hon and Walker (1991). Similar to the previous test, both LIA and the M1 KK methods are used to validate the dynamical aspects of the filament code. The parameters used for this test are listed in table 5.2. The hairpin filament is initially inclined at 45° with

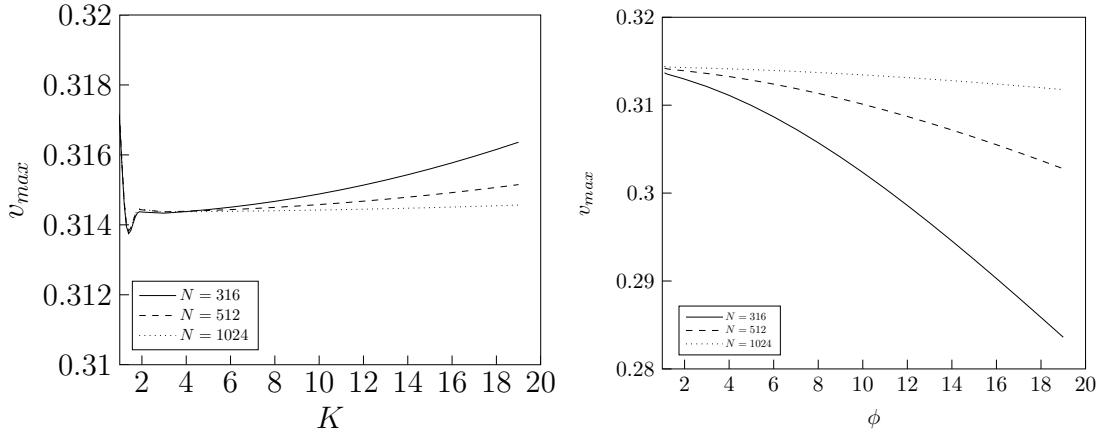

Figure 5.8: Similar to figure 5.7, the static test is repeated by varying the values of K (Left) and ϕ (Right) and the maximum binormal velocity is plotted. The solid, dashed and dotted lines show the differences with the number of nodes N.

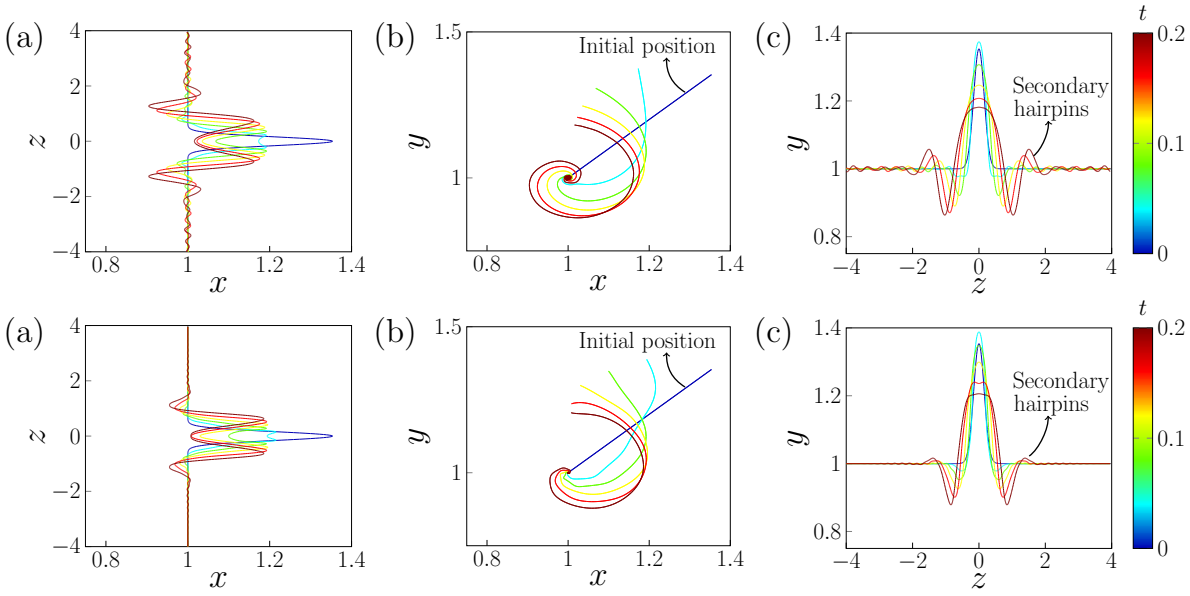

Figure 5.9: Temporal evolution of a hairpin vortex in a stagnant background flow. (a, b, c) are the top, side and front view of the hairpin respectively. The simulation performed with LIA and M1 KK schemes are shown in the top and bottom panels respectively.

Parameter	Value	Parameter	Value
Core size parameter, δ	0.02	Initial wall-normal position, y_{initial}	1
Circulation, Γ	1	Domain length, L	4
Spread parameter, β	20	Number of nodes, N	700
Amplitude, A	0.5	Time step (LIA), $\triangle t$	10^{-5}
Angle of inclination, θ_i	45°	Time step (M1 KK), $\triangle t$	10^{-3}
Initial streamwise position, x_{initial}	1		

Table 5.2: Parameters used for the stagnant flow test.

respect to the wall and a spatial discretization of 700 nodes are used for both methods. It should be noted that for all simulations performed in this thesis, an adequate number of nodes satisfying the overlap condition is used to ensure that further refinement does not alter the findings and conclusions. The results of the simulation are shown in figure 5.9.

To ensure a smooth evolution, a small time step $\triangle t = 10^{-5}$ is chosen for LIA and a much larger $\triangle t = 10^{-3}$ for the M1 KK method. Larger time steps are possible with the M1 KK scheme as it not only avoids computations with the local curvature term $\kappa\mathbf{b}$ for which higher order derivatives need to be computed, but also is much better conditioned owing to the Richardson-type extrapolation from the artificially enlarged to the actual core size in the correction scheme M1. It can be seen from both side view panels in figure 5.9(b) that the hairpin head (or tip region) bends backward and downward towards the wall as shown in Hon and Walker (1991). Similar results were also reported in Moin et al. (1986) who studied the evolution of an isolated parabolic vortex with a cut-off method. Formation of the "corkscrew" shape is also observed with both methods. The top panel in 5.9(a, c) shows that, for LIA, small "wiggles" develop and start moving towards the end of the domain. Therefore, the simulation is stopped at $t = 0.2$. Simulation with the M1 KK method is also stopped at the same time so that the results are comparable with LIA. In later stages, formation of secondary hairpins on either side of the initial perturbation and the development of hairpin "legs" in the curved regions close to the wall are also visible.

It is clear from the results presented in figure 5.9 that both LIA and M1 KK methods produce similar results to the cut-off method of Hon and Walker (1991). Now, the differences between LIA and M1 KK methods are compared by repeating the simulation with two values of the spread parameter $\beta = 15, 50$. It is important to note that larger values of the spread parameter constrict the width of the perturbation and vice versa. For the same amplitude and a shorter width, i.e., $\beta = 50$, a large number of nodes are necessary to obtain a stable evolution. In this case, 1300 nodes are used. For LIA, a smaller time step $\triangle t = 10^{-6}$ is also necessary. From the insets of figure 5.10(a, b, c, d), it can be seen that by changing the spread parameter from $\beta = 15$ to $\beta = 50$, LIA effectively maintains the corkscrew spiral and at $\beta = 50$ (smaller width), there appears to be further coiling around the origin of the filament. With the M1 KK method, this corkscrew pattern cannot be seen in both cases. Further magnification near the origin of the filament as shown in figure 5.10(e) reveals only slight coiling for the M1 KK case at $t = 0.1$ for larger β. However, continuing the simulation (not shown in the thesis) eventually reveals the corkscrew spiral for $\beta = 15$ as early as $t = 0.13$ while it is delayed further for $\beta = 50$ and is accompanied by further outwards stretching of the hairpin legs than in the former case. This suggests that as the spanwise width of the filament is decreased, the nonlocal effects become important which is ignored by LIA. This gives a direct comparison to the hairpin evolution under the absence of nonlocal effects with LIA where the legs of the filament do not "see" each other when they approach closely and when the nonlocal effects are correctly represented by the M1 KK method which results in self-stretching of the filament. Since the M1 KK method can capture the nonlocal effects accurately, further simulations are carried out only with this method.

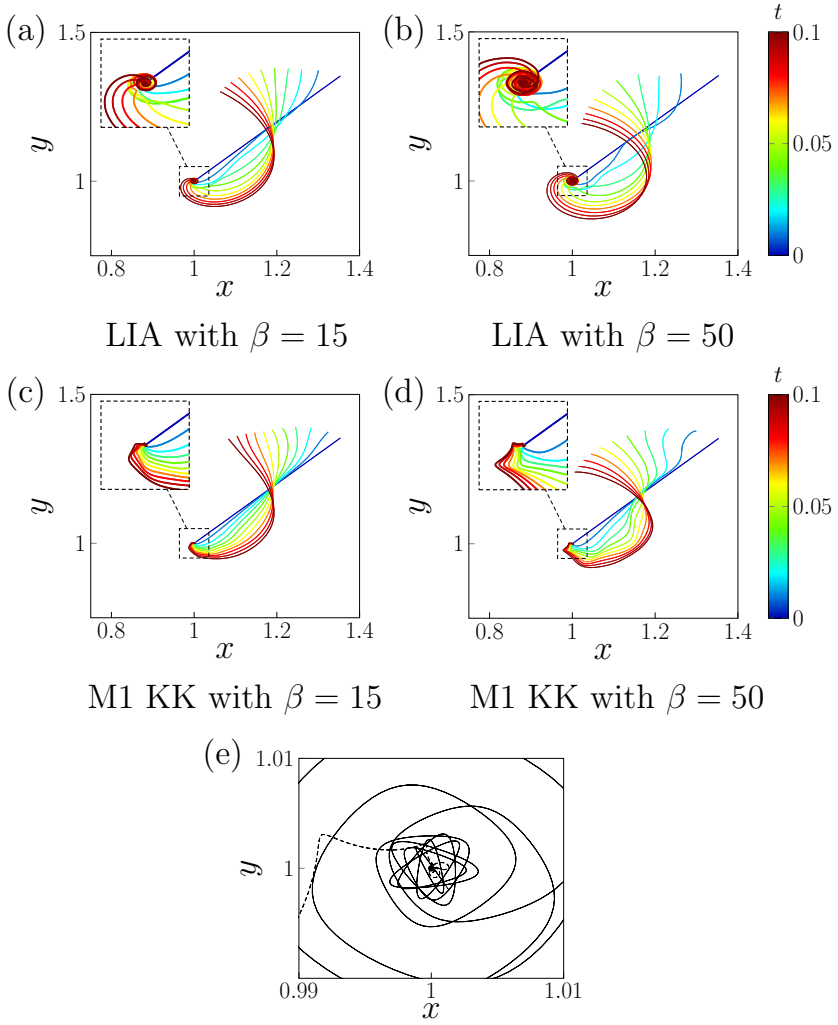

Figure 5.10: The test shown in figure 5.9 is repeated with $\beta = 15, 50$ for both schemes. (a, b) show the temporal evolution of the hairpin with LIA whereas (c, d) shows the temporal evolution with the M1 KK scheme. The insets in (a, b, c, d) show magnified portion of the filaments. Further magnified portion of the LIA (solid line) and the M1 KK (dashed line) cases with $\beta = 50$ at $t = 0.1$ is plotted in (e) with the scatter point indicating the origin of the filament.

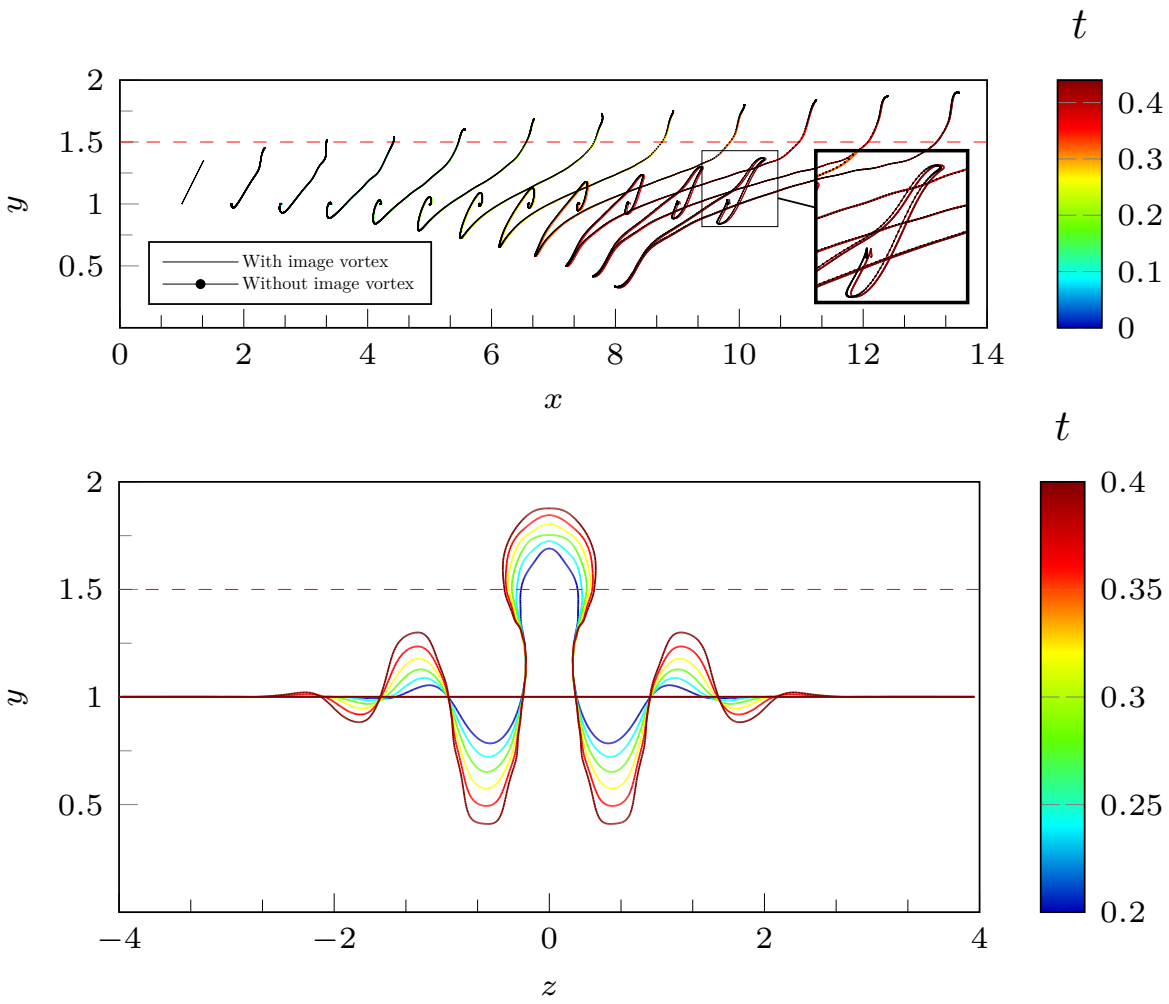

Figure 5.11: Temporal evolution of a hairpin vortex in a shear background flow. The top panel shows the side view until $t = 0.44$ and the solid line indicates that the wall boundary condition was enforced. The bottom panel shows the front view from $t = 0.2$ to $t = 0.4$. The red dashed line indicates y_s which is the top of the shear flow.

Parameter	Value	Parameter	Value
Core size parameter, δ	0.02	Initial wall-normal position, y_{initial}	1
Circulation, Γ	1	Domain length, L	4
Spread parameter, β	20	Number of nodes, N	1500
Amplitude, A	0.5	Time step, $\triangle t$	10^{-3}
Angle of inclination, θ_i	45°	Shear flow height, y_s	1.5
Initial streamwise position, x_{initial}	1	Velocity, V	30

Table 5.3: Parameters used for the shear flow test.

5.3.3 Hairpin evolution in shear flow

In this test, the hairpin is allowed to evolve in the presence of a simple shear background flow. The goal of this test is to validate the code against a background flow profile and also to account for the presence of a wall. Following Hon and Walker (1991), a simple shear flow is given by,

$$\mathbf{Q}_2 = \begin{cases} yV/y_s, & \text{if } y \leq y_s \\ V, & y > y_s \end{cases}$$

This describes a shear flow which is linear near the wall until y_s, after which the flow is uniform with a velocity V. The parameters used in this simulation are listed in table 5.3.

Aref and Flinchem (1984) noted that using a Blasius or boundary layer background flow will require the boundary condition of a rigid wall without which the filament approaching the wall closely will simply pass through it. Moin et al. (1986) showed that the effect of wall can be accounted with the help of an image vortex, i.e., by placing a vortex at an equal and opposite wall-normal distance as that of the one being simulated. They also note that the presence of the wall appears to enhance the streamwise advection of the filament and moves the legs of the of the filament close to each other. To incorporate an image vortex, an additional step is included in the calculation presented in subsection 5.2.2.

The results of the simulation are shown in figure 5.11. In agreement with the results shown in Hon and Walker (1991), the hairpin filament is convected downstream and stretches in the wall-normal direction due to the shear flow. Eventually, the tip region contacts the uniform flow region above y_s. The legs of the filament also progressively move downward towards the wall which presents an opportunity to compare the results with and without an image vortex. It should be noted that the image vortex is placed behind the wall at $y = -1$. It is apparent from figure 5.11(a) that the effect of the image vortex increases as the filament approaches the wall closely as demonstrated in Moin et al. (1986) with a parabolic vortex.

5.4 Hairpin evolution in ABL background flow

In this section, the M1 KK method is used to study the motion of hairpin filaments immersed in an atmospheric boundary layer background flow. Before the initial conditions and the

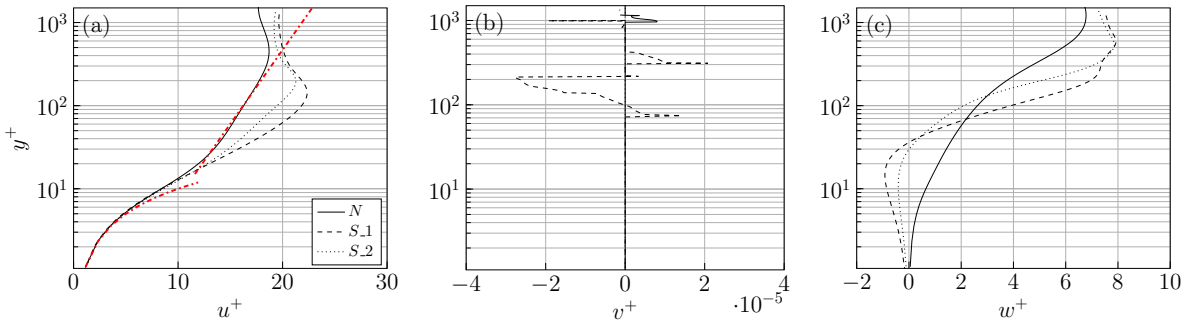

Figure 5.12: Mean velocity profiles for each wall-normal height are plotted until $y^+ = 1500$ for all velocity components. $(\cdot)^+$ indicates viscous or wall units. (a, b, c) corresponds to the streamwise, wall-normal and spanwise velocities, respectively. In (a), the red dash dot line shows both the viscous law of the wall $u^+ = y^+$ and the logarithmic law $u^+ = \kappa_v^{-1} \log(y^+) + A$ with the von Kármán constant $\kappa_v = 0.41$ and $A = 5$ for the neutrally stratified case.

results of the simulation are discussed, some suitable arguments are first presented to address the validity of the results.

- Although the effect of the background flow on the motion of the hairpin filament is studied, it should be noted that this is simply an approximation since there is no feedback mechanism in place, i.e., the action of the filament on the background flow is neglected. Aref and Flinchem (1984) show with an order of magnitude estimate that the neglected effect (including vortex stretching) is small provided that the core size of the filament is very small but non-zero compared to the length scale of the background flow field. This condition is fulfilled in our simulations in which the core size is several orders of magnitude smaller than the vertical length scale of background flow field.

- The current method also assumes that the viscous effects are very small such that core structure of the filament is practically unchanged during its evolution. Moin et al. (1986) suggest that these viscous effects gain importance during a later stage of the hairpin filament evolution when the vortex cores start interacting with each other. This aspect can also be seen in DNS simulations of reconnecting vortex tubes which show an appreciable amount of core deformation, even for very small core sizes (Yao and Hussain, 2020; Yao and Hussain, 2022). Since reconnecting vortex cores are not the focus of this work, our inviscid core calculations remain valid. Notice, however, that Callegari and Ting (1978) provide proper evolution equations for the filament vortex core subject to viscous effects, and the M1 KK method would allow us to straightforwardly include them if needed. Their main impact would be a slow thickening of the vortex cores and an associated reduction of the curvature-binormal term in the filament equation of motion.

- While the impact of gravity on the motion of the filament is felt through the external background flow, its effect on the self-induced motion of the filament is not included. By extending the work of Callegari and Ting (1978) to include weak gravitational forces, Harikrishnan et al. (2023) showed that the contribution from gravity is important only for non-closed and non-periodic filaments that begin and end at different heights. For infinitely long vortex filaments whose ends are at the same height, which are the focus of this work, it is indeed valid to ignore the effect of gravity on their self-induced motion.

Core size parameter	Ekman flow case								
	N			S_1			S_2		
	H1	H2	H3	H1	H2	H3	H1	H2	H3
δ_{min}	0.024	0.016	0.12	0.026	0.17	0.13	0.048	0.025	0.026
δ_{max}	1.26	1.89	1.63	1.92	3.45	5.57	5.79	4.18	1.31
δ_{mean}	0.52	0.49	0.74	0.52	1.1	1.05	0.92	0.70	0.33

Table 5.4: The minimum, maximum and mean values of the dimensionless core size parameter estimated along the centerline of three hairpin-like structures are shown for case N, S_1 and S_2.

5.4.1 Background flow profiles and initial conditions for the simulation

For the three Ekman flow simulations listed in table 4.1, i.e., two stably stratified cases S_1 and S_2 and the neutrally stratified case N, the background flow is obtained by computing the mean velocity at every wall-normal height. These velocity profiles are shown in figure 5.12. To enable a comparison among the different degrees of stratification, the space coordinates (x, y, z) are expressed in viscous or wall units with (1.6) which is reiterated below,

$$y^+ = \frac{y\, u_\tau}{\nu} \tag{5.35}$$

where u_τ and ν are the friction velocity and kinematic viscosity respectively. In a similar manner, the velocity components and time can also expressed in viscous units,

$$u^+ = \frac{u}{u_\tau}, \quad t^+ = \frac{t\,\nu}{\delta_\nu^2} \tag{5.36}$$

where $\delta_\nu = \nu/u_\tau$ is the viscous length scale. Once the background flow profiles are obtained, the initial conditions for the simulation are set-up. To aid with the selection of unknown physical and numerical parameters, the DNS data is inspected.

First, the core size parameter is fixed. Three hairpin-like Q-criterion structures are randomly selected and extracted for each case N, S_1, S_2. With the block-wise skeletonization algorithm of Fouard et al. (2006), the centerline of each hairpin is obtained. To estimate the dimensionless core size parameter, the diameter d of the structure and the local radius of curvature R needs to be computed. The diameter is first obtained by fitting the largest sphere within the Q-criterion structure. Next, the radius of curvature is calculated at every point along the centerline $\mathbf{X}$ which is given by (Gray et al., 2017),

$$R = \frac{1}{\kappa} = \frac{|\mathbf{X}_s|^3}{\sqrt{|\mathbf{X}_s|^2|\mathbf{X}_{ss}|^2 - (\mathbf{X}_s \cdot \mathbf{X}_{ss})^2}} \tag{5.37}$$

where $\mathbf{X}_s, \mathbf{X}_{ss}$ are the first and second derivatives of the space curve. The ratio d/R is the local dimensionless core size parameter of the filament (not to be confused with the asymptotic parameter δ from (5.7), which is a characteristic value of this quantity for a given filament). The minimum, maximum and mean values of δ estimated from all hairpin structures are tabulated in 5.4.

From figure 5.13(b), it can be seen that δ varies throughout the hairpin with smaller values (indicating a thinner core) near the legs and larger values near (thicker core) the head region.

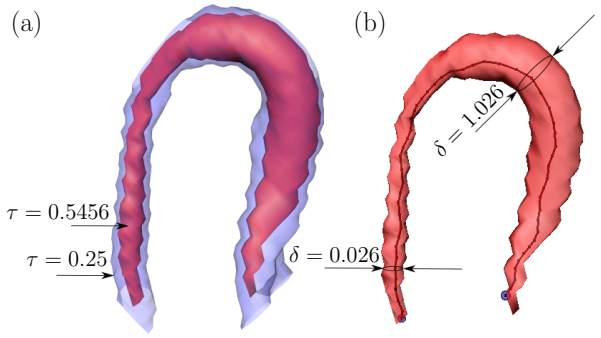

Figure 5.13: The uncertainty of core size estimation is shown in (a) where the isosurface of the same structure at at two thresholds are visualized. The core size is illustrated at two points in (b). Here, τ is the threshold and δ is the dimensionless core size parameter.

Circulation	Ekman flow case								
	N			S_1			S_2		
	H1	H2	H3	H1	H2	H3	H1	H2	H3
Γ_{min}	0.09 −0.107	0.018 −0.24	0.015 −0.217	0.02 −0.042	0.049 −0.22	0.047 −0.137	0.026 −0.01	0.0076 −0.26	0.0014 −0.035
Γ_{max}	0.17 −0.009	0.115 −0.02	0.318 −0.185	0.048 −0.048	0.13 0.0013	0.11 −0.032	0.38 −0.0071	0.225 −0.0098	0.049 0.18
Γ_{mean}	0.134 −0.045	0.077 −0.084	0.124 −0.204	0.034 −0.025	0.094 −0.119	0.08 −0.071	0.202 −0.0425	0.113 −0.122	0.031 0.11

Table 5.5: The minimum, maximum and mean values of Circulation estimated along the centerline of three hairpin-like structures are shown for case N, S_1 and S_2.

It is important to note that the estimations are strongly dependent on the threshold (τ) which is used to extract the hairpin structure. Large values of τ would imply thinner cores and vice versa as illustrated in figure 5.13(a). Here, optimum thresholds identified through percolation analysis are used. For case S_1, which is strongly intermittent, the optimum thresholds are obtained with multilevel percolation analysis as discussed in subsection 3.1.5. For other cases, the global percolation threshold (τ_p) is sufficient to identify individual structures. Apart from its dependence on the threshold, it is also important to note that these estimations are made at a later stage in the developmental cycle of a hairpin structure. For most of the hairpin structures considered here, the minimum value of core size parameter is about 0.02 whereas maximum value can reach up to 5.79 (see table 5.4). To study the effect of changes in δ, two values $\delta = 0.01, 0.05$ are conservatively chosen.

For all the extracted hairpin structures, circulation within the $Q-$criterion structure is calculated on both legs for every wall-normal height until its head region. From table 5.5, it can be seen that most hairpin structures have a positive circulation value on one leg and a negative value on the other which indicates opposite swirling directions. Similar to the core size parameter, two circulation values are chosen $\Gamma = 0.01, 0.05$ to study its impact on the evolution of the hairpin filament.

Another important parameter is the initial width of the hairpin filament which is controlled through β. From the stagnant flow test, it is clear that for larger β (and consequently smaller initial width), the nonlocal effects of self-induction become important and tend to have a

Case	Core size (δ)	Circulation (Γ)	Spread (β)	Inclination (θ_i)	Amplitude (A)	Length (L)
R_1	0.01	0.01	7500	0.1°	10	200
R_2	0.05	0.01				
R_3	0.01	0.05				
R_4	0.05	0.05				

Table 5.6: The four initial configurations of the hairpin chosen for the simulations with ABL background flow.

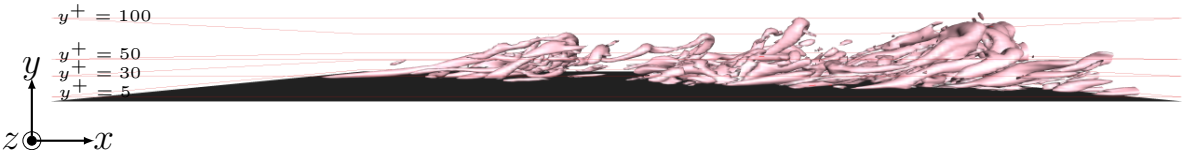

Figure 5.14: Side view of an active/turbulent patch of $Q-$criterion criterion structures for the case S_1 until $y^+ = 100$.

significant impact on the evolution of the filament. Therefore, this parameter needs to be carefully chosen. In their experimental study, Acarlar and Smith (1987) test the hypothesis that hairpin structures are generated from the breakup of low-speed streaks by artificially creating low-speed streak regions (with periodic injection of fluid in a water-channel) in a sub-critical laminar boundary layer. They concluded that these artificial low-speed streaks tend to oscillate over time and later breakup to form hairpin vortices. Therefore, the mean spanwise width computed over all individual low-speed streaks can be used to choose the initial width of our hairpin filament. At $y^+ = 50$, where numerous hairpin-like structures can be seen from figure 5.14, the mean spanwise width of low-speed streaks is about 60 viscous units which corresponds to $\beta = 7500$.

The hairpin filament is also initialized with a length of 200 viscous units and an initial inclination angle of 0.1° (near-planar disturbance). An initial amplitude of 10 viscous units is also chosen to represent a small perturbation. All parameters used in the simulations are listed in table 5.6.

5.4.2 Temporal evolution of hairpin filaments in the outer layer

A final parameter which needs to be chosen is the initial starting height, y^+_{initial}. If $Q-$criterion structures are visualized for the case S_1 (cf. figure 5.14), the hairpin-like structures at various stages of evolution can be seen around $y^+ = 50$. Therefore, the first set of simulations are run with $y^+_{\text{initial}} = 50$.

The hairpin filament is discretized with 500 nodes for all four initial configurations listed in table 5.6 and three background flow profiles. In all cases, a time step of $\triangle t = 5 \times 10^{-5}$ is used to obtain a smooth evolution. The temporal evolution with S_1 background flow is plotted every 20 time steps (or $\triangle t^+ = 1.11$) until $t^+ = 7.8$ (or 140 time steps) in figure 5.15. It should be noted that when comparisons are made among the different Ekman flow cases, it is always done in terms of viscous time units. This is because the friction velocity is not a

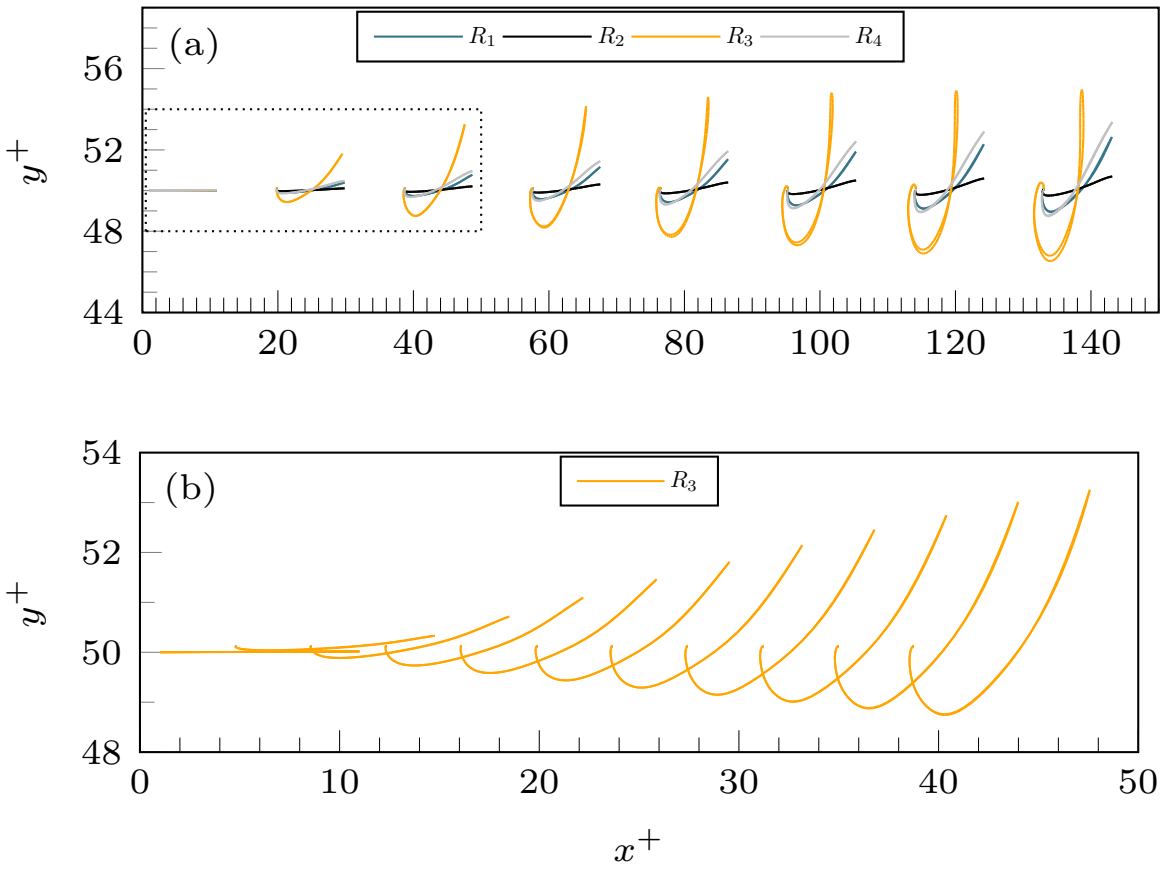

Figure 5.15: (a) Temporal evolution for all four cases listed in table 5.6 are plotted every 20 time steps for case S_1. The dotted region is zoomed in for initial condition R_3 in (b).

fixed parameter in Ekman flow simulations (Ansorge, 2016). For instance, 140 time steps for case N and S_2 corresponds to $t^+ = 9.75, 8.1$ respectively.

Similar to the shear flow test, it can be seen from figure 5.15 that the head of the hairpin filament starts tilting backward and stretches in the wall-normal direction regardless of changes in δ and Γ, albeit with different rates of evolution. This is in agreement with the results reported by Zhou et al. (1999), who found that the hairpin vortex qualitatively experiences the same curl-up process regardless of changes in Γ but with different subsequent evolution. These changes are due to variations in the balance of self-induced velocity which is responsible for curl-up and the mean shear which causes stretching both in the streamwise and wall-normal direction.

From figure 5.15(a), it is clear that the initial condition R_3 (thinner core and stronger circulation) evolves faster than the other initial conditions and R_2 (thicker core and weaker circulation) is the slowest. If changes in the inclination angle $\theta_i = \arctan(\triangle y^+/\triangle x^+)$ are calculated and plotted over time for all cases, it can be seen from figure 5.16 that R_3 has a faster inclination rate. From a near planar disturbance, the hairpin filament quickly reaches an inclination angle of 50° and plateaus over time for all three background flows N, S_1, S_2. This is close to the results reported by Head and Bandyopadhyay (1981), who found hairpin vortices inclined between 45° in the outer regions of the boundary layer.

Also from figure 5.16(a), the maximum inclination angle reached is approximately 50° regardless of the strength of stratification. This is due to the relatively large values of self-induced velocity of the filament dominating over the mean shear which, in turn is due to large

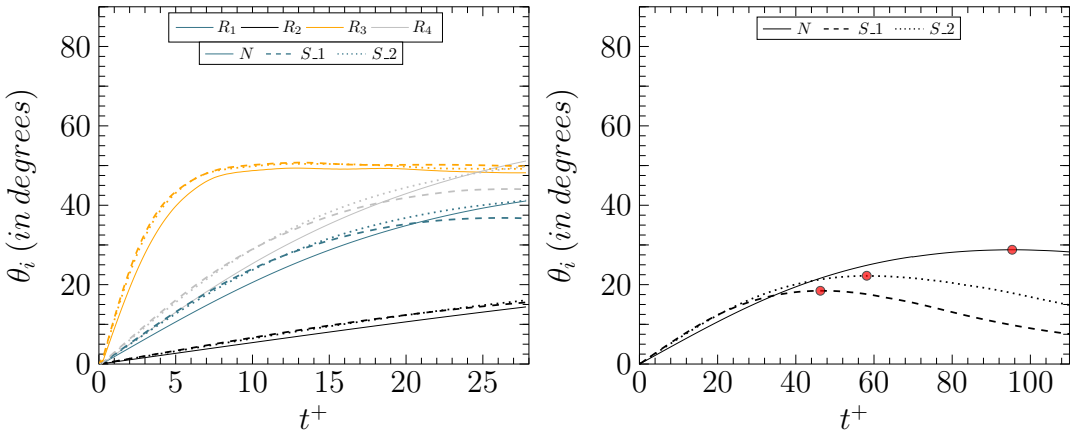

Figure 5.16: Time history of the inclination angle θ_i computed for (a) all four initial conditions from table 5.6 until $t^+ = 28$ and (b) only initial condition R_2 until $t^+ = 110$. The solid, dashed and dotted lines correspond to the different cases N, S_1, S_2 respectively. The red markers indicate the time at which the hairpin filament reaches the maximum inclination angle.

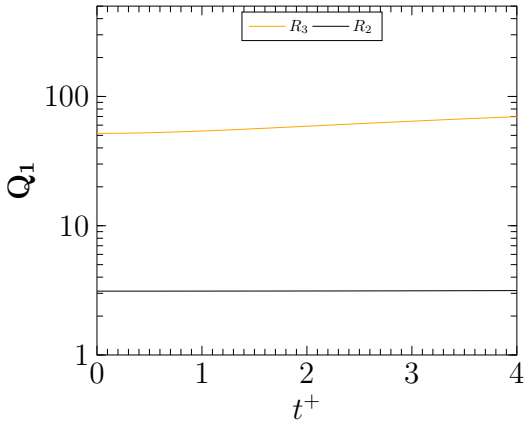

Figure 5.17: A comparison of self-induced velocity summed over the all nodes of the filament is shown for the initial conditions R_2 and R_3 with the mean background flow of S_1.

Γ and small δ. In fact, if the total self-induced velocity is computed by summing up the self-induced velocity over each node, it can be seen from figure 5.17 that the self-induced velocity of R_3 is at least 16 times the self-induced velocity of R_2. However, for smaller self-induced velocities, the maximum inclination angle has a dependence on the strength of stratification. For instance, if the integration is continued for the initial condition R_2 as shown in figure 5.16(b), the maximum inclination angle reached is $\theta_{i,\max} = 18.4°, 22.2°, 28.7°$ for S_1, S_2, N respectively. This suggests that the hairpin evolution strongly hinges on the delicate balance between self-induction and the mean background flow.

During their temporal evolution, hairpin filaments with the ABL background flow (figures 5.15 and 5.18) exhibit similar features as seen in shear flow test. From its initial position, these filaments are advected downstream, stretch in the streamwise direction leading to the formation of hairpin legs and develop secondary hairpins on either side of the main disturbance. Comparing the initial conditions R_2 and R_3 for the strongly stratified case S_1, it can be seen from figure 5.18 that the development of these features occur at a later time for R_2. For instance, secondary hairpins can be seen at a viscous time $t^+ = 3.9$ for R_3 and at a much later viscous time $t^+ = 53$ for R_2. Although not shown, similar trends can also be seen with the

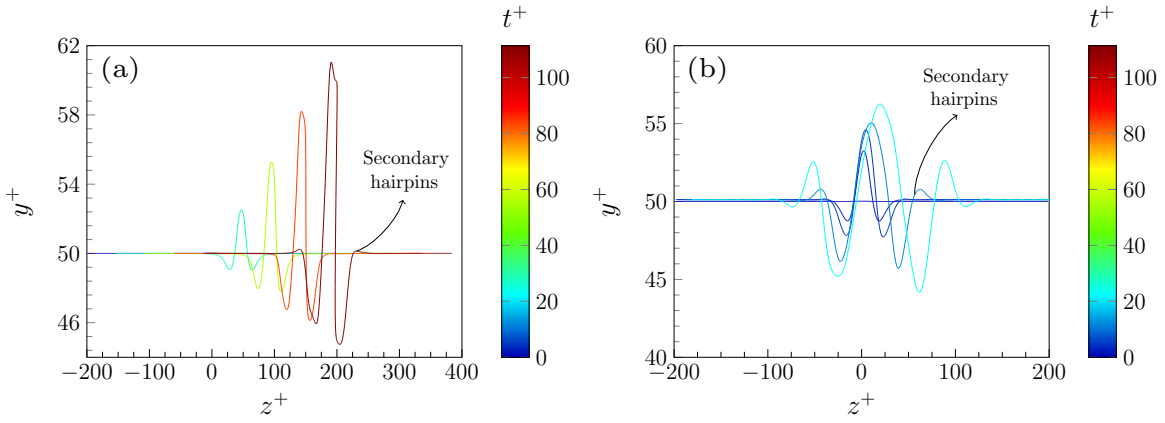

Figure 5.18: Temporal evolution of a hairpin filament for case S_1 with (a) initial condition R_2 and (b) initial condition R_3. Front view of the filaments are plotted at $t^+ = 0, 27.8, 55.7, 83.5, 111.4$ in (a) and $t^+ = 0, 2.2, 4.4, 11.1, 22.3$ in (b).

other cases N and S_2. This suggests that R_2, which has a slower inclination rate, may have a longer lifetime in the flow (assuming no interactions exist).

Furthermore, the temporal evolution of R_2 as shown in the top panel of figure 5.19 illustrates the differences in streamwise advection among the three stratified cases. At time instance $t^+ = 56$, it can be observed that the hairpin filament is advected about $973, 832, 607$ viscous units for case S_1, S_2, N respectively. This is to be expected since the mean velocity profiles (cf. figure 5.12) already suggest larger streamwise velocity at $y^+ = 50$ for the stratified flows. Ansorge and Mellado (2016) show with conditional analysis that the streamwise velocity in the turbulent/active regions of the strongly stratified flow are lower than their non-turbulent/inactive counterparts which implies a reduction of shear intensity in the turbulent/active regions of the flow.

Visualizing the temporal evolution with the front view reveals further interesting characteristics. From the bottom panel of figure 5.19, one can observe that the hairpin filament becomes asymmetric over time, although it started as a small disturbance that is symmetric about $z^+ = 0$. One can attribute the development of this asymmetry to the spanwise velocity gradient where the head of the hairpin filament may encounter a larger velocity than its leg thereby causing it to tilt in one direction. This is in line with the presence of an Ekman sprial where the velocity vector rotates with increasing height (Ansorge and Mellado, 2016). In addition, by inspecting the DNS database of flat-plate boundary layers, Robinson (1991) found that asymmetric vortical structures having a hook-like geometry were more common than symmetric ones. Figure 5.19 also shows that the asymmetry is more pronounced for the stably stratified cases and the degree of tilt increases with increasing stratification.

Apart from the development of asymmetry, the hairpin filament is also strongly advected in the spanwise direction. Figure 5.20 shows a plot of the midpoint of the hairpin in the (x, z) plane for every instantaneous time step. The neutrally stratified case experiences stronger spanwise advection than the stably stratified cases. With respect to the streamwise direction, the hairpin filament has drifted $\triangle z^+ = 74, 46, 33$ viscous units for case N, S_1, S_2 respectively at time $t^+ = 56$. These trends remain unchanged for other initial conditions.

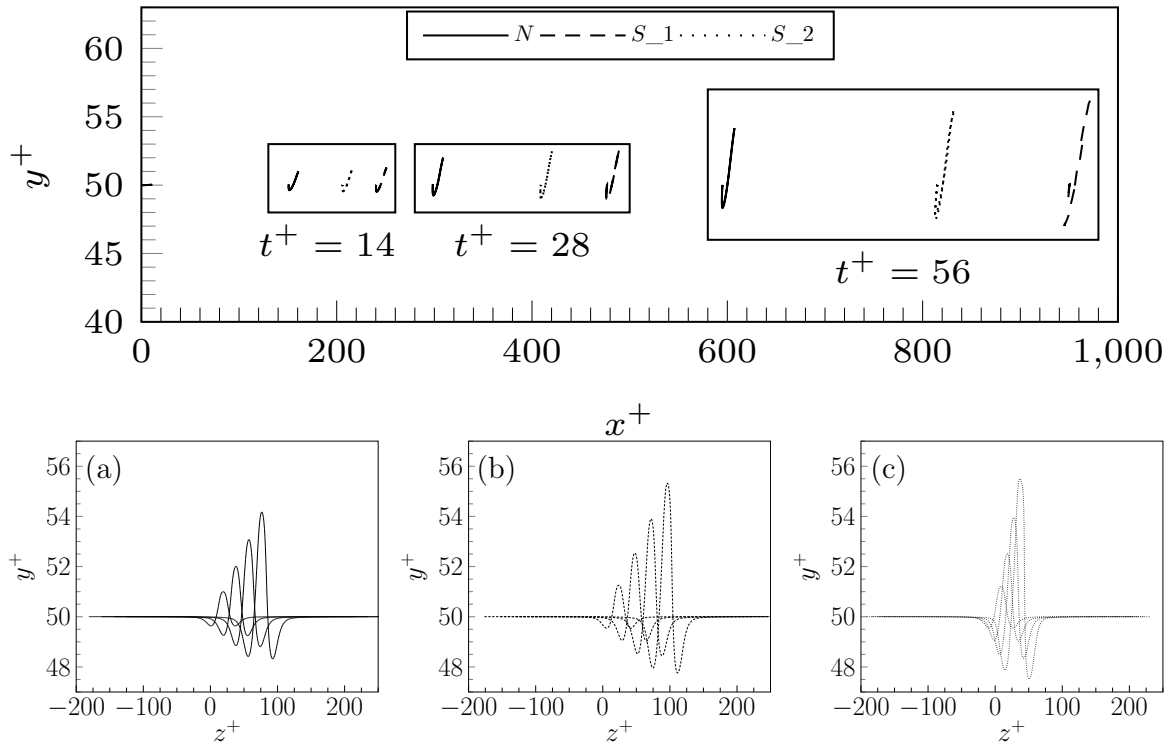

Figure 5.19: Temporal evolution for R_2 is shown for cases N, S_1, S_2. The top panel shows a side view of the filaments and the bottom panel shows the front view. In the bottom panel, (a, b, c) correspond to case N, S_1 and S_2 respectively. The filaments are plotted at $t^+ = 0, 14, 28, 42, 56$ in the bottom panel.

5.4.3 Evolution of hairpin filaments at other heights

In this subsection, the analysis is continued by studying the dynamical hairpin characteristics for two other initial starting heights $y^+_{\text{initial}} = 15, 30$. Since these filaments are initialized much closer to the wall, the effect of wall impermeability is included in these simulations. The same parameters listed in table 5.6 are used with R_2 as an initial condition.

Consider the figure 5.21 where inclination angles computed for both initial heights are shown. The trend is similar to the results seen for $y^+_{\text{initial}} = 50$ where the maximum inclination angle reduces with increase in the strength of stratification. In the case of $y^+_{\text{initial}} = 15$, $\theta_{i,\max} = 9.9°, 10.6°, 11.8°$ and $y^+_{\text{initial}} = 30$, $\theta_{i,\max} = 14.2°, 17.2°, 21.1°$ for cases S_1, S_2 and N

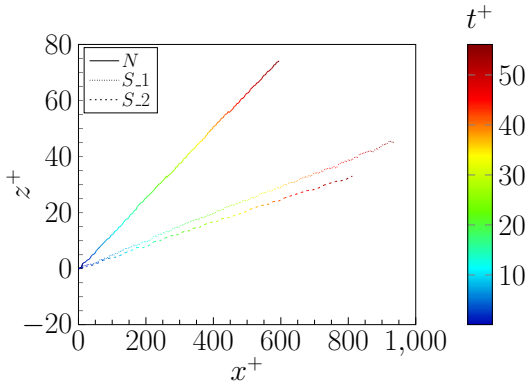

Figure 5.20: A comparison of the spanwise advection among the three cases N, S_1 and S_2 is shown until $t^+ = 56$ where the hairpin is initialized at $y^+ = 50$.

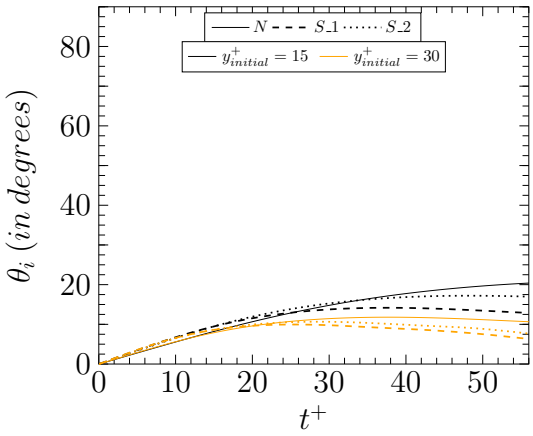

Figure 5.21: Time history of the inclination angle θ_i computed for initial condition R_2. The solid, dashed and dotted lines correspond to the different cases N, S_1, S_2 respectively.

respectively. It is also evident that the hairpins are inclined at shallower angles with decreasing initial height. Similar observations were reported by Adrian et al. (2000) who suggested θ_i to be a strong function of the hairpin location and found hairpin vortices inclined between 15° to 75° with 45° being typical.

The temporal evolution from figure 5.22 also confirms the trends established at $y^+_{\text{initial}} = 50$ where the streamwise advection increases with increasing stratification. The streamwise displacement, however, increases as the filament is initialized farther away from the wall for all cases, which is to be expected in wall-bounded flows. The spanwise advection, plotted in figure 5.23, shows that the neutrally stratified case exhibits only minor variations with increasing height. On the other hand, both stably stratified cases are strongly affected where an anticlockwise change in spanwise orientation can be seen with increasing height reflecting the Ekman spiral. This result suggests that, under stable stratification, the spanwise orientation of the hairpin filament is linked to its initial height, i.e., its origin. Following Deusebio et al. (2014), if the height at which the maximum horizontal velocity is attained is used to estimate the boundary-layer thickness for the strongly stratified case S_1, this is at $y^+ = 156$ viscous units which is about one fourth of that observed in the neutrally stratified case. This suggests that all the hairpin simulations were initialized well within the Ekman layer enabling us to observe the spiral as seen in figure 5.23.

5.5 Comparison with MLPT tracking

Since hairpin-like structures were already tracked in time with temporally well-resolved DNS data in the previous chapter (see section 4.3), it presents an opportunity to qualitatively compare their evolution with those obtained through filament simulation. The candidate structure chosen for comparison is from the strongly stratified case S_1, visualized in figure 5.24 until $t^+ \approx 74.4$, and was tracked for 674 time steps (or $t^+ \approx 84$). The centerlines for the structures are obtained through the block-wise skeletonization method of Fouard et al. (2006). From figure 5.25, it can be seen that this structure exists in the outer layer in the range $80 < y^+ < 180$. To enable an appropriate comparison with the filament simulation, a hairpin filament with a large amplitude $A = 80$ is initialized at a higher wall-normal height

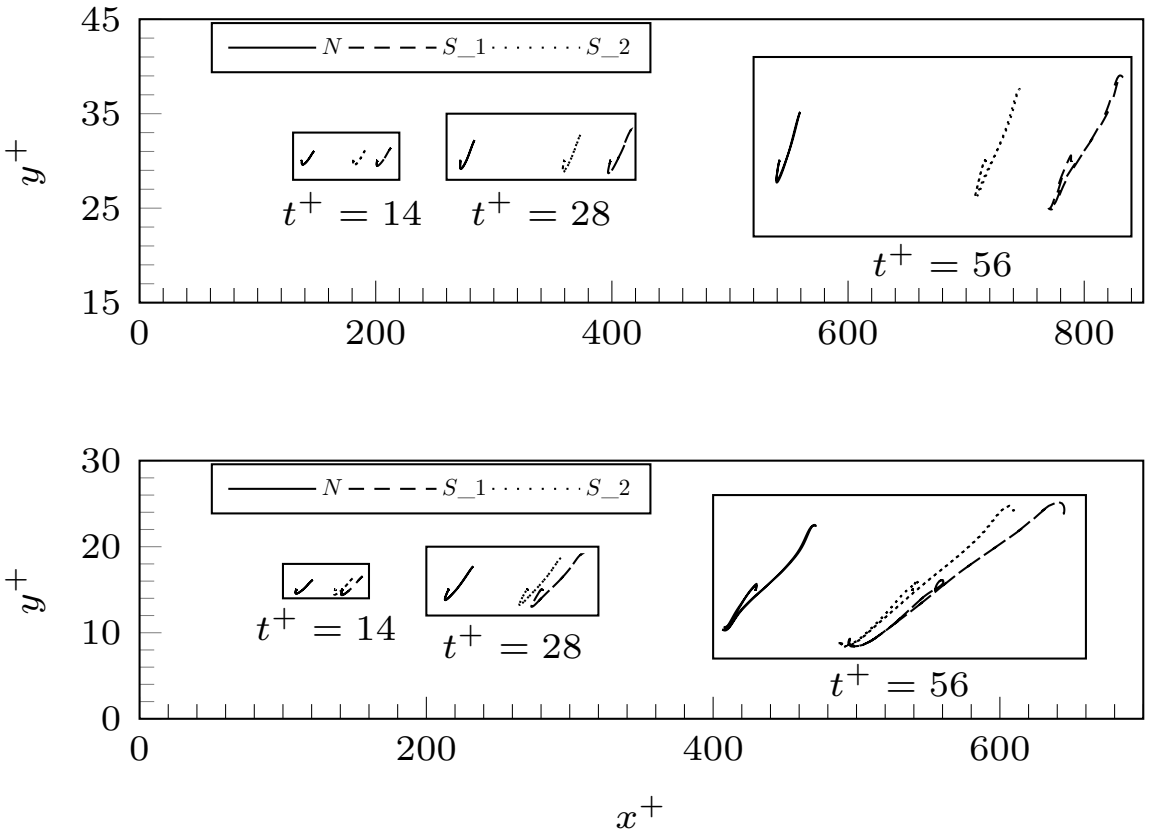

Figure 5.22: Temporal evolution for R_2 is shown for cases N, S_1, S_2. The top and bottom panels show the side view of the filaments at $y^+_{\text{initial}} = 30$ and $y^+_{\text{initial}} = 15$ respectively.

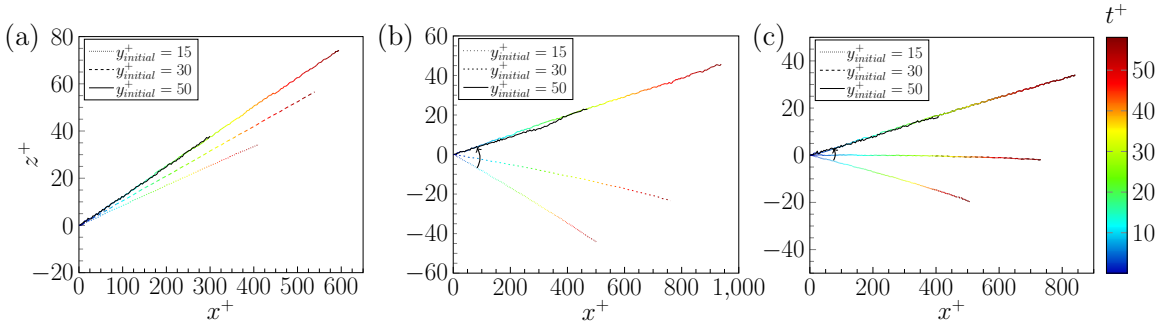

Figure 5.23: Comparison of spanwise advection for case (a) N (b) S_1 and (c) S_2 at three initial heights $y^+ = 15, 30, 50$. The solid black line shows the spanwise advection with initial condition R_3 wheras all others are shown with initial condition R_2.

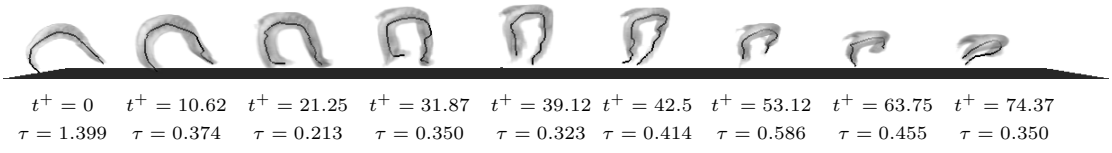

Figure 5.24: Track of a hairpin-like structure from the strongly stratified case S_1 with MLPT thresholding. The complex geometry of the extracted structures may result in a network of centerlines. Since we are only interested in the main centerline defining the hairpin structure, the remaining are discarded.

Parameter	Value
Core size parameter, δ	0.01
Circulation, Γ	0.05
Spread parameter, β	500
Amplitude, A	80
Angle of inclination, θ_i	0.1°
Initial wall-normal position, y^+_{initial}	125
Domain length, L	400

Table 5.7: Initial condition for comparison with feature tracking results.

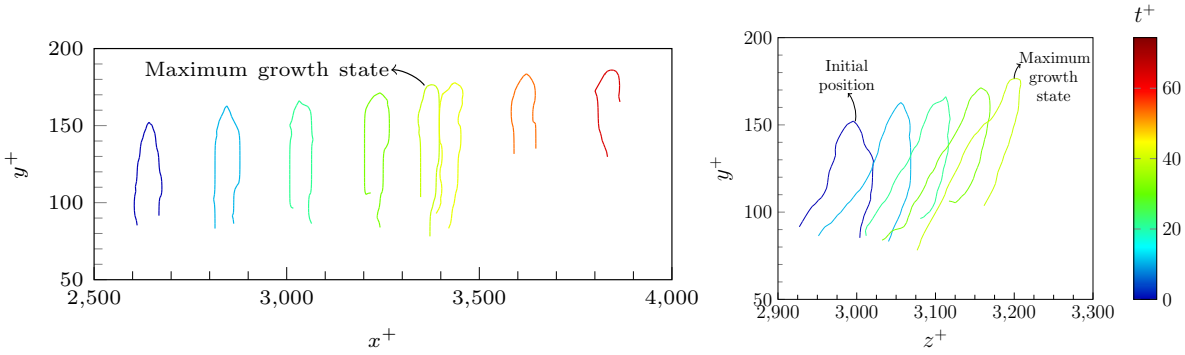

Figure 5.25: Temporal evolution of the tracked hairpin-like structure with MLPT thresholding. Left and right figures show the side view and the front view of the feature tracking results respectively.

$y^+_{\text{initial}} = 125$ and a correspondingly larger width. The initial conditions are listed in table 5.7. Overlap is ensured with a spatial discretization of 1500 nodes and the simulation is carried out until the overlap condition is violated. Results of the simulation are shown in figure 5.26.

It should be noted that in the feature tracking results, the initial state of the hairpin-like structure is unknown and tracking is started only from a later point in its lifetime. While this makes it practically impossible to establish a direct comparison with the simulation results, some qualitative comparisons regarding their temporal evolution can be made. The streamwise advection of the tracked structure and filament simulation for a viscous time $t^+ = 84$ are 1621 and 1682 viscous units respectively. At this height, the hairpin-like structure is mainly driven by the mean background flow and the minor discrepancy can be attributed to the choice of the initial starting height of the filament which suggests that the hairpin structure may have originated from a lower height. The discrepancy can also be attributed to effects of mutual induction of neighboring structures. Figure 5.27 shows the initial state of the tracked hairpin-like structure (colored blue) where at least one other structure can be identified in close proximity which can influence later temporal developments.

Even at the first time step of tracking, the asymmetry of the hairpin-like structure can be observed from figure 5.25. The legs of the structure are at heights 91 and 85 viscous units. This asymmetry grows over time and at the maximum growth state, the legs are at heights 78 and 103 viscous units. Starting with a symmetric perturbation, it can be seen from the filament simulation that asymmetry develops and grows over time and at $t^+ = 84$, the legs of the hairpin filament are at wall-normal heights of 73 and 106 viscous units. As seen from

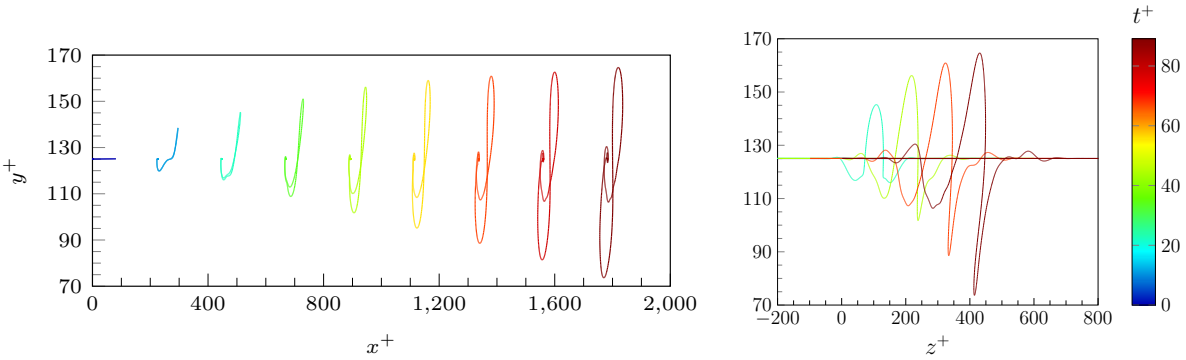

Figure 5.26: Temporal evolution for a larger hairpin filament at $y^+_{\text{initial}} = 125$. Left and right figures show the side and front view of the temporal development respectively.

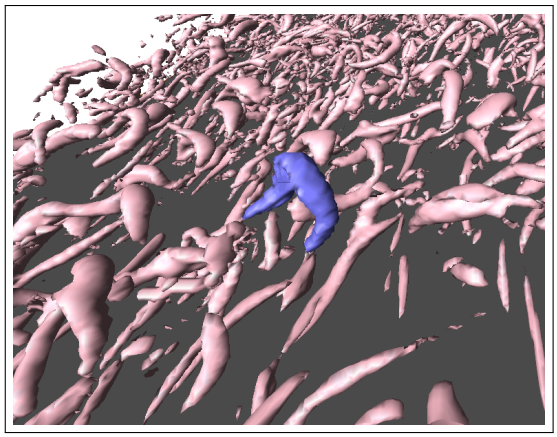

Figure 5.27: Isosurfaces of the Q-criterion for case S_1 are shown here for the initial time step. The structure tracked with MLPT is highlighted in blue.

previous sections, the persistence of asymmetry is due to the influence of spanwise velocity. This contradicts the results reported by Zhou et al. (1999) who suggested that an initial asymmetric configuration is necessary to produce asymmetric hairpin vortices. Our results indicate that asymmetry develops naturally as a consequence of the mean background flow.

5.6 Summary and conclusions

In this chapter, the similar orientations of hairpin-like structures observed in chapter 3 for the strongly stratified case S_1 have been investigated. To circumvent the limitations of the feature tracking methodology from the previous chapter, a thin filament approach (TFA) is used to study the dynamics of hairpin structures with the ABL as a background flow.

The hairpin filaments are initialized as small, symmetric, three-dimensional disturbances inclined at an angle θ_i having a spanwise width β and amplitude A. In the first part of the chapter, the temporal evolution of hairpin filaments with no background flow were studied with two methods namely, the local induction approximation (LIA) and the corrected thin-tube model of Klein and Knio (1995) with the method 1 optimization technique (Knio and Klein, 2000) (M1 KK). For a filament initially inclined at $\theta_i = 45°$ with respect to the wall with width $\beta = 20$, results from subsection 5.3.2 indicate that both methods correctly capture the effects of self-induction where the tip region of the filament bends backward and moves rapidly downward towards the wall resulting in a corkscrew shape, previously observed in Moin et al.

(1986) and Hon and Walker (1991). If the simulation is rerun with different initial spanwise widths $\beta = 15, 50$, a major drawback of LIA is highlighted. From side views of figures 5.9, 5.10, a marked difference in the development of hairpin "legs" can be observed, particularly for $\beta = 50$. This gives a direct comparison when nonlocal effects of vortex self-induction are neglected by LIA and when they are correctly represented with the M1 KK method. Therefore, for simulations with the ABL background flow the M1 KK method is preferred.

The impact of the presence/absence of a wall on the motion of the hairpin filament is examined in subsection 5.3.3 with a simple shear background flow. Wall impermeability is accounted with the help of an image vortex placed behind the wall at an equal and opposite wall-normal distance to the filament being simulated. With the parameters described in table 5.3, the simulation was run with/without a wall and the results are shown in figure 5.11. In agreement with Moin et al. (1986), it can be seen that the hairpin vortex in the presence of a wall is advected further downstream than the one without the wall. If the simulation is run further (not shown), it can be seen that the effect of the image vortex becomes stronger as it approaches the wall closely.

Finally, the motion of hairpin filaments with the Ekman background flow were studied for three cases: two stably stratified (S_1, S_2) cases at different degrees of stratification and a neutrally stratified (N) case with the M1 KK scheme. The hairpin was initialized at a wall normal height $y^+_{\text{initial}} = 50$, i.e., in the outer layer as a small, nearly two-dimensional perturbation with an initial inclination angle $\theta_i = 0.1°$ and four initial conditions were investigated to examine the effect of varying core size δ and circulation Γ values (see table 5.6). In all cases, the hairpin filament lifts up and bends backward away from the wall due to self-induction, thereby increasing its inclination angle. Particularly for the initial condition R_3, which has a large self-induced velocity (as a result of a relatively thinner core and stronger circulation), the maximum inclination angle reached is approximately 50° regardless of the strength of stratification. For all other initial conditions, where the self-induced velocity is weaker, the background flow influences the motion of the filament and the maximum inclination angle reached reduces with an increase in the strength of stratification ($\theta_{i,\max} = 28.7°, 22.2°, 18.4°$ for cases N, S_2, S_1 respectively). The experiment was repeated at other heights $y^+_{\text{initial}} = 15, 30$ in subsection 5.4.3 where the effect of wall impermeability was included. At $y^+_{\text{initial}} = 15$, $\theta_{i,\max} = 11.8°, 10.6°, 9.9°$ and at $y^+_{\text{initial}} = 30$, $\theta_{i,\max} = 21.1°, 17.2°, 14.2°$ for cases N, S_2, S_1. This suggests that the inclination angle is a strong function of its location and $\theta_{i,\max}$ increases with increasing height.

Since Ekman flow includes both effects of stratification and rotation, the latter has an influence on the spanwise dynamics of the filament. Figure 5.19 clearly shows that the hairpin filament, initially symmetric, becomes asymmetric over time, thereby tilting the filament in one direction. The degree of tilt increases with an increase in the strength of stratification. This asymmetry can also be observed in the DNS feature tracking results (see figure 5.25) in which the degree of asymmetry increases as the hairpin-like structure grows in size. The rotation also influences the spanwise advection of the filament. In figure 5.23, a comparison of the spanwise advection at three initial heights $y^+_{\text{initial}} = 15, 30, 50$ are shown. An appreciable change in the spanwise orientation can be observed, particularly for the stratified cases S_1 and S_2 for which the orientation changes in the anticlockwise direction with increasing height

reflecting the Ekman spiral. This suggests that hairpins initialized at the same wall-normal height will have similar spanwise orientations under stable stratification.

Although a link between the spanwise orientation of the filament and its initial starting height is suggested for the stable regime, it is still not clear if this is solely responsible for the similar orientation of structures observed in chapter 3. As suggested in section 5.5, the effect of mutual induction of neighboring filaments may have an impact on the dynamics of the filament and remains unexplored. Margerit et al. (2004) have shown that the mutual induction of several filaments can be computed by summing their self-induced velocities. However, as the filaments approach each other closely, viscous effects become important leading to the deformation of the core structure as seen in Yao and Hussain (2022). Incorporation of viscous diffusion was already pursued in Klein et al. (1996) which should lead to a straightforward modification of the slender vortex code presented in this thesis. Additionally, the simulations carried out here do not include the impact of gravity on the self-induced motion of the filament as Harikrishnan et al. (2023) showed that contribution from gravity becomes important when the filament is tilted with respect to the vertical direction. Therefore, the impact of gravity on the motion of tilted filaments is currently an open question.

6

Summary and conclusions

> ... turbulent boundary layers also promote increased mixing, heat transfer, and exchange processes; thus, when they occur on an atmospheric scale, they have important meteorological and climatological implications.
>
> *Marusic et al., Science, 2010*

In this thesis, direct numerical simulations of rotating and stably stratified Ekman flows over a smooth wall have been investigated with the help of coherent structures (chapters 1 - 4) and vortex filaments (chapter 5). As explained in the introduction, the primary motivation to study the stable boundary layer stems from the need to improve existing/develop newer parametrizations through a better understanding of the underlying physical processes and dynamics. With a structure-based approach, a detailed comparison was established between the stably and neutrally stratified Ekman flow by (i) comparing the geometry of Robinson structures in an instantaneous flow field, (ii) comparing the temporal evolution of the geometry of Robinson structures and (iii) comparing the temporal evolution of hairpin-like structures obtained through feature tracking and vortex filament schemes. A brief summary of the main results and methods developed during the course of this work are discussed in this chapter.

6.1 Geometry of coherent structures with increasing stability

In chapter 2, a methodology for the extraction and geometrical characterization of quantitative Robinson structures was developed. To extract individual visualization accurate (see the description in section 2.2) structures from three-dimensional scalar fields, the neighbor scanning (NS) algorithm of Moisy and Jiménez (2004) was improved with the marching cubes (MC) algorithm (Lorensen and Cline, 1987). The speed and accuracy of the NS+MC algorithm even at very small thresholds was demonstrated in subsection 2.2.3. Next, a non-subjective threshold value was identified for each indicator with the following steps: (i) nondimensionalizing the indicator with its root mean square over every wall-normal plane which accounted for the inhomogeneity of the flow in the wall-normal direction everywhere, except in the viscous sublayer, such that a single global threshold could be used for the entire flow field (see figure 2.13) and (ii) identifying the region of percolation transition by varying the threshold between two limits and calculating its mean. It was seen that this method was insufficient to educe individual structures for the strongly stratified case S_1. Therefore, a novel method called

multilevel percolation analysis (MLP) was proposed in subsection 2.3.1 where percolation analysis could be applied in an iterative manner to break down the complex cluster into individual structures, all of which exist at unique thresholds. Finally, the extracted individual structures were geometrically characterized with the non-local methodology of Bermejo-Moreno and Pullin (2008). All of these steps taken together constitute a framework for the extraction and geometrical characterization of coherent structures in wall-bounded flows.

The geometrical characterization framework described above was applied for all three stably stratified cases (S_1, S_2, S_3) and the neutrally stratified case (N). Results of this analysis are presented in the first part of chapter 3. For an instantaneous time step of each case, all quantitative Robinson structures were computed with the indicators listed in table 2.1. Subsequently, the structures were extracted at the percolation threshold τ_p and geometrically characterized. In total, about 10^6 structures were analysed across all cases.

It should be noted that the geometrical characterization was excluded for the viscous sublayer ($y^+ < 5$) as structures having a mean fractal dimension $\langle D_\alpha > 1 \rangle$ which start within this region are not fully formed and generally extend into the buffer layer and sometimes beyond. In this region, it was observed from figures 3.1, C.1 that low-speed streaks ($u' < 0$) show an increase in their streamwise coherence with increase in the strength of stratification. In particular, a single low-speed streak can be seen spanning a large portion of the domain (cf. figure 3.1(b)) for the case S_1. Unlike other low-speed streaks, this large low-speed streak has only few ejections arising out of it, most of which are confined to the outer edges and the inner region is completely devoid of ejections. This is reminiscent of the non-turbulent regions observed above and suggests that global intermittency has a direct impact in this layer as well. This means that global intermittency can be generalized to indicate active/inactive regions rather than turbulent/non-turbulent regions to include its effect in the viscous sublayer.

Results of the geometrical characterization shown in figures 3.6, C.5, C.6 suggest that the quantitative Robinson structures range from moderately stretched tube-like or moderate to strongly stretched sheet-like structures. No blob-like structures exist. Plotting the geometry of all structures for each case as shown in figure 3.22 indicates similar envelopes of joint pdfs for all cases. This means that no affinity towards sheet-like (or pancake-like) structures could be established with increasing stability. This result is important since changes in geometry from hairpin vortices to thermal plumes were found to have an impact on the momentum transport efficiency under increasing instability (Li and Bou-Zeid, 2011). Likewise, previous studies have also reported an increase in the inclination angles of hairpin structures with increasing instability (e.g., Carper and Porté-Agel (2004)). From subsection 3.1.5, examining near wall hairpin-like structures from each case did not reveal any significant changes in inclination angles with increase in stratification. While all these results suggest no significant changes in geometry or inclination angles with increase in stability, it can be seen from numerous visualizations (for instance, figures 3.1, 3.3, 3.4, 3.13, 3.14) that the quasi-laminar patches due to global intermittency extend throughout the vertical column of the strongly stratified case S_1, thereby having a significant impact on the *spatial organization* of coherent structures.

Since the percolation analysis points to a range of thresholds which approximately span a decade rather than pointing to a single value, it presents an ambiguity in choosing an "optimum" threshold value. In the present work, the mean value was chosen. However, values above and

below the mean can also be considered reasonable choices. Due to this ambiguity, conclusions derived from the geometrical characterization are complemented with those obtained from conditional one-point statistics. The flow field is conditioned into turbulent and non-turbulent subvolumes with an intermittency factor γ. The definition of γ is generalized as shown in (3.2) such that any vortex indicator can be used to segregate the turbulent and non-turbulent parts of the flow. As shown in figure 3.18, using an alternate indicator such as Q-criterion overcomes the drawback of vorticity magnitude which produces false-positives in shear-dominated regions. Consequently, the wall region appears less filled even at the lowest possible threshold.

With the Q-criterion based γ, the conditioning is applied for four quantitative indicators namely, high- and low-speed streaks, sweeps and ejections. While the geometrical analysis was limited to grid B (1/3 of the domain), conditional analysis was applied to grid A (full domain). Vertical profiles obtained through horizontal averaging are shown in figure 3.19. Results indicate a dominant presence of low-speed streaks close to the wall for the case S_1 as seen from the previous analysis. This signifies the impact of global intermittency close to the wall under very strong stratification. Although it is initially suspected that these non-turbulent regions are decelerated regions of the flow, analyzing the volume fraction occupied by low-and high-speed streaks in the non-turbulent regions reveals a switching behavior for all stably stratified cases (see figure 3.20) where the outer non-turbulent regions appear to be occupied by high-speed streaks.

Although analyzing an instantaneous snapshot of the Ekman flow under neutral and stable stratification suggested that the geometry of the Robinson structures is similar, the spatio-temporal variability of global intermittency can have an impact on the dynamics of coherent structures, thereby influencing their geometry. This is investigated in the first part of chapter 4. Initially, the geometrical characterization framework is modified with an additional step as shown in figure 4.1 to track the Robinson structures in time. Tracking is accomplished with a region-based method where correspondence is measured with the degree of spatial overlap of features between consecutive time steps. Next, tracking for the six quantitative Robinson structures (low-and high-speed streaks, sweeps, ejections, vortices and shear layers) is initiated by identifying structures having a similar geometry i.e., having similar values of $\hat{S}, \hat{C}$ and λ. A sphere of radius $r = 0.05$ with origin at the centroid of the cluster of all geometries analysed in chapter 3 is chosen to identify the required structres (an example with high-speed streaks is shown in figure 4.5). Since merging with larger structures significantly alters the geometry (see figure 4.6 for an example), a constraint is imposed where tracking is terminated when such merges occur. About 600 structures have been temporally tracked and geometrically characterized. Similar to the instantaneous case, results as seen from figure 4.7 suggest a complete lack of blob-like geometry and most structures are moderately stretched tube-like and moderate to strongly stretched sheet-like structures regardless of the strength of stratification. Even though this hints that the spatio-temporal variability of global intermittency does not have a significant impact on the geometry of coherent structures with increasing stability, the results should not be seen as conclusive due to the constraint imposed on the tracking technique, limitations of the tracking technique (such as using a constant threshold in time, using a subjective overlap threshold) and a small sample size. Similar to the instantaneous

snapshot case, these results need to be complemented with those obtained through statistical means.

6.2 Abundance and similar orientation of hairpin-like structures

The next set of results attempt to explain the abundance and similar orientation of hairpin-like structures observed from figure 3.14(a) for the strongly stratified case S_1. A new methodology, called multilevel percolation thresholding in time (MLPT), which overcomes the limitation of using a constant threshold in time is developed for tracking hairpin-like structures. As shown in figure 4.9, an optimum threshold is computed for the subsequent time step by adjusting the threshold such that the structure at t_{n+1} remains simple, i.e., having a $V_{\max}/V > 0.5$ over the entire threshold range. This allows the structure to freely grow or shrink in time when the threshold is decreased or increased respectively. Development of this method is motivated from previous observations where hairpin-like structures were observed to grow in time as they are advected downstream due to the competing effects self-induced velocity generated by the hairpin itself and the shear induced stretching as a result of the mean background flow (for instance, see Zhou et al. (1999)). Results of the comparison between tracking with constant and MLPT thresholds are shown for a candidate hairpin-like structure in figure 4.10. It clearly shows that when tracking is accomplished with constant threshold in time the structure is constantly shrinking whereas, with MLPT thresholds, the hairpin-like structure can be initially seen growing until $t^+ = 42.5$, after which it starts shrinking. This suggests that MLPT is capable of capturing the dynamical changes in the size of a structure by actively modifying the thresholds in time.

To investigate the abundance of hairpin-like structures in the strongly stratified case S_1, manually probed structures from subsection 3.1.5 are tracked in time with MLPT thresholds for both stably stratified cases (S_1, S_2) and the neutrally stratified case (N). Only the primary branches are tracked and the results are reported in the second half of chapter 4. It can be seen from figure 4.14(a) that the average lifetime of the primary branch is relatively higher for the stably stratified cases than the neutrally stratified case. Figure 4.14(b) clearly suggests that the number of interactions (split or merge events) experienced by the hairpin-like structure over a period of 10 viscous time units increases with an increase in the strength of stratification. Case S_1 experiences nearly three times the number of interactions than the case N, 67% of which are merge events. The number of split events are also three times higher than that of case N and an explanation of this may involve the autogeneration mechanism (see figure 4.13 and section 3.4 for an explanation) where new hairpin-like structures are generated from the legs of a primary hairpin that later splits off and continues as a separate entity. The high number of splits may lead to a higher autogeneration rate which is suggested to be the likely cause of the abundance of hairpin-like structures seen in the strongly stratified case S_1. However, it is currently not known if an older primary hairpin is capable of continuously autogenerating new secondary hairpins that split away as it is being advected downstream and away from the wall.

Chapter 5 attempts to provide an explanation of the similar orientation of hairpin-like structures observed in figure 3.14(a) for the strongly stratified case S_1. Due to the limitations of the tracking technique (see the introduction of chapter 5), a somewhat fundamental approach was adopted where hairpin-like structures were treated as slender vortex filaments where the diameter d of the vortex core is much smaller than its characteristic radius of curvature R.

Studying the temporal evolution of the hairpin filament in a stagnant background flow with the local induction approximation (LIA) and the corrected thin-tube model of Klein-Knio with the M1 optimization technique (M1 KK) revealed that both methods correctly capture the corkscrew spiral shape as shown in the work of Hon and Walker (1991). However, when the initial width of the filament is reduced, LIA effectively maintains the spiral pattern while the appearance of this pattern is delayed for the M1 KK technique and is accompanied by outwards stretching of the filament. This is of prime importance since it indicates that the M1 KK method represents the nonlocal effects of self-stretching of the filament accurately.

Finally, with the M1 KK method, the temporal evolution of hairpin filaments with the mean background flow were studied for both stably stratified (S_1, S_2) cases and the neutrally stratified case (N). The filament was initialized as a small, nearly two-dimensional perturbation at a wall-normal height $y^+_{\text{initial}} = 50$ with an inclination angle $\theta_i = 0.1$. Four initial conditions (see table 5.6) with varying δ and Γ were tested initially. For initial condition R_3, with small δ and large Γ, the inclination rate is similar for all background flow profiles and the maximum inclination angle reached $\theta_{i,\max} = 50^\circ$ regardless of the strength of stratification. This is a result of a large self-induced velocity. For other initial conditions, where the self-induced velocity is weaker, $\theta_{i,\max}$ reduces with an increase in the strength of stratification. Repeating the simulation at other heights further shows that $\theta_{i,\max}$ reaches shallower angles with decrease in initial height. The effect of rotation in the Ekman flow has an impact on the spanwise dynamics of the filament. It can be seen from figure 5.19 that the initially symmetric filament becomes asymmetric over time, thereby tilting the vortex in one direction. This degree of tilt increases with an increase in the strength of stratification. Furthermore, the hairpin filament experiences strong advection in the spanwise direction. From figure 5.23, it can be observed that the orientation of the filament changes with increasing height for the stably stratified cases S_1 and S_2. This suggests that hairpins initialized at the same height may have a similar orientation under stable stratification and presents a link between the spanwise orientation of the filament and its initial starting height.

In summary, this thesis finds that despite the effect of global intermittency extending throughout the entire vertical column of the flow including the viscous sublayer, what changes is the spatial organization of coherent structures, particularly that of hairpin-like vortex structures which display an increased abundance and specific orientation characteristics with increasing stability, rather than the geometry of coherent structures which remains mostly unchanged even at strong stability.

6.3 Computing facilities

The computational requirements to analyze the Ekman flow dataset far exceed the resources offered by a traditional desktop or laptop. Initial algorithms were developed and tested on a

Institute	Server name	Storage used (approx.)
Freie Universität Berlin	Department internal storage	2 TB
Zuse Institute Berlin	multiscal storage	2.5 TB
Jülich Supercomputing Centre	JUDAC storage, project dns2share & hku24	120 TB

Table 6.1: List of storage facilities used for this work.

fast desktop machine. Testing was done one on smaller subsets of the channel flow dataset from the John Hopkins Turbulence Database (Graham et al., 2016). The raw and post-processed data were stored at multiple computing facilities as indicated in table 6.1.

6.4 Future perspectives

Minor improvements to the methods developed during the course of this work and improvements to existing techniques (such as addition of viscous diffusion to the simulation of slender vortex filaments) have already been suggested in the conclusion section of other chapters. Here, the focus is placed upon the next stage of research.

Inclination angles of energy carrying structures: By analyzing data from field experiments of the ABL, Carper and Porté-Agel (2004) found silhouettes of inclined vortical features with opposite rotations (resembling hairpin-like structures) in conditionally averaged fields of velocity, vorticity and temperature for strong positive (forward-scatter) and negative (backscatter) subfilter-scale dissipation of energy. Recently, in the poster of Harikrishnan et al. (2022), the authors used the energy budget for weak solutions of incompressible Navier-Stokes equations (see Duchon and Robert (2000)) to study the local (in scale, space and time) energy transfers and dissipation for the strongly stratified case S_1. Close to the Kolmogorov scale, they linked large values of energy transfer and dissipation with hairpin-like structures (educed through the Q-criterion).

Carper and Porté-Agel (2004) further noted that the inclination angles (θ_i) of these structures were a function of atmospheric stability with near-neutral conditions having an inclination of 16° which increases to around $24° - 34°$ under unstable conditions. Various θ_i under the neutral regime for numerous Reynolds numbers have been summarized in table 1 of Liu et al. (2017). In our case, the mean θ_i calculated from the manually identified hairpin-like structures which start within the buffer layer from subsection 3.1.5 was 19.7° for case N and $19.2° - 21°$ for the stably stratified cases. For hairpin filaments initialized at $y^+ = 30$, $\theta_{i,\max} = 21.1°, 17.2°, 14.2°$ for cases N, S_2, S_1, which clearly decreases with increasing stability. Although similar trends were reported for $y^+_{\text{initial}} = 15, 50$, it was also found that $\theta_{i,\max}$ is a strong function of the location of the initial structure and $\theta_{i,\max}$ increases with increasing height. Structure inclination angle is a necessary parameter in the model of Marusic et al. (2010) where near-wall turbulence is predicted with large-scale information from the outer layer. They suggested that VLSMs or superstructures which exist in the logarithmic layer of turbulent boundary layers have a direct impact on near-wall turbulence. In particular,

they noted that within a large low-speed event, the small-scale fluctuations are attenuated whereas within a high-speed event, they are amplified. With this "amplitude modulation" effect linking the VLSMs and the near-wall fluctuations, they suggest a model of the form,

$$u_P^+ = u^*(1 + \beta u_{OL}^+) + \alpha u_{OL}^+ \tag{6.1}$$

where u_P^+ is the signal predicted at a particular wall-normal height y^+, u_{OL}^+ corresponds to the fluctuating large-scale signal at the center of the classical log layer which corresponds to $y^+ = 3.9(Re_\tau)^{(1/2)}$, u^* is the statistically universal signal at y^+ and α, β are coefficients corresponding to superimposition and modulation. The only user-input is u_{OL}^+, which is low-pass filtered retaining streamwise wavelengths $\lambda_x^+ > 7000$. As noted by Marusic et al. (2010), since this signal is equated to one close to the wall, it is shifted in the streamwise direction (Δx) to account for the structure inclination angle θ_i. The streamwise shift Δx can be calculated from the mean inclination angles of hairpin-like structures with $\theta_i = \arctan(\Delta y/\Delta x)$. This type of predictive model can be used as a "wall model" for large eddy simulation (LES) as shown in the work of Inoue et al. (2012).

Similarly, as suggested in the work of Chauhan et al. (2013), the streamwise shift Δx can also be used to accurately estimate the surface shear stress, thereby improving wall models of large eddy simulation (LES). For instance, the shifted Schumann-Grötzbach model (Piomelli et al., 1989) is written as,

$$\tau_{i2}(x, z, t) = \frac{\langle \tau \rangle}{\langle \widetilde{u}(y) \rangle} \widetilde{u}_i(x + \Delta x, y, z, t), \quad (i = 1, 3) \tag{6.2}$$

where Δx is the streamwise shift, $\langle \cdot \rangle$ indicates averaging over horizontal planes, $\widetilde{(\cdot)}$ indicates spatial filtering, $\langle \tau \rangle$ is the mean shear stress, $\langle \widetilde{u}(y) \rangle$ is the mean horizontal velocity at a wall-normal position y and $\widetilde{u}_i(x + \Delta x, y, z, t)$ is the instantaneous filtered velocity obtained at a shifted streamwise location based on the inclination angle of vortical features. The idea of using streamwise shift Δx stems from the observation that the inclined hairpin-structures are associated with large values of energy transfer and essential for forward-scatter and backscatter subfilter-scale dissipation of energy in LES, as elucidated in the beginning of this section. This should prove useful for stable boundary layers, particularly under strong stratification, where the turbulent regions are primarily composed of hairpin-like structures.

Morphology of turbulence under stable conditions: Results of the geometrical characterization from chapter 3 and the temporal evolution of the geometry of Robinson structures from chapter 4 suggest that the geometry of coherent structures are not affected much with increase in stability. This means that the factorized parametrization suggested by Ansorge and Mellado (2016) where the intermittency factor γ, expressed as a function of the Obukhov length, can be used along with the standard approach for modelling the weakly stable boundary layer. However, it should be noted that all the results presented here are for a simplified configuration of the atmospheric boundary layer without the influence of surface heterogeneities. In a recent review paper focusing on heterogeneity over mostly flat, non-mountainous terrain, Bou-Zeid et al. (2020) identified four different classes of heterogeneity (semi-infinite interfaces, statistically-homogeneous patches, large individual patches and unstructured heterogeneity)

and pointed out that even after five decades of careful research, numerous open questions remain, thus highlighting the complexity of the physical processes brought about by surface heterogeneity. This does not even include the small-scale variability arising due to buildings and trees which make up the "roughness sublayer" or hilly terrains. It has been shown that even weak topography and local obstacles, i.e., buildings and trees can induce local circulations on multiple scales (Acevedo and Fitzjarrald, 2003; Mahrt, 2014) which may alter the spatio-temporal distribution of global intermittency. With direct numerical simulations, Coceal et al., 2007 studied the impact of three-dimensional roughness on coherent structures by using a regular array of cubes spread over the surface. While they suggest that there are some qualitative similarities with structures from smooth walls, they note differences in the flow structure close to the roughness elements and relatively larger vortices in the rough case. In a later part of the paper, they examine the feasibility of the hairpin vortex packet model of Adrian et al. (2000) and conclude that the hairpin structures are substantially larger and more inclined than the smooth wall case. They also suggest that not all low momentum regions, i.e., low-speed streaks can be associated with hairpin structures, thus hinting a complex mechanism for the generation of hairpin structures. The hairpin packet model was discussed for the ABL with smooth wall in section 3.4 and future studies can extend the discussion for rough walls. Such studies may lead to a universal hairpin packet model documenting the complete lifecycle of hairpin structures for various situations and the mechanisms involved.

Further complex studies can also involve marginal ice zones (regions of mixed ice and open water surfaces), which are critical for climate models (Fogarty and Bou-Zeid, 2023) or urban canopies involving bluff buildings and permeable trees (Wang et al., 2014). One could also consider a study similar to Huang et al. (2009b) who vary the leaf area index, going from extremely sparse canopy (boundary-layer-like flow) to extremely dense canopy (mixing-layer-like flow). All of the above suggest that more comprehensive studies are necessary before it can be conclusively stated that the geometry of structures do not change much with increasing stability.

A multi-scale approach: The geometrical characterization framework described in chapter 2 can be easily extended for multi-scale analysis similar to that of Bermejo-Moreno and Pullin (2008). In this scenario, a multi-scale decomposition based on, for instance, shearlets (Labate et al., 2005), can be applied on the scalar field of interest to obtain a finite set of component three-dimensional fields, each corresponding to a single scale. The rest of the procedure may remain similar to chapter 2, where each component field is subjected to percolation analysis to determine the optimum threshold, after which the geometrical characterization method (from subsection 2.4) can be applied. This may help clarify if the continuous blob-like to sheet-like transition with decreasing scale seen in isotropic turbulence (Moisy and Jiménez, 2004; Bermejo-Moreno and Pullin, 2008; Leung et al., 2012) can also be observed in wall-bounded flows with rotation and stratification. Bermejo-Moreno and Pullin (2008) linked the change in geometry to the transition seen in volume-data pdfs of the passive scalar fluctuation where the pdfs are Gaussian at larger scales and exponential at smaller scales. Such an analysis may enable the usage of simulation techniques other than LES or DNS such as coherent vortex simulation (Farge et al., 1999; Farge and Schneider, 2001) where a wavelet filter is used to decompose the flow into coherent and incoherent parts and the temporal evolution of the

former is computed while the latter is assumed to be Gaussian and modelled.

Acknowledgements

The work presented in this thesis is a direct result of the unconditional support I received from my supervisors - Prof. Dr. Nikki Vercauteren (U. Köln) and Prof. Dr.-Ing. Rupert Klein (FU Berlin). Prof. Vercauteren, in particular, ensured that my working conditions would remain the same even after she moved to U. Oslo and later, U. Köln by holding regular meetings and actively participating in discussions. My supervisors also gave me complete freedom in pursuing my ideas which led to very interesting results and always kept me motivated. I thank them for giving me the opportunity to pursue this Ph.D. which is supported by the Deutsche Forschungsgemeinschaft (DFG) through grant CRC 1114 "Scaling Cascades in Complex Systems", Project Number 235221301, *Project B07: Self-similar structures in turbulent flows and the construction of LES closures.* My deepest gratitude goes to Dr. Cedrick Ansorge who gave me access to his large DNS database and computing time at Jülich Supercomputing Centre without which these calculations would have not been possible.

I would like to thank Prof. Dr. Bérengère Dubrulle who found my ideas interesting when I presented them during a research visit in November 2019 to her lab in CEA Paris-Saclay. This led to a three month long research stay from November 2021 to January 2022 during which I had ample opportunities to have a peek at the experimental side of fluid mechanics. I would like to thank the entire EXPLOIT team, particularly Dr. Hugues Faller and Dr. Damien Geneste for making my stay in Paris-Saclay a comfortable one with both academic and nonacademic discussions. In conjunction, I would also like to thank the Deutscher Akademischer Austauschdienst (DAAD) and their program "Forschungsstipendien für Doktorandinnen und Doktoranden" which provided the necessary funding for my stay.

I would also like to thank Prof. Dr. Omar M. Knio and Dr. Daniel Margerit for the discussions and support on simulating the hairpin filaments. Special thanks also goes to the Zuse Institute Berlin for providing me with their visualization software Amira with which I was able to produce many of the beautiful results seen this thesis, my paper and the posters submitted to the Gallery of Fluid Motion. I offer my sincerest thanks to all the past members of Project B07, including Dr. Johannes von Lindheim and Marie Rodal, for the many discussions which laid the groundwork for the thesis. I am grateful to the members of AG Klein, AG Vercauteren and other members of the department, particularly Dr. Siva Prasad Chakri Dhanakoti, Dr. Vyacheslav Boyko, Dr. Tom Dörffel and Dr. Mark Schlutow for the warm reception when I first came to Berlin and for providing a nice working atmosphere.

Finally, my deepest thanks goes to my parents, Vijaya and Harikrishnan, and my wife Srishti. Without their encouragement and support, this thesis would not have been possible.

References

Acarlar, MS and CR Smith (1987). "A study of hairpin vortices in a laminar boundary layer. Part 2. Hairpin vortices generated by fluid injection". In: *Journal of Fluid Mechanics* 175, pp. 43–83.

Acevedo, Otávio C and David R Fitzjarrald (2003). "In the core of the night-effects of intermittent mixing on a horizontally heterogeneous surface". In: *Boundary-layer meteorology* 106.1, pp. 1–33.

Adrian, Ronald J, Carl D Meinhart, and Christopher D Tomkins (2000). "Vortex organization in the outer region of the turbulent boundary layer". In: *Journal of fluid Mechanics* 422, pp. 1–54.

Alfredsson, P Henrik, Arne V Johansson, and John Kim (1988). "Turbulence production near walls: the role of flow structures with spanwise asymmetry". In: *Studying Turbulence Using Numerical Simulation Databases-I1* 89, p. 131.

Ansorge, Cedrick (2016). *Analyses of turbulence in the neutrally and stably stratified planetary boundary layer*. Springer.

Ansorge, Cedrick and Juan Pedro Mellado (2016). "Analyses of external and global intermittency in the logarithmic layer of Ekman flow". In: *Journal of Fluid Mechanics* 805, pp. 611–635.

— (2014). "Global intermittency and collapsing turbulence in the stratified planetary boundary layer". In: *Boundary-layer meteorology* 153.1, pp. 89–116.

Aref, Hassan and Edward P Flinchem (1984). "Dynamics of a vortex filament in a shear flow". In: *Journal of Fluid Mechanics* 148, pp. 477–497.

Arms, RJ and Francis R Hama (1965). "Localized-induction concept on a curved vortex and motion of an elliptic vortex ring". In: *The Physics of fluids* 8.4, pp. 553–559.

Atlaskin, Evgeny and Timo Vihma (2012). "Evaluation of NWP results for wintertime nocturnal boundary-layer temperatures over Europe and Finland". In: *Quarterly Journal of the Royal Meteorological Society* 138.667, pp. 1440–1451.

Badel, Raphael (2021). "Registration-based Tracking of Regions Defined by Level Sets of Time-dependent Scalar Fields". MA thesis. Universität Potsdam.

Ballard, D. H. and C. M. Brown (1982). *Computer Vision*. New Jersey, USA: Prentice Hall.

Banisch, Ralf and Péter Koltai (2017). "Understanding the geometry of transport: Diffusion maps for Lagrangian trajectory data unravel coherent sets". In: *Chaos: An Interdisciplinary Journal of Nonlinear Science* 27.3.

Batchelor, GK (1967). *An introduction to fluid dynamics*. Cambridge university press.

Beale, J Thomas and Andrew Majda (1985). "High order accurate vortex methods with explicit velocity kernels". In: *Journal of Computational Physics* 58.2, pp. 188–208.

REFERENCES

Belušić, D and L Mahrt (2012). "Is geometry more universal than physics in atmospheric boundary layer flow?" In: *Journal of Geophysical Research: Atmospheres* 117.D9.

Bermejo-Moreno, Ivan and DI Pullin (2008). "On the non-local geometry of turbulence". In: *Journal of Fluid Mechanics* 603, pp. 101–135.

Besl, Paul J (2012). *Surfaces in range image understanding*. Springer Science & Business Media.

Betchov, Robert (1965). "On the curvature and torsion of an isolated vortex filament". In: *Journal of Fluid Mechanics* 22.3, pp. 471–479.

Bisset, David K, Julian CR Hunt, and Michael M Rogers (2002). "The turbulent/non-turbulent interface bounding a far wake". In: *Journal of Fluid Mechanics* 451, pp. 383–410.

Bogard, DG and WG Tiederman (1986). "Burst detection with single-point velocity measurements". In: *Journal of Fluid Mechanics* 162, pp. 389–413.

Bou-Zeid, Elie et al. (2020). "The persistent challenge of surface heterogeneity in boundary-layer meteorology: a review". In: *Boundary-Layer Meteorology* 177, pp. 227–245.

Brown, Garry L and Andrew SW Thomas (1977). "Large structure in a turbulent boundary layer". In: *The Physics of fluids* 20.10, S243–S252.

Bußmann, A et al. (2022). "Tracking and analysis of interfaces and flow structures in multiphase flows". In: *Computers & Fluids* 248, p. 105665.

Butcher, John Charles (2016). *Numerical methods for ordinary differential equations*. John Wiley & Sons.

Cabral, Brian and Leith Casey Leedom (1993). "Imaging vector fields using line integral convolution". In: *Proceedings of the 20th annual conference on Computer graphics and interactive techniques*, pp. 263–270.

Callegari, AJ and Lu Ting (1978). "Motion of a curved vortex filament with decaying vortical core and axial velocity". In: *SIAM Journal on Applied Mathematics* 35.1, pp. 148–175.

Carper, Matthew A and Fernando Porté-Agel (2004). "The role of coherent structures in subfilter-scale dissipation of turbulence measured in the atmospheric surface layer". In: *Journal of Turbulence* 5.1, p. 040.

Cermak, Jack E (1971). "Laboratory simulation of the atmospheric boundary layer". In: *Aiaa Journal* 9.9, pp. 1746–1754.

Chakraborty, Pinaki, S Balachandar, and Ronald J Adrian (2005). "On the relationships between local vortex identification schemes". In: *Journal of fluid mechanics* 535, p. 189.

Chauhan, Kapil et al. (2013). "Structure inclination angles in the convective atmospheric surface layer". In: *Boundary-layer meteorology* 147.1, pp. 41–50.

Chen, Chyan-Hai P and Ron F Blackwelder (1978). "Large-scale motion in a turbulent boundary layer: a study using temperature contamination". In: *Journal of Fluid Mechanics* 89.1, pp. 1–31.

Choi, Taejin et al. (2004). "Turbulent exchange of heat, water vapor, and momentum over a Tibetan prairie by eddy covariance and flux variance measurements". In: *Journal of Geophysical Research: Atmospheres* 109.D21.

Chong, Min S, Anthony E Perry, and Brian J Cantwell (1990). "A general classification of three-dimensional flow fields". In: *Physics of Fluids A: Fluid Dynamics* 2.5, pp. 765–777.

Chorin, Alexandre Joel (1980). "Flame advection and propagation algorithms". In: *Journal of computational physics* 35.1, pp. 1–11.

Chu, CC and RE Falco (1988). "Vortex ring/viscous wall layer interaction model of the turbulence production process near walls". In: *Experiments in Fluids* 6.5, pp. 305–315.

Coceal, O et al. (2007). "Structure of turbulent flow over regular arrays of cubical roughness". In: *Journal of Fluid Mechanics* 589, pp. 375–409.

Corino, Edward Robert and Robert S Brodkey (1969). "A visual investigation of the wall region in turbulent flow". In: *Journal of Fluid Mechanics* 37.1, pp. 1–30.

Corrsin, Stanley and Alan L Kistler (1955). "Free-stream boundaries of turbulent flows". In: *NACA Report No. 1244*.

Crow, Steven C (1970). "Stability theory for a pair of trailing vortices". In: *AIAA journal* 8.12, pp. 2172–2179.

Cucitore, R, Maurizio Quadrio, and Arturo Baron (1999). "On the effectiveness and limitations of local criteria for the identification of a vortex". In: *European Journal of Mechanics-B/Fluids* 18.2, pp. 261–282.

Da Silva, Carlos B, Rodrigo R Taveira, and Guillem Borrell (2014). "Characteristics of the turbulent/nonturbulent interface in boundary layers, jets and shear-free turbulence". In: *Journal of Physics: Conference Series*. Vol. 506. 1. IOP Publishing, p. 012015.

Del Álamo, Juan C et al. (2006). "Self-similar vortex clusters in the turbulent logarithmic region". In: *Journal of Fluid Mechanics* 561, pp. 329–358.

Deusebio, Enrico et al. (2014). "A numerical study of the unstratified and stratified Ekman layer". In: *Journal of fluid mechanics* 755, pp. 672–704.

Dey, Tamal K and Joshua A Levine (2008). "Delaunay meshing of isosurfaces". In: *The Visual Computer* 24.6, pp. 411–422.

Dice, Lee R (1945). "Measures of the amount of ecologic association between species". In: *Ecology* 26.3, pp. 297–302.

Do Carmo, Manfredo P (2016). *Differential geometry of curves and surfaces: revised and updated second edition*. Courier Dover Publications.

Drobinski, Philippe and Ralph C Foster (2003). "On the origin of near-surface streaks in the neutrally-stratified planetary boundary layer". In: *Boundary-layer meteorology* 108.2, pp. 247–256.

Duchon, Jean and Raoul Robert (2000). "Inertial energy dissipation for weak solutions of incompressible Euler and Navier-Stokes equations". In: *Nonlinearity* 13.1, p. 249.

Elsas, JH and L Moriconi (2017). "Vortex identification from local properties of the vorticity field". In: *Physics of Fluids* 29.1, p. 015101.

Falco, R (1980). "The production of turbulence near a wall". In: *13th Fluid and PlasmaDynamics Conference*, p. 1356.

Falco, RE (1977). "Coherent motions in the outer region of turbulent boundary layers". In: *The Physics of Fluids* 20.10, S124–S132.

Fang, Jiannong and Fernando Porté-Agel (2015). "Large-eddy simulation of very-large-scale motions in the neutrally stratified atmospheric boundary layer". In: *Boundary-Layer Meteorology* 155, pp. 397–416.

Farge, Marie and Kai Schneider (2001). "Coherent vortex simulation (CVS), a semi-deterministic turbulence model using wavelets". In: *Flow, Turbulence and Combustion* 66, pp. 393–426.

Farge, Marie, Kai Schneider, and Nicholas Kevlahan (1999). "Non-Gaussianity and coherent vortex simulation for two-dimensional turbulence using an adaptive orthogonal wavelet basis". In: *Physics of Fluids* 11.8, pp. 2187–2201.

Fiedler, HE (1988). "Coherent structures in turbulent flows". In: *Progress in Aerospace Sciences* 25.3, pp. 231–269.

Flores, O and JJ Riley (2011). "Analysis of turbulence collapse in the stably stratified surface layer using direct numerical simulation". In: *Boundary-Layer Meteorology* 139.2, pp. 241–259.

Fogarty, Joseph and Elie Bou-Zeid (2023). "The atmospheric boundary layer above the marginal ice zone: scaling, surface fluxes, and secondary circulations". In: *Boundary-Layer Meteorology* 189.1, pp. 53–76.

Foias, Ciprian et al. (2001). *Navier-Stokes equations and turbulence*. Vol. 83. Cambridge University Press.

Fouard, Céline et al. (2006). "Blockwise processing applied to brain microvascular network study". In: *IEEE Transactions on Medical Imaging* 25.10, pp. 1319–1328.

Gardner, Martin (1971). *Sixth book of mathematical games from Scientific American*. WH Freeman.

Garratt, John Roy (1994). "The atmospheric boundary layer". In: *Earth-Science Reviews* 37.1-2, pp. 89–134.

Graham, J et al. (2016). "A web services accessible database of turbulent channel flow and its use for testing a new integral wall model for LES". In: *Journal of Turbulence* 17.2, pp. 181–215.

Gray, Alfred, Elsa Abbena, and Simon Salamon (2017). *Modern differential geometry of curves and surfaces with Mathematica*. Chapman and Hall/CRC.

Green, Melissa A, Clarence W Rowley, and George Haller (2007). "Detection of Lagrangian coherent structures in three-dimensional turbulence". In: *Journal of Fluid Mechanics* 572, p. 111.

Gucci, Federica et al. (2023). "Sources of anisotropy in the Reynolds stress tensor in the Stable Boundary Layer". In: *Quarterly Journal of the Royal Meteorological Society*.

Günther, Tobias and Holger Theisel (2018). "The state of the art in vortex extraction". In: *Computer Graphics Forum*. Vol. 37. Wiley Online Library, pp. 149–173.

Ha, Kyung-Ja et al. (2007). "Evaluation of boundary layer similarity theory for stable conditions in CASES-99". In: *Monthly Weather Review* 135.10, pp. 3474–3483.

Hairer, Ernst, Gerhard Wanner, and Syvert P Nørsett (1993). "Runge-kutta and extrapolation methods". In: *Solving Ordinary Differential Equations I: Nonstiff Problems*, pp. 129–353.

Halios, Christos H, Costas G Helmis, and Dimosthenis N Asimakopoulos (2014). "Studying geometric structures in meso-scale flows". In: *Frontiers in Environmental Science* 2, p. 47.

Haller, George (2015). "Lagrangian coherent structures". In: *Annu. Rev. Fluid Mech* 47.1, pp. 137–162.

Haller, George et al. (2016). "Defining coherent vortices objectively from the vorticity". In: *Journal of Fluid Mechanics* 795, pp. 136–173.

Hama, Francis R (1962). "Progressive deformation of a curved vortex filament by its own induction". In: *The Physics of Fluids* 5.10, pp. 1156–1162.

Harikrishnan, Abhishek et al. (2021). "Lagrangian hairpins in atmospheric boundary layers". In: *Gallery of Fluid Motion*.

Harikrishnan, Abhishek et al. (2023). "On the motion of hairpin filaments in the atmospheric boundary layer". In: *arXiv:2303.09302. Accepted - Physics of Fluids*.

Harikrishnan, Abhishek et al. (2022). "Scale-to-scale energy transfers in the atmospheric boundary layer". In: *Gallery of Fluid Motion*.

Harikrishnan, Abhishek et al. (2020). "The curious nature of hairpin vortices. Gallery of Fluid Motion." In: *Gallery of Fluid Motion*.

Head, MR and P Bandyopadhyay (1981). "New aspects of turbulent boundary-layer structure". In: *Journal of fluid mechanics* 107, pp. 297–338.

Heisel, Michael et al. (2018). "The spatial structure of the logarithmic region in very-high-Reynolds-number rough wall turbulent boundary layers". In: *Journal of Fluid Mechanics* 857, pp. 704–747.

Hommema, Scott E and Ronald J Adrian (2003). "Packet structure of surface eddies in the atmospheric boundary layer". In: *Boundary-Layer Meteorology* 106.1, pp. 147–170.

Hon, T-L and J David A Walker (1991). "Evolution of hairpin vortices in a shear flow". In: *Computers & fluids* 20.3, pp. 343–358.

Hopfinger, EJ (1987). "Turbulence in stratified fluids: A review". In: *Journal of Geophysical Research: Oceans* 92.C5, pp. 5287–5303.

Horiguchi, Mitsuaki et al. (2010). "Observations of coherent turbulence structures in the near-neutral atmospheric boundary layer". In: *Boundary-layer meteorology* 136.1, pp. 25–44.

Huang, J, M Cassiani, and JD Albertson (2009a). "Analysis of coherent structures within the atmospheric boundary layer". In: *Boundary-layer meteorology* 131, pp. 147–171.

— (2009b). "The effects of vegetation density on coherent turbulent structures within the canopy sublayer: a large-eddy simulation study". In: *Boundary-layer meteorology* 133, pp. 253–275.

Hunt, Julian CR, Alan A Wray, and Parviz Moin (1988). "Eddies, streams, and convergence zones in turbulent flows". In: *Proceedings of the CTR Summer Program 1988*.

Hutchins, N and Ivan Marusic (2007). "Evidence of very long meandering features in the logarithmic region of turbulent boundary layers". In: *Journal of Fluid Mechanics* 579, pp. 1–28.

Hutchins, Nicholas et al. (2012). "Towards reconciling the large-scale structure of turbulent boundary layers in the atmosphere and laboratory". In: *Boundary-layer meteorology* 145.2, pp. 273–306.

Inagaki, Atsushi and Manabu Kanda (2010). "Organized structure of active turbulence over an array of cubes within the logarithmic layer of atmospheric flow". In: *Boundary-layer meteorology* 135.2, pp. 209–228.

Inoue, M et al. (2012). "Inner-layer intensities for the flat-plate turbulent boundary layer combining a predictive wall-model with large-eddy simulations". In: *Physics of Fluids* 24.7.

REFERENCES

Jayaraman, Balaji and James G Brasseur (2021). "Transition in atmospheric boundary layer turbulence structure from neutral to convective, and large-scale rolls". In: *Journal of Fluid Mechanics* 913.

Jeong, Jinhee and Fazle Hussain (1995). "On the identification of a vortex". In: *Journal of fluid mechanics* 285, pp. 69–94.

Ji, Guangfeng and Han-Wei Shen (2006). "Feature tracking using earth mover's distance and global optimization". In: *Pacific graphics*. Vol. 2.

Jiang, Xianyang et al. (2022). "The evolution of coherent vortical structures in increasingly turbulent stratified shear layers". In: *Journal of Fluid Mechanics* 947, A30.

Jiménez, Javier (2018). "Coherent structures in wall-bounded turbulence". In: *Journal of Fluid Mechanics* 842.

Johansson, Arne V, P Henrik Alfredsson, and John Kim (1991). "Evolution and dynamics of shear-layer structures in near-wall turbulence". In: *Journal of Fluid Mechanics* 224, pp. 579–599.

Johansson, AV, PH Alfredsson, and J Kim (1987). "Shear-layer structures in near-wall turbulence". In: *Proceedings of the CTR Summer Program 1987*.

Ju, Tao et al. (2002). "Dual contouring of hermite data". In: *Proceedings of the 29th annual conference on Computer graphics and interactive techniques*, pp. 339–346.

Katul, Gabriel et al. (1997a). "The ejection-sweep character of scalar fluxes in the unstable surface layer". In: *Boundary-Layer Meteorology* 83.1, pp. 1–26.

Katul, Gabriel et al. (2006). "The relative importance of ejections and sweeps to momentum transfer in the atmospheric boundary layer". In: *Boundary-layer meteorology* 120.3, pp. 367–375.

Katul, Gabriel et al. (1997b). "Turbulent eddy motion at the forest-atmosphere interface". In: *Journal of Geophysical Research: Atmospheres* 102.D12, pp. 13409–13421.

Katul, GG (2019). "The anatomy of large-scale motion in atmospheric boundary layers". In: *Journal of Fluid Mechanics* 858, pp. 1–4.

Khanna, Samir and James G Brasseur (1998). "Three-dimensional buoyancy-and shear-induced local structure of the atmospheric boundary layer". In: *Journal of Atmospheric Sciences* 55.5, pp. 710–743.

Kim, H, SJ Kline, and WC Reynolds (1971). "The production of turbulence near a smooth wall in a turbulent boundary layer". In: *Journal of Fluid Mechanics* 50.1, pp. 133–160.

Kim, John, Parviz Moin, and Robert Moser (1987). "Turbulence statistics in fully developed channel flow at low Reynolds number". In: *Journal of fluid mechanics* 177, pp. 133–166.

Klein, Rupert and Omar M Knio (1995). "Asymptotic vorticity structure and numerical simulation of slender vortex filaments". In: *Journal of Fluid Mechanics* 284, pp. 275–321.

Klein, Rupert, Omar M Knio, and Lu Ting (1996). "Representation of core dynamics in slender vortex filament simulations". In: *Physics of Fluids* 8.9, pp. 2415–2425.

Klein, Rupert and Andrew J Majda (1991a). "Self-stretching of a perturbed vortex filament I. The asymptotic equation for deviations from a straight line". In: *Physica D: Nonlinear Phenomena* 49.3, pp. 323–352.

— (1991b). "Self-stretching of perturbed vortex filaments: II. Structure of solutions". In: *Physica D: Nonlinear Phenomena* 53.2-4, pp. 267–294.

Kline, Stephen J (1978). “The role of visualization in the study of the structure of the turbulent boundary layer”. In: *Coherent Structure of Turbulent Boundary Layers*, pp. 1–26.

Kline, Stephen J et al. (1967). “The structure of turbulent boundary layers”. In: *Journal of Fluid Mechanics* 30.4, pp. 741–773.

Knio, Omar M and Ahmed F Ghoniem (1990). “Numerical study of a three-dimensional vortex method”. In: *Journal of Computational Physics* 86.1, pp. 75–106.

— (1991). “Three-dimensional vortex simulation of rollup and entrainment in a shear layer”. In: *Journal of Computational Physics* 97.1, pp. 172–223.

Knio, Omar M and R Klein (2000). “Improved thin-tube models for slender vortex simulations”. In: *Journal of Computational Physics* 163.1, pp. 68–82.

Koenderink, Jan J and Andrea J Van Doorn (1992). “Surface shape and curvature scales”. In: *Image and vision computing* 10.8, pp. 557–564.

Kovasznay, Leslie SG, Valdis Kibens, and Ron F Blackwelder (1970). “Large-scale motion in the intermittent region of a turbulent boundary layer”. In: *Journal of Fluid Mechanics* 41.2, pp. 283–325.

Kral, Stephan T et al. (2021). “The innovative strategies for observations in the Arctic Atmospheric Boundary Layer Project (ISOBAR): Unique finescale observations under stable and very stable conditions”. In: *Bulletin of the American Meteorological Society* 102.2, E218–E243.

Küchemann, D (1965). “Report on the IUTAM symposium on concentrated vortex motions in fluids”. In: *Journal of Fluid Mechanics* 21.1, pp. 1–20.

Labate, Demetrio et al. (2005). “Sparse multidimensional representation using shearlets”. In: *Wavelets XI*. Vol. 5914. SPIE, pp. 254–262.

Lee, Moon Joo, John Kim, and Parviz Moin (1990). “Structure of turbulence at high shear rate”. In: *Journal of Fluid Mechanics* 216, pp. 561–583.

Lenschow, Donald H et al. (1988). “The stably stratified boundary layer over the Great Plains: I. Mean and turbulence structure”. In: *Topics in Micrometeorology. A Festschrift for Arch Dyer*, pp. 95–121.

Leonard, Anthony (1985). “Computing three-dimensional incompressible flows with vortex elements”. In: *Annual review of fluid mechanics* 17.1, pp. 523–559.

Leung, T, N Swaminathan, and PA Davidson (2012). “Geometry and interaction of structures in homogeneous isotropic turbulence”. In: *Journal of Fluid Mechanics* 710, pp. 453–481.

Lewiner, Thomas et al. (2003). “Efficient implementation of marching cubes’ cases with topological guarantees”. In: *Journal of graphics tools* 8.2, pp. 1–15.

Li, Dan and Elie Bou-Zeid (2011). “Coherent structures and the dissimilarity of turbulent transport of momentum and scalars in the unstable atmospheric surface layer”. In: *Boundary-layer meteorology* 140.2, pp. 243–262.

Lin, Ching-Long et al. (1996). “Coherent structures and dynamics in a neutrally stratified planetary boundary layer flow”. In: *Physics of Fluids* 8.10, pp. 2626–2639.

Lindheim, Johannes von et al. (2021). “Definition, detection, and tracking of persistent structures in atmospheric flows”. In: *arXiv:2111.13645*.

Liu, Hong-You, Tian-Li Bo, and Yi-Rui Liang (2017). "The variation of large-scale structure inclination angles in high Reynolds number atmospheric surface layers". In: *Physics of Fluids* 29.3, p. 035104.

Lorensen, William E and Harvey E Cline (1987). "Marching cubes: A high resolution 3D surface construction algorithm". In: *ACM siggraph computer graphics* 21.4, pp. 163–169.

Lozano-Durán, Adrián, Oscar Flores, and Javier Jiménez (2012). "The three-dimensional structure of momentum transfer in turbulent channels". In: *Journal of Fluid Mechanics* 694, pp. 100–130.

Lozano-Durán, Adrián and Javier Jiménez (2014). "Time-resolved evolution of coherent structures in turbulent channels: characterization of eddies and cascades". In: *Journal of fluid mechanics* 759, pp. 432–471.

Lugt, Hans J (1979). "The dilemma of defining a vortex". In: *Recent developments in theoretical and experimental fluid mechanics*. Springer, pp. 309–321.

Mahrt, L (2010). "Common microfronts and other solitary events in the nocturnal boundary layer". In: *Quarterly Journal of the Royal Meteorological Society* 136.652, pp. 1712–1722.

— (1998a). "Nocturnal boundary-layer regimes". In: *Boundary-layer meteorology* 88.2, pp. 255–278.

Mahrt, L and Dean Vickers (2003). "Formulation of turbulent fluxes in the stable boundary layer". In: *Journal of the atmospheric sciences* 60.20, pp. 2538–2548.

Mahrt, Larry (1989). "Intermittency of atmospheric turbulence". In: *Journal of the Atmospheric Sciences* 46.1, pp. 79–95.

— (2014). "Stably stratified atmospheric boundary layers". In: *Annu. Rev. Fluid Mech* 46.1, pp. 23–45.

— (1998b). "Stratified atmospheric boundary layers and breakdown of models". In: *Theoretical and computational fluid dynamics* 11.3-4, pp. 263–279.

Malhi, Yadvinder S (1995). "The significance of the dual solutions for heat fluxes measured by the temperature fluctuation method in stable conditions". In: *Boundary-Layer Meteorology* 74.4, pp. 389–396.

Margerit, Daniel, Pierre Brancher, and André Giovannini (2004). "Implementation and validation of a slender vortex filament code: Its application to the study of a four-vortex wake model". In: *International Journal for Numerical Methods in Fluids* 44.2, pp. 175–196.

Marusic, I, R Mathis, and N Hutchins (2010). "Predictive model for wall-bounded turbulent flow". In: *Science* 329.5988, pp. 193–196.

Marusic, Ivan and Weston DC Heuer (2007). "Reynolds number invariance of the structure inclination angle in wall turbulence". In: *Physical review letters* 99.11, p. 114504.

Mason, Paul J (1989). "Large-eddy simulation of the convective atmospheric boundary layer". In: *Journal of Atmospheric Sciences* 46.11, pp. 1492–1516.

McNider, RT, JR Christy, and A Biazar (2010). "A stable boundary layer perspective on global temperature trends". In: *IOP Conference Series: Earth and Environmental Science*. Vol. 13. 1. IOP Publishing, p. 012003.

Misra, Ashish (1997). "Large-eddy simulation using the stretched-vortex SGS model". In: *Advances in DNS/LES, Proceedings of the 1st AFOSR International Conference on DNS/LES*. Citeseer, pp. 385–392.

Misra, Ashish and Dale I Pullin (1997). "A vortex-based subgrid stress model for large-eddy simulation". In: *Physics of Fluids* 9.8, pp. 2443–2454.

Moin, Parviz, Anthony Leonard, and John Kim (1986). "Evolution of a curved vortex filament into a vortex ring". In: *The Physics of fluids* 29.4, pp. 955–963.

Moisy, Frédéric and Javier Jiménez (2004). "Geometry and clustering of intense structures in isotropic turbulence". In: *Journal of fluid mechanics* 513, pp. 111–133.

Monin, AS (1970). "The atmospheric boundary layer". In: *Annual Review of Fluid Mechanics* 2.1, pp. 225–250.

Moore, DW (1972). "Finite amplitude waves on aircraft trailing vortices". In: *Aeronautical Quarterly* 23.4, pp. 307–314.

Nagaosa, Ryuichi and Robert A Handler (2003). "Statistical analysis of coherent vortices near a free surface in a fully developed turbulence". In: *Physics of Fluids* 15.2, pp. 375–394.

Nieuwstadt, FTM and PG Duynkerke (1996). "Turbulence in the atmospheric boundary layer". In: *Atmospheric Research* 40.2-4, pp. 111–142.

O'Farrell, Clara and M Pino Martín (2009). "Chasing eddies and their wall signature in DNS data of turbulent boundary layers". In: *Journal of Turbulence* 10, N15.

Ohya, Yuji, David E Neff, and Robert N Meroney (1997). "Turbulence structure in a stratified boundary layer under stable conditions". In: *Boundary-Layer Meteorology* 83, pp. 139–162.

Oncley, Steven P, Oscar Hartogensis, and Chenning Tong (2016). "Whirlwinds and hairpins in the atmospheric surface layer". In: *Journal of the Atmospheric Sciences* 73.12, pp. 4927–4943.

Optis, Michael, Adam Monahan, and Fred C Bosveld (2016). "Limitations and breakdown of Monin–Obukhov similarity theory for wind profile extrapolation under stable stratification". In: *Wind Energy* 19.6, pp. 1053–1072.

— (2014). "Moving beyond Monin–Obukhov similarity theory in modelling wind-speed profiles in the lower atmospheric boundary layer under stable stratification". In: *Boundary-layer meteorology* 153, pp. 497–514.

Pal, Nikhil R and Sankar K Pal (1993). "A review on image segmentation techniques". In: *Pattern recognition* 26.9, pp. 1277–1294.

Panton, Ronald L (2001). "Overview of the self-sustaining mechanisms of wall turbulence". In: *Progress in Aerospace Sciences* 37.4, pp. 341–383.

Piomelli, Ugo et al. (1989). "New approximate boundary conditions for large eddy simulations of wall-bounded flows". In: *Physics of Fluids A: Fluid Dynamics* 1.6, pp. 1061–1068.

Pope, Stephen B (2001). *Turbulent flows*.

Post, Frits H et al. (2003). "The state of the art in flow visualisation: Feature extraction and tracking". In: *Computer Graphics Forum*. Vol. 22. 4. Wiley Online Library, pp. 775–792.

Poulos, Gregory S et al. (2002). "CASES-99: A comprehensive investigation of the stable nocturnal boundary layer". In: *Bulletin of the American Meteorological Society* 83.4, pp. 555–582.

Puthenveettil, Baburaj A and Jaywant H Arakeri (2005). "Plume structure in high-Rayleigh-number convection". In: *Journal of Fluid Mechanics* 542, pp. 217–249.

Robinson, Stephen Kern (1991). "The kinematics of turbulent boundary layer structure". In: *NASA STI/Recon Technical Report N* 91.

Rosenhead, Louis (1930). "The spread of vorticity in the wake behind a cylinder". In: *Proceedings of the Royal Society of London. Series A, Containing papers of a mathematical and physical character* 127.806, pp. 590–612.

Salesky, ST and W Anderson (2018). "Buoyancy effects on large-scale motions in convective atmospheric boundary layers: implications for modulation of near-wall processes". In: *Journal of Fluid Mechanics* 856, pp. 135–168.

Samtaney, Ravi et al. (1994). "Visualizing features and tracking their evolution". In: *Computer* 27.7, pp. 20–27.

Schmidt, Helmut and Ulrich Schumann (1989). "Coherent structure of the convective boundary layer derived from large-eddy simulations". In: *Journal of Fluid Mechanics* 200, pp. 511–562.

Schreiner, John, Carlos E Scheidegger, and Claudio T Silva (2006). "High-quality extraction of isosurfaces from regular and irregular grids". In: *IEEE Transactions on Visualization and Computer Graphics* 12.5, pp. 1205–1212.

Schumacher, Joerg, Katepalli R Sreenivasan, and PK Yeung (2005). "Very fine structures in scalar mixing". In: *Journal of Fluid Mechanics* 531, pp. 113–122.

Shadden, Shawn C, Francois Lekien, and Jerrold E Marsden (2005). "Definition and properties of Lagrangian coherent structures from finite-time Lyapunov exponents in two-dimensional aperiodic flows". In: *Physica D: Nonlinear Phenomena* 212.3-4, pp. 271–304.

Shah, Stimit and Elie Bou-Zeid (2014a). "Very-large-scale motions in the atmospheric boundary layer educed by snapshot proper orthogonal decomposition". In: *Boundary-layer meteorology* 153.3, pp. 355–387.

Shah, Stimit K and Elie Bou-Zeid (2014b). "Direct numerical simulations of turbulent Ekman layers with increasing static stability: modifications to the bulk structure and second-order statistics". In: *Journal of Fluid Mechanics* 760, pp. 494–539.

Sharan, Maithili and SG Gopalakrishnan (1997). "Bhopal gas accident: a numerical simulation of the gas dispersion event". In: *Environmental Modelling & Software* 12.2-3, pp. 135–141.

Shaw, Roger H, Jahangir Tavangar, and David P Ward (1983). "Structure of the Reynolds stress in a canopy layer". In: *Journal of Applied Meteorology and Climatology* 22.11, pp. 1922–1931.

Siggia, Eric D (1994). "High Rayleigh number convection". In: *Annual review of fluid mechanics* 26.1, pp. 137–168.

Silver, Deborah (1995). "Object-oriented visualization". In: *IEEE Computer Graphics and Applications* 15.3, pp. 54–62.

Silver, Deborah and Xin Wang (1997). "Tracking and visualizing turbulent 3d features". In: *IEEE Transactions on Visualization and Computer Graphics* 3.2, pp. 129–141.

— (1998). "Tracking scalar features in unstructured data sets". In: *Proceedings Visualization'98 (Cat. No. 98CB36276)*. IEEE, pp. 79–86.

— (1996). "Volume tracking". In: *Proceedings of Seventh Annual IEEE Visualization'96*. IEEE, pp. 157–164.

Smedman, Ann-Sofi, Michael Tjernström, and Ulf Högström (1993). "Analysis of the turbulence structure of a marine low-level jet". In: *Boundary-layer meteorology* 66, pp. 105–126.

Stalling, Detlev, Malte Westerhoff, and Hans-Christian Hege (2005). "Amira: a Highly Interactive System for Visual Data Analysis". In: *The Visualization Handbook*. Elsevier, pp. 749–767.

Stull, Roland B (1988). *An introduction to boundary layer meteorology*. Vol. 13. Springer Science & Business Media.

Sun, Jielun et al. (2004). "Atmospheric disturbances that generate intermittent turbulence in nocturnal boundary layers". In: *Boundary-layer meteorology* 110.2, pp. 255–279.

Sun, Jielun et al. (2002). "Intermittent turbulence associated with a density current passage in the stable boundary layer". In: *Boundary-Layer Meteorology* 105, pp. 199–219.

Sun, Jielun et al. (2015). "Review of wave-turbulence interactions in the stable atmospheric boundary layer". In: *Reviews of geophysics* 53.3, pp. 956–993.

Sun, Jielun et al. (2012). "Turbulence regimes and turbulence intermittency in the stable boundary layer during CASES-99". In: *Journal of the Atmospheric Sciences* 69.1, pp. 338–351.

Terradellas, E et al. (2005). "Analysis of oscillations in the stable atmospheric boundary layer using wavelet methods". In: *Boundary-layer meteorology* 114, pp. 489–518.

Theodorsen, Theodore (1952). "Mechanisms of turbulence". In: *Proceedings of the 2ˆ< nd> Midwestern Conference on Fluid Mechanics, 1952*.

Ting, Lu and Rupert Klein (1991). *Viscous vortical flows*. Vol. 374. Springer.

Townsend, AA (1961). "Equilibrium layers and wall turbulence". In: *Journal of Fluid Mechanics* 11.1, pp. 97–120.

— (1948). "Local isotropy in the turbulent wake of a cylinder". In: *Australian Journal of Chemistry* 1.2, pp. 161–174.

Van de Wiel, BJH et al. (2002). "Intermittent turbulence and oscillations in the stable boundary layer over land. Part I: A bulk model". In: *Journal of the atmospheric sciences* 59.5, pp. 942–958.

Van de Wiel, BJH et al. (2012). "The minimum wind speed for sustainable turbulence in the nocturnal boundary layer". In: *Journal of the Atmospheric Sciences* 69.11, pp. 3116–3127.

Vercauteren, Nikki et al. (2019). "Scale interactions and anisotropy in stable boundary layers". In: *Quarterly Journal of the Royal Meteorological Society* 145.722, pp. 1799–1813.

Wallace, James M, Helmut Eckelmann, and Robert S Brodkey (1972). "The wall region in turbulent shear flow". In: *Journal of Fluid Mechanics* 54.1, pp. 39–48.

Wang, Linlin et al. (2014). "Turbulent transport of momentum and scalars above an urban canopy". In: *Boundary-Layer Meteorology* 150, pp. 485–511.

Watanabe, Tomoaki et al. (2019). "Hairpin vortices and highly elongated flow structures in a stably stratified shear layer". In: *Journal of Fluid Mechanics* 878, pp. 37–61.

Widnall, Sheila E (1975). "The structure and dynamics of vortex filaments". In: *Annual Review of Fluid Mechanics* 7.1, pp. 141–165.

Willis, GE and JW Deardorff (1974). "A laboratory model of the unstable planetary boundary layer". In: *Journal of Atmospheric Sciences* 31.5, pp. 1297–1307.

— (1979). "Laboratory observations of turbulent penetrative-convection planforms". In: *Journal of Geophysical Research: Oceans* 84.C1, pp. 295–302.

Willmarth, WW and SS Lu (1972). "Structure of the Reynolds stress near the wall". In: *Journal of Fluid Mechanics* 55.1, pp. 65–92.

Yao, Jie and Fazle Hussain (2020). "On singularity formation via viscous vortex reconnection". In: *Journal of Fluid Mechanics* 888.

— (2022). "Vortex reconnection and turbulence cascade". In: *Annual Review of Fluid Mechanics* 54, pp. 317–347.

Young, George S et al. (2002). "Rolls, streets, waves, and more: A review of quasi-two-dimensional structures in the atmospheric boundary layer". In: *Bulletin of the American Meteorological Society* 83.7, pp. 997–1002.

Zhang, Cha and Tsuhan Chen (2001). "Efficient feature extraction for 2D/3D objects in mesh representation". In: *Proceedings 2001 International Conference on Image Processing (Cat. No. 01CH37205)*. Vol. 3. IEEE, pp. 935–938.

Zhou, Hong (1996). *Numerical analysis of slender vortex motion*. University of California, Berkeley.

Zhou, Jigen, Ronald J Adrian, and S Balachandar (1996). "Autogeneration of near-wall vortical structures in channel flow". In: *Physics of Fluids* 8.1, pp. 288–290.

Zhou, Jigen et al. (1999). "Mechanisms for generating coherent packets of hairpin vortices in channel flow". In: *Journal of fluid mechanics* 387, pp. 353–396.

A

Grouping indices for marching cubes correction

Case	Indices	Case	Indices	Case	Indices	Case	Indices	Case	Indices
0	-	52	[2], [4, 5]	104	[3], [5, 6]	156	-	208	-
1	-	53	[2], [0, 4, 5]	105	[0, 3], [5, 6]	157	-	209	-
2	-	54	-	106	[3], [1, 5, 6]	158	-	210	[1], [4, 6, 7]
3	-	55	-	107	-	159	-	211	-
4	-	56	[3], [4, 5]	108	-	160	[5], [7]	212	-
5	[0], [2]	57	-	109	-	161	[0], [5], [7]	213	-
6	-	58	[3], [1, 4, 5]	110	-	162	[1, 5], [7]	214	-
7	-	59	-	111	-	163	[0, 1, 5], [7]	215	[3], [5]
8	-	60	[2, 3], [4, 5]	112	-	164	[2], [5], [7]	216	-
9	-	61	-	113	-	165	[0], [2], [5], [7]	217	-
10	[1], [3]	62	-	114	-	166	[1, 2, 5], [7]	218	[1], [3, 4, 6, 7]
11	-	63	-	115	-	167	[0, 1, 2, 5], [7]	219	-
12	-	64	-	116	-	168	[3, 7], [5]	220	-
13	-	65	[0], [6]	117	-	169	[0, 3, 7], [5]	221	-
14	-	66	[1], [6]	118	-	170	[1, 5], [3, 7]	222	-
15	-	67	[0, 1], [6]	119	-	171	-	223	-
16	-	68	-	120	[3], [4, 5, 6]	172	[2, 3, 7], [5]	224	-
17	-	69	[0], [2, 6]	121	-	173	[0, 2, 3, 7], [5]	225	[0], [5, 6, 7]
18	[1], [4]	70	-	122	[3], [1, 4, 5, 6]	174	-	226	-
19	-	71	-	123	-	175	-	227	-
20	[2], [4]	72	[3], [6]	124	-	176	-	228	-
21	[0, 4], [2]	73	[0, 3], [6]	125	[1], [7]	177	-	229	[0], [2, 5, 6, 7]
22	[1, 2], [4]	74	[1], [3], [6]	126	-	178	-	230	-
23	-	75	[0, 1, 3], [6]	127	-	179	-	231	-
24	[3], [4]	76	-	128	-	180	[2], [4, 5, 7]	232	-
25	-	77	-	129	[0], [7]	181	[2], [0, 4, 5, 7]	233	-
26	[1], [3], [4]	78	-	130	[1], [7]	182	-	234	-
27	-	79	-	131	[0, 1], [7]	183	-	235	[2], [4]
28	[2, 3], [4]	80	[4], [6]	132	[2], [7]	184	-	236	-
29	-	81	[0, 4], [6]	133	[0], [2], [7]	185	-	237	-
30	[1, 2, 3], [4]	82	[1], [4], [6]	134	[1, 2], [7]	186	-	238	-
31	-	83	[0, 1, 4], [6]	135	[0, 1, 2], [7]	187	-	239	-
32	-	84	[4], [2, 6]	136	-	188	-	240	-
33	[0], [5]	85	[0, 4], [2, 6]	137	-	189	-	241	-
34	-	86	[1, 2, 6], [4]	138	[1], [3, 7]	190	[0], [6]	242	-
35	-	87	-	139	-	191	-	243	-
36	[2], [5]	88	[3], [4], [6]	140	-	192	-	244	-
37	[0], [2], [5]	89	[0, 3, 4], [6]	141	-	193	[0], [6, 7]	245	-
38	-	90	[1], [3], [4], [6]	142	-	194	[1], [6, 7]	246	-
39	-	91	[0, 1, 3, 4], [6]	143	-	195	[0, 1], [6, 7]	247	-
40	[3], [5]	92	[2, 3, 6], [4]	144	-	196	-	248	-
41	[0, 3], [5]	93	-	145	-	197	[0], [2, 6, 7]	249	-
42	[1, 5], [3]	94	[1, 2, 3, 6], [4]	146	[1], [4, 7]	198	-	250	-
43	-	95	-	147	-	199	-	251	-
44	[2, 3], [5]	96	-	148	[2], [4, 7]	200	-	252	-
45	[0, 2, 3], [5]	97	[0], [5, 6]	149	[2], [0, 4, 7]	201	-	253	-
46	-	98	-	150	[1, 2], [4, 7]	202	[1], [3, 6, 7]	254	-
47	-	99	-	151	-	203	-	255	-
48	-	100	-	152	-	204	-		
49	-	101	[0], [2, 5, 6]	153	-	205	-		
50	-	102	-	154	[1], [3, 4, 7]	206	-		
51	-	103	-	155	-	207	-		

Figure A.1: Grouped indices for every case in the marching cubes algorithm.

B

Surface curvature

B.1 Regular surfaces and fundamental forms

A definition of a *regular surface* in $\mathbb{R}^3$ is introduced following Do Carmo (2016),

DEFINITION 1 *Let $M \subset \mathbb{R}^3$ be a regular surface if, for each point $p \in M$, there exists a neighborhood $V \in \mathbb{R}^3$ and a map $\mathbf{x} : U \to V \cap M$ of an open set $U \subset \mathbb{R}^2$ onto $V \cap M$ such that,*

(i) $\mathbf{x}$ is differentiable i.e., if

$$\mathbf{x}(u, v) = (x(u, v), y(u, v), z(u, v)), \quad (u, v) \in U \tag{B.1}$$

the functions $x(u, v), y(u, v), z(u, v)$, have continuous partial derivatives.

(ii) $\mathbf{x}$ is a homeomorphism i.e., the inverse $\mathbf{x}^{-1} : V \cap M \to U$ is continuous since $\mathbf{x}$ is continuous by condition (i).

(iii) each map $\mathbf{x} : U \to M$ is a regular patch for which its Jacobian $J(x)(u, v)$ has rank 2 $\forall (u, v) \in U$.

With the parametrization of a regular surface shown above, the *first fundamental form* is defined so that measurements on the surface such as arc length, area and angles of tangent vectors can be made. The first fundamental form, denoted by I, is the inner product of tangent vectors, i.e.,

$$I(\mathbf{k}_p, \mathbf{l}_p) = \langle \mathbf{k}_p, \mathbf{l}_p \rangle \tag{B.2}$$

where $\langle \cdot, \cdot \rangle$ denotes the inner product of $\mathbf{k}_p, \mathbf{l}_p$ which are points belonging to the tangent space M at p, denoted by T_pM. If the tangent plane of the regular surface is defined by the tangent vectors $\{\mathbf{x}_u, \mathbf{x}_v\}$[1], then the first fundamental form satisfies,

$$I(a\mathbf{x}_u + b\mathbf{x}_v, a\mathbf{x}_u + b\mathbf{x}_v) = a^2E + 2abF + b^2G \tag{B.3}$$

The coefficients of (B.3) are given by,

$$E = ||\mathbf{x}_u||^2, \tag{B.4}$$

$$F = \mathbf{x}_u.\mathbf{x}_v, \tag{B.5}$$

$$G = ||\mathbf{x}_v||^2, \tag{B.6}$$

[1] $\mathbf{x}_u, \mathbf{x}_v$ are partial derivatives of $\mathbf{x}$ w.r.t. (u, v) and are defined as $\mathbf{x}_u = \left(\frac{\partial x}{\partial u}, \frac{\partial y}{\partial u}, \frac{\partial z}{\partial u}\right), \mathbf{x}_v = \left(\frac{\partial x}{\partial v}, \frac{\partial y}{\partial v}, \frac{\partial z}{\partial v}\right)$

To define the curvature of a surface, the *second fundamental form* on the regular surface M at a point p is defined as the symmetric bilinear form[2] on the tangent space,

$$II(\mathbf{k}_p, \mathbf{l}_p) = S(\mathbf{k}_p).\mathbf{l}_p \tag{B.7}$$

Here, S is the shape operator or the Weingarten map which is defined as,

$$S(m) = -D_m\mathbf{N} \tag{B.8}$$

where $\mathbf{N}$ is the unit normal of the regular surface M and $-D_m$ is the negative derivative along m. Therefore, $D_m\mathbf{N}$ signifies the variation of the tangent planes of M in the m direction which shows how M is curving in $\mathbb{R}^3$. (B.7) satisfies,

$$II(a\mathbf{x}_u + b\mathbf{x}_v, a\mathbf{x}_u + b\mathbf{x}_v) = a^2L + 2abM + b^2N \tag{B.9}$$

The coefficients of (B.9) are,

$$L = \mathbf{N}.\mathbf{x}_{uu}, \tag{B.10}$$

$$M = \mathbf{N}.\mathbf{x}_{uv} = \mathbf{N}.\mathbf{x}_{vu}, \tag{B.11}$$

$$N = \mathbf{N}.\mathbf{x}_{vv} \tag{B.12}$$

These coefficients can also be expressed in terms of E, F, G as follows,

$$L = \frac{\det(\mathbf{x}_{uu}, \mathbf{x}_u, \mathbf{x}_v)}{\sqrt{EG - F^2}}, \tag{B.13}$$

$$M = \frac{\det(\mathbf{x}_{uv}, \mathbf{x}_u, \mathbf{x}_v)}{\sqrt{EG - F^2}} = \frac{\det(\mathbf{x}_{vu}, \mathbf{x}_u, \mathbf{x}_v)}{\sqrt{EG - F^2}}, \tag{B.14}$$

$$N = \frac{\det(\mathbf{x}_{vv}, \mathbf{x}_u, \mathbf{x}_v)}{\sqrt{EG - F^2}} \tag{B.15}$$

B.2 Principal, Gaussian and mean curvatures

The *normal curvature*, denoted by k of a regular surface M is defined in terms of the shape operator as,

$$k(\mathbf{t}_p) = S(\mathbf{t}_p).\mathbf{t}_p \tag{B.16}$$

where t_p is a unit tangent vector at a point $p \in M$. For any non-zero tangent vector v_p, (B.16) becomes,

$$k(\mathbf{v}_p) = \frac{S(\mathbf{v}_p).\mathbf{v}_p}{||\mathbf{v}_p||^2} = \frac{II(\mathbf{v}_p, \mathbf{v}_p)}{I(\mathbf{v}_p, \mathbf{v}_p)} = \frac{a^2L + 2abM + b^2N}{a^2E + 2abF + b^2G} \tag{B.17}$$

[2]The symmetric bilinear form is a bilinear function $Q : V \times V \to \mathbb{R}$ which maps a pair of elements (u, v) from a vector space V such that $Q(u, v) = Q(v, u) \quad \forall u, v \in V$.

	$k_1 < 0$	$k_1 = 0$	$k_1 > 0$
$k_2 < 0$	peak	ridge	saddle
$k_2 = 0$	ridge	flat	valley
$k_2 > 0$	saddle	valley	pit

Table B.1: Surface shapes with the signs of principal curvatures k_1 and k_2. Table is extracted from figure 3.4(a) of Besl (2012).

The maximum and minimum values of k are called the *principal curvatures* and are denoted as k_1 and k_2 respectively. They are formally defined as the eigenvalues of the shape operator $S(p)$. A possible method of distinguishing surface shapes with the signs of principal curvatures alone is discussed by Besl (2012) which results in six basic shapes which are peak, ridge, saddle, flat, valley and pit (see table B.1).

The *Gaussian curvature* of a regular surface at point p can be defined with the shape operator as,

$$K(p) = \det(S(p)) \tag{B.18}$$

In terms of the first and second fundamental forms, it can be written as,

$$K = \frac{\det(II)}{\det(I)} = \frac{LN - M^2}{EG - F^2} \tag{B.19}$$

or equivalently with principal curvatures,

$$K = k_1 k_2 \tag{B.20}$$

A point p is classified as elliptic or hyperbolic if $K(p) > 0$ or $K(p) < 0$ respectively. Similarly, when $K(p) = 0$ but $S(p) \neq 0$, the point is said to be parabolic and when $K(p) = 0$ but $S(p) = 0$, the point is said to be planar. If $K > 0$ everywhere on the surface, the surface is called synclastic. An anticlastic surface ensues when $K < 0$ everywhere on the surface.

The *mean curvature* of a regular surface at point p is formally defined with the shape operator as,

$$H(p) = \frac{1}{2}\mathrm{tr}(S(p)) \tag{B.21}$$

In terms of the first and second fundamental forms, it can be written as,

$$H = \frac{1}{2}\frac{LG - 2MF + NE}{EG - F^2} \tag{B.22}$$

or equivalently with principal curvatures,

$$H = \frac{k_1 + k_2}{2} \tag{B.23}$$

Using (B.20) and (B.23), the principal curvatures can be written in terms of the Gaussian and mean curvatures as,

	$K < 0$	$K = 0$	$K > 0$
$H < 0$	peak	ridge	saddle ridge
$H = 0$	(none)	flat	minimal
$H > 0$	pit	valley	saddle valley

Table B.2: Surface shapes with the signs of Gaussian K and mean curvature H. Table is extracted from figure 3.4(b) of Besl (2012).

$$k_1 = H + \sqrt{H^2 - K}, \qquad k_2 = H - \sqrt{H^2 - K} \tag{B.24}$$

An important property of Gaussian curvature is that it is invariant under local isometry i.e., it is an intrinsic property of the surface depending only on its first fundamental form and not on the embedding of the surface in a higher dimensional space. This result was shown in Gauss' *Theorema Egregium*. On the other hand, the mean curvature is an extrinsic property of the surface and depends upon its embedding. For instance, the surface of a sheet of paper on a flat table has $K = 0$ and $H = 0$. Bending the paper without kinks will result in $H \neq 0$ but $K = 0$ as the intrinsic properties of the surface remain unchanged. However, if the paper were to deform (like rubber) while bending then K would also change. Similar to using the signs of principal curvatures, Besl (2012) suggests another method to determine surface shapes with the signs of H and K (see table B.2). This results in eight basic shapes being identified with saddle surfaces split into saddle ridges, saddle valleys and minimal surfaces. The shapes of all eight surfaces can be seen in figure 3.5 of Besl (2012).

B.3 Shape index and curvedness

Koenderink and Van Doorn (1992) introduced two measures of local surface shape, namely the *shape index* Υ and *curvedness* Λ which are defined as,

$$\Upsilon = -\frac{2}{\pi} \arctan\left(\frac{\kappa_1 + \kappa_2}{\kappa_1 - \kappa_2}\right), \quad \Lambda = \sqrt{\frac{\kappa_1^2 + \kappa_2^2}{2}} \tag{B.25}$$

and in terms of K and H, they can be expressed as,

$$\Upsilon = -\frac{2}{\pi} \arctan\left(\frac{H}{\sqrt{H^2 - K}}\right), \quad \Lambda = \sqrt{2H^2 - K} \tag{B.26}$$

The shape index is a dimensionless parameter in the range $[-1, 1]$. At the extreme ends where $\Upsilon = \pm 1$, the surface represents spherical shapes such as a cup ($\Upsilon = -1$) or cap ($\Upsilon = 1$). Minor variations from spherical shapes pushes the value of Υ towards cylindrical shapes ($\Upsilon = \pm 0.5$), thereby making $\Upsilon = \pm 1$ to be the endpoints of the shape scale. In the range, $0.5 < |\Upsilon| < 1$, the shape is ellipsoidal becoming more sphere-like when $|\Upsilon| \to 1$ and more cylinder-like when $|\Upsilon| \to 0.5$. For $-0.5 < \Upsilon < 0.5$, the shapes are saddle-like with a symmetrical saddle at $\Upsilon = 0$. The shape index scale provides a continuous gradation from concave shapes ($\Upsilon < 0$) to symmetrical saddle ($\Upsilon = 0$) to convex shapes ($\Upsilon > 0$). Koenderink and Van Doorn (1992) divide it into nine categories as illustrated in figure 5 of their paper.

The curvedness parameter which measures the intensity of surface curvature has a dimension of reciprocal length. For a unit sphere and unit saddle, the curvedness is unity. Unlike Gaussian curvature which vanishes for cylindrical shapes, the curvedness of a unit cylinder is $1/\sqrt{2}$ and curvedness becomes null for a planar patch, for which $k_1 = k_2 = 0$. As noted by Koenderink and Van Doorn (1992), while the information present within the shape index and curvedness parameters are formally equivalent to either the two principal curvatures or Gaussian and mean curvatures, the main advantage is the decoupling of size and shape of a surface i.e., the shape index alone can specify the shape with a single number while curvedness specifies the size.

C

Geometry of structures for case S_2 and S_3

C.1 Viscous sublayer

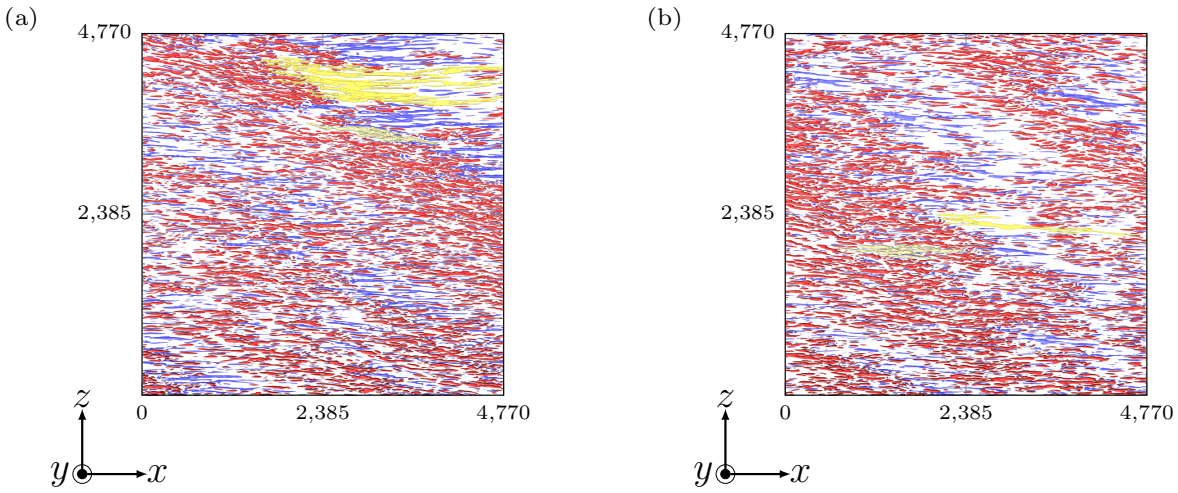

Figure C.1: Isosurfaces of $u' < 0$ (low-speed streak) and $u' > 0$ (high-speed streak) are shown for case (a) S_2 and (b) S_3 in the viscous sublayer with grid C. The color specification for the structures is according to table 2.1 for the low-and high-speed streak. The longest structure for the former is highlighted with light green and the longest structure for the latter is highlighted in pale yellow.

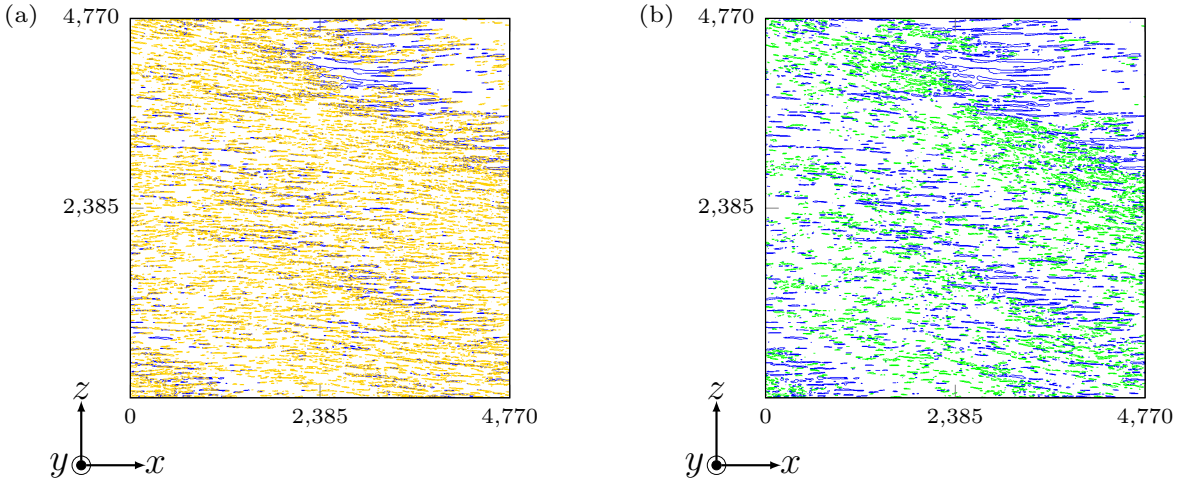

Figure C.2: Contour plots for case S_2 are shown with (a) ejections and low-speed streaks, (b) sweeps and low-speed streaks at $y^+ \approx 3.58$ with grid C. The color specification is according to table 2.1.

C. Geometry of structures for case S_2 and S_3

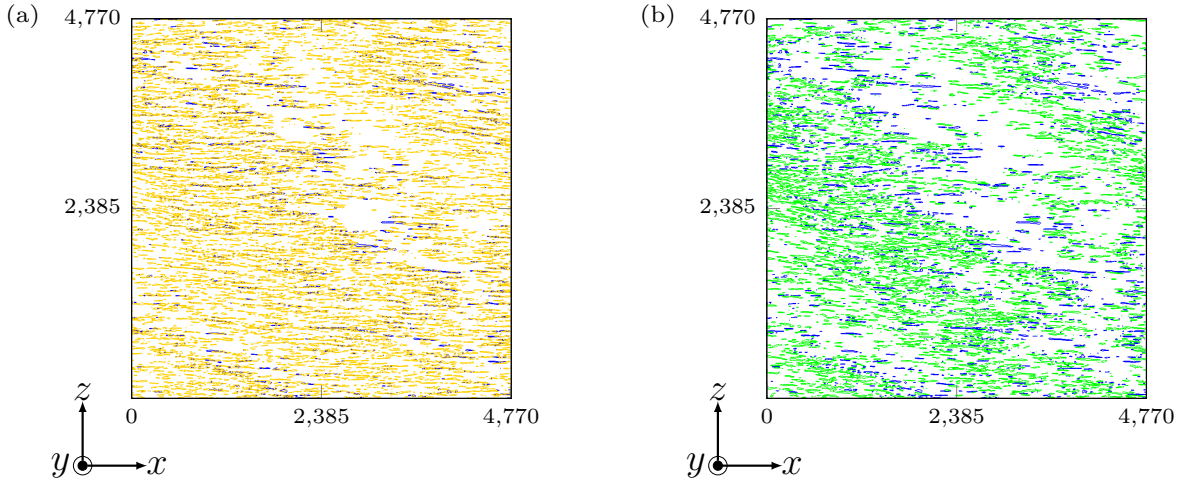

Figure C.3: Contour plots for case S_3 are shown with (a) ejections and low-speed streaks, (b) sweeps and low-speed streaks at $y^+ \approx 3.58$ with grid C. The color specification is according to table 2.1.

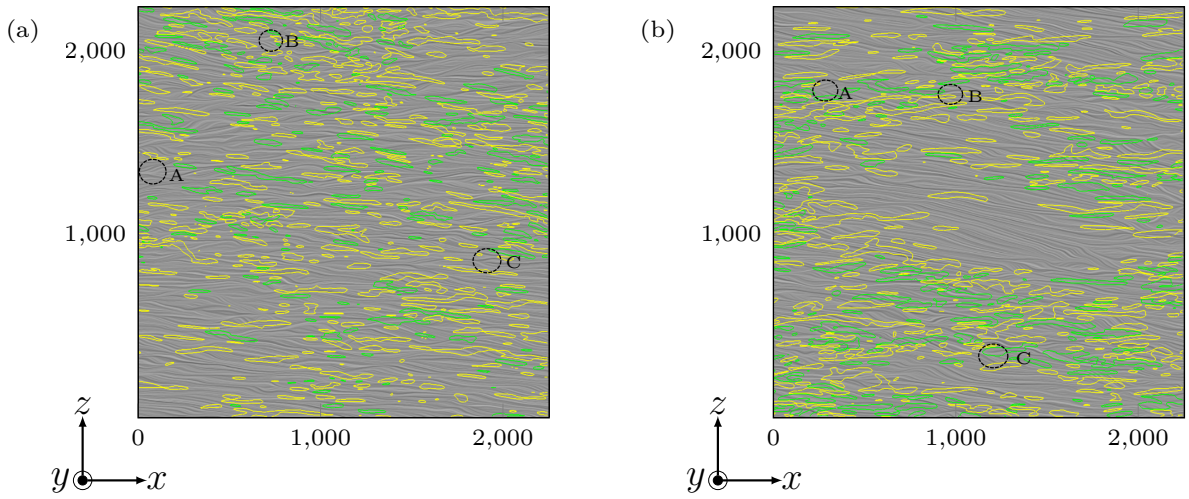

Figure C.4: Three pocket regions are highlighted with diverging streamlines for (a) case S_2 and (b) case S_3 at $y^+ \approx 3.58$. Overlayed are sweeps and ejections. Color specification for sweeps and ejections is according to table 2.1.

C.2 Buffer layer

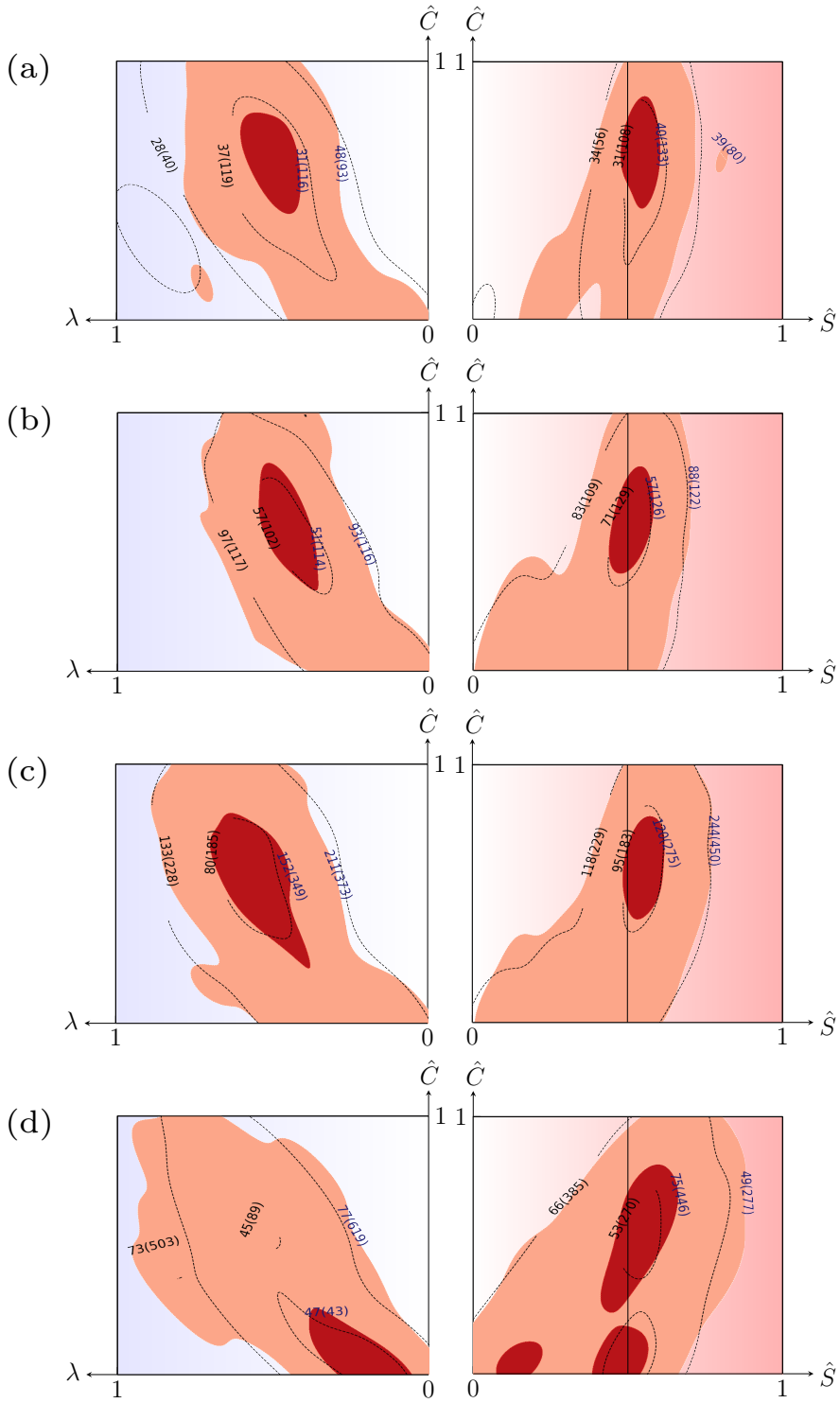

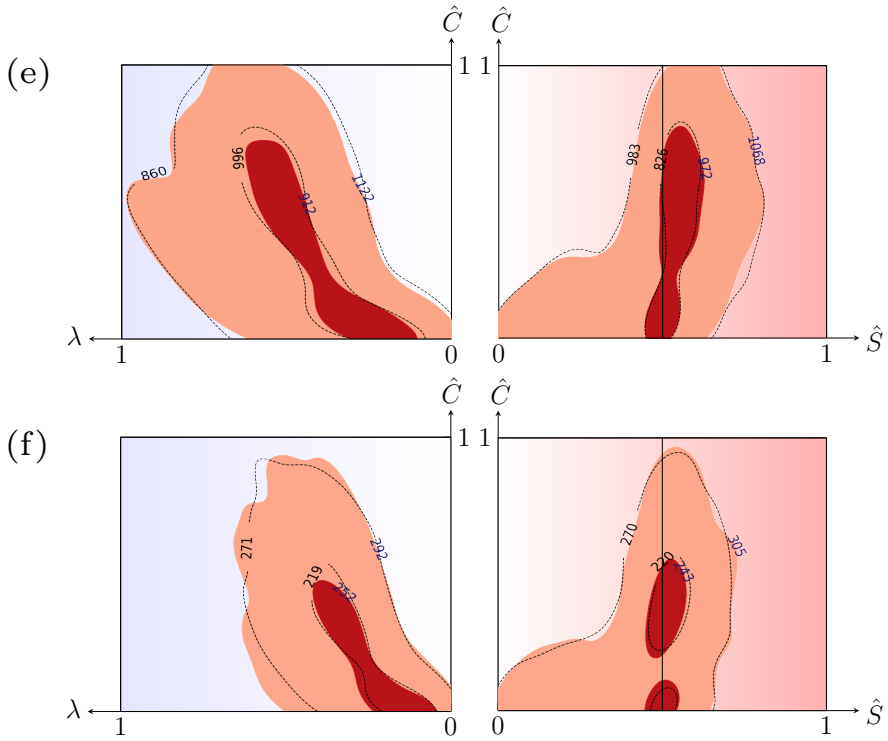

Figure C.5: Similar to figure 3.6, visualization space for all quantitative Robinson structures except backs are shown with joint pdfs. From (a - f) are the high-speed streaks, low-speed streaks, sweeps, ejections, vortices and shear layers. The geometry of structures is compared between case S_3 (unfilled contours with dashed lines) and case S_2 (filled cotours). The number of structures for each contour level is indicated in black for case S_3 and dark blue for case S_2. Numbers within paranthesis (a - d) are those which start from the viscous sublayer and end in the buffer layer. Numbers outside paranthesis are those which start and end within the buffer layer itself. $\hat{S}, \hat{C}, \lambda$ are the shape index, curvedness and stretching parameters respectively.

C.3 Inner and outer layer

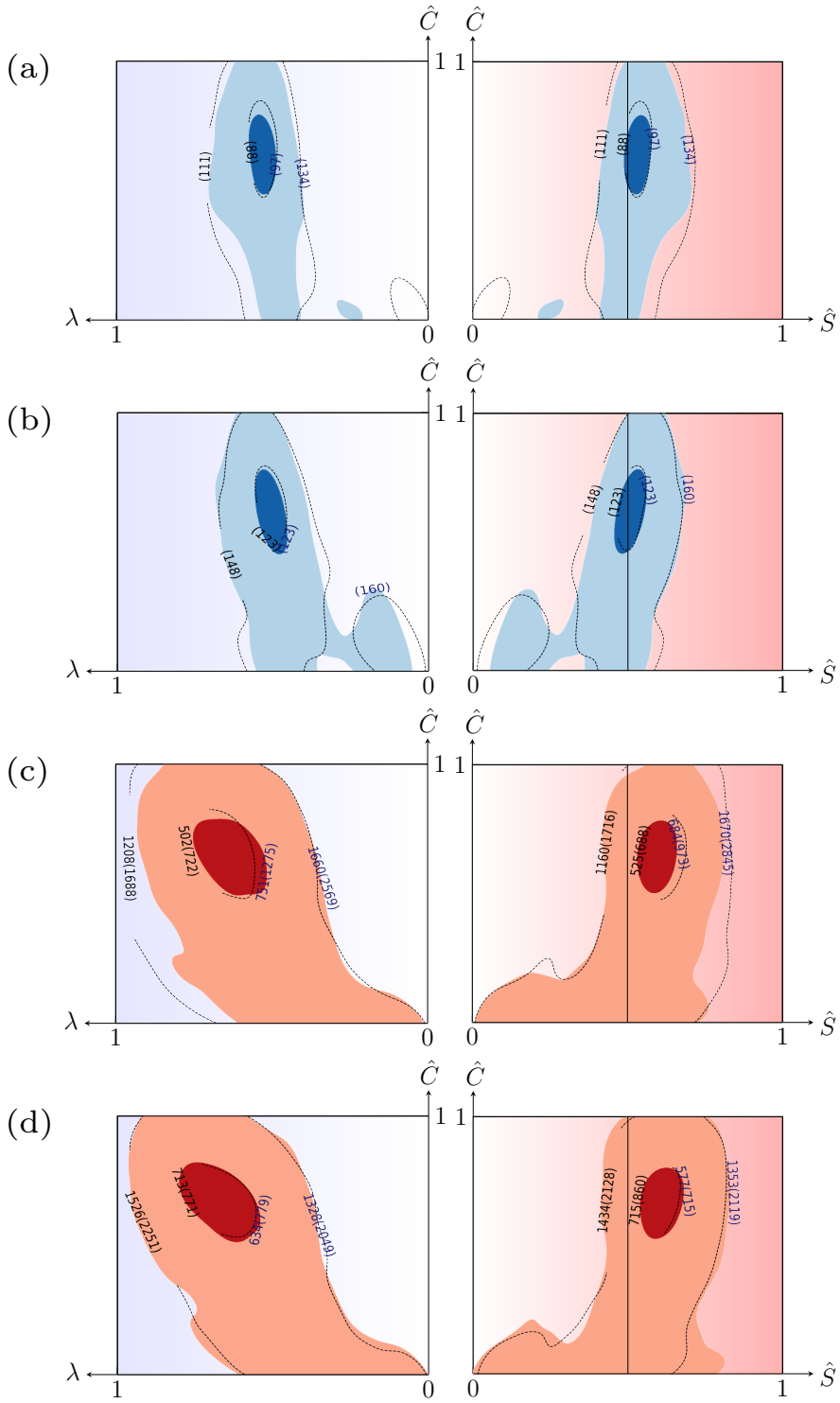

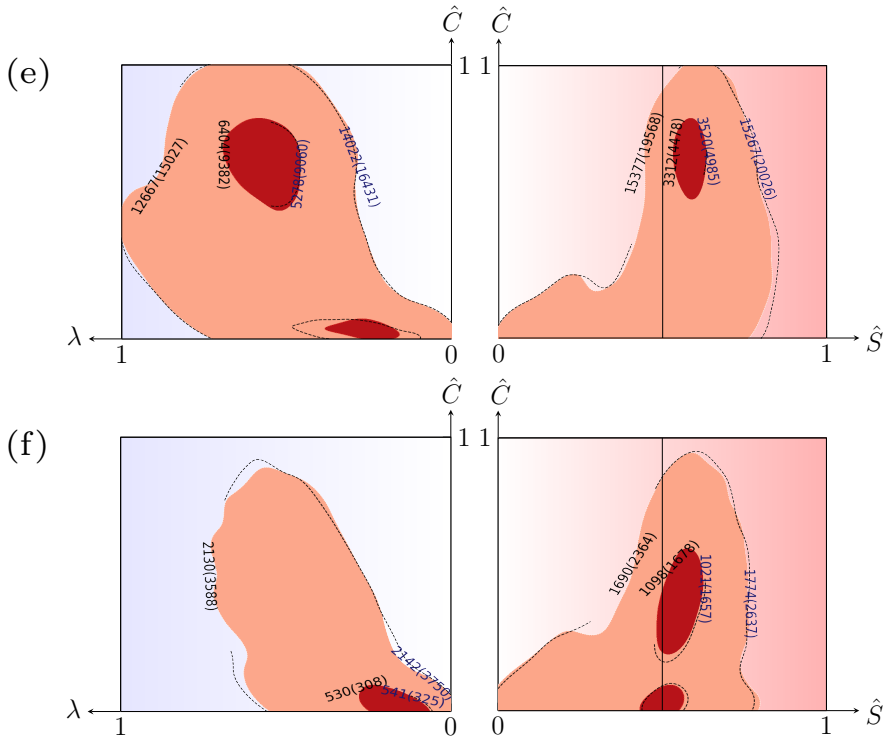

Figure C.6: Similar to figure 3.10, visualization space for all quantitative Robinson structures except backs are shown with joint pdfs. From (a - f) are the high-speed streaks, low-speed streaks, sweeps, ejections, vortices and shear layers. The geometry of structures is compared between case S_3 (unfilled contours with dashed lines) and case S_2 (filled cotours). The number of structures for each contour level is indicated in black for case S_3 and dark blue for case S_2. Numbers within paranthesis (a - d) are those which start from the viscous sublayer and end in the outer layer. Numbers outside paranthesis are those which start beyond the buffer layer and end within the outer layer. $\hat{S}, \hat{C}, \lambda$ are the shape index, curvedness and stretching parameters respectively.

C.4 $\delta-$scale structures

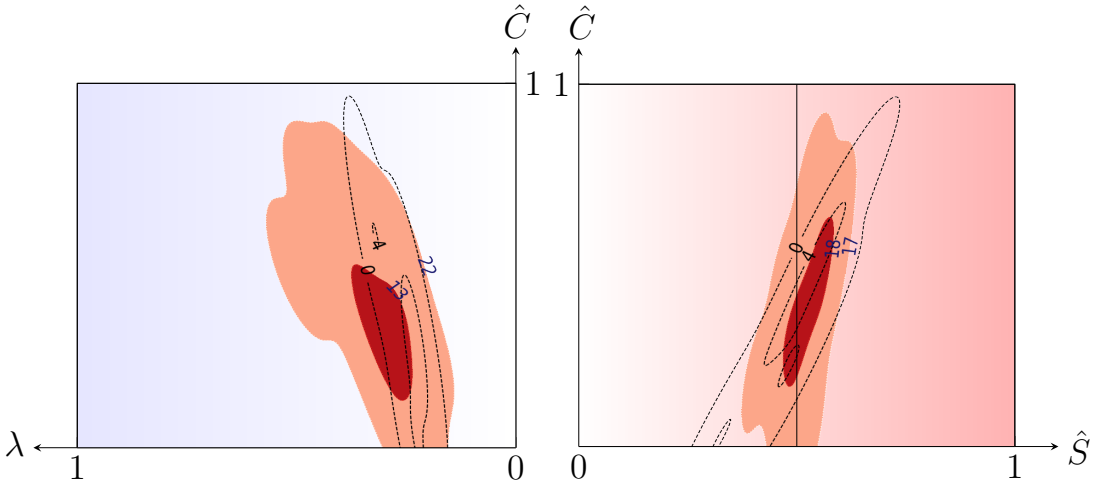

Figure C.7: Visualization space for backs is shown for case S_3 with unfilled contours and S_2 with filled contours. The number of structures between contours are indicated in dark blue for case S_2 and black for case S_3. $\hat{S}, \hat{C}, \lambda$ are the shape index, curvedness and stretching parameters respectively.

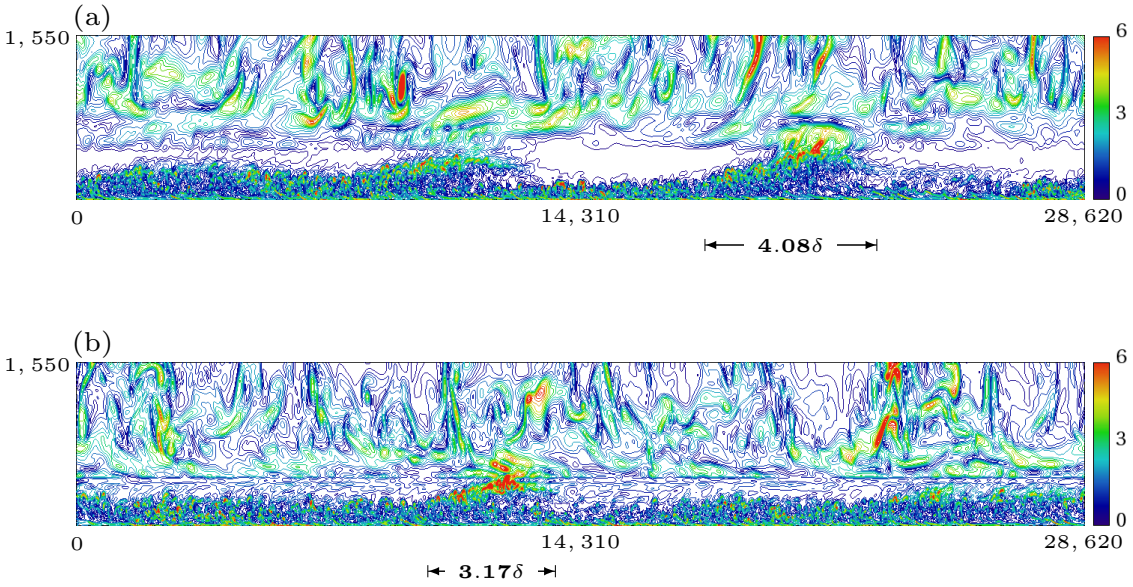

Figure C.8: Vorticity magnitude contours along the (x, y) plane are shown here for case (a) S_2 and (b) S_3 for grid A until $y^+ \approx 1550$. For each case, a $\delta-$scale bulge is highlighted. The wall-normal direction is exaggerated three times to show the structures clearly.

C.5 Hairpin-like structures

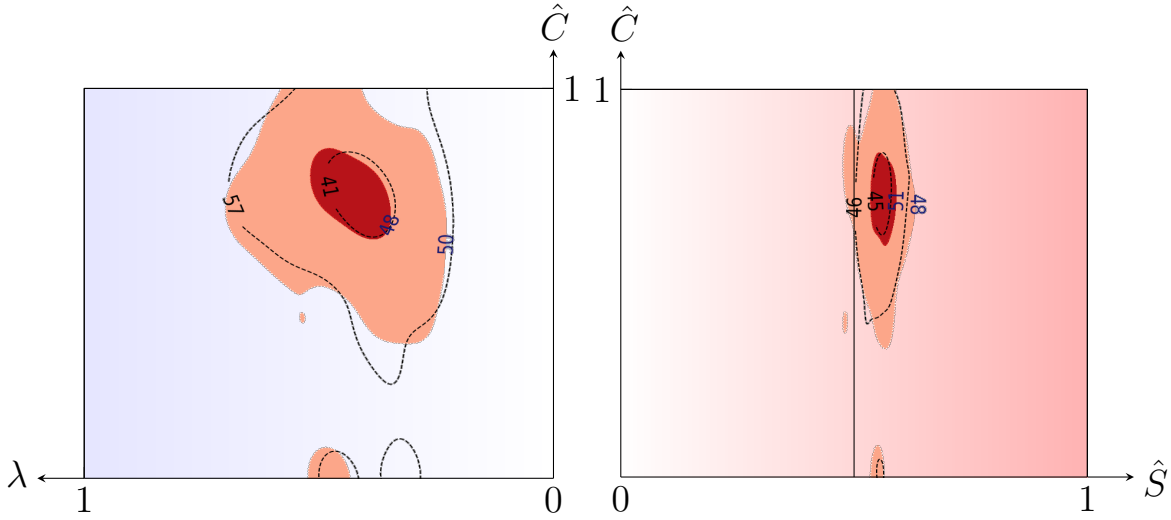

Figure C.9: Geometry of 100 hairpin-like structures are compared in the visualization space for case S_2 (filled contours) and S_3 (unfilled contours). $\hat{S}, \hat{C}, \lambda$ are the shape index, curvedness and stretching parameters respectively.

D

Supporting results for chapter 4

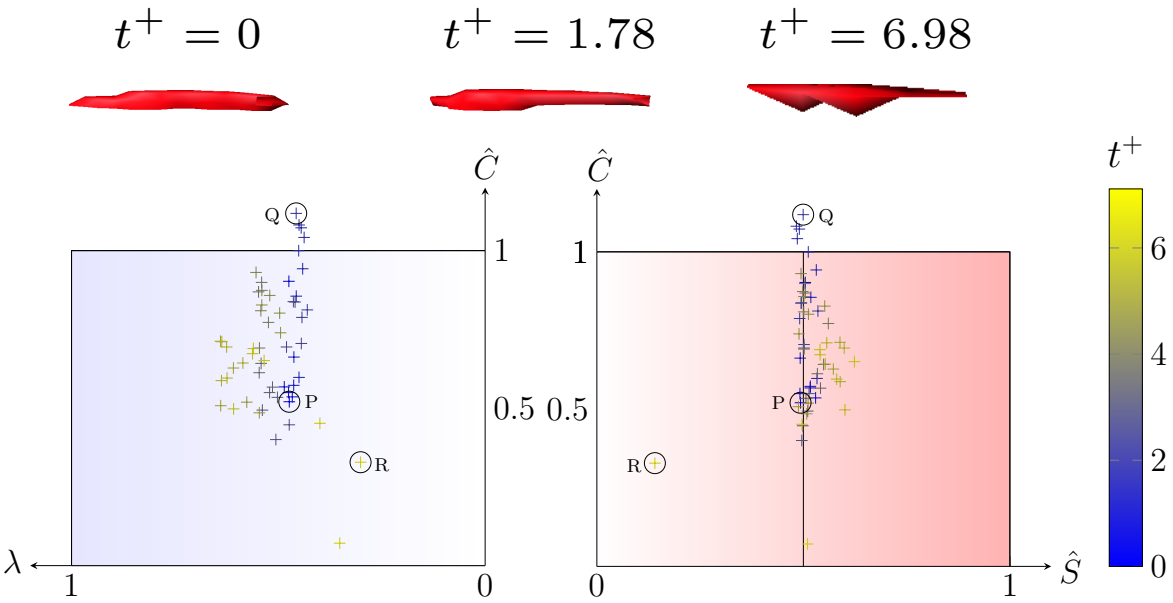

Figure D.1: Top panel shows the isosurfaces of a tracked high-speed streak at different viscous times for the case S_2. The temporal evolution of the geometry of this streak is shown in the bottom panel. P, Q, R correspond to viscous times $t^+ = 0, 1.78, 6.98$ respectively.

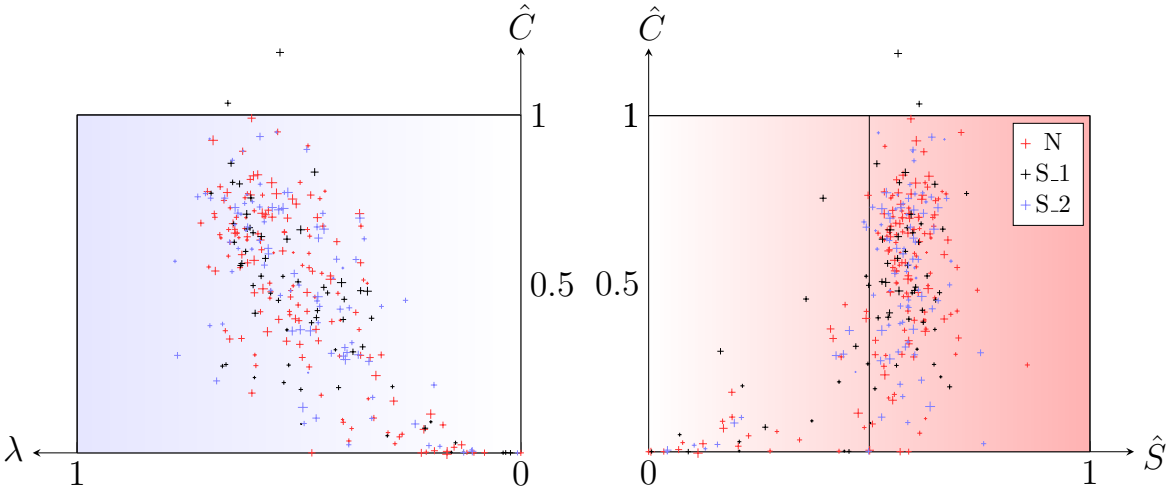

Figure D.2: The final time instant for all tracked vortex structures are shown for stably stratified (S_1, S_2) and neutrally stratified (N) cases. The size of the markers represents (in logarithmic scale) the volume of the structure.

E

Data and code availability

All Ekman flow datasets analyzed in this thesis can be requested from Dr. Cedrick Ansorge. A subset of it, pertaining to Chapter 3, is available at the Mathematics institute of the Freie Universität Berlin. It contains 5 uncorrelated instantaneous snapshots for all flow cases (N, S_1, S_2 and S_3) and is stored at /bigdata/ag_klima/. Please contact the Mathematics institute or Prof. Rupert Klein for further details. The mean velocity profiles for all Ekman flow cases have been made available as a part of the slender vortex filament code and can be accessed at https://github.com/Phoenixfire1081/SlenderVortexSimulation/.

A major effort has been made to make the codes as fast and efficient as possible to analyze these large datasets. Most of the codes used this thesis are available at https://github.com/Phoenixfire1081. Some python codes can be installed with the pip package manager. An ongoing effort is being directed towards making all programs pip installable. Detailed instructions on usage of these programs have been provided.

It should be noted that the geometry calculations, particularly Shape Index and Curvedness have been carried out with the visualization software Amira, which was available as a part of our collaboration with the Zuse Institute Berlin. The codes for tracking of coherent structures including MLPT, performed in chapter 4, were also made to work with Amira. These codes have not been made available online but can be requested from the author. Most visualizations in this thesis were also produced with this software.